Speciation, techniques and facilities for radioactive materials at synchrotron light sources

Actinide XAS 2008

Proceedings of the 5ᵗʰ workshop
Saint-Aubin, France
15-17 July 2008

NUCLEAR ENERGY AGENCY
Organisation for Economic Co-operation and Development

ORGANISATION FOR ECONOMIC CO-OPERATION AND DEVELOPMENT

The OECD is a unique forum where the governments of 30 democracies work together to address the economic, social and environmental challenges of globalisation. The OECD is also at the forefront of efforts to understand and to help governments respond to new developments and concerns, such as corporate governance, the information economy and the challenges of an ageing population. The Organisation provides a setting where governments can compare policy experiences, seek answers to common problems, identify good practice and work to co-ordinate domestic and international policies.

The OECD member countries are: Australia, Austria, Belgium, Canada, the Czech Republic, Denmark, Finland, France, Germany, Greece, Hungary, Iceland, Ireland, Italy, Japan, Korea, Luxembourg, Mexico, the Netherlands, New Zealand, Norway, Poland, Portugal, the Slovak Republic, Spain, Sweden, Switzerland, Turkey, the United Kingdom and the United States. The Commission of the European Communities takes part in the work of the OECD.

OECD Publishing disseminates widely the results of the Organisation's statistics gathering and research on economic, social and environmental issues, as well as the conventions, guidelines and standards agreed by its members.

This work is published on the responsibility of the Secretary-General of the OECD. The opinions expressed and arguments employed herein do not necessarily reflect the official views of the Organisation or of the governments of its member countries.

NUCLEAR ENERGY AGENCY

The OECD Nuclear Energy Agency (NEA) was established on 1st February 1958 under the name of the OEEC European Nuclear Energy Agency. It received its present designation on 20th April 1972, when Japan became its first non-European full member. NEA membership today consists of 28 OECD member countries: Australia, Austria, Belgium, Canada, the Czech Republic, Denmark, Finland, France, Germany, Greece, Hungary, Iceland, Ireland, Italy, Japan, Luxembourg, Mexico, the Netherlands, Norway, Portugal, Republic of Korea, the Slovak Republic, Spain, Sweden, Switzerland, Turkey, the United Kingdom and the United States. The Commission of the European Communities also takes part in the work of the Agency.

The mission of the NEA is:

– to assist its member countries in maintaining and further developing, through international co-operation, the scientific, technological and legal bases required for a safe, environmentally friendly and economical use of nuclear energy for peaceful purposes, as well as

– to provide authoritative assessments and to forge common understandings on key issues, as input to government decisions on nuclear energy policy and to broader OECD policy analyses in areas such as energy and sustainable development.

Specific areas of competence of the NEA include safety and regulation of nuclear activities, radioactive waste management, radiological protection, nuclear science, economic and technical analyses of the nuclear fuel cycle, nuclear law and liability, and public information.

The NEA Data Bank provides nuclear data and computer program services for participating countries. In these and related tasks, the NEA works in close collaboration with the International Atomic Energy Agency in Vienna, with which it has a Co-operation Agreement, as well as with other international organisations in the nuclear field.

Foreword

"Actinide-XAS" is a series of workshops on Speciation, Techniques and Facilities for Radioactive Materials at Synchrotron Light sources, which provides every two or three years a unique opportunity for scientists involved in the field as well as newcomers, to present, discuss and exchange on the applications and results from synchrotron-based techniques in radionuclide/actinide sciences. Previous editions of the workshop were held in Grenoble, France (1998 and 2000), in Berkeley, USA (2004) and in Karlsruhe, Germany (2006).

Ten years after the inaugural conference, "Actinide-XAS-2008", the 5th edition in the series, was successfully held in Saint-Aubin (near Paris) from 15-17 July 2008 at Synchrotron SOLEIL, where MARS, the new French hard X-ray beamline dedicated to the study of radioactive matter, will be opening to users in 2009.

The workshop was co-organised by SOLEIL, the *Comissariat à l'Energie Atomique* (CEA) and the *Centre National de la Recherche Scientifique* (CNRS), and was financially supported by SOLEIL, CEA, the interdisciplinary programme PACEN of the CNRS, the region Ile-de France, OECD's Nuclear Energy Agency (NEA) for the proceedings publication, and the European Network of Excellence for Actinide Sciences (ACTINET) for the payment of the participation of students and post-docs. Also, for the first time, the workshop was organised as a satellite meeting of the 5th edition of the international topical conference on plutonium and actinides, Plutonium Futures –The Science 2008 (held in Dijon).

More than one hundred people registered for the conference and 83 were effectively present. The audience was composed of 61 scientists or staff members, 15 post-doctoral students and 7 PhD students originating from laboratories belonging to 10 different countries, including the United States, Japan and Russia.

Table of contents

---

* The full papers being unavailable at the time of publication, only the abstracts are included.

Executive summary

The world-wide increasing capability for performing studies on radioactive samples on partially or fully dedicated beamlines, in particular in Europe on beamlines such as INE at ANKA, ROBL at ESRF, MicroXAS at SLS and MARS at SOLEIL, has stimulated a surge in synchrotron-based radioactive investigations covering a diverse range of applied and basic research, spanning, for example, from nuclear waste disposal research to superconductivity in actinide materials. These three days were thus the occasion to present and discuss the latest results of research on radionuclides and actinides based on a wide range of synchrotron techniques (X-ray absorption spectroscopy, high resolution inelastic X-ray scattering, resonant magnetic soft X-ray scattering, diffraction, surface diffraction, and micro-focused fluorescence analysis).

On the first day, the conference was opened by Prof. Michel van der Rest, general director of SOLEIL who welcomed the audience and briefly presented the status of SOLEIL. This was followed by the first topical session dedicated to "Solution and Co-ordination Chemistry of the Radionuclides", with presentations related to the general co-ordination properties of actinide complexes or more directly related with the nuclear fuel cycle (extraction and separation processes, in particular with ion melts).

The afternoon started with the second session dedicated to "Radionuclides in Environmental and Life Sciences", with presentations on the interaction of actinides with bacterial strains or bioligands, as well as presentations on interactions with cement systems and groundwater systems. The evening followed with the poster session and a banquet in SOLEIL's central hall.

On the following day, the first session in the morning was dedicated to "Solid State Chemistry and Physics of the Radionuclides", with presentations related to the general electronic or vibrational properties of the actinides or more directly related to radiation damage problems or to the improvement of nuclear fuels.

The workshop continued in the afternoon with the session dedicated to "Modelling and Simulations Tools", with presentations on the quantum chemistry of actinide complexes, on the simulations of electronic and magnetic structures of actinide metals, and on the molecular dynamics of hydrated lanthanides. This was followed by a guided visit of the SOLEIL facility and in particular of the MARS beamline. The evening was then concluded with a marvellous cruising dinner on the Seine in Paris.

The final topical session was held on the third day and was dedicated to "Facility Tools and Upcoming techniques", with presentations on the European beamlines dedicated to radionuclide studies, and on the ALS and SPring-8 synchrotrons. The meeting was then closed by a synthesis presented by Dr. Steven Conradson and a discussion with the participants moderated by the chairman.

The latest results were presented in roughly 30 contributed talks and 26 poster contributions. Fruitful and intense scientific discussions were achieved during the meeting and particularly during the poster and closing sessions and also during the evening reception and the social dinner on the "bateau-mouche". On this occasion Dr. Tsuyoshi Yaita was invited to organise the 6th edition of the Actinide-XAS workshop series, which is foreseen to take place at SPring-8, Japan, in September 2010.

The present proceedings includes the written contributions related to all the oral and poster presentations that were held during the workshop. Several contributions appear as brief articles which have been peer reviewed; the remainder appear just as abstracts.

We are grateful to all the persons at SOLEIL that have helped us in organising the event, to the members of the Local Organising Committee and of the International Scientific Advisory Committee, to the sponsoring institutions and to all the participants and contributors to these proceedings.

Bruno Sitaud, Pier Lorenzo Solari, Stéphane Lequien

Group picture of the participants in front of Synchrotron Soleil

Session I

Solution and co-ordination
chemistry of the radionuclides

Chair: Tobias Reich

EXAFS investigation of uranium(VI)-*N,N*-dialkylamide complexes

Shinichi Suzuki, Tsuyoshi Yaita, Yoshihiro Okamoto, Hideaki Shiwaku
Actinide Co-ordination Chemistry Group, Synchrotron Radiation Research Centre (SRRC)
Quantum Beam Science Directorate, Japan Atomic Energy Agency (JAEA)
2-4 Shirakatashirane, Tokai-mura, Naka-gun, Ibaraki 319-11958, Japan

Abstract

Recovery of uranium with a high decontamination factor from spent nuclear fuels that includes about 95% uranium for light water reactor (LWR) and about 85% uranium for fast breeder reactor (FBR) is a key technique for a reprocessing during the transition periods from LWR to FBR cycle. However, the requirements for the process development are gradually becoming severe as time progresses, e.g. economic efficiency, environmental loading, nuclear proliferation etc.

On background, we have focused on the local structures around the metal in various kinds of these extracted complexes to understand the extraction mechanism and design a new separation process. In this presentation, the following topics will be introduced. U(VI)-N,N-di-alkylamides extraction system: branched N,N-di-alkylamides, showing a high separation factor of An(VI) over An(IV), make it possible to reduce the decontamination process of UO_2^{2+} from Pu^{4+} in a reprocessing. So, the structural analysis of the extracted complexes, i.e. $UO_2(NO_3)_2(amide)_2$, are performed by EXAFS. This selective separation of UO_2^{2+} has been believed to be due to only steric hindrance of BAMA on the complexation with the metals. The steric property around oxygen donor is more dominant for uranium extraction by N,N-dilakylamides than donor ability of oxygen.

Introduction

In the development for the fast breeder reactor (FBR) fuels cycle, uranium isolation is an important step because uranium is the principal ingredient of spent nuclear fuel (SF), and isolation of U can simplify the following process for the recovery of transuranics (TRU). Until now, the uranium isolation techniques based on the solvent extraction technique are the UREX (Uranium Extraction) process and the ARTIST (Amide-Based Radio-Resourced Treatment Interim Storage of Transuranics) process [1]. The UREX process used tri-butyl-phosphate (TBP) with acetohydroxamic acid (AHA) as reduction reagent for plutonium and neptunium. On the other hand, the ARTIST process used only branching alkyl chain introduced *N,N*-dialkyl monoamides for U(VI) isolation.

N,N-dialkyl monoamides are noted as one of the alternative extractants of tri-butyl phosphate (TBP) in the field of nuclear fuel reprocessing [2-9]. Extraction behaviour of U(VI) and Pu(IV) with N,N-dialkylamides is almost similar to those with TBP. *N,N*-dialkyl monoamides have some advantages, namely, their complete incinerability (CHON principle) and high stability for hydrolysis and radiolysis. Further, the synthesis of *N,N*-dialkyl monoamides is relatively easy.

In our laboratory, the innovative chemical separation process (ARTIST), has been proposed, which is organised by the solvent extraction techniques. The mutual separation of U, TRU and fission products (FP) is included into the schematic diagram of the ARTIST process, and our goal is to establish a simple process for the treatment of SF. One of the main steps of the ARTIST is the isolation of uranium from SF by branched alkyl monoamide (BAMA). The BAMA extractants have steric hindrance on the co-ordination with actinide ions, which gives higher distribution coefficient of U(VI) than that of Pu(IV). In previous a paper, the extraction behaviour of U(VI), Pu(IV), Np(IV) and Np(VI) by several kinds of BAMA has been reported [10]. The BAMA extractants have steric hindrance on the co-ordination with actinide ions, which gives higher distribution coefficients of U(VI) and Np(VI) than those of Pu(IV) and Np(IV).

In order to understand the extraction behaviour of U, Pu and Np with BAMA and to investigate the basic characteristic of actinide elements, the complex structures of U, Pu and Np-BAMA in the solution is important and indispensable. Furthermore, the complex structure of extracted species shows the important information for molecular design, especially BAMA structure design. However, in the research on *N,N*-dialkyl monoamide compounds until now, the report about extracted complex structures of U, Pu and Np is little [11-16].

In this study, local structure analysis of BAMA-U(VI) complexes was carried out by extended X-ray absorption fine structure (EXAFS) spectroscopy, and the correlation between the bond distance of carbonyl oxygen with U and the distribution coefficient was examined.

Experimental

Chemicals
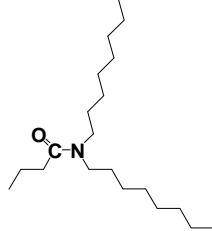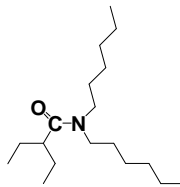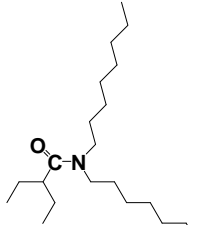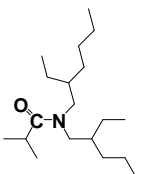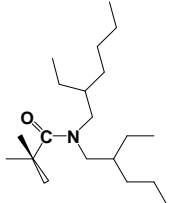
Six kinds of *N,N*-dialkyl amides: *N,N*-dioctylbutanamide (DOBA), *N,N*-dihexyl(2-ethyl) butanamide (DH2EBA), *N,N*-dioctyl(2-ethyl)butanamide (DO2EBA), *N,N*-di-(2-ethyl)hexyl(2-methyl)propanamide (D2EHMPA), *N,N*-di(2-ethyl)hexyl(2,2-dimethyl)propanamide (D2EHDMPA) were synthesised. The synthetic method is described in a previous paper [9]. The carboxylic chloride reacted with the secondary amine dissolved in chloroform at 273 K, and tri-ethylamine as a scavenger of chloride was also added in the glass reactor. The mixture was stirred for several hours, and then the sample was washed with water, 1.0 mol/L HCl and 1.0 mol/L NaOH in order to remove mainly the quaternary ammonium salt and the initial materials. The organic samples obtained were purified by distillation under vacuum. All amide compounds were identified by NMR (UNITY plus 400, Varian), FT-IR (FTS-135, BIO-RAD), Liquid Chromatography (LC-7100, Hitachi) and Gas Chromatography (GC-14A, Shimadzu). The high degree of purity of these *N,N*-dialkylamides was confirmed by gas chromatography: DOBA 97.0%, DH2EBA 99.7%, DO2EBA 97.0%, D2EHMPA 99.7%, D2EHDMPA 99.0%, respectively. The structures of used *N,N*-dialkyl amides are shown in Table 1.

The distribution ratio (*D*) of uranium: D_U and plutonium: D_{Pu} were defined as the concentration ration of the metal ion in the organic phase to that in the aqueous phase.

The U(VI) extraction mechanism of amides involves a solvation mechanism similar to other oxygen donor extractant like TBP. As with TBP, the extracted complex appears to be two *N,N*-dialkylamides associate with the uranium complex.

Table 1: *N,N*-dialkylamide structure in this study and comparison of distribution ratio ($D_{U(VI)}$ and $D_{Pu(IV)*}$) of U(VI) and Pu(IV) from nitric acid solution

*These values were determined by solvent extraction with 1.0 mol/L *N,N*-dialkylamide in dodecane from 3.0 mol/L HNO$_3$

DOBA	DH2EBA	DO2EBA	D2EHMPA	D2EHDMPA
$D_{U(VI)}$: 9.6 $D_{Pu(IV)}$: 14.0	$D_{U(VI)}$: 6.1 $D_{Pu(IV)}$: 0.5	$D_{U(VI)}$: 7.5 $D_{Pu(IV)}$: 0.1	$D_{U(VI)}$: 2.7 $D_{Pu(IV)}$: < 0.01	$D_{U(VI)}$: 1.5 $D_{Pu(IV)}$: < 0.01

Sample preparation for EXAFS measurement

Equal volumes (0.5 mL) of aqueous and pre-equilibrated organic phases containing U(VI) were shaken for 10 minutes in a thermostatic atmosphere at 298 K within ±0.1 K. After the equilibration, the system was centrifuged at 5 000 rpm for five minutes. After centrifugation, 0.45 mL organic solution was separated and used as sample. The concentrations of uranium(VI) and nitric acid used in the extraction were 1.0 M for U(VI) and 3.0 mol/L HNO$_3$, respectively.

EXAFS measurements and analysis

0.45 mL U(VI)-*N,N*-dialkylamide complex solution was enclosed in polyethylene tube and double bags. The EXAFS measurement was carried out at beam line BL27B station of the synchrotron radiation laboratory (3.0 GeV) of the High-energy Accelerator Research Organisation (KEK) by using the fluorescence method under the condition of beam current 300-450 mA. The measurement was carried out at the U L_{III} absorption edge (17.16 keV). The energy of spectra was calibrated by recording the Zr K-edge spectrum of a Zr-foil (first inflection point at 17.998 keV).

The extraction of EXAFS oscillations from the absorption spectra was carried out by WinXAS Ver. 3.1 [17]. The theoretical parameters for curve fitting the EXAFS spectra were calculated using FEFF 8.20 [18].

Results and discussion

Figure 1 shows the radial structural function (RSF; the phase shift were not corrected) of typical uranium-branched amide complexes. In this RSF, the peak were mainly attributed to A: axial uranyl oxygen (single scattering: SS), B: oxygen of carbonyl group for *N,N*-dialkylamide (SS), C, D: oxygen and nitrogen of nitrate ion (SS), E: axial uranyl oxygen (multiple scattering: MS), F: U → C (carbonyl) → O (carbonyl) → U (MS), and G: oxygen of nitrate ion (MS). The insertion structure shows typical uranium-amide structure based on theoretical fitting. Two nitrate ions co-ordinated to uranium by bidentate fashion, and the two amide molecules co-ordinate to uranium symmetrically.

Figure 1: The radial structural function (RSF) of typical uranium-amide complexes

The phase shift was not corrected. The insertion structure [UO$_2$(NO$_3$)$_2$(amide)$_2$] showed typical uranium-amide structure based on theoretical fitting (green: uranium, red: oxygen, blue: nitrogen, gray: carbon, white: hydrogen).
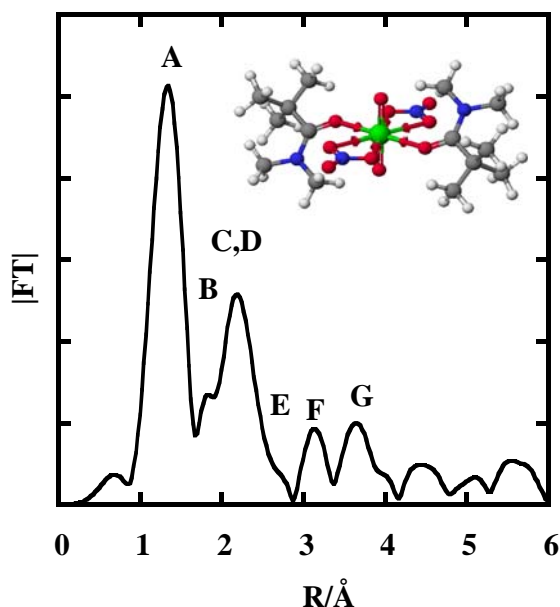
Figure 2(a) shows the RSF and the fitting results of uranyl nitrate-*N,N*-dialkylamides complexes. The RSF's phase shifts associated with absorber-scatter interactions were also not corrected in the range of 0.2-0.5 Å. These functions mainly consist of three big peaks at about 1.3-2.2 Å and broad peaks above 2.6 Å for all amide samples.

Figure 2(b) shows the raw k^3-weighted U L$_{III}$-edge EXAFS oscillations and the fitting results of single and multi scattering contributions in the samples. We confirmed fitting qualities for each shell by fitting to the Fourier transform. The fitting result for five kinds amides are listed in Table 2. On the theoretical fitting, co-ordination number were fixed [U-O(O=C): 2, U-O(O-N): 4, U-N(N-O$_2$): 2].

The bond distance between uranium and axial oxygen is 1.76 Å for all samples. The second peak position of DOBA is 2.40 Å, and which is same position when compared to TBP [19]. For the other amides, the second peak position is 2.35 Å for DH2EBA, 2.36 Å for DO2EBA, 2.33 Å for D2EHMPA and 2.31 Å for D2EHDMPA, respectively. Unexpectedly, we observed that the other amides interact with uranium more strongly than DOBA. In the solvent extraction results shown in Table 1, distribution ratio of uranium: D_U for DOBA is the highest in the used amide compounds. Furthermore, D_U for D2EHDMPA is one-five of that for DOBA and D_U for D2EHMPA is one-third of that for DOBA. As shown in Table 1, the intra structure of D2EHMPA and D2EHDMPA has substituent that branch both of carbonyl alkyl group and nitrogen alkyl group, and therefore these alkyl branching seem to cause steric hindrance around carbonyl oxygen. In this study, however, branching for D2EHMPA and D2EHDMPA make the donor ability of oxygen increase. Rabbe, *et al.* reported that the following sequence was observed: electronic > steric >> lipophilicity using SAR (Structure Activity Relationships) among the influencing factors for uranyl nitrate by *N,N*-dialkylamides [20]. However, from our extraction results, steric effect is more important role of uranium extraction by *N,N*-dialkyamides than electric property.

Conclusion

The local structure of uranium(VI)-DOBA, DH2EBA, DO2EBA, D2EHMPA and D2EHDMPA complexes in dodecane was determined by EXAFS. The bond distance of U-O (amide) for D2EHDMPA is about 0.1 Å shorter than that for DOBA, indicating that D2EHDMPA interacts with uranium more strongly than the other amides. This result dose not correlate with the extractability of the uranium, and steric property around oxygen donor is more dominant for uranium extraction by *N,N*-dialkylamides than donor ability of oxygen.

**Figure 2(a): The FT of the EXAFS spectra of the
U-*N,N*-dialkylamides complexes in n-dodecane solutions**

The phase shifts are not corrected. Experimental data (blue line), theoretical fit (red line).
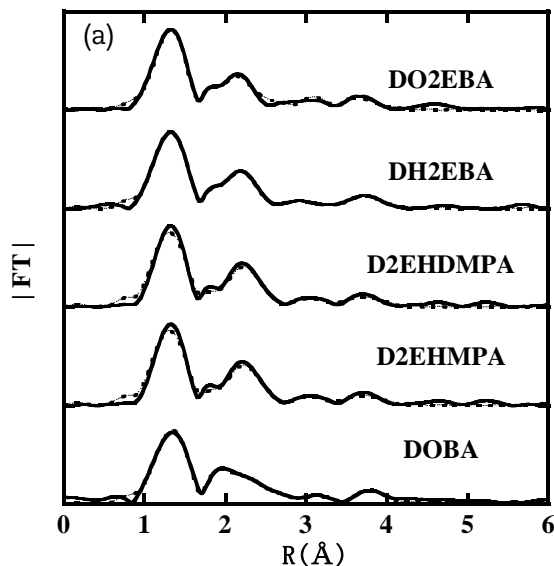
**Figure 2(b): The raw k^3-weighted U L$_{III}$-edge EXAFS spectra
of the U-*N,N*-dialkylamides complexes in n-dodecane solutions**

Experimental data (bold line), theoretical fit (dashed line)
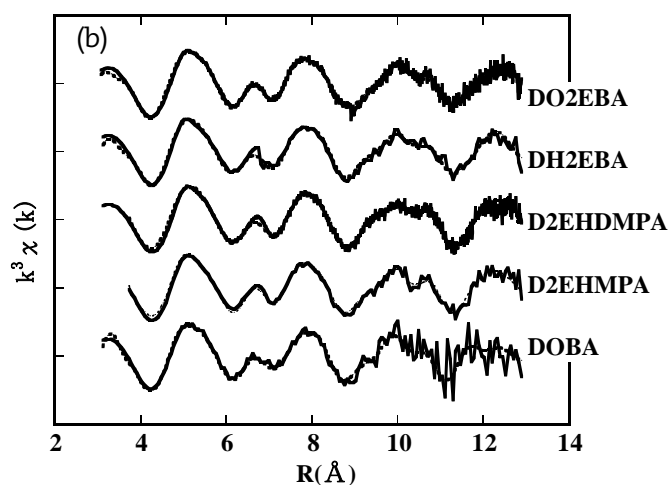
Table 2: Structural parameters of U(VI)-*N,N*-dialkylamides complexes

	U=O			U-O(O=C)			U-O(O-N)			U-N(N-O)		
	R(Å)[a]	N[b]	σ^2(Å^2)[c]	R(Å)[a]	N[b]	σ^2(Å^2)[c]	R(Å)[a]	N[b]	σ^2(Å^2)[c]	R(Å)[a]	N[b]	σ^2(Å^2)[c]
DOBA	1.76	2	0.0015	2.40	2	0.003	2.52	4	0.006	2.92	2	0.010
DH2EBA	1.76	2	0.0015	2.35	2	0.004	2.49	4	0.004	2.89	2	0.005
DO2EBA	1.76	2	0.0015	2.36	2	0.005	2.50	4	0.004	2.90	2	0.006
D2EHMPA	1.76	2	0.0015	2.33	2	0.004	2.50	4	0.004	2.90	2	0.004
D2EHDMPA	1.76	2	0.0015	2.31	2	0.004	2.50	4	0.004	2.90	2	0.005

[a] Bond distance. Error: R < ± 0.01Å, [b] Co-ordination number: fixed, [c] Error: Debye-Waller factors. σ^2 < ± 0.0005Å^2, ΔE_0 used same values.

References

[1]   Tachimori, S., S. Suzuki, S. Sasaki, *J. Nucl. Sci. Tech.*, 43, 1235 (2001) (in Japanese).

[2]   Siddall, T.H. III, *J. Phys. Chem.*, 64, 1863 (1960).

[3]   Siddall, T.H. III, US AEC Report DP-541, E.I. Du Pont de Nemours and Co., Aiken, SC (1961).

[4]   Gasparini, G.M., G. Grossi, *Sep. Sci. Technol.*, 15, 825 (1980).

[5]   Gasparini, G.M., G. Grossi, *Solv. Extr. Ion Exch.*, 4, 1233 (1986).

[6]   Musikas, C., *Sep. Sci. Technol.*, 23,1211 (1988).

[7]   Musikas, C., N. Condamine, C. Cuillerdier, *Anal. Sci.*, 7, 11 (1991).

[8]   Condamine, N., C. Musikas, *Solv. Extr. Ion Exch.*, 10, 69 (1992).

[9]   Thiollet, G., C. Musikas, *Solv. Extr. Ion Exch.*, 7 (5), 813 (1989).

[10]   Suzuki, S., Y. Sasaki, T. Yaita, T. Kimura, *Proceedings of International Conference on Advances for Nuclear Fuel Cycle (ATALANTE2004)*, Nîmes, France, 21-24 June, P1-63 (2004).

[11]   Berthon, C., C. Chachaty, *Solv. Extr. Ion Exch.*, 13 (5), 781 (1995).

[12]   Yang, L., H. Takeuchi, *Solv. Extr. Ion Exch.*, 15 (2), 189 (1997).

[13]   Yaita, T., H. Narita, S. Suzuki, S. Tachimori, S. Shiwaku, H. Motohashi, *J. Alloys Compd.*, 271-273, 184 (1998).

[14]   Chadha, R.K., J.E. Drank, M.A. Khan, *Acta. Cryst.*, C39, 45 (1983).

[15]   Charpin, P.P., M. Lance, N.D. Vigner, C. Musikas, *Acta. Cryst.*, C43, 231 (1987).

[16]   Charpin, P.P., M. Lance, M. Nierlich, N.D. Vigner, C. Musikas, *Acta. Cryst.*, C42, 560 (1986).

[17]   Ressler, T., *J. Synch. Rad.*, 5, 118 (1998) (*www.winxas.de*).

[18]   Ankudinov, A.L., B. Ravel, J.J. Rehr, S.D. Conradson, *Phys. Rev. B58*, 7565-7576 (1998).

[19]   Auwer, C. den, C. Lexouteux, M.C. Charbonnel, C. Madic, R. Guillaumont, *Polyhedron*, 16 (13), 2233 (1997).

[20]   Rabbe, C., C. Sella, C. Madic, A. Godard, *Solv. Extr. Ion Exch.*, 17 (1), 87 (1999).

XAFS analysis on the molten chlorides containing uranyl ions

Haruaki Matsuura,[1] **Atsushi Nezu,**[1] **Hiroshi Akatsuka,**[1] **Takayuki Nagai,**[2] **Akihiro Uehara,**[2]
Toshiyuki Fujii,[2] **Osamu Shirai,**[2] **Hajimu Yamana,**[2] **Munetaka Myochin,**[3] **Yoshihiro Okamoto**[4]
[1]Research Laboratory for Nuclear Reactors, Tokyo Institute of Technology, Tokyo, Japan
[2]Research Reactor Institute, Kyoto University, Osaka, Japan
[3]Japan Atomic Energy Agency, Ibaraki, Japan
[4]Japan Atomic Energy Agency, Kansai Photon Science Institute, Hyogo, Japan

Abstract

XAFS experiments of uranyl species in various molten chlorides have been performed in order to contribute to the development of a co-electrodeposition process at pyrochemical reprocessing. It is found that the ratio of interatomic distances, $R_{U-Cl}/R_{U=O}$ was well related to the "stabilisation" of uranyl species, and NaCl-RbCl melt was one of alternative candidates of NaCl-2CsCl melt. To expect much drastic modification of the co-ordination environment around a focused cation, XAFS experiments of molten chlorides containing small amount of fluorides have also been measured. It was confirmed that even small amount of fluoride anion could be selectively co-ordinated in the first co-ordination sphere around an yttrium cation, thus molten NaCl-KCl-NaF system was also one of alternative candidates of NaCl-2CsCl melt. To promote the application of molten salts to the nuclear engineering field, XAFS can play an important role.

Introduction

Under the development of pyrochemical reprocessing of oxide nuclear fuels, one of key issues remains how realise the uranium-plutonium oxides (MOX) co-electrodeposition process [1]. Determining an alternative candidate to the melt bath is essential since the current melt bath, *i.e.* 2CsCl-NaCl, contains Cs and one of long-lived fission products, [135]Cs is built up with the treatment of spent fuels for many times. Thus it is important to evaluate the local structure around actinides depending upon various melt baths by XAFS in order to find out the melts containing the uranyl ions which has similar local co-ordination environment to that in molten 2CsCl-NaCl.

XAFS investigations on the molten salts containing uranium species have been already reported. Okamoto, *et al.* has been successfully evaluated the local structural parameters of uranium ions in the molten chlorides [2]. Scientists at Manchester University have also published the results on XAFS measurements of the chloride melts containing uranium ions at high temperature [3]. Although the importance of speciation of the actinide elements in molten salts has increased, the practical information is still lacking in order to draw the global model for molten chlorides containing actinides.

In this paper, the systematic study on the melts containing uranyl has been presented for the first time. We have performed XAFS measurements using molten caesium, yttrium and lead chlorides to optimise the confinements for molten salts and then applied to uranyl chlorides in various molten alkali chlorides. To contribute the development on pyrochemical reprocessing of oxide nuclear fuels, a variety of XAFS studies can be performed. After local structural analyses of chloride melts as well as the mixtures with fluoride melts, alternative candidates of ionic melt baths adaptable to pyrochemical processes have been suggested.

Experimental

UO_2Cl_2 in various melt baths were prepared in a dried argon circulated glove box in Research Reactor Institute, Kyoto University (KURRI). Concentrated uranyl hexavalent ions with each melt bath have been synthesised by the chlorination and dissolution of powdered U_3O_8 in each melt bath at the temperature over the melting point. The uranyl hexavalent ions were verified by spectroscopic studies in advance [4], and were stable in quartz cells during the measurement of XAFS, since the absorption edges of these samples are almost constant (17.166 ± 0.001 keV). After the dilution into the same melt bath at molten phase, a certain amount of the solidified samples was sealed in a specially designed quartz cell [2], and transferred to KEK to perform the XAFS experiments at high temperatures.

The electric furnace used was the similar to that originally designed for the laboratory XAFS equipment, but slightly modified to improve thermal homogeneity around the sample area as well as vacuum tightness of the furnace chamber as shown in Figure 1. The XAFS measurements of uranyl chlorides were carried out in various alkali chlorides both at molten and solid phases, using Si (111) double crystal monochromator at U-L$_{III}$ X-ray absorption edge at BL27B/PF/KEK, Japan. Figure 2 shows the experimental set-ups of the furnace at the beamline with a seven-element germanium solid state ditector (SSD) to perform the fluorescence mode. In XAFS measurements on fluorescence mode, the Lα1 fluorescence X-ray (13.61 keV) released from the sample has been detected by the SSD. After the samples in the quartz cell were heated, the molten samples were moving down to the centre of the quartz cells where is approximately optimised to the thickness of the X-ray absorption, as shown in Figure 1 (inset).

After several tries and errors of XAFS measurements in fluorescence mode, the best conditions have been optimised as follows: *i)* the sample where is irradiated by X-ray should be in flat surface, not be in cylindrical; *ii)* the global shape of the cell should be kept in cylindrical form enough in order to avoid from the destruction on the solidification of the sample; *iii)* X-ray beam should be kept the same size as that in transmission mode. Finally the thickness of the flat part of the quartz cell has been optimised to 0.5 mm each.

To focus on the additional effect of fluoride anion to chloride melts, NaCl-KCl (equimolar ratio) – YCl$_3$ (x_{YCl3} = 0.01) – NaF (x_{NaF} = 0, 0.02 and 0.08) system had been chosen. These mixtures were pre-molten in several glassy carbon crucibles, and installed inside the carbon containers coated by pyrographite and thoroughly put inside the rectangular parallelepiped quartz containers. The double

Figure 1: An electric furnace and the sample in a quartz container (inset)

Figure 2: The electric furnace fixed between two ionic chambers at BL27B/PF/KEK. A Ge SSD is located on right-hand side of the furnace.
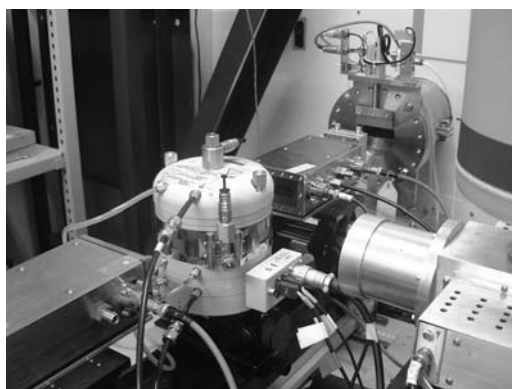
Results and discussion

All quartz cells could successfully confine any samples during the experiments at high temperatures without destruction. XAFS oscillations and radial structure factors of both molten and solidified NaCl-KCl (1:1 molar ratio) – UO_2Cl_2 (xUO_2Cl_2 = 10 wt.%) using transmission mode are shown in Figures 3 and 4, respectively. On the contrary to the results on molten LiCl-KCl (eutectic)-UCl_3 [2], similar phase and different phases were somewhat mixed in XAFS oscillations between solid and molten samples, as identified in Figure 3. These features were clearly indicated in the structural functions, Figure 4. The shorter correlation peaks were attributed to the closest U-O contributions, and decreasing intensity upon melting was due to temperature effect, since $O=U=O_2$ ion was known to be rigid. However, the peaks of longer correlation were corresponding to U-Cl co-ordination, that is, chlorides were expected to exist in equatorial plane if $O=U=O_2$ was fixed in axial. This second co-ordination sphere became much looser upon melting. Although unharmonic effect increased at high temperature, the distance between U-Cl decreased upon melting. Thus, the second co-ordination spheres comparing with first co-ordination spheres in various conditions is good indication of modification of the local environment around uranyl ions, which would be highly related to electrochemical behaviour.

XAFS oscillations and radial structure functions of various molten alkali chlorides – UO_2Cl_2 are shown in Figures 5 and 6, respectively. The result of the melt containing 2CsCl-NaCl was obtained by fluorescence mode under the 3 GeV operation of the storage ring at PF, otherwise transmission modes under the 2.5 GeV operations. We note that the quality of the data on 2CsCl-NaCl system was one of the best resolved data and enough comparable to the oscillations those obtained by transmission modes. However the quality of the data on RbCl-NaCl was relatively poor, mainly due to the considerable X-ray absorption of Rb atoms in the background spectra.

Figure 3: XAFS oscillations of NaCl-KCl (1:1 molar ratio)-UO$_2$Cl$_2$ (10 wt.%) mixture both in solid and liquid phases
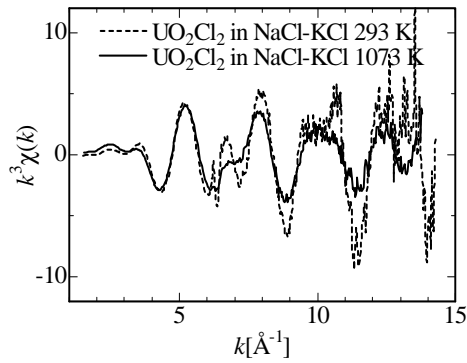
Figure 4: Fourier transformed radial structure functions of NaCl-KCl (1:1 molar ratio)-UO$_2$Cl$_2$ (10 wt.%) mixture both in solid and liquid phases
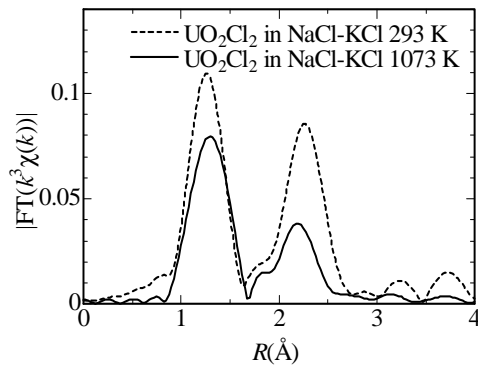
Figure 5: XAFS oscillations of various molten alkali chlorides containing UO$_2$Cl$_2$
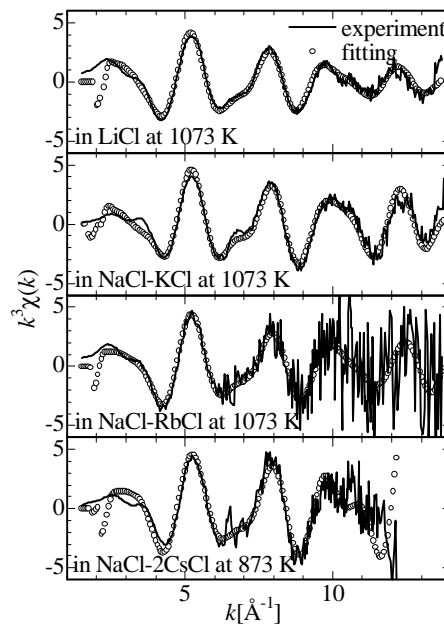
**Figure 6: Fourier transformed radial structure functions
of various molten alkali chlorides containing UO₂Cl₂**
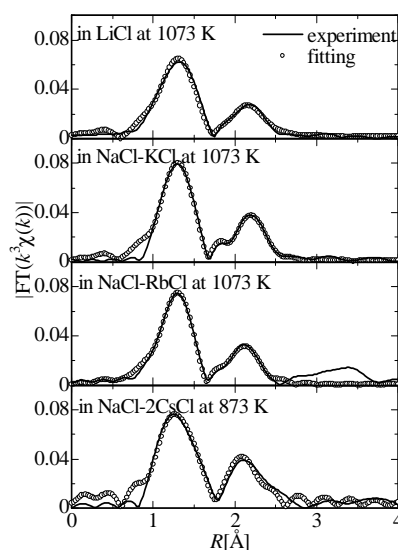
To discuss in detail about the "stabilisation effect" of uranyl ions, the local structural parameters of each sample at solid and liquid phases have been shown in Table 1. Because of unharmonic effect, especially, the second co-ordination spheres of U-Cl correlation at high temperature have been analysed by introducing third and fourth cumulants. The error bars of the structural parameters were estimated by more than five times iteration of the fitting procedures. However, the structural parameters of solid phases would include larger inherent errors caused by chemical and statistical reasons. First, in all mixtures, several crystallographic phases can be expected. Thus, the structural parameters shown in Table 1 were averaged structures of each phase that would be sometimes considerably distorted from the symmetric structures. Second, due to hetero-crystallisation during solidification, the samples at X-ray path were not necessarily homogeneous, so statistical errors of spectra also would be larger. Thus, for comparisons of each structural parameter, we introduce the distance ratio of U-Cl/U=O to compensate those inherent errors relatively. Figure 7 shows that the plot of the distance ratios of U-Cl/U-O versus averaged cationic radii of melt bath. The smaller value of the ratio means the equatorial chloride ion approaches much closer to vertical uranyl ion. The most striking feature is, in the solids, $UO_2Cl_4^{2-}$ species in RbCl-NaCl exist similarly those in 2CsCl-NaCl, while, in the liquids, this feature is more diminished and even closer to that in NaCl-KCl. Thus we conclude that RbCl-NaCl melt would be better than NaCl-KCl melt, but not the best choice of alternative candidates of melt baths which was applicable to MOX co-electrodeposition process.

XAFS oscillations and radial structure functions of the NaCl-KCl-NaF-YCl₃ are shown in Figures 8 and 9, respectively. The double wall construction functioned well, and no problem occurred during XAFS measurements. With increasing fluoride amount, the XAFS oscillations were drastically modified, as shown in Figure 8. In Figure 9, it was easily identified that the interionic distance between yttrium cation and anion were shortened, c.a. even more than 0.5 Å, which was corresponding exactly to the difference of the ionic radii between chloride and fluoride anions. Thus, the additional fluoride anions were selectively co-ordinated in the first co-ordination sphere. We have not yet performed the XAFS measurements of chloride and fluoride mixtures containing uranyl species, however, for the uranyl systems, the similar effect would be expected to equatorial co-ordinated chlorides by addition of fluorides. It would be much stabilised of uranyl ions in molten salts, and drastic change of electrochemical behaviour is expected.

One of the examples how to contribute the local structural analyses to the real development of pyrochemical treatment for spent fuels has been described. As we explained in this article, there were still some difficulties to perform the XAFS measurements using actinide elements, but the XAFS must be one of the conventional methods to evaluate the local structure. The importance of "speciation" at high temperature has been expressed by the several groups [7], thus several synchrotron facilities adapted to actinide materials would be very expected shortly.

Figure 7: Ratios of $R_{U\text{-}Cl}/R_{U=O}$ versus averaged cationic radii of melt baths
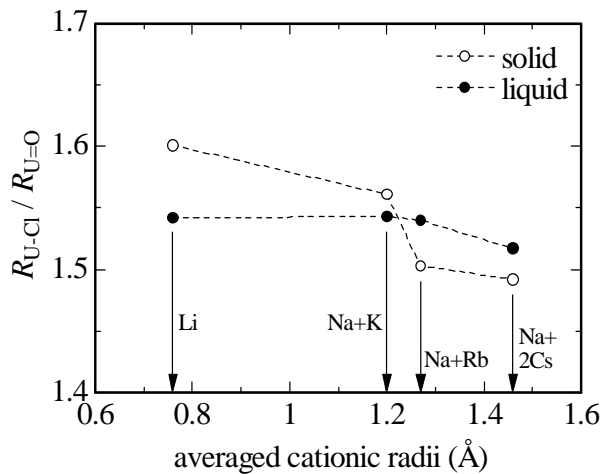
Figure 8: XAFS oscillations of molten NaCl-KCl (1:1 molar ratio)-NaF (0, 2 and 8 mol.%)-YCl$_3$ (1 mol%) mixture
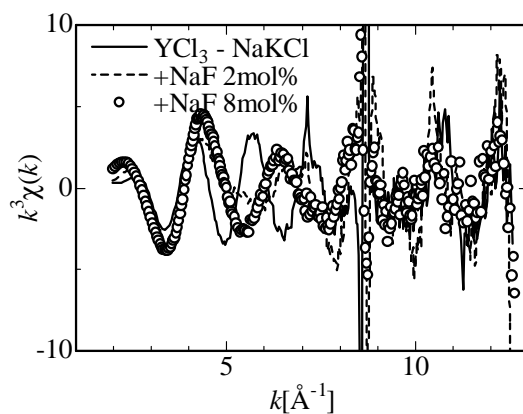
Figure 9: Fourier transformed radial structure functions of molten NaCl-KCl (1:1 molar ratio)-NaF (0, 2 and 8 mol%)-YCl$_3$ (1mol%) mixture

References

[1]   Mizuguchi, K., Y. Shoji, T. Kobayashi, M. Asou, S. Tamura, *Proc. Int. Conf. Future Nuclear Systems, GLOBAL'97*, 2, 1123 (1997); Bychkov, A.V., S.K. Vavilov, O.V. Skiba, P.T. Porodnov, A.K. Pravdin, G.P. Popkov, K. Suzuki, Y. Shoji, T. Kobayashi: *Proc. Int. Conf. Future Nuclear Systems, GLOBAL'97*, 2, 912 (1997); Vavilov, S., T. Kobayashi, M. Myochin, *J. Nucl. Sci. Technol.*, 41, 1018 (2004).

[2]   Okamoto, Y., M. Akabori, A. Itoh, T. Ogawa, *J. Nucl. Sci. Technol.*, Suppl. 3, 638 (2002).

[3]   Bhatt, A.I., H. Kinoshita, A.L. Koster, I. May, C.A. Sharrad, V.A. Volkovich, O.D. Fox, C.J. Jones, B. Lewin, J.M. Charnock, C. Henning, *Proceedings of ATALANTE 2004*, O13-04 (2004); Volkovich, V.A., I. May, T.R. Griffiths, J.M. Charnock, B. Lewin, *Proceedings of Euchem 2004 Molten Salts Conference*, 93 (2004); Volkovich, V.A., I. May, T.R. Griffiths, J.M. Charnock, A.I. Bhatt, B. Lewin, *J. Nucl. Mater.*, 344, 100 (2005); Sharrad, C.A., I. May, H. Kinoshita, A.I. Bhatt, V.A. Volkovich, I.B. Polovov, J.M. Charnock, R.G. Lewin, *Recent Advances in Actinide Science*, 794 (2006).

[4]   Nagai, T., T. Fujii, O. Shirai, H. Yamana, *J. Nucl. Sci. Technol.*, 41, 690 (2004); Nagai, T., A. Uehara, T. Fujii, O. Shirai, H. Yamana, *J. Nucl. Sci. Technol.*, 43, 1511 (2006).

[5]   Ressler, T., *J. Phys. IV*, 7, C2 (1997).

[6]   Zabinski, S.I., J.J. Rehr, A. Ankudinov, R.C. Albers, M.J. Eller, *Phys. Rev. B*, 52, 2995 (1995).

[7]   Sharrad, C.A., H. Kinoshita, I. May, I.B. Polovov, V.A. Volkovich, J.M. Charnock, B. Kralj, R.G. Lewin; and Pauvert, O., C. Tephany, H. Matsuura, D. Zanghi, B. Sitaud, C. Bessada, these proceedings.

Table 1: Structural parameters derived by fitting analyses

Sample	T (K)	U–?	S_0^2	N	R (Å)	σ^2 (10^{-2} Å^2)	ΔE (eV)	C_3 (10^{-3} Å^3)	C_4 (10^{-4} Å^4)	Residual (%)
NaCl-KCl	298	U=O	0.92	2.05±0.19	1.71±0.00	0.01±0.00	−0.22±0.05	0 (fix)	0 (fix)	8.1
10 wt.%		U–Cl		2.34±0.19	2.67±0.00	0.14±0.01	15.2±0.0	0 (fix)	0 (fix)	
NaCl-KCl	1 073	U=O	0.88	1.97±0.12	1.75±0.00	0.14±0.02	10.1±0.3	0 (fix)	0 (fix)	7.3
10 wt.%		U–Cl		3.56±0.52	2.70±0.00	1.60±0.10	16.7±0.0	0.31±0.01	2.00±0.10	
LiCl	298	U=O	0.91	1.80±0.06	1.73±0.00	0.22±0.00	10.0±0.1	0 (fix)	0 (fix)	12.8
10 wt.%		U–Cl		3.47±0.13	2.77±0.00	0.72±0.04	11.0±0.0	0 (fix)	0 (fix)	
LiCl	1 073	U=O	0.90	2.36±0.20	1.77±0.00	0.48±0.00	14.3±0.0	0 (fix)	0 (fix)	6.9
10 wt.%		U–Cl		1.87±0.15	2.73±0.00	0.98±0.01	18.1±0.0	0.74±0.01	0.58±0.00	
NaCl-RbCl	298	U=O	0.93	2.28±0.36	1.83±0.01	0.03±0.01	25.4±3.5	0 (fix)	0 (fix)	13.9
10 wt.%		U–Cl		2.31±0.18	2.75±0.01	0.41±0.01	26.2±0.8	0 (fix)	0 (fix)	
NaCl-RbCl	1 073	U=O	0.96	1.85±0.17	1.74±0.00	0.24±0.14	10.8±2.3	0 (fix)	0 (fix)	7.7
10 wt.%		U–Cl		3.42±1.19	2.68±0.01	1.92±0.47	12.9±0.7	0.70±0.11	2.65±0.11	
NaCl-2CsCl	298	U=O	0.90	1.64±0.29	1.79±0.01	0.07±0.05	21.4±3.8	0 (fix)	0 (fix)	15.3
10 wt.%		U–Cl		4.52±0.21	2.67±0.00	0.55±0.08	17.3±0.2	0 (fix)	0 (fix)	
NaCl-2CsCl	873	U=O	0.83	2.17±0.19	1.76±0.00	0.14±0.02	16.8±0.0	0 (fix)	0 (fix)	14.8
10 wt.%		U–Cl		2.84±0.42	2.67±0.01	1.37±0.32	13.6±1.3	0.24±0.16	2.50±0.80	

X-ray absorption studies of the interaction between uranium(VI) and silica-gel-bound tetraazamacrocycles

Lisa Giachini, Michel Meyer, Lé Vi Nguyen,* Roger Guilard
Institut de Chimie Moléculaire de l'Université de Bourgogne (ICMUB)
Dijon, France

Sébastien Faure, Béatrice Batifol, Hervé Chollet
*Commissariat à l'Énergie Atomique, Centre de Valduc
Département de Traitement des Matériaux Nucléaires
France

Andreas C. Scheinost, Christoph Hennig
Forschungszentrum Dresden-Rossendorf
The Rossendorf Beamline at ESRF (ROBL-CRG)
Grenoble, France

Abstract

We have investigated by means of X-ray absorption fine structure (XAFS) spectroscopy the co-ordination scheme of uranyl cations on the surface of silica-gel beads that have been chemically modified with N-functionalised cyclam (1,4,8,11-tetraazacyclotetradecane) bearing either three acetate or three propionate dangling arms. Uranyl nitrate adsorbed on amorphous Kieselgel 60, used as solid support for these materials, was also studied as a reference. The uranium L_{III}-edge XAFS data of the three samples give evidence of two well-separated oxygen co-ordination shells in the equatorial plane at 2.3 and 2.5 Å, suggesting the formation of uranyl surface complexes for both hybrid gels. Taking into account multiple scattering contributions, the spectral morphology could be best reproduced by a binding model that involves a penta-co-ordinate uranium centre interacting with oxygen atoms belonging both to the silica support and the organic ligand. Similarly to bare Kieselgel, each uranyl ion is bound to a surface silanolate group in a bidentate fashion, thus forming an inner sphere complex. In the presence of macrocyclic chelators, carboxylate groups provide two oxygen atoms belonging either to a pair of monodentate or, more likely, to a single bidentate $-CO_2^-$ binding unit.

Introduction

The development of separation processes aimed at the selective uptake of toxic metal ions from dilute wastewaters and industrial process streams is of paramount importance for preventing environmental contamination, but still remains a challenging scientific task [1]. From that point of view, solid-liquid extraction using chelating agents covalently grafted on hydrophilic supports is appealing, mainly because the affinity and selectivity of the scavenging material towards the targeted species can be fine-tuned by molecular design. Over the past decade, we have prepared a range of such hybrid organic-inorganic materials by attaching N-functionalised tetraazamacrocyclic ligands on the surface of mesoporous silica-gel beads (Figure 1), which proved to be efficient extracting agents for various metal cations, including lead and actinides (U, Pu, Am) [2,3].

**Figure 1: Schematic representation of the Si2323trAc ($n = 0$) and
Si2323trPr ($n = 1$) solid/liquid extracting materials considered in this work**
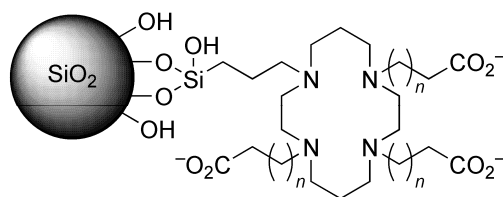
In aqueous solutions, the oxophilic uranyl cation is the most ubiquitous and stable form of uranium, characterised by a +VI oxidation state, a linear geometry of the O=U=O covalent bounds, and co-ordination numbers ranging from 4 to 6 in the equatorial plane. Numerous studies have evidenced the sorption capacity of silica-based materials, including amorphous Kieselgel 60 used for general-purpose column chromatographic separations. Adsorption of hydrated UO_2^{2+}, as well as its monomeric and polymeric hydrolysis products, proceeds through an ion exchange process where the uranium atom interacts either in a monodentate or bidentate fashion with the negatively charged silanolate groups present at the surface [4,5].

Barbette, *et al.* have reported a systematic improvement of the uranium(VI) uptake efficiency when tricarboxylic tetraazamacrocycles were covalently attached to the silica gel surface [6]. Exploring the influence of both the macrocyclic ring size and chain-length of the carboxylic substituents on the static partitioning coefficient of UO_2^{2+}, these authors found the highest value for the Si2323trPr material bearing 14-membered cyclam derivatives possessing three dangling propionate arms, while the acetate-based Si2323trAc gel (Figure 1) was about three times less efficient. In collaboration with the Commissariat à l'Énergie Atomique (CEA Centre of Valduc, France), one of these modified gels (Si2323trPr) has been produced on the ten-kilogram scale and implemented in the final decontamination step of real aqueous effluents for removing the residual α-emitters (U, Pu, Am) at sub-ng/L concentration levels [7,8]. Packed in a semi-industrial pilot extraction column, the selected modified silica gel enabled to successfully decontaminate more than 50 m³ wastewaters, with a residual radioactivity level of less than 2.5 Bq/m³ [6]. These remarkable extraction properties were rationalised in terms of metal complexation phenomena with the macrocyclic ligands present mainly in the anfractuosities.

Unravelling the binding mode of the immobilised ligands is of crucial importance for understanding the extraction mechanism at the molecular level, as a better knowledge of the structural requirements might eventually enable designing second-generation materials with even improved uptake properties. Unlike spherical lanthanides which are commonly bound simultaneously to the nitrogen and oxygen donors of small macrocyclic polyaminocarboxylates [9], the UO_2^{2+} cation has very different structural requirements and is therefore unable to form inclusion complexes by entering into the cyclam ring. UO_2^{2+} has a strictly linear geometry, which only allows formation of bonds in the equatorial plane. In turn, the X-ray crystal structure of $[UO_2(H_6TETPr)(H_2O)_2](NO_3)_4$ reproduced in Figure 2 stresses the tendency of cyclam N,N',N'',N'''-tetrapropionate ($TETPr^{4-}$) to form co-ordination polymers, in this particular case a one-dimensional chain-like arrangement of UO_2^{2+} ions (U⋯U = 16.34 Å) alternating with H_6TETPr^{2+} units [10]. Each uranium atom is surrounded in the equatorial plane by six oxygen atoms provided by two trans-located water molecules and two bidentate propionate groups belonging to a pair of adjacent ligand molecules. The resulting co-ordination sphere resembles that reported for bisacetato uranium(VI) [11].

Figure 2: View of the X-ray crystal structure of [UO$_2$(H$_6$TETPr)(H$_2$O)$_2$](NO$_3$)$_4$ showing the chain-like arrangement of uranyl ions alternating with H$_6$TETPr^{2+} molecules [10]

For the sake of clarity, hydrogen atoms are omitted. Ellipsoids are drawn at the 50% probability level.
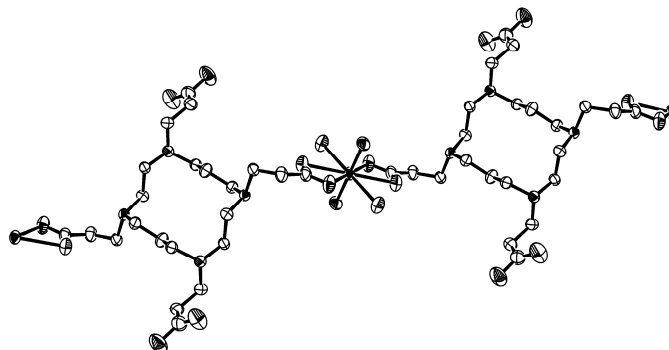
As far as the modified silica gels Si2323trPr and Si2323trAc are concerned, it is however conceivable that both the solid support and the macrocycles contribute in a synergetic manner to the surface retention of radionuclides. This assumption relies on the propensity of UO$_2^{2+}$ ions to interact with mineral silicates and silanolates. In order to probe the actinide environment, uranyl-loaded samples of the two aforementioned hybrid materials were investigated by XAFS spectroscopy. The present study encompasses also unmodified Kieselgel 60 for comparison. Hereafter, the various hypothesised binding modes of sorbed uranyl are discussed in light of the U L$_{III}$-edge EXAFS spectra recorded at cryogenic conditions (T ~ 20 K).

Experimental section

Sample preparation

Caution! Since uranyl salts are chemotoxic and slightly radioactive (α-radiation), all preparations were conducted in a ventilated fume hood dedicated to radiochemistry work. Standard procedures applicable to radiochemical laboratories were followed.

Kieselgel 60 (BET specific surface = 516 m²/g, BJH average pore width = 60 Å, pore volume = 0.76 cm³/g) was purchased from Merck and sieved to retain only the 0.25-0.40 mm fraction. Both extracting materials were synthesised following general procedures outlined in Ref. [6]. The amount of grafted macrocycles [0.44(2) mmol/g for Si2323trAc and 0.40(2) mmol/g for Si2323trPr] was deduced from the nitrogen content measured with a Fisons EA 1108 CHNS elemental micro-analyser.

Before use, the silica particles were rapidly washed with 0.02 M KOH and abundantly rinsed with ultra-pure water. 100 mg of solid were suspended in 10 mL of water to which 1 mL of an acidic uranyl nitrate solution containing 50 g/L U$_{nat}$ was added. The pH was adjusted to 4.8 by adding ca. 1.4 mL of 1 M KOH. Magnetic stirring was maintained only for three minutes in order to avoid mechanical grinding of the silica beads. Thereafter, each sample was left to stand for 24 h at room temperature without taking special precautions to exclude CO$_2$, after which the solid was recovered by filtration, thoroughly washed with water, and finally dried in a desiccator. The amount of sorbed uranium was quantified directly by gamma spectrometry using the ^{235}U line (estimated relative error: 20%): Kieselgel 60, 38 mg/g; Si2323trAc, 97 mg/g; Si2323trPr, 88 mg/g.

For the XAFS measurements, samples were finely ground and mixed with boron nitride in an agate mortar. The resulting powder, containing about 3.5 mg uranium per gram, was compacted with a hand press to yield pellets of 7 mm in diameter and ca. 1 mm in thickness. Once covered on both sides with a piece of adhesive Kapton tape, each pellet was confined inside a heat-sealed Rilsan bag which was itself placed in a custom-designed sample holder made of a polyethylene cuvette and body that snap into each other. To ensure the tightness of the assembly, both parts were glued together and then heat-sealed with a soldering iron to obstruct the chink.

EXAFS measurements and data processing

Uranium L_{III} edge (17.166 keV) X-ray absorption spectroscopic measurements were carried out on the Rossendorf Beamline (BM20) at the European Synchrotron Radiation Facility, Grenoble (France). Low-temperature spectra ($T \sim 20$ K) were recorded in transmission mode by using a closed-cycle helium cryostat. The monochromator, equipped with a Si(111) double-crystal, was used in channel-cut mode. Higher harmonics were rejected by a Pt coated mirror. The spectra were collected in transmission mode using ionisation chambers filled with 20% Ar and 80% N_2 before the sample (I_0) and with 100% Ar after the sample (I_1, I_2). Across the EXAFS region, data points were collected with equidistant k steps of 0.05 Å^{-1}. The monochromator energy scale was calibrated to the K-edge of Y metal foil (first inflection point assigned to 17 038 eV).

The EXAFS oscillations were extracted from the raw data using the AUTOBK program [12] as implemented in the ATHENA package (version 0.8.054) [13], using a linear function for the pre-edge region and a cubic spline to mimic the atomic background. Theoretical amplitude and phase shift functions were calculated using the *ab initio* code FEFF8.2 [14]. The data were analysed using the FEFFIT program as implemented in the ARTEMIS package (version 0.8.011) [13]. The fits were performed both in k and in R space, with a k weight of 3, in order to test the reproducibility of the results. The k range used was 3.5-13.5 Å^{-1} for all samples. The amplitude reduction factor (S_0^2) was held constant to 1. The uranium L_{III} threshold energy (E_0) was set at the first inflection point of the absorption edge (17 173 eV) and allowed to vary as a global parameter for all paths, resulting in energy shifts (ΔE_0) of 5 ± 1 eV for all samples excepted for UO_2^{2+} sorbed onto Kieselgel 60 ($\Delta E_0 = 3 \pm 1$ eV). Several plausible three-dimensional structural models supported by first shell analysis, characteristics of the Fourier Transform (FT), and literature data were built in MOLDRAW [15] using an approach similar to that described in Refs. [16,17]. They were subsequently fitted to the experimental spectra by using a rigid body refinement scheme (see the following section for a detailed description).

Results and discussion

Figure 3 shows the experimental k^3-weighted EXAFS functions recorded at the U L_{III} edge and their corresponding Fourier transforms calculated in the 3.5–13.5 Å^{-1} k range. Some artefact-like features delimited by dashed lines in Figure 3 are recognisable in the k region extending from 10 to 11 Å^{-1}, which can be assigned to double-electron excitations (*e.g.* [2p4f]) [18,19]. The excited photoelectron can indeed promote a second electron into unoccupied states (shake up) or even eject it into the continuum (shake off). However, the appearance of the associated signal is often masked by the single-electron EXAFS oscillation, since the intensity of double-electron excitation is usually only a

Figure 3: Experimental U L_{III}-edge k^3-weighted EXAFS functions (left) and the corresponding amplitudes of the phase-shift uncorrected Fourier transforms (right) for the three uranium(VI) loaded samples

Solid lines represent the best-fit curves. Data were refined in the 3.5-13.5 Å^{-1} range. The vertical dashed lines delimit the region where double-electron excitations are detectable in the raw data.
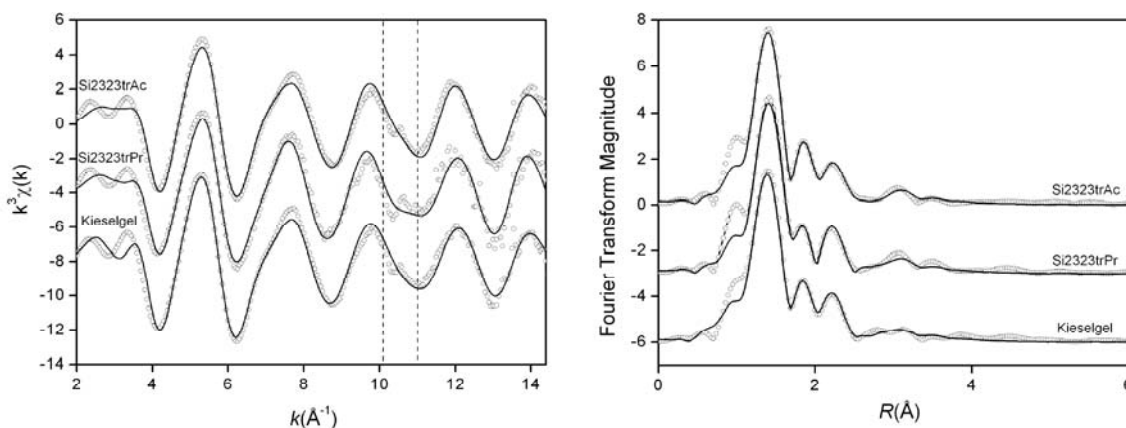
few per cent of a single-electron excitation. Although this double-excitation might bias the EXAFS amplitude and hence impacts some of the refined parameters such as co-ordination number and Debye-Waller (DW) factors, the frequency of the main electron excitation channel is not modified. As a consequence, the calculated distances are not influenced. Deviations between the atomic absorption coefficient μ_0 and its spline approximation give rise to spurious peaks at $R \sim 1$ Å (Figure 3).

The phase-shift uncorrected FT is dominated by the backscattering signal from both axial uranyl oxygen atoms located at a distance of 1.79 Å, whereas two well-separated peaks are clearly detectable in the 1.8–2.4 Å region, which reflect the presence of most likely five donor atoms in the equatorial plane surrounding the uranium atom (U-O_{eq}). The best fit of the experimental data in that range was obtained by assuming two shells of oxygen atoms separated by approximately 0.2 Å from each other, at distances of about 2.3 and 2.5 Å, respectively (see Table 1). The co-ordination number (N) corresponding to the first U-O_{eq} shell is approximately two, while a somewhat larger value was found for the second shell. Based on these facts, uranium centres were supposed to be equatorially penta-co-ordinated, as most frequently observed. Hence, the number of oxygen atoms in both shells were fixed in the final refinement cycle to $N = 2$ and 3, respectively. However, one should keep in mind that co-ordination numbers are spoilt by large errors because of correlations with the associated DW factors.

Table 1: Best-fit XAFS structural parameters for uranyl nitrate sorbed onto Kieselgel 60, Si2323trAc and Si2323trPr at pH = 4.8 obtained by fitting directly in _k_-space[a]

Sample	Structural model	ΔE_0 (eV)	Scattering path[b]	N[c]	R (Å)[d]	$\sigma^2 \times 10^3$ (Å²)[e]
Kieselgel 60	*gem*-disilanolate	3(1)	U=O_{ax}	2	1.787(6)	2.5(4)
			U-O_{Si}	2	2.30(2)	7(2)
	R-factor = 0.03		U-O_w	3	2.49(2)	5(1)
			U-Si	1	3.14(6)	11(7)
Si2323trAc	*gem*-disilanolate	5(1)	U=O_{ax}	2	1.792(5)	2.3(3)
	+ 2 monodentate		U-O_{Si}	1	2.31(2)	6(2)
	carboxylate groups		U-O_w	1	2.50(3)	3(3)
			U-O_{mono}	2	2.50(5)	13(7)
	R-factor = 0.03		U-Si	1	3.10(4)	9(4)
			U-C	2	3.50(3)	1(2)
Si2323trAc	*gem*-disilanolate	5(1)	U=O_{ax}	2	1.794(5)	2.3(3)
	+ 1 bidentate		U-O_{Si}	2	2.33(2)	6(2)
	carboxylate group		U-O_w	1	2.50(2)	2(2)
			U-O_{bid}	2	2.55(4)	15(7)
	R-factor = 0.03		U-Si	1	3.13(7)	13(8)
			U-C	1	2.91(4)	3(3)
Si2323trPr	*gem*-disilanolate	5(1)	U=O_{ax}	2	1.800(7)	2.3(4)
	+ 2 monodentate		U-O_{Si}	1	2.29(2)	5(1)
	carboxylate groups		U-O_w	1	2.50(4)	2(2)
			U-O_{mono}	2	2.52(5)	13(9)
	R-factor = 0.05		U-Si	1	3.14(5)	11(8)
			U-C	2	3.50(4)	1(2)
Si2323trPr	*gem*-disilanolate	5(1)	U=O_{ax}	2	1.800(7)	2.2(4)
	+ 1 bidentate		U-O_{Si}	2	2.29(2)	5(1)
	carboxylate group		U-O_w	1	2.49(3)	2(2)
			U-O_{bid}	2	2.54(3)	10(5)
	R-factor = 0.05		U-Si	1	3.21(8)	12(9)
			U-C	1	2.90(8)	5(8)

[a] Similar values are found by fitting in R-space. The amplitude reduction factor S_0^2 was defined as 1.0. The threshold energy was set at the first inflection point of the absorption edge (17 173 eV) and varied as a global fit parameter, resulting in the energy shift ΔE_0. Standard deviations (1σ) are given in parenthesis as the last-significant digit.

[b] Equatorial oxygen atoms are assigned as follows: O_{Si}, silanolate; O_w, water; O_{mono}, monodentate carboxylate; O_{bid}, bidentate carboxylate.

[c] Co-ordination numbers were fixed during the refinement procedure.

[d] Refined distances.

[e] Refined Debye-Waller factors.

Similar spectral characteristics have been reported for uranium(VI) sorbed onto silicic acid and silica gel [4,20-22], kaolinite [23], albite [5], montmorillonite [4], ferrihydrite [21,24], as well as for uranium-bearing Si/Al- and Fe-rich gels [22]. In all these studies, the splitting of the equatorial U-O distances into two distinct groups has been assigned to the formation of surface complexes, while no such significant differentiation has been reported for various mono- or polymetallic uranyl compounds, like dimeric and trimeric hydroxides [25], carbonates [26], sulphates [19], or carboxylates [27-29].

According to the aforementioned literature data, it is expected that XAFS spectra pertaining to uranyl-sorbed minerals reflect the participation of at least one silicon atom in the second co-ordination sphere. The expected distance and number of silicon atoms depend on the type of complex that is formed. Basically, three different binding modes have been proposed and evaluated for describing the interaction of UO_2^{2+} with a silicate-based material, including amorphous silica gel. These structural models are depicted in Figure 4 and are referred to as monosilanolate, bidentate *gem*-disilanolate and bidentate *vic*-disilanolate [4,5,21]. In the first and third cases, the U-Si distance is expected to be within 3.8-3.9 Å, whereas a bidentate geminal co-ordination results in significantly shorter distances ranging between 2.9 and 3.2 Å, in agreement with the value of 3.15 Å derived from the X-ray crystal structure of the naturally occurring diuranyl silicate soddyite of $(UO_2)_2SiO_4 \bullet 2H_2O$ general formula [20]. Either three or four water molecules (O_w) located in the equatorial plane are assumed to fulfil the co-ordination sphere around the metallic centre.

Figure 4: Structural models used to probe the binding modes of UO_2^{2+} with silanolate groups.

(a) monosilanolate   (b) *gem*-disilanolate   (c) *vic*-disilanolate
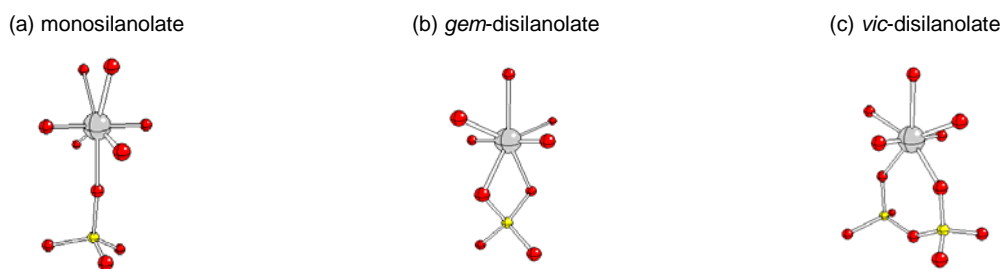
Experimentally, a peak centred at 2.8 Å is observed in the phase-uncorrected FT spectra, which translates into a U-Si distance of about 3.14 Å. Accordingly, a bidentate *gem*-disilanolate surface complex with uranium(VI) can be inferred. In order to validate this hypothesis, theoretical simulations of the EXAFS signal generated by the clusters depicted in Figure 4 have been performed. These models were built in MOLDRAW [15] by using the structural parameters reported by Walter, *et al.* [5]. In addition to single scattering, up to four-legged multiple scattering paths were also considered in the calculations. These include contributions coming from the uranyl cation, which produce the marked peak at approximately 3 Å (Figure 3), but also from the silanolate fragment (U-Si-O). For uranyl sorbed onto Kieselgel, reasonable fitting parameters together with a satisfactory goodness of fit factor were returned only when the EXAFS oscillations were modelled with the bidentate structural motif shown in Figure 4(b). In the final refinement step, all scattering paths up to 4 Å were included and all co-ordination numbers were fixed. The resulting optimal distances and DW factors are summarised in Table 1. Similar structural parameters, supporting the formation of a bidentate *gem*-disilanolate surface complex with uranium(VI), have been reported by Sylvester, *et al.* for analogous sample types [4].

Nevertheless, the spectral features occurring around 2.9 and 4 Å were only imperfectly reproduced in the FT spectra corresponding to the modified silica gels Si2323trAc and Si2323trPr. Since the experimental signal is more intense than the one calculated for the aforementioned model, additional contributions had to be taken into account for the materials bearing macrocyclic polyaminocarboxylates. In the next step, the possible interaction of the acetate or propionate groups attached to the cyclam ligands with the surface-bound uranyl cations was evaluated. To that end, some of the three remaining water molecules were successively substituted by one or two carboxylates, while keeping a total of five oxygen atoms in the periphery of UO_2^{2+}. As it is well known that carboxylate-type ligands can co-ordinate in either mono- or bidentate mode, these two possibilities were also tested. The backscattering contribution produced by the second-shell carbon atoms is the key that enables to discriminate both ligation modes. For a monodentate interaction an U-C contribution at approximately 3.5 Å is expected,

while a bidentate structure affords a much shorter distance of about 2.9 Å [30]. However, for both binding modes multiple scattering signals, which involve the second-shell carbon atom, have to be taken into account since their contribution to the total EXAFS signal is significant. Monodentate binding is characterised by a three-legged (U-O-C-U) scattering path at a distance of about 3.4 Å, while bidentate co-ordination produces non-negligible three-legged (U-O-C-U) and four-legged (U-O-C-O-U) multiple scattering paths at a distance of about 3.7 Å. These contributions were included in the fitting procedure. In order to avoid multiple solutions due to the increase of refined parameters, the fitting procedure was performed following a step-by-step approach (see Ref. [31] and references therein). In a first step, only structural parameters were varied, by adopting a rigid body refinement scheme [32]. The DW factors were kept fixed to reasonable values. Structural parameters were then set to the best-fit values determined in Step 1, while DW factors were allowed to vary. Finally, DW factors were fixed to the best-fit values found in Step 2 and the structural refinement was run again in order: i) to check if the calculations converged to the previously determined values; ii) to improve the precision of structural parameters. The rigid body refinement procedure avoids data over-interpretation because selected sets of scattering atoms pertaining to the same ligand are treated as units with limited degrees of freedom. For silanolate and carboxylate groups, starting models were built according to X-ray crystal data available in the literature [30,33]. Intraligand distances were kept fixed during the fitting procedure while the distance of the entire group from the absorber and some angles (O_{Si}-Si-O_{Si} of the silanolate group and U-O-C, O-C-O of the carboxylate group) were allowed to vary. The best adjustments were obtained when two carboxylic groups were bound in a monodentate fashion and when a single carboxylic group was co-ordinated in a bidentate fashion. The structural results obtained for these two models are reported in Table 1. The reasonableness of the values found for both structural and disorder parameters support the reliability of the models. The difficulty to determine unequivocally the correct structure is due to the fact that several paths contribute, constructively or destructively, to the same region of the FT spectrum (i.e. to the peak centred at about 3 Å). These include the linear O=U=O multiple scattering path (2×1.79 Å), the U-Si-O multiple scattering path of the silanolate fragment, single and multiple scattering paths involving the second-shell carbon atom pertaining to carboxylic arms. The most likely structural models that emerge from the analysis of the EXAFS spectra of uranyl-loaded Si2323trAc and Si2323trPr samples (Figure 3), are consistent with a five-co-ordinate uranium atom interacting with one *gem*-disilanolate group, one or two carboxylate arms, and respectively two or one water molecules as shown in Figure 5, the structural parameters being reported in Table 1. With one exception, it is noteworthy that all refined bond distances assigned to carboxylic groups perfectly match those reported by Denecke, *et al.* for several crystalline uranyl carboxylate complexes [30]. Indeed, the monodentate carboxylate U-O bonds were found to be about 0.1 Å longer than expected according to the literature data (U-$O_{mono} \sim 2.4$ Å). This rather large discrepancy speaks in favour of the bidentate binding mode of the -CO_2^- fragment as depicted in Figure 5(b), although the coexistence of different surface species cannot be excluded.

Figure 5: Suggested binding schemes of UO$_2^{2+}$ (*gem*-disilanolate + 2 monodentate carboxylate groups and *gem*-disilanolate + 1 bidentate carboxylate group) at the surface of the modified silica gels Si2323trAc and Si2323trPr

All scattering contributions up to 4 Å were included in the data analysis. Although the entire carboxylic groups are shown for sake of clarity, the methylenic carbon and unbound oxygen atoms were excluded from the modelling.

(a)

(b)

Conclusion

Although the exact number and the binding mode remains uncertain, at least one but more probably two carboxylate groups are co-ordinated to each uranyl cation together with a bidentate silanolate, while water molecules complete the equatorial oxygen shell to five atoms. These acetate or propionate fragments belong either to identical or most likely to distinct macrocycles grafted on the silica gel

surface. The present findings highlights the synergy between a reactive solid support and the chelation faculties of the immobilised ligand, which translates into higher uptake efficiencies of the hybrid materials when compared to those of bare Kieselgel 60 [6]. Based on the linear structure of UO_2^{2+}, the cyclic topology of the molecular receptor selected in the present study provides obviously no clear-cut advantage over a non-cyclic chelator as the tetraazamacrocycle is not involved in the co-ordination. However, such acetate bearing ligands are well suited for the encapsulation of spherical cations such as trivalent and tetravalent actinides as evidenced by the crystal structures reported for some isolated model complexes of Eu^{3+}, taken as a surrogate of Am^{3+} [9]. Analysis of XAFS spectra pertaining to Eu^{3+} and Pu^{4+}-loaded gels is currently underway and will be reported in due course in order to rationalise the extraction capabilities of both materials with respect to americium and plutonium and to check whether or not these ions are picked up by the macrocyclic cavity.

Acknowledgement

References

[1]   Roundhill, D.M., "Extraction of Metals from Soils and Waters", *Modern Inorganic Chemistry*, Kluwer Academic/Plenum Publishers, New York (2001).

[2]   Cuenot, F., M. Meyer, A. Bucaille, R. Guilard, *J. Mol. Liq.* 118, 89-99 (2005).

[3]   Brandès, S., F. Denat, M. Meyer, R. Guilard, *L'Act. Chim.*, 290-291, 108-117 (2005).

[4]   Sylwester, E.R., E.A. Hudson, P.G. Allen, *Geochim. Cosmochim. Acta,* 64, 2431-2438 (2000).

[5]   Walter, M., T. Arnold, G. Geipel, A. Scheinost, G. Bernhard, *J. Colloid Interface Sci.*, 282, 293-305 (2005).

[6]   Barbette, F., F. Rascalou, H. Chollet, J.L. Babouhot, F. Denat, R. Guilard, *Anal. Chim. Acta,* 502, 179-187 (2004).

[7]   Guilard, R., H. Chollet, P. Guiberteau, M. Guerin, PCT Application WO 96 11478 (1996).

[8]   Chollet, H., J.L. Babouhot, F. Barbette, R. Guilard, PCT Application WO 01 15806 (2001).

[9]   Meyer, M., V. Dahaoui-Gindrey, C. Lecomte, R. Guilard, *Coord. Chem. Rev.*, 178-180, 1313-1405 (1998).

[10]   Meyer, M., E. Espinosa, R. Guilard, unpublished results.

[11]   Grigoriev, M.S., M.Y. Antipin, N.N. Krot, *Acta Crystallogr.*, Sect. E 61, m2078-m2079 (2005).

[12]   Newville, M., P. Livins, Y. Yacoby, J.J. Rehr, E.A. Stern, *Phys. Rev.,* B 47, 14126-14131 (1993).

[13]   Ravel, B., M. Newville, *J. Synchrotron Rad.*, 12, 537-541 (2005).

[14]   Ankudinov, A.L., B. Ravel, J.J. Rehr, S.D. Conradson, *Phys. Rev.*, B 58, 7565-7576 (1998).

[15]   Ugliengo, P., D. Viterbo, G. Chiari, *Z. Kristallogr.*, 207, 9-23 (1993).

[16]   Rossberg, A., A. Scheinost, *Anal. Bioanal. Chem.*, 383, 56-66 (2005).

[17]   Giachini, L., F. Francia, G. Veronesi, D.W. Lee, L.S. Huang, E.A. Berry, T. Cocco, S. Papa, F. Boscherini, G. Venturoli, *Biophys. J.*, 93, 2934-2951 (2007).

[18]   Hennig, C., *Phys. Rev.*, B 75, 35120-35121-35120-35127 (2007).

[19]   Hennig, C., K. Schmeide, V. Brendler, H. Moll, S. Tsushima, A.C. Scheinost, *Inorg. Chem.*, 46, 5882-5892 (2007).

[20]   Reich, T., H. Moll, M.A. Denecke, G. Geipel, G. Bernhard, H. Nitsche, *Radiochim. Acta*, 74, 219-223 (1996).

[21]   Reich, T., H. Moll, T. Arnold, M.A. Denecke, C. Hennig, G. Geipel, G. Bernhard, H. Nitsche, P.G. Allen, J.J. Bucher, N.M. Edelstein, D.K. Shuh, *J. Electron Spectrosc. Relat. Phenom.*, 96, 237-243 (1998).

[22]   Allard, T., P. Ildefonse, C. Beaucaire, G. Calas, *Chem. Geol.*, 158, 81-103 (1999).

[23]   Thompson, H.S., G.A. Parks, G.E. Brown, "Structure and Composition of Uranium[VI] Sorption Complexes at the Kaolinite-water Interface", in *Adsorption of Metals by Geomedia*, E.A. Jenne (Ed.), Academic Press, pp. 349-370 (1998).

[24]   Waite, T.D., J.A. Davis, T.E. Payne, G.A. Waychunas, N. Xu, *Geochim. Cosmochim. Acta*, 58, 5465-5478 (1994).

[25]   Tsushima, S., A. Rossberg, A. Ikeda, K. Müller, A.C. Scheinost, *Inorg. Chem.*, 46, 10819-10826 (2007).

[26]   Ikeda, A., C. Hennig, S. Tsushima, K. Takao, Y. Ikeda, A.C. Scheinost, G. Bernhard, *Inorg. Chem.*, 46, 4212-4219 (2007).

[27]   Jiang, J., L. Rao, P. Di Bernardo, P.L. Zanonato, A. Bismondo, *J. Chem. Soc.*, Dalton Trans., 1832-1838 (2002).

[28]   Vazquez, J., C. Bo, J.M. Poblet, J. de Pablo, J. Bruno, *Inorg. Chem.*, 42, 6136-6141 (2003).

[29]   Schlosser, F., S. Kruger, N. Rosch, *Inorg. Chem.*, 45, 1480-1490 (2006).

[30]   Denecke, M.A., S. Pompe, T. Reich, H. Moll, M. Bubner, K.H. Heise, R. Nicolai, H. Nitsche, *Radiochim. Acta*, 79, 151-159 (1997).

[31]   Giachini, L., F. Francia, L. Cordone, F. Boscherini, G. Venturoli, *Biophys. J.*, 92, 1350-1360 (2007).

[32]   Binsted, N., R.W. Strange, S.S. Hasnain, *Biochemistry*, 31, 12117-12125 (1992).

[33]   Nyfeler, D., T. Armbruster, *Am. Mineral.*, 83, 119-125 (1998).

Systematic XAS studies on uranium co-ordination complexes featuring the U^{3+} to U^{6+} series

Oanh P. Lam,[1,2] **Melissa Denecke,**[3] **Steven Conradson,**[4] **Karsten Meyer**[2]
[1]University of California, San Diego, Department of Chemistry, La Jolla, CA, USA
[2]Univ. of Erlangen-Nürnberg, Dept. of Chemistry & Pharmacy, Inorganic Chemistry, Erlangen, Germany
[3]Forschungzentrum Karlsruhe, Institut für Nukleare Entsorgung, Karlsruhe, Germany
[4]Los Alamos National Laboratory, Los Alamos, New Mexico USA

Abstract

Low-valent uranium complexes, $[((N_3O_3)U^{III})]$, supported by sterically encumbering tris-aryloxide triazacyclononane ligands have been successful at activating small molecules such as CO, CO_2, organic azides, and ketones due to their highly reducing nature. Determining the oxidation state of the uranium is a crucial step in understanding the electronic structure and reactivity of these complexes. For certain complexes where the oxidation state is more ambiguous, as in the cases of charge-separated uranium complexes bearing radical anionic ligands $[((^{Ad}ArO)_3tacn)U(CO_2^{\bullet-})]$ and $[((^{t\text{-}Bu}ArO)_3tacn)U(^{t\text{-}Bu}Ph_2CO^{\bullet-})]$, XAS is an unparalleled method for determining the oxidation state of the metal centre. The XANES studies of the complete uranium series $[((N_3O_3)U^{n+}{-}L)]^{m+}$ (L = $NCCH_3$, N_3^-, Me_3SiN^{2-} and n = 3, 4, 5, m = 0; n = 6, m = 1) where the first co-ordination sphere remains unaltered, $(N_3O_3)U{-}L$, except at the axial position of the uranium have been obtained. In combination, XANES and other spectroscopic data add a new dimension to a better understanding of the electronic structure of uranium in inorganic and organometallic co-ordination compounds.

Understanding actinide behaviour in high temperature molten salts

Clint A. Sharrad,[1] **Hajime Kinoshita,**[1] **Iain May,**[1] **Ilya B. Polovov,**[2]
Vladimir A. Volkovich,[2] **John M. Charnock,**[3] **Brett Kralj,**[4] **Robert G. Lewin**[4]
[1]Centre for Radiochemistry Research, School of Chemistry, University of Manchester, United Kingdom
[2]Department of Rare Metals, Ural State Technical University, Ekaterinburg, Russia
[3]CCLRC Daresbury Laboratory, Daresbury, United Kingdom
[4]Nexia Solutions, Sellafield, United Kingdom

Abstract

Ionic melt technologies, at both high and room temperature, have been considered for a range of applications in the nuclear industry, including the electrolytic separation of uranium from irradiated nuclear fuel and plutonium purification for military applications [1]. Many of these processes are relatively poorly understood from a fundamental chemical viewpoint. This is due to the harsh chemical environment given the very high melting points of some of the salts used and the radiological hazards.

We have investigated actinide speciation in high temperature chloride melts using a variety of spectroscopic techniques including electronic absorption spectroscopy (EAS), Raman spectroscopy and X-ray absorption spectroscopy (XAS). We have conducted molten salt XAS experiments using chemically and electrolytically generated U species. Our current interest is to link our understanding of actinide speciation in ionic melt systems with electrochemical properties, including the industrially relevant processes of anodic dissolution and cathodic deposition, and to develop our techniques for the investigation of high specific activity nuclides in these harsh environments.

Reference

[1]   (a) Lovering, D.G. (Ed.), *Molten Salt Technology*, Plenum, New York (1982), and references therein.
(b) Gale, R.J., D.G. Lovering (Eds.), *Molten Salt Techniques*, Plenum, New York (1984).
(c) Lambertin, D., S. Ched'homme, G. Bourges, S. Sanchez, G.S. Picard, *J. Nucl. Mater.*, 341, 131 (2005).

Combining EXAFS, UV-Vis and XRD to extract uranyl chloride speciation and co-ordination in solution

Christoph Hennig,[1] **Kelly Servaes,**[2] **Peter Nockemann,**[2] **Rik Van Deun**[2]
[1]Forschungszentrum Dresden-Rossendorf, Institute of Radiochemistry, Dresden, Germany
(and Rossendorf Beamline at ESRF, Grenoble, France)
[2]Katholieke Universiteit Leuven, Department of Chemistry, Leuven, Belgium

Abstract

The safety assessment of nuclear waste disposal in geological salt formations, e.g. the Waste Isolation Pilot Plant (USA) and the Gorleben test site (Germany), raises the question of chloride speciation in highly concentrated chloride solutions due to the possible migration through concerned aquifers. The chloride anion is a weak ligand in aqueous solution which is reflected by the fact that e.g. for UO_2^{2+} only two stability constants are reported in the most recent NEA thermodynamic database; $\log \beta_1^0 = 0.17 \pm 0.02$ and $\log \beta_2^0 = -1.1 \pm 0.02$ for the reaction $UO_2^{2+} + nCl^- \rightleftharpoons UO_2Cl_n^{2-n}$ [1]. The specific ion interaction theory (SIT) [2] and the Pitzer model [3] work at high ionic strengths but suffer from the problem of ill-defined interaction coefficients.

Spectroscopic techniques may overcome, at least partly, the limitation of classical thermodynamic data extraction especially in solutions with high ionic strength. Quantitative species distribution of $[UO_2]^{2+}$, $[UO_2Cl]^+$ and $[UO_2Cl_2]^0$ in aqueous solution have been extracted by principal component analysis of UV-vis spectra [4]. Up to three U(VI) chloro complexes, $[UO_2Cl]^+$, $[UO_2Cl_2]^0$ and $[UO_2Cl_3]^-$, have been observed by EXAFS and UV-vis spectroscopy in aqueous solution [5,6]. Nguyen-Trung, et al. even found evidence for $[UO_2Cl_5]^{3-}$ using Raman spectroscopy, a species which is not yet confirmed by other methods according to our knowledge [7].

In contrast to aqueous solutions, the chloride anion forms with U(VI) strong complexes in organic solvents. Such chloro complexes, e.g. in ionic liquids, may have some importance for the reprocessing by partitioning and further transmutation of highly radioactive waste [8]. Several experimental and theoretical attempts have been made to reveal U(VI) chloro complexes with higher co-ordination numbers than those provided in the thermodynamic database. However, these complexes, especially the interactions of intermediate species with solvent molecules, are not yet fully understood. Therefore, we combined UV-vis spectroscopy, EXAFS and XRD measurements at the same sample series to determine the species distribution and the individual species co-ordination. The individual parameters have been extracted mainly with statistical methods like principal component analysis.

We intend to describe as example the complex formation of UO_2^{2+} with chloride ions in acetonitrile. As a function of increasing $[Cl^-]/[UO_2^{2+}]$ ratio, principal component analysis of UV-vis absorption suggested five solution species. The combination with the structural parameters from EXAFS allowed to identify the species co-ordination as $[UO_2(H_2O)_5]^{2+}$, $[UO_2Cl(H_2O)_2(MeCN)_2]^+$, $[UO_2Cl_2(H_2O)(MeCN)_2]$, $[UO_2Cl_3(MeCN)_2]^-$ and $[UO_2Cl_4]^{2-}$ [9]. Not only the U:Cl ratio could be extracted from the EXAFS data, but also the stoichiometry of H_2O and MeCN.

UV-Vis spectroscopy is sensitive to the complex symmetry. This makes it possible to exclude the existence of $[UO_2Cl_5]^{3-}$ at chloride concentrations above the stability range of $[UO_2Cl_4]^{2-}$, because the D_{4h} symmetry can be clearly distinguished from the D_{5h} symmetry.

The information from EXAFS spectra is limited to radial distribution functions, and one has therefore to consider several isomers for the intermediate species. This limitation might be avoided, if it is possible to preserve the solution species in crystal structures. In this case EXAFS is a useful tool to check whether the structure of the species is preserved or a rearrangement of the ligands occurred during crystallisation. Both preservation and rearrangement of the co-ordination during crystallisation have been observed by this technique [10]. Within this study a crystalline material has been obtained from the intermediate solution with the [Cl⁻]/[UO_2^{2+}] ratio of 2, where [$UO_2Cl_2(H_2O)(MeCN)_2$] is the dominating species. The EXAFS measurements show that the co-ordination of the solution species [$UO_2Cl_2(H_2O)(MeCN)_2$] undergoes partly a rearrangement during the formation of the crystal structure. The structure analysis of the solid sample revealed a tetrameric complex, [$(UO_2)_4(\mu_2\text{-}Cl)_4(\mu_3\text{-}O)_2(H_2O)_2(CH_3CN)_4$]·($CH_3CN$) [9]. However, the co-ordination of two Cl⁻ atoms, one H_2O and one MeCN molecule per uranium atom remain preserved in the crystal structure, whereas one MeCN is replaced by an bridging –O– or –OH– group.

This study demonstrates that the combination of EXAFS, UV-Vis and XRD allows gaining much more insight in the co-ordination of solution species than the individual experimental techniques may provide. UV-Vis and EXAFS are insofar an appropriate combination for solution spectroscopy, because both are especially sensitive in the same concentration range. At the other hand, XRD is nowadays a standard technique to reveal atomic structures of single crystals. However, there is often no link between structures in solution and solid state. The capability of EXAFS to detect the general co-ordination in solution and solid state provides the unique opportunity to follow structural modifications during the crystallisation process and to use the solid state structure or its modifications to reveal the co-ordination including potential isomers in the solution.

References

[1]   Guillaumont, R., T. Fanghänel, J. Fuger, I. Grenthe, V. Neck, D.A. Palmer, M.H. Rand, *Update on the Chemical Thermodynamics of Uranium, Neptunium, Plutonium, Americium and Technetium*, Elsevier Science Publishers, Amsterdam (2003).

[2]   Grenthe, I., A.V. Plyasunov, K. Spahiu, *Estimation of Medium Effects on Thermodynamic Data*, OECD, NEA, Paris (1997).

[3]   Pitzer, K.S., "Thermodynamics of Electrolytes. I. Theoretical Basis and General Equations", *J. Chem. Phys.*, 77, 268 (1973).

[4]   Paviet-Hartmann, P., M.R. Lin, *Mat. Res. Soc. Symp. Proc., 556*, 977 (1999).

[5]   Allen, P.G., J.J. Bucher, D.K. Shuh, N.M. Edelstein, T. Reich, T. *Inorg. Chem., 36*, 4676 (1997).

[6]   Hennig, C., J. Tutschku, A. Rossberg, G. Bernhard, A.C. Scheinost, *Inorg. Chem., 44*, 6655 (2005).

[7]   Nguyen-Trung, C., G.M. Begun, D.A. Palmer, *Inorg. Chem., 31*, 5280 (1992).

[8]   Gaillard, C., A. Chaumont, I. Billard, C. Hennig, A. Ouadi, G. Wipff, *Inorg. Chem., 46,* 4815 (2007).

[9]   Hennig, C., K. Servaes, P. Nockemann, K. Van Hecke, L. Van Meervelt, J. Wouters, L. Fluyt, C. Görrler-Walrand, R. Van Deun, R. *Inorg. Chem.,* published on web 03/14/2008.

[10] Hennig, C., W. Kraus, F. Emmerling, A. Ikeda, A.C. Scheinost, *Inorg. Chem., 47*, 1634 (2008).

Session II

Radionuclides in environmental and life sciences

Chair: Melissa A. Denecke

Uranium dioxide behaviour in hydrothermal oxidising conditions

Olga N. Batuk,[1] **Stepan N. Kalmykov,**[1] **Elena V. Zakharova,**[2]
Michiel Klimenkov,[3] **Vladimir V. Kriventsov**[4]
[1]Chemistry Department of Lomonosov Moscow State University, Moscow, Russia
[2]Institute of Physical Chemistry and Electrochemistry RAS, Moscow, Russia
[3]Institute for Material Research, Forschungzentrum Karlsruhe, Germany
[4]Institute of Catalysis RAS, Novosibirsk, Russia

Abstract

One of the key concerns for safe disposal of spent nuclear fuel (SNF) and radioactive wastes is the possibility of leaching of radionuclides and their migration to the environment. Geochemical conditions, i.e. pH, Eh, dissolved oxygen concentration, carbonate and other anion concentrations as well as high radiation and thermal fields would affect the leaching rates and radionuclide speciation. In this work we investigated the behaviour of microcrystalline UO_{2+x} in hydrothermal conditions at 70°C and 150°C in simulated groundwater. The experiments were run during six months with periodical sampling of aliquots for various spectroscopic and microscopic analysis. The phase transformation of UO_{2+x} was studied by powder X-ray diffraction (XRD) and X-ray absorption fine structure (XAFS) at U L_{III} edge. The micro and nano-scale surface characterisation of solid phases collected during the experiment was done by scanning electron microscopy with energy dispersive X-ray analysis (SEM-EDX) and high-resolution transmission electron microscopy (HR-TEM) with selected area electron diffraction (SAED). The neptunium(V) was added to the suspension at the beginning of the experiment as the element of high concern due to its high migration ability in geological conditions. The rapid (within the first month) bulk oxidation of UO_{2+x} at 70°C was observed with insignificant U(VI) secondary phase formation. For the sample leached at 150°C relatively slower oxidation was established due to fast and intense U(VI) secondary phase formation. It was shown by HR-TEM that UO_{2+x} surface is covered by schoepite nanoparticles that prevent oxygen diffusion within fluorite structure of UO_{2+x}. Neptunium was sorbed quantitatively after less than one week at both temperatures and according to the sequential extraction (leaching) tests, it was found in refractory low soluble fractions.

Introduction

Uranium dioxide is the main component of the spent nuclear fuel (SNF) and therefore the understanding of its behaviour in geological conditions is important for performance assessment of SNF repositories. The UO_{2+x} oxidation and subsequent dissolution is the surface mediated process that is controlled by the geochemical conditions, presence of corrosive fluids, thermal and radiation fields.

The dissolution and alteration rates of UO_2 in natural waters depend on its oxidation state and on the composition of the surface layer. The oxidation of UO_2 in CO_2-free conditions could lead to the formation of different uranium oxides and to the formation of an oxidised surface layer with a composition of UO_{2+x} where $0 \leq x < 1$ depending primarily on the temperature, pH and Eh values [1]. The same oxidation reactions may also proceed in water exposed to oxidising atmosphere at ambient CO_2 [2,3]. Under these conditions the oxidation of UO_{2+x} leads to the formation of secondary uranyl phases. The oxidative dissolution of UO_2 in case if aqueous phase is not removed, leads to the increase of U(VI) concentration in solution and then to saturation in respect to schoepite or other U(VI) solid depending on the conditions. This results in precipitation of U(VI) secondary phases.

Depending on the composition of aqueous solution in contact with SNF, uranyl silicates, phosphates and carbonates could be formed on the UO_{2+x} surface. These secondary uranyl phases may control the rate of SNF corrosion as well as the effect of colloid particles formation and radionuclide release from SNF matrix. Alteration phases may also influence the diffusion of dissolved components, oxidants, and other reactants to or from the SNF surface.

The aim of this research is to study the behaviour of UO_{2+x} under hydrothermal oxidising conditions and to trace changes in its structure and colloid generation in simulated groundwater. The interaction of Np(V) with UO_{2+x} was also studied at these temperatures. The choice of this radionuclide is explained by the concern associated with its high migration ability under oxidising geochemical conditions. Earlier Berns, *et al.* [4] studied the inclusion of Np(V) to the structure of different U(VI) minerals and concluded that such inclusion is possible only for minerals having IA or IIA group cations in their structure (*e.g.* Na-compreignacite) that could compensate the negative charge arise from U(VI) – Np(V) substitution.

Experimental section

We used industry produced microcrystalline UO_{2+x} powder sample in all experiments. The solid/solution ratio was equal to 60 g/L. Hydrothermal leaching of the sample was performed in sealed Teflon vessels placed into steel autoclaves as shown in Figure 1 in simulated groundwater as a background solution, which composition is presented in Table 1 or in deionised water. The ^{237}Np was added to the suspensions in pentavalent form at the total concentration of 1×10^{-6} M. The pH and Eh were measured each time when aliquots were taken for analysis and no changes of these values were observed. The pressure in the vessels was not measured, but they were most likely equal to the vapour pressure of water [5]. We have applied polarography, powder-XRD, SEM-EDX, HR-TEM and XAFS to characterise the investigated samples of UO_{2+x}. The experiments were run during six months with periodical sampling of suspension aliquots for analysis. Before the analysis we rinsed the solid phase by deionised water to remove residual of the background solution.

Table 1: The composition of simulated groundwater (pH 7.0, Eh 350 mV)

Compound	Content (mg/L)
$NaHCO_3$	167.0
$KHCO_3$	12.0
$MgCl_2$	7.9
KCl	0.6
CaF_2	3.8
$CaCl_2$	1.5
$CaSO_4$	26.0
$Ca(NO3)_2$	11.6
HF	0.4

**Figure 1: Picture of the equipment used for hydrothermal
leaching: Teflon vessels and steel autoclaves**

Polarography is a routine method which allows one to determine the stoichiometry of UO_{2+x} sample. The method is based on the detection of U(VI) concentration, after sample dissolution in orthophosphoric acid. The powder XRD data were recorded using Cu Kα radiation (RXD-6000 Shimadzu diffractometer). Lattice parameters were determined using Powder V2.00 software and phase identification was performed using PCPDFWIN database. Examination of the samples by SEM-EDX was done with a Supra 50VP Leo scanning electron microscope at acceleration voltage of 10 kV. We fixed UO_{2+x} powder samples on a conductive tape and sputter covered with a thin layer of carbon to avoid charging effects. All XAFS measurements were done at U L_3 edge at VEPP-3 synchrotron radiation source in Novosibirsk, Russia, under dedicated operating conditions of 2 GeV, 50-100 mA, at room temperature using Si(111) crystal to monochromate the beam. The spectra were recorded in transmission mode using Ar filled first ionisation chamber and Kr filled second ionisation chamber. Interval between data points was 0.4 eV for XANES region and 1.5 eV for EXAFS region. Energy calibration was accomplished using data reported by Conradson, *et al.* [6].

The [237]Np concentrations in solutions were determined by alpha spectroscopy (Si surface barrier detector) after microfiltration of periodically sampled suspensions. The changes in composition of the background solution and uranium concentration in solution were analysed by ICP-MS. The partitioning of neptunium with the solid phase was studied by sequential leaching by deionised water, 0.5 M acetic acid and 3 M nitric acid to remove physically adsorbed or precipitated neptunium, then neptunium sorbed by surface complexation mechanism and finally neptunium bound to residual low soluble oxides [4].

Results and discussion

Leaching behaviour and secondary uranium phase formation

The investigated UO_{2+x} sample had the bulk composition of $UO_{2.075}$ according to polarography data and a stoichiometry on the surface close to U_4O_9 as determined by XPS analysis earlier [7]. The lattice parameter according to XRD is 5.4638±0.0007 Å and no preferred crystalline orientation is observed for the initial sample.

We have to admit even visual difference in colour of the samples leached during six months at two temperatures (Figure 2). The sample leached at 70°C keeps a dark grey colour, which is the same as for the initial sample before hydrothermal treatment; in contrast the sample leached at 150°C get brownish colour common for uranium(VI) minerals.

The evolution of XRD patterns for sample leached at 70°C is shown in Figure 3. The leached sample keeps cubic structure even after a half year at hydrothermal conditions, however decrease and broadening of the relative intensities of (222), (400), (331) and (420) lines are observed. The calculated

Figure 2: The photographs of uranium dioxide samples leached at 70 and 150°C
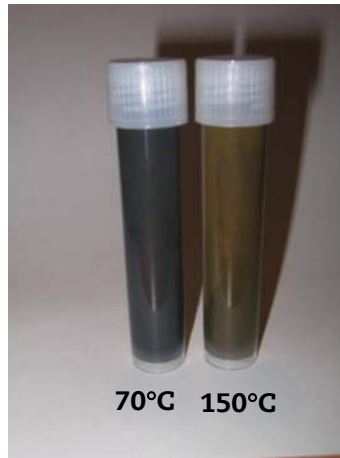
**Figure 3: The evolution of diffraction data for periodically
sampled solid phases of uranium dioxide leached at 70°C**

The decrease and broadening of intensities (222), (400), (331) and (420) are shown in the frame in up right corner
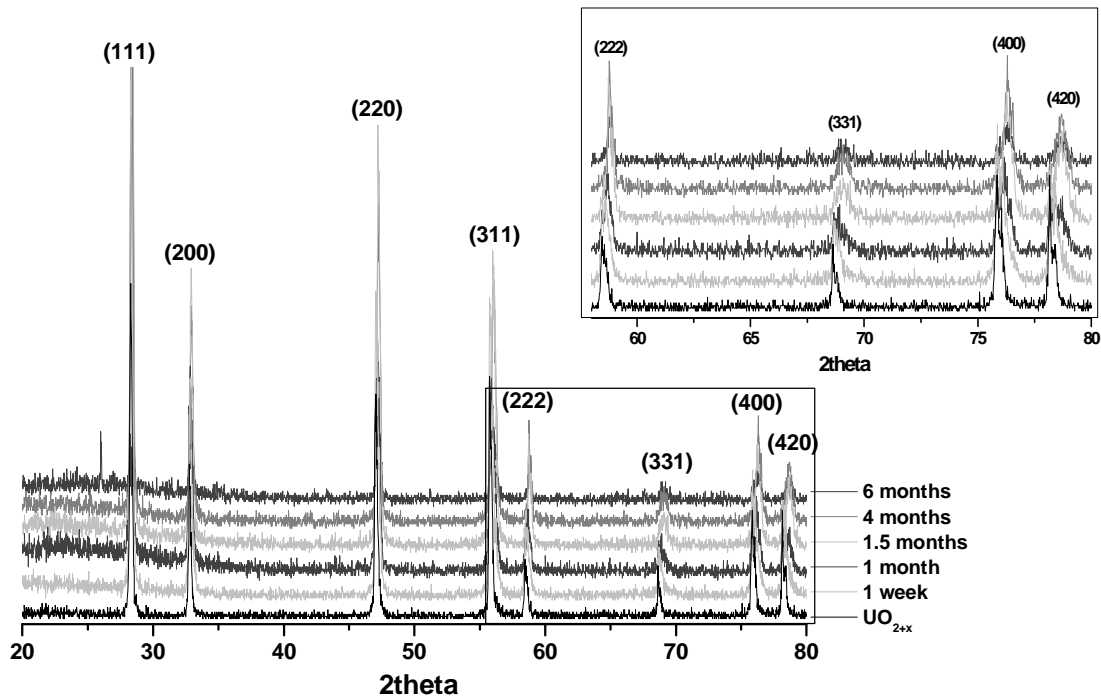
lattice parameter decreases with increase of leaching duration (Table 2). The decrease of lattice parameter and the broadening of mean lines are evidences of the bulk sample oxidation at 70°C. After the first 1.5 months of leaching the lattice parameter becomes constant with a value equal to 5.43 Å that most likely corresponds to U_4O_9 phase [8]. Lattice parameter and cell volume in uranium oxide system depend on uranium/oxygen ratio in the interval UO_2-U_4O_9 [9]. The correlation between lattice parameter and UO_{2+x} composition given in literature [8-20] has wide data spread; however, the main trend of decrease is evident. The existence of cubic lattice parameter is described by some authors through $UO_{2.33}$ phase [21]. The U_4O_9 formed after rapid bulk oxidation is stable at subsequent leaching. The presence of a uraninite phase at various stages of dissolution and alteration was found in natural

Table 2: Lattice parameters of UO$_{2+x}$ samples leached at 70°C and 150°C

Sampling interval after beginning of experiment	Lattice parameter, Å	
	70°C	150°C
1 week	5.460(3)	5.460(1)
1 month	5.442(2)	5.462(1)
1.5 months	5.432(4)	5.464(1)
2.5 months	-	5.464(1)
4 months	5.430(3)	5.436(1)
6 months	5.432(2)	5.431(1)

reactors in Oklo [8] that is the proof of the long-term stability of uranium dioxide. In spite of significant bulk oxidation, the presence of the secondary phases in samples of uranium dioxide leached at 70°C was not detected by XRD analysis.

The evolution of XRD patterns for sample leached at 150°C is shown in Figure 4. For this sample the decrease of lattice parameter was slower than for sample leached at 70°C, the lattice parameter reached the value of 5.43 Å only after four months of leaching. At 150°C uranium dioxide also keeps its cubic structure during half of the year, but the intense secondary phase formation was established. According to XRD data, the formation of schoepite (UO$_2$(OH)$_2$), Na and K uranium oxides, (Ca,Na,K)U$_2$O$_7 \times 2$H$_2$O and both compreignacite and Na compreignacite [(Na,K)$_2$[(UO$_2$)$_3$O$_2$(OH)$_3$]$_2$(H$_2$O)$_7$] is found, whereas no silicon- or carbon-containing phases were observed in the leached sample. These results are matching with thermodynamic data published by various authors [22-23]. The formation of layered U(VI) structures is more reasonable, than formation of silicon containing framework structures. The formation of carbonate minerals is not likely due to their relatively higher solubility.

Figure 4: The evolution of diffraction data for periodically sampled solid phases of uranium dioxide leached at 150°C

The reflexes corresponded to schoepite (UO$_2$(OH)$_2$), Na and K uranium oxides, compreignacite (Na$_2$[(UO$_2$)$_3$O$_2$(OH)$_3$]$_2$(H$_2$O)$_7$) and (Ca,Na,K)U$_2$O$_7 \times 2$H$_2$O phases are shown in up right corner
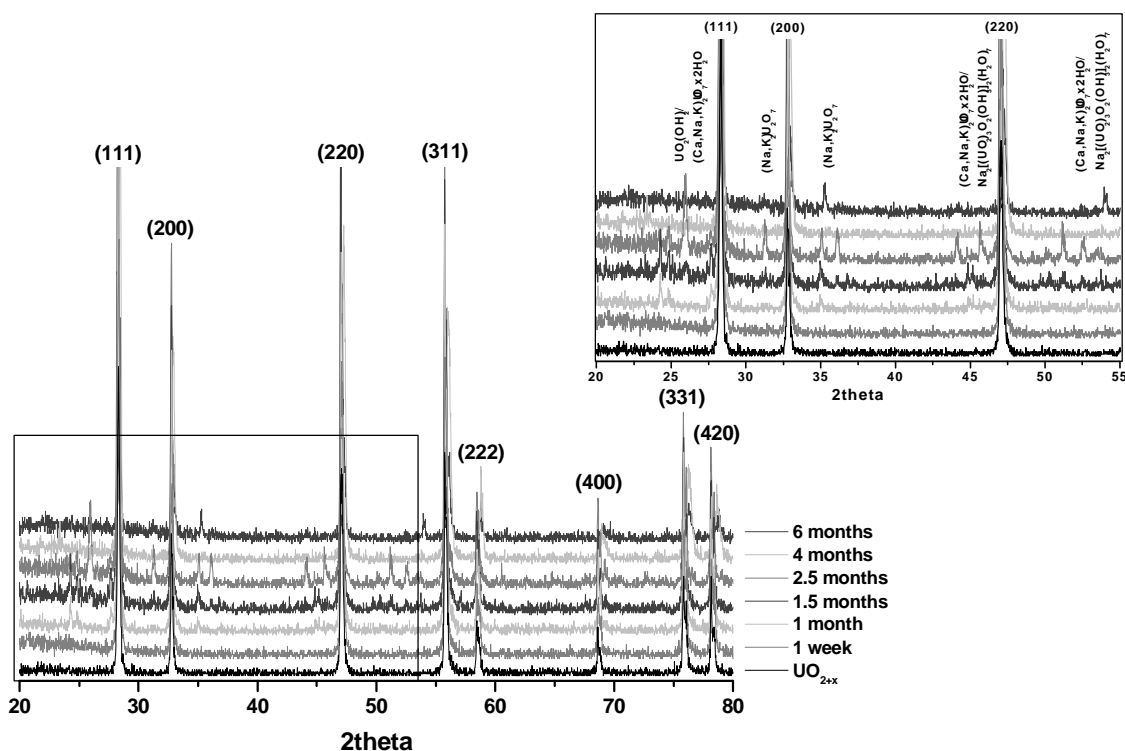
The changes in surface morphology and the evolution of secondary phase growth were observed by SEM-EDX. In case of sample leached at 70°C we observed the presence of some needle-like crystals on the solid surface that correspond to secondary uranium oxide phases as determined by EDX analysis. For sample leached at 150°C a higher concentration of secondary phase crystals was detected that is in a good agreement with XRD data. The concentration of secondary phases formed on the uranium dioxide sample leached at 70°C is below detection limit of the XRD method. For sample leached at 150°C, the formation of microcrystals was observed even after one week of leaching at hydrothermal conditions. The morphology of these microcrystals and the evolution of their growth are shown in Figure 5.

Figure 5: SEM images of samples leached at 70°C (A, B, C) and at 150°C (D, E, F). Sampling interval after beginning of experiment: A and D – 1 week, B and E – 1.5 months, C and F – 6 months.
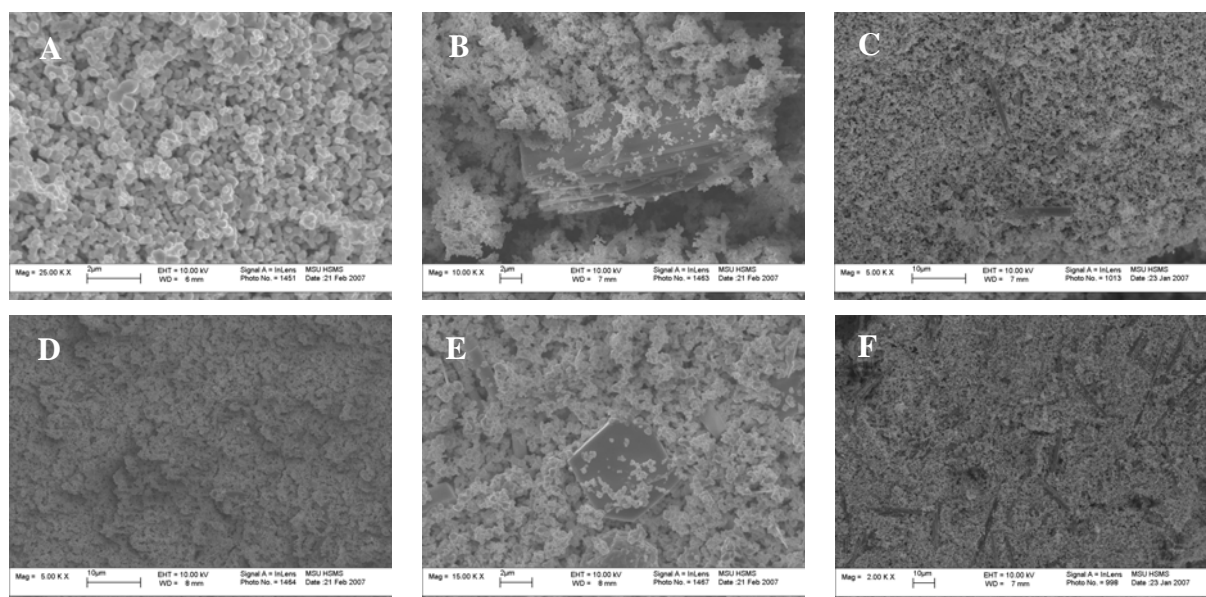
We applied XAFS to investigate uranium local structure in the leached samples as presented in Figure 6. No difference was observed in XANES spectra: both the shape and the intensities for samples leached at 70 and 150°C temperatures remain the same within various time intervals. As reference we used UO_2, U_3O_8 and $UO_2(OH)_2$ powder solids. We established that even after six months of hydrothermal leaching the sample correspond to UO_2 phase. The Fourier Transformed (FT) spectra are shown in Figure 7. The intensities of FT spectra decrease with increase of leaching interval: this denotes an increase of disorder in the investigated samples. The peak correspond to uranium-oxygen interaction is spited due to the presence of two shorter and longer distances. Furthermore, the contribution of short distance at 1.8 Å typical for U-O interaction in uranyl moiety grows in time. The tendencies demonstrated by XAFS and XRD are the same: FT intensities decrease more slowly for samples treated at 150°C and bulk oxidation goes more slowly as well.

The results obtained by XRD, SEM-EDX and XAFS demonstrate the difference in behaviour of UO_{2+x} samples treated under hydrothermal conditions at various temperatures, however the nature of the processes is not yet fully understood. For nanoscale characterisation of the solid surface we applied HR-TEM to distinguish the competition of the two processes which take place for uranium dioxide under hydrothermal conditions: bulk oxidation and secondary phase formation. The results of HR-TEM examination for UO_{2+x} samples leached a half of year at 70 and 150°C are shown in Figure 8. The sample kept at 70°C stays keeps its cubic structure as demonstrated by SAED and HR-TEM images. The surface of sample leached at 150°C is covered by nanoparticles oriented in different directions. Following the SAED examination these nanoparticles are schoepite colloids. Following this observation the most likely explanation of the difference in UO_{2+x} behaviour at 70 and 150°C is that the formation of schoepite nanoparticles prevents the diffusion of oxygen into the bulk volume of the sample and thus inhibits its further oxidation. Uranium dioxide and schoepite have difference in type and volume of crystalline lattice and as a result difference in oxygen diffusion coefficients [24-26].

Figure 6: XANES spectra of uranium dioxide samples leached under hydrothermal conditions
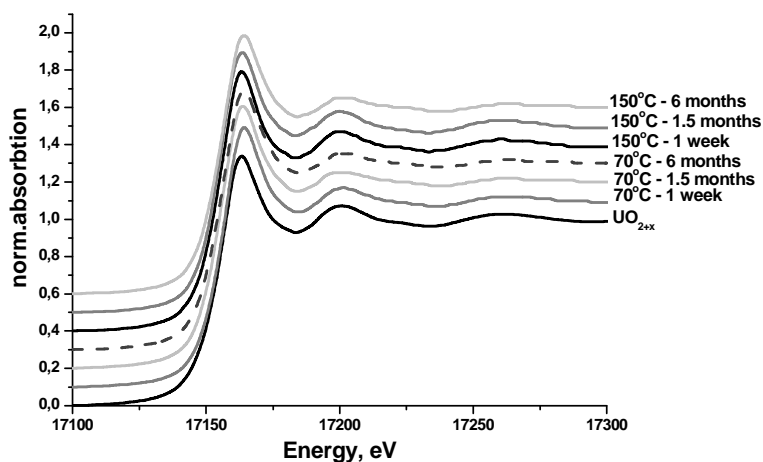
Figure 7: FT spectra of UO$_{2+x}$ leached samples
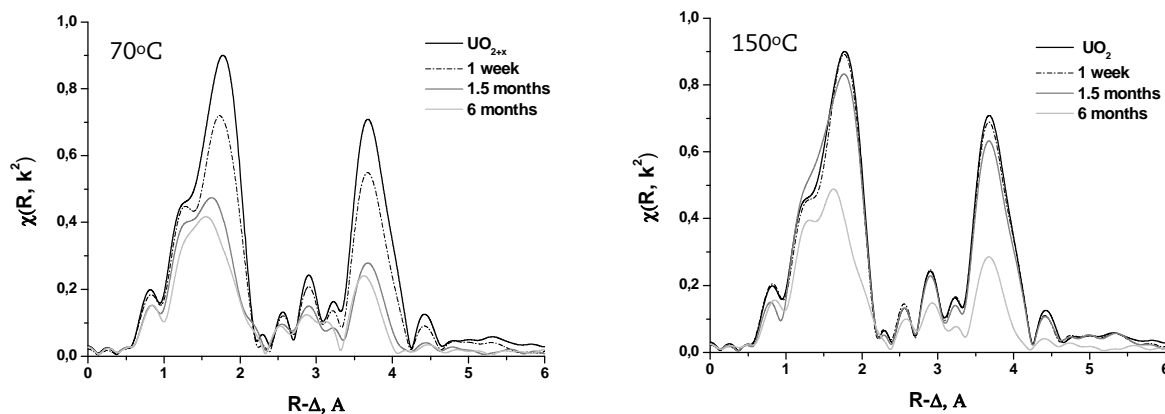
The results of experiments in deionised water

The same tendencies were observed in the experiments done in deionised water as in the simulated groundwater solution however the corrosion rates were slower. This observation allows us to conclude that the temperature is the main parameter governing the leaching behaviour of UO$_{2+x}$ while the influence of simulated groundwater chemical composition has the minor effect. The composition of the background solution has influence on the kinetics of the processes.

Table 3: Lattice parameters of leached UO$_{2+x}$ samples

Sample	Lattice parameter, Å
Initial UO$_{2+x}$	5.4638
Leached a half of year in simulated groundwater at RT	5.4655(6)
Leached a half of year in MilliQ water at RT	5.459(2)
Leached a half of year in MilliQ water at 70°C	5.445(2)
Leached a half of year in MilliQ water at 150°C	5.4636(7)

**Figure 8: HR-TEM images of uranium dioxide samples
leached during 6 months under hydrothermal conditions**

A and B: The HR-TEM image and SAED for the sample leached at 70°C
C and D: HR-TEM image and SAED for the sample leached at 150°C
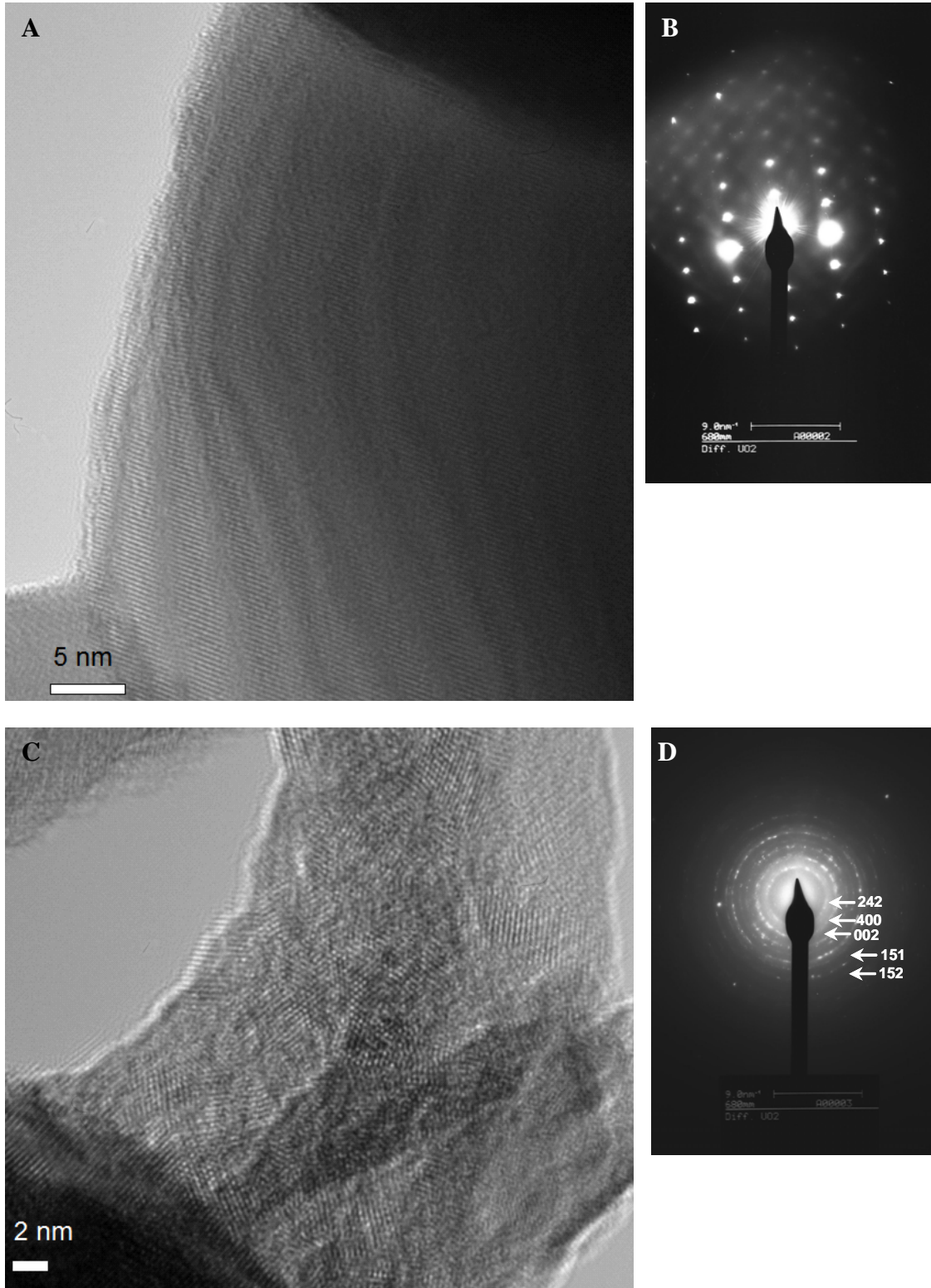
Interaction of neptunium with UO_{2+x}

After less than one week of experiment in simulated groundwater solution under hydrothermal conditions a quantitative sorption of neptunium is observed at both temperatures. According to the results of sequential extraction, about 1% of the [237]Np was washed either by deionised water or 0.5 M acetic acid. It was demonstrated earlier that the sorption of neptunium onto UO_{2+x} under ambient conditions follows the surface complexation mechanism for both Np(IV) and Np(V) at low and neutral pH intervals correspondingly [7]. Almost quantitative Np recovery was established only by complete dissolution of the solid with 3 M nitric acid. The possible mechanism of Np sequestration could be explained either by formation of insoluble NpO_2 or its incorporation to U(VI) secondary phases. The possibility of the second mechanism was reported earlier by Burns, *et al.* [4] who established Np(V) incorporation to Na-compregnacite and uranophane while meta-shoepite did not incorporate Np.

Conclusion

The competition between two processes is established in case of uranium dioxide hydrothermal leaching: bulk oxidation of UO_{2+x} and U(VI) secondary phase formation. The temperature is the main parameter that governs the route of leaching behaviour at the primary stages (few several months). It was established that at 150°C the schoepite is formed as randomly oriented nanoparticles on the UO_{2+x} surface. These nanoparticles passivate the surface and inhibit UO_{2+x} oxidation due to the difference in oxygen diffusion between UO_2 and $UO_2(OH)_2$.

References

[1] Shoesmith, D.W., *J. Nucl. Mater.*, Vol. 282, pp. 1-31 (2000).

[2] McGillivray, G.W., D.A. Geeson, R.C. Greenwood, *J. Nucl. Mater.*, Vol. 208, pp. 81-97 (1994).

[3] Trocellier, P., Ch. Cachoir, S. Guilbert, *J. Nucl. Mater.*, Vol. 256, pp. 197-206 (1998).

[4] Burns, P.C., K.M. Deely, S. Kanthakumar, *Radiochim. Acta*, Vol. 92, pp. 151-159 (2004).

[5] Amme, M., T. Wiss, H. Thiele, P. Boulet, H. Lang, *J. Nucl. Mater.*, Vol. 341, pp. 209-223 (2005).

[6] Conradson, S.D., D. Manara, F. Wastin, D.L. Clark, G.H. Lander, L.S. Morales, J. Rebizant, V.V. Rodinella, *Inorg. Chem.*, Vol. 43, pp. 6922-6935 (2004).

[7] Batuk, O.N., St.N. Kalmykov, V.G. Petrov, E.V. Zakharova, Yu.A. Teterin, A.Yu. Teterin, V.I. Shapovalov, M.J. Haire, *J. Nucl. Mater.*, Vol. 362 (2-3), pp. 426-430 (2007).

[8] "Uranium: Mineralogy, Geochemistry and the Environment", *Reviews in Mineralogy*, P.C. Burns, R. Finch (Eds.), Vol. 38, Mineralogical Society of America, Washington, DC (1999).

[9] Voronov, N.M., R.M. Sofronova, E.A. Voytekhova, "High-temperature Chemistry of Uranium Oxides and Other Uranium Compounds", *Atomizdat*, Moscow (1971) (in Russian).

[10] Gronvold, F., *J. Inorganic and Nuclear Chemistry*, Vol. 1, pp. 357-370 (1955).

[11]   Masaki, N., K. Doi, *Acta Cryst.*, Vol. 28, pp. 785-791 (1972).

[12]   Bevan, D.J.M., I.E. Grey, B.T.M. Willis, *J. of Solid State Chem.*, Vol. 61, pp. 1-7 (1986).

[13]   Garrido, F., L. Nowicki, A. Stonert, A. Pietraszko, E. Wendler, *Nucl. Instr. and Meth. in Phys. Res.*, Vol. 249, pp. 497-500 (2006).

[14]   Garrido, F., A.C. Hannon, R.M. Ibberson, L. Nowicki, B.T.M. Willis, *Inorg. Chem.*, Vol. 45, pp. 8408-8413 (2006).

[15]   Chernia, Z., Y. Ben-Eliyahu, G. Kimmel, G. Braun, J. Sariel, *J. Phys. Chem. B*, Vol. 110, pp. 23041-23051 (2006).

[16]   Higgs, J.D., W.T. Thompson, B.J. Lewis, S.C. Vogel, *J. of Nucl. Mater.*, Vol. 366, pp. 297-305 (2007).

[17]   Masaki, N., *J. Appl. Cryst.*, Vol. 7, pp. 247-250 (1974).

[18]   Willis, B.T.M., *Acta Cryst. A*, Vol. 34, pp. 88-90 (1978).

[19]   Lauriat, J-P., G. Chevrier, J-X. Boucherle, *J. of Solid State Chem.*, Vol. 80, pp. 80-93 (1989).

[20]   Cooper, R.I., B.T.M. Willis, *Acta Cryst. A*, Vol. 60, pp. 322-325 (2004).

[21]   Garrido, F., R.M. Ibberson, L. Nowicki, B.T.M. Willis, *J. Nucl. Mater.*, Vol. 322, pp. 87-89 (2003).

[22]   Clark, S.B., R.C. Ewing, J.C. Schaumloffel, *J. Alloys and Compounds*, Vol. 271-273, pp. 189-193 (1998).

[23]   Kubatko, K-A., K. Helean, A. Navrotsky, P.C. Burns, *American Mineralogist*, Vol. 91, pp. 658-666 (2006).

[24]   Yasuda, I., M. Hishinuma, *J. Solid State Chemistry*, Vol. 123, pp. 382-390 (1996).

[25]   Berenov, A.V., J.L. MacManus-Driscoll, J.A. Kilner, *Solid State Ionics*, Vol. 122, pp. 41-49 (1999).

[26]   De Souza, R.A., J.A. Kilner, *Solid State Ionics*, Vol. 126, pp. 153-161 (1999).

Soft X-ray scanning transmission spectromicroscopy of metal uptake by nuclear waste repository materials

R. Dähn,[1,2] **M. Vespa,**[1] **D.K. Shuh,**[2] **T. Tyliszczak,**[2] **E. Wieland**[1]
[1]Paul Scherrer Institute, Villigen, Switzerland
[2] Lawrence Berkeley National Laboratory, Berkeley, CA, USA

Abstract

The safe disposal of radioactive wastes in deep geological repositories is a challenging task. Although new technologies focusing on radioactive waste minimisation will undoubtedly reduce the waste arising in the future, strategies ensuring its safe disposal are still needed. The radionuclide release from a deep geological repository can be controlled and reduced by a suitable choice of the engineered and geological barriers. Cement-based materials play an important role in multi-barrier concepts developed world wide for the disposal of low and intermediate level radioactive wastes. In Switzerland, for example, it is planned to dispose of cement-stabilised radioactive wastes arising from electricity production in nuclear power plants as well as medicine, industry and research in a deep geological repository. Therefore, a mechanistic understanding of the processes governing the binding of heavy metals in cement systems is essential for long-term predictions of the environmental impact of cement-stabilised waste forms. From a chemical standpoint, cement is a very heterogeneous material with discrete particles in the nano to micrometre size range, which makes it an ideal system to be investigated with scanning transmission X-ray microscopy (STXM).

In this study the soft X-ray STXM end station at the Advanced Light Source-Molecular Environmental Science (ALS-MES) Beamline 11.0.2 has been utilised to investigate elements inherent to the cement matrix such as Al, and metal precipitates formed in Ni- and Co-doped cement pastes. The ALS-MES STXM collects both images and near-edge X-ray absorption fine structure (NEXAFS) spectra with a spatial resolution of 30 nm. NEXAFS spectra of the Al-K edge and Ni- and Co-L$_{III}$-edges were collected to gain spectroscopic information on the Al and Ni/Co-speciation in the cement matrix. The STXM investigations revealed that variations in the Al speciation and in the formation of precipitates in Ni- and Co-doped cement pastes occur on the nanometre scale. Recently, the investigations were extended to investigate the immobilisation of naturally occurring radionuclides such as U in the cement matrix. The study demonstrated that STXM is a powerful tool to gain information on the nanometre scale on the distribution and speciation in systems that are relevant in connection with the safe disposal of cement-stabilised hazardous and radioactive waste.

The impact of micro-organisms on the behaviour of actinides in natural environments

Sonja Selenska-Pobell
Institute of Radiochemistry, Forschungszentrum Dresden-Rossendorf
Dresden, Germany

Abstract

The behaviour of uranium and other actinides in the environment is strongly influenced by a broad range of biogeochemical factors and also by their own, often very complex chemistry. The major biotic factors in the radioactively polluted environments are the unicellular prokaryotic micro-organisms (bacteria and archaea) which, in contrast to the other forms of life on Earth, possess fascinating robustness to these extremely harsh and life-unfriendly surroundings. Micro-organisms have developed very effective protection mechanisms against radionuclides and other heavy metals which are based on their ability for oxidative or reductive biotransformations, bioaccumulation, and/or biomineralisation of these toxic elements [1-3].

Interactions of different bacterial strains with U, Np, Pu, Am, and Cm were studied in our and also in other laboratories at conditions favourable for both actinide chemistry and bacterial physiology [4-13]. By using XAS in combination with other spectroscopic methods, namely FTIR and TRLFS, and also with TEM-EDX we were able to demonstrate formation of microbial-specific actinide precipitates and even biomineralisation in the case of U [7,11,13]. Recent results on interactions of different bacterial and archaeal strains with radionuclides will be presented in the first part of the talk.

Although most of the investigated microbial strains were recovered from actinide contaminated sites, it is difficult to predict on the basis of the above mentioned laboratory studies the behaviour of both micro-organisms and actinides in the natural environments which have extremely complex chemical composition and are occupied by a large variety of micro-organisms [3]. Therefore the second part of the talk will be focused on the behaviour of U(VI) in natural environments.

At first the bio-stimulated reduction of soluble U(VI) to insoluble U(IV) was studied in uranium contaminated waters and sediments. This reduction had only limited or temporary effects [14,15], however. It was demonstrated that the size of the uranium-reducing bacterial populations which were stimulated by the addition of organic electron donors such as lactate, acetate, or ethanol was strongly reduced after the depletion of the added nutrients and that the initially immobilised uranium was re-oxidised and returned to the treated habitat [14,15].

Moreover, the natural conditions of the uranium mining wastes or depository sites are as a rule oligotrophic and the major naturally changing ingredients, along with the uranium, are inorganic, in particular – nitrate and sulphate [16] but not organic. Because the reduction of nitrate is thermodynamically more favourable than the reduction of U(VI), or sulphate, it is preferably used by the natural micro-organisms in the subsurface of the uranium wastes for anaerobic respiration [16].

Recently, we were able to demonstrate that the addition of uranyl nitrate to the natural oligotrophic samples of a uranium mining waste pile does not stimulate uranium-reducing bacteria neither under aerobic nor under anaerobic conditions [17,18]. Instead, many other microbial populations able to immobilise U(VI) via sorption, bioaccumulation and biomineralisation were stimulated. The stimulated micro-organisms, which were present in very low numbers in the original, untreated samples, were affiliated with bacterial and archaeal species able to respire nitrate and/or Fe(III) under anaerobic conditions. Noteworthy, the studied natural samples contained iron in very high concentrations [17].

By using Mössbauer spectroscopy of [57]Fe we found that, when the added nitrate was consumed by the natural microbial community, strong reduction of the naturally present Fe(III) occurred. TRLFS spectroscopic analysis of the uranyl nitrate supplemented samples revealed that almost the whole amount of the added U(VI) was bound in a mixture of organic and inorganic phosphate compounds both of biotic origin [13,18]. Our first data obtained by using EXAFS spectroscopic analysis about the de novo formed uranyl phosphate compounds in the studied environmental samples will be discussed at the end of the talk.

References

[1] Francis, J., *J. Alloys Comp.,* 271, 78-84 (1998).

[2] Pedersen, K., *J. Nucl. Radiochem. Sci.,* 6, 11-15 (2005).

[3] Selenska-Pobell, S., "Diversity and Activity of Bacteria in Uranium Waste Piles," in *Interactions of Microorganisms with Radionuclides,* M.J. Keith-Roach, F.R. Livens (Eds.), Elsevier Sciences Ltd, Oxford, UK (2002), pp. 225-254.

[4] Francis, A.J., J.B. Gillow, C.J. Dodge, R. Harris, T.J. Beveridge, H.W. Papenguth, *Radiochim. Acta* 92, 481-488 (2004).

[5] Lloyd, J.R., *FEMS Microbiology Reviews*, 27, 411-425 (2003).

[6] Merroun, M., C. Hennig, A. Rossberg, T. Reich, S. Selenska-Pobell, *Radiochim. Acta,* 91, 583-592 (2003).

[7] Merroun, M., J. Raff, A. Rossberg, C. Hennig, T. Reich, S. Selenska-Pobell, *Appl. Environ. Microbiol.,* 71, 5532-5543 (2005).

[8] Merroun, M., N. Nedelkova, A. Rossberg, C. Hennig, S. Selenska-Pobell, *Radiochim. Acta,* 94, 723-729 (2006).

[9] Moll, H., M. Merroun, C. Hennig, A. Rossberg, S. Selenska-Pobell, G. Bernhard, *Radiochim. Acta,* 94, 815-824 (2006).

[10] Moll, H., Th. Stumpf, M.L. Merroun, A. Rossberg, S. Selenska-Pobell, G. Bernhard, *Environ. Sci. Technol.*, 38, 1455-1459 (2004).

[11] Nedelkova, M., M.L. Merroun, A. Rossberg, C. Hennig, S. Selenska-Pobell, *FEMS Microbiol. Ecol.,* 59, 694-705 (2007).

[12] Rugiero, E., H. Boukhalfa, J. Forsythe, J.G. Lack, L.E. Hersman, M.P. Neu, *Environ. Microbiol.,* 7, 88-97 (2005).

[13] Selenska-Pobell, S., M. Merroun, "Accumulation of Heavy Metals by Microorganisms: Biomineralization and Nanocluster Formation", in *Prokaryotic Cell Wall Components – Structure and Biochemistry*, Elsevier Publishers (2008) (in press).

[14] Anderson, R.T., H.A. Vrionis, I. Ortiz-Bernad, C.T. Resch, P.E. Lonh, R. Dayvault, K. Karp, S. Marutzky, D.R. Metzler, A. Peacock, D.C. White, M. Lowe, D.R. Lovley, *Appl. Environ. Microbiol.,* 69, 5884-5891 (2003).

[15] Nyman, J.L., T.L. Marsh, M.A. Ginder-Vogel, M. Gentile, S. Fendorf, C. Criddle, *Biodegradation,* 17, 303-316 (2006).

[16] Finneran, K.T., M.E. Housewright, D.R. Lovley, *Environ. Microbiol.,* 4, 510-516 (2002).

[17] Geissler, A., S. Selenska-Pobell, *Geobiology*, 3, 275-285 (2005).

[18] Geissler, A., G. Geipel, M. Merroun, H. Reuther, S. Selenska-Pobell, *Geobiology,* (2008) (submitted).

Uranium(VI) complexation with pyoverdins and related model compounds studied by EXAFS

H. Moll, M. Glorius, A. Roßberg, G. Bernhard
Forschungszentrum Dresden-Rossendorf e.V., Institute of Radiochemistry
Dresden, Germany

Abstract

Synchrotron-based EXAFS spectroscopy is a powerful technique to obtain structural information on radionuclide bioligand species in solution. As an example pyoverdin-type siderophores are a unique class of bioligands, with a high potential to dissolve, bind, and thus transport uranium in the environment. Pyoverdins are secreted from fluorescent Pseudomonas species which are ubiquitous soil bacteria. The functional groups of the pyoverdin molecule, LH_4, participating in metal binding are the catechol group of the chromophore and two ligand sites in the peptide chain, i.e. one or two hydroxamate groups and one or two α-hydroxy acid moieties [1]. The formation of complexes of UO_2^{2+} with pyoverdins released by the groundwater bacterium Pseudomonas fluorescens (CCUG 32456) isolated at a depth of 70 m in the Äspö Hard Rock Laboratory, Sweden, was investigated in our previous study [2]. Two UO_2^{2+}-P. fluorescens pyoverdin species, UO_2LH_2 and UO_2LH_-, could be distinguished on the basis of UV-vis spectroscopy and fs-TRLFS.

Little structural information is available regarding the U(VI) pyoverdin species formed in aqueous solutions. We therefore performed U L_{III}-edge EXAFS measurements of test solutions containing 5×10^{-4} or 0.001 M UO_2^{2+} and pyoverdins or related model compounds at an ionic strength of 0.1 M $NaClO_4$. The pH was varied between 2 and 8 depending on the bioligand. EXAFS measurements were carried out on the Rossendorf Beamline (ROBL) BM20 at the ESRF [3]. The samples were measured at room temperature using a water-cooled Si(111) double-crystal monochromator in channel cut mode (5-35 keV). The spectra were collected either in fluorescence mode using a 13-element Ge solid-state detector or in transmission mode using Ar filled ionisation chambers. The model compounds simulate the hydroxamate function (simple hydroxamate and a trihydroxamate compound) and the chromophore of the pyoverdin molecule. The obtained structural information for the axial and equatorial oxygen atoms surrounding the uranium atom will be presented. Estimations of the near order surrounding of uranyl in pyoverdin complexes are based on the comparison with those found in uranium(VI) model ligand species.

References

[1]   Budzikiewicz, H., *Fortschr. Chem. Org. Naturst.*, 87, 83 (2004).

[2]   Moll, H., M. Glorius, G. Bernhard, A. Johnsson, K. Pedersen, M. Schäfer, H. Budzikiewicz, *Geomicrobiol. J.* (2008), forthcoming.

[3]   Matz, W., N. Schell, G. Bernhard, F. Prokert, T. Reich, J. Claussner, W. Oehme, R. Schlenk, S. Dienel, H. Funke, F. Eichhorn, M. Betzl, D. Prohl, U. Strauch, G. Hüttig, H. Krug, W. Neumann, V. Brendler, P. Reichel, M. A. Denecke, H. Nitsche, J. *Synchrot. Radiat.,* 6, 1076 (1999).

Structural determination of biogenic actinide-oxides using X-ray absorption spectroscopy

Alison Costello,[1] **Eleanor Schofield,**[2] **John Bargar,**[2] **Hakim Boukhalfa**[1]
[1]Earth and Environmental Sciences Division-Hydrology, Geochemistry and Geology (EES-6)
Los Alamos National Laboratory, Los Alamos, NM
[2]Stanford Synchrotron Radiation Laboratory, Menlo Park, CA

Abstract

Dissimilatory metal reducing bacterial (DMRB) utilise iron(III) oxides as electron acceptors for their anaerobic respiration. DMRB have also been shown to utilise other oxidised metals [e.g. U(VI), Tc(VII), Cr(VI)] as electron receptors to support their anaerobic respiration. We have examined the reduction of Pu(VI) by Shewenella oneidensis MR1 and Geobacter metallireducens GS15 under cell suspension conditions. Our data indicate that Pu(VI) and Pu(V) are reduced enzymatically by these micro-organisms. The characterisation of biogenic PuO_2 oxides indicates that Pu solids deposited on the cell surface are aggregates of crystalline nano-particulates. These solids have a high surface area and are expected to have a higher reactivity compared to synthetic aged PuO_2 and oxides. Thus far, the structure, stability and reactivity of the plutonium-oxides produced by bacterial reduction (biogenic) have not been well characterised. Here we present X-ray absorption (XAS) spectroscopic studies of biogenic plutonium-oxides produced by direct enzymatic reduction and indirect non-enzymatic reduction by Shewenella oneidensis MR1 and Geobacter metallireducens GS15. These results will be compared to the XAS spectra of inorganic plutonium-oxides and biogenic UO_2. These studies will help to structurally distinguish the biogenic and inorganic species and help to define their environmental behaviour.

Session III

Solid state chemistry and physics of the radionuclides

Chair: Stepan N. Kalmykov

Soft X-ray studies of Pu electronic structure:
Past lessons from XAS and future directions with BIS

J.G. Tobin,[1] **S.W. Yu,**[1] **B.W. Chung,**[1] **G.D. Waddill,**[2] **A.L. Kutepov**[3]
[1]Lawrence Livermore National Laboratory, Livermore, CA, USA
[2]Missouri University of Science and Technology, Rolla, MO, USA
[3]University of California-Davis, Davis, CA, USA

Abstract

Synchrotron-radiation-based spectroscopies such as X-ray Absorption Spectroscopy (XAS) have contributed greatly to our improved understanding of Pu electronic structure. However, significant questions remain concerning the nature of Pu electronic structure. Perhaps the missing piece of the puzzle is the direct experimental determination of the unoccupied electronic structure using high energy inverse photoelectron spectroscopy (IPES) or Bremstrahlung Isochromat Spectroscopy (BIS). Past BIS studies of Th and U indicate the feasibility and utility of Pu studies. To this end, a new BIS capability has been developed in our laboratory. Electron stimulated emission of photons has been carried out using the XES-350 monochromator and detector system. Our preliminary results and future plans will be presented.

Introduction

Significant questions remain concerning the nature of Pu electronic structure. [1-5] While chemically toxic and highly radioactive, Pu may be the most scientifically interesting element in the periodic table. Its properties include the following: six different phases, close to each other in energy and sensitive to variations of temperature, pressure and chemistry; the face-centered-cubic phase (delta) is the *least* dense; Pu expands when it solidifies from the melt; and it is clearly the nexus of the actinide binary phase diagram of the actinides. In a sense, it is the boundary between the light (ostensibly delocalised 5f electrons) and heavy (ostensibly localised or correlated 5f electrons) actinide elements, but this is an over-simplification. The localised atomic 5f states are naturally correlated, but important regimes of correlated electron states are conceivable as extended states on the delocalised side of the possible Mott transition. The proximity to this crossover may be the driving force behind all these exotic properties. Pu remains of immense technological importance and the advancement to a firm, scientific understanding of the electronic structure of Pu and its compounds, mixtures, alloys and solutions is a crucial issue.

Photoelectron Spectroscopy [1] and X-ray Absorption Spectroscopy [2-4] have contributed greatly to our improved understanding of Pu electronic structure (see Figure 1). From these and related measurements, the following has been determined.

- The Pu 5f spin-orbit splitting is large.

- The number of Pu5f electrons is 5.

- The Pu 5f spin-orbit splitting effect dominates 5f itineracy.

Figure 1: X-ray absorption spectra (XAS) of alpha-U and alpha-Pu
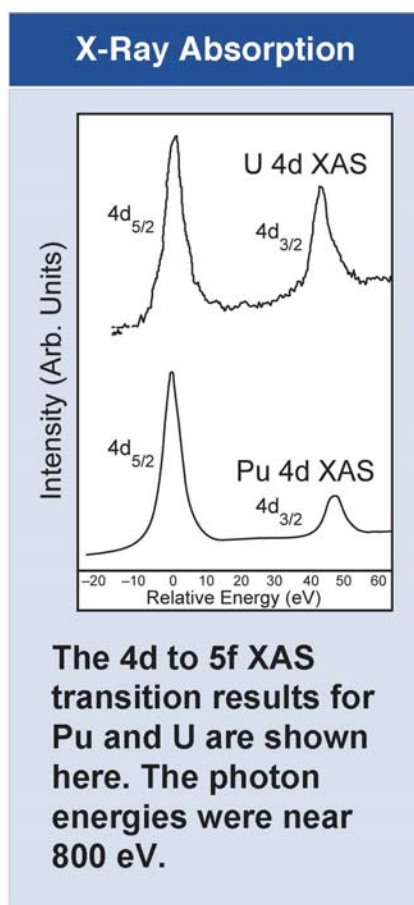
BIS and the uDOS

Perhaps the missing piece of the puzzle is the direct experimental determination of the unoccupied density of states (uDOS) using high energy inverse photoelectron spectroscopy (IPES) or Bremsstrahlung Isochromat Spectroscopy (BIS) [5]. Past BIS studies of Th and U indicate the feasibility and utility of Pu studies [6].

To this end, a new BIS capability has been developed in our laboratory [5,7,8]. Electron stimulated emission of photons has been carried out using the XES-350 monochromator and detector system. Our preliminary results and future plans will be presented.

Moreover, while there are a number of ongoing experimental efforts directed at determining the occupied (valence band, below the Fermi Energy) electronic structure of Pu, there is essential no experimental data on the unoccupied (conduction band, above the Fermi Energy) electronic structure of Pu.

The central technique is BIS, or high energy Inverse Photoelectron Spectroscopy [9]. BIS is the high-energy variant of inverse photoelectron spectroscopy (IPES: electron in, photon out), which is essentially the time reversal of photoelectron spectroscopy (PES: photon in, electron out), as illustrated in Figure 2. Photoelectron spectroscopy is a widely utilised technique with multiple applications (see Refs. [1,2,9] and references therein). However, the underlying event is always the same: i) a photon impinges upon the sample and is absorbed; ii) the energy passes to an electron, which is ejected. In the case of valence band photoelectron spectroscopy, one can either map the occupied band structure in angle resolving experiments upon single crystals or probe the occupied density of states (oDOS) by angle-averaging with polycrystalline samples, usually at higher energies. Generally speaking, IPES is the time reversal of the valence band PES, only now the unoccupied states (uDOS) are interrogated. (For metals with their short screening lengths, the inconsistencies due to differences in final state charges become negligible.) IPES can be used to follow the dispersion of unoccupied electronic states in ordered samples [9]. Due to its low energies, IPES is usually very surface and band sensitive. However, by working at higher energies and using polycrystalline samples, we will sample preferentially for the bulk density of states, downgrading the impact of surface and band effects.

Figure 2: Schematic of the inverse photoelectron process

KE is kinetic energy of the incoming electron, θ is the work function, H^F is the energy of the state relative to the Fermi Level, and hν is the energy of the emitted photon. A defining characteristic of IPES/BIS is that hν ≈ KE.
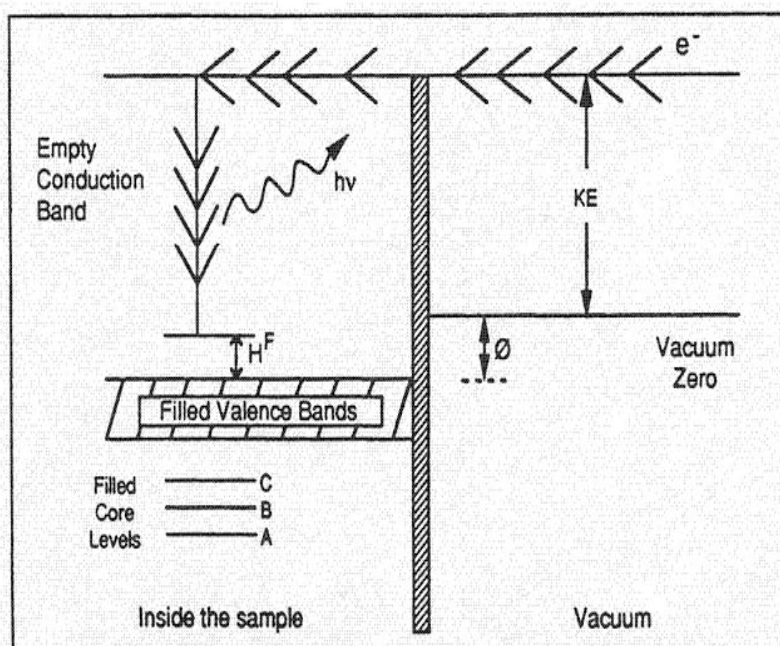
Thus, from BIS, we would argue that we should have a direct measure of the conduction band or unoccupied electronic structure of the bulk Pu. In support of this contention, we present the comparison shown below. Here, experimental BIS data from Baer and Lang [6] is directly compared to a simulated BIS spectrum generated from a calculation of the density-of-states of alpha-U. The match is excellent, strongly supporting the validity of this approach.

**Figure 3: Comparison of an earlier BIS measurement by
Baer and Lang [6] of uranium with a simulated density of states**

The simulation is generated by starting with a calculation by Kutepov (in red) [4], which is truncated at the Fermi Energy (only unoccupied states can contribute to BIS) and then smoothed to reflect broadening from the instrumental band-pass (in black) [8]. Top: Experimental BIS result of Baer and Lang. Bottom: Red: DOS calculations by A.L. Kutepov, black: DOS calculation times inverse Fermi function, with some instrumental broadening [8].
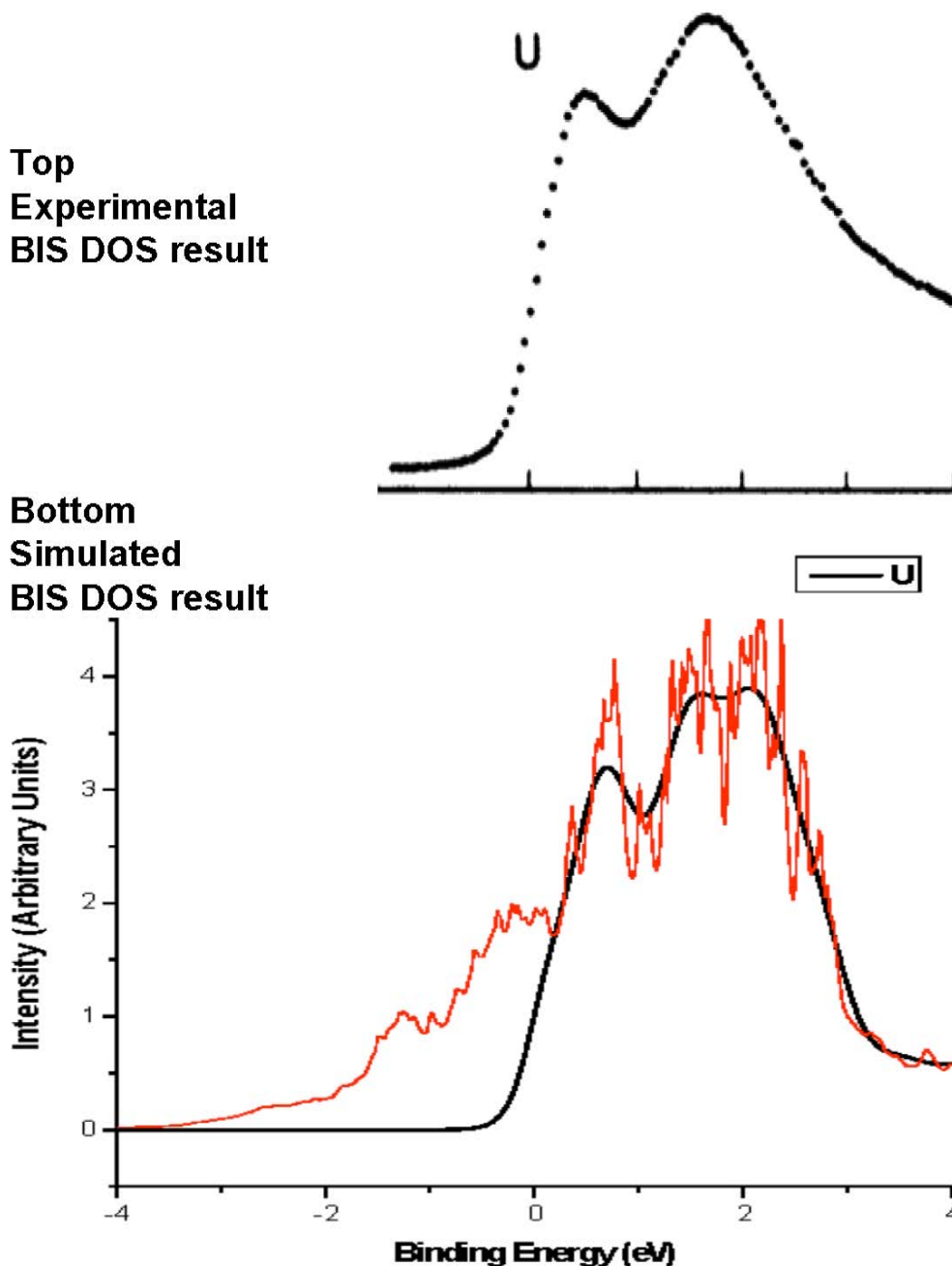
Experimental instrumentation: Fano/Bis Spectrometer

A new Fano/BIS Spectrometer has been developed in our laboratory, as shown schematically in Figures 4 and 5 below. Fano Spectroscopy is a type of specialised photoelectron spectroscopy, which combines true spin detection with chirally configured excitation [10]. Under these conditions, it is possible to get detailed information concerning the interaction of spins and spin-orbit splitting, even within non-magnetic systems. In this Fano/BIS Spectrometer, three separate photon sources are utilised, designated as UV1, UV2 and X-ray in Figure 4. The BIS capability is provided by the XES-350 monochromator/detector and an electron gun (not shown) (see Figure 4 caption for more detail).

Figure 4: Sketch for BIS and spin resolved photoelectron spectroscopy (SRPES) experimental set-up installed recently at Lawrence Livermore National Lab for the electronic structure study of actinides

For BIS, the detection of the photons is performed with the XES-350 monochromator and multi-channel detector. For SRPES, unpolarised light hits sample at an angle of 45° with respect to the surface normal. The energies and the spins of the normally emitted photoelectrons are analysed by hemispherical electron energy analyser and Mott detector, which has a thorium target operated at 25 keV with Sherman function of 0.16 ± 0.04, respectively. Two transversal spin components PX and PY can be measured in Mott detector simultaneously.
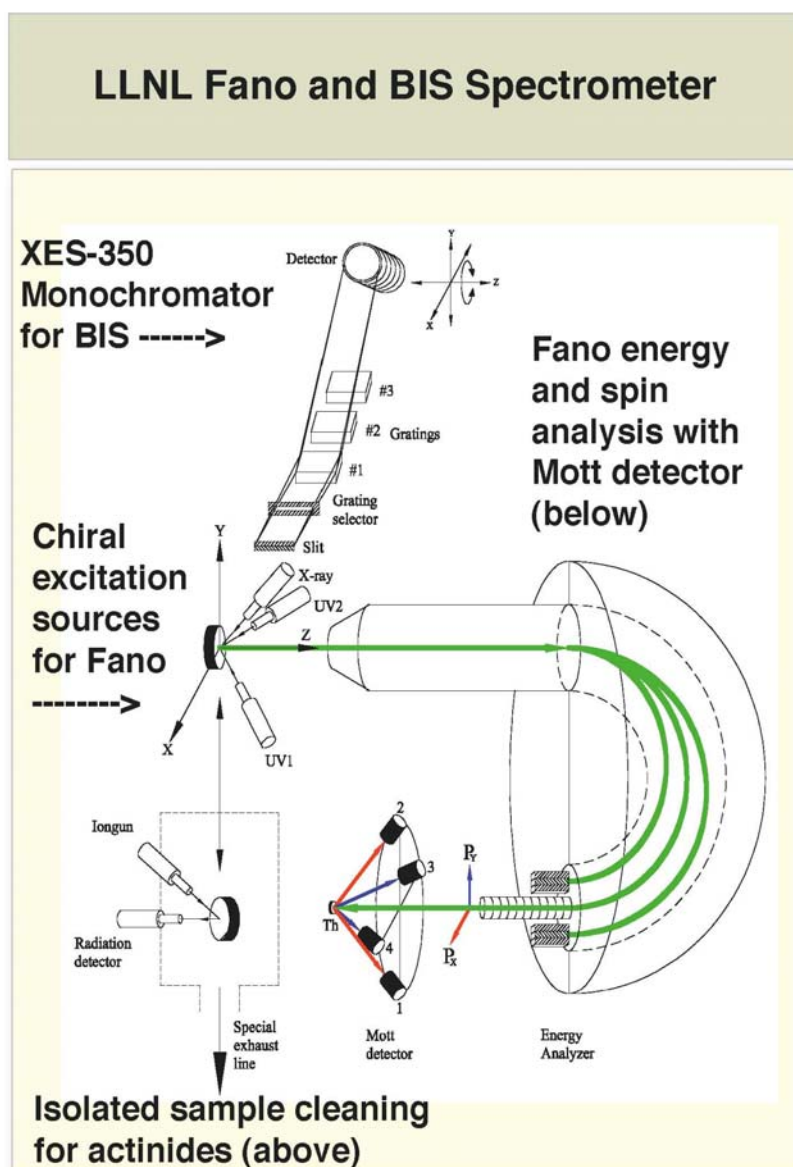
Figure 5: Schematic of the XES-350 monochromator and detector is shown here

Figure provided by Scienta
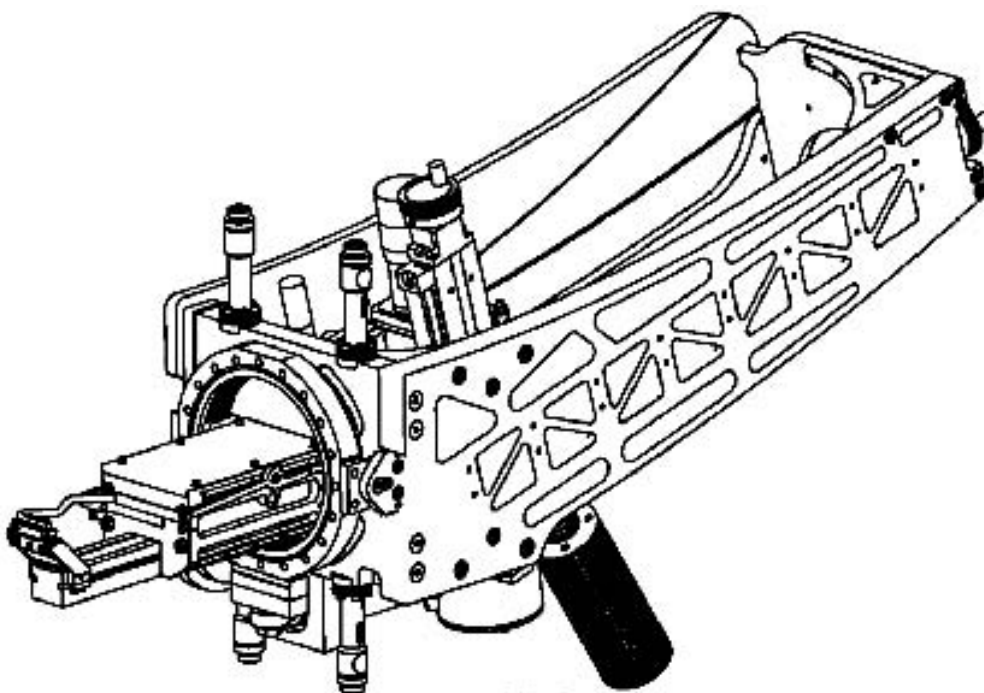
BIS photon detection

The XES-350 uses three overlapping gratings to cover the energy range from below 100 eV to above 1 000 eV. The image of the exit slit of the monochromator then falls upon a multi-channel detector, which can be summed in the non-energy direction to provide energy dispersive spectra of the photon emission. In the case of IPES/BIS, the photon energy (hv) and kinetic energy (KE) are approximately equal. This is a demanding experiment, in which the cross-sections are relatively low [9]. In some of our initial measurements in the Fano/BIS spectrometer, a relatively low current electron gun was used. To aid in data collection in IPES/BIS, we have installed a new high current electron gun and are presently commissioning it. As a preliminary test of the XES-350 system, electron stimulated emission of photons had been carried out using the XES-350 monochromator and detector system. Some of our preliminary results are shown below in Figures 6 and 7, using an electron-excitation-beam-energy of 3 000 eV. These preliminary tests were performed under fairly poor vacuum using untreated bulk metal samples, which had been exposed to the laboratory atmosphere, and thus may be considered a worst-case test.

X-Ray Emission Spectroscopy

X-ray Emission Spectroscopy (XES) is a generic name that includes BIS. However, the spectra shown in Figures 6 and 7 correspond to core level XES. Here, a high-energy electron beam (3 000 eV) is used to generate holes in the core levels. This would correspond to the levels A, B and C shown in Figure 2. Subsequently, a decay process can occur, where electrons in less tightly bound levels transition into the core hole. If the extra energy is transferred to an electron, Auger Spectroscopy is the result. If the extra energy is emitted as an X-ray photon, then XES is the result. If one were to substitute photonic excitation for electronic excitation, then this process would be called fluorescence or phosphorescence.

In the case of Figures 6 and 7, the XES is coming from the core levels of zinc and oxygen. For the zinc, the source is the Zn2p doublet: the Lα1 and Lα2 at 1 011.7 eV and the Lβ1 at 1 034.7 eV. In the case of the oxygen, it is the O1s level: Kα1 at 524.9 eV [11].

**Figure 6: Zn L (2p) and O K (1s) emission in first order,
measured at the calculated positions on Grating 1**
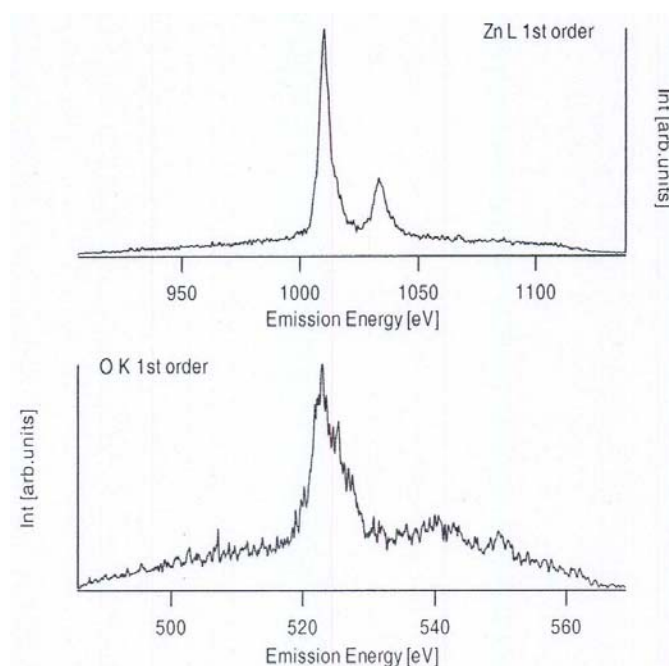
**Figure 7: Zn L (2p) and O K (1s) emission in first order,
measured at the calculated positions on Grating 2**
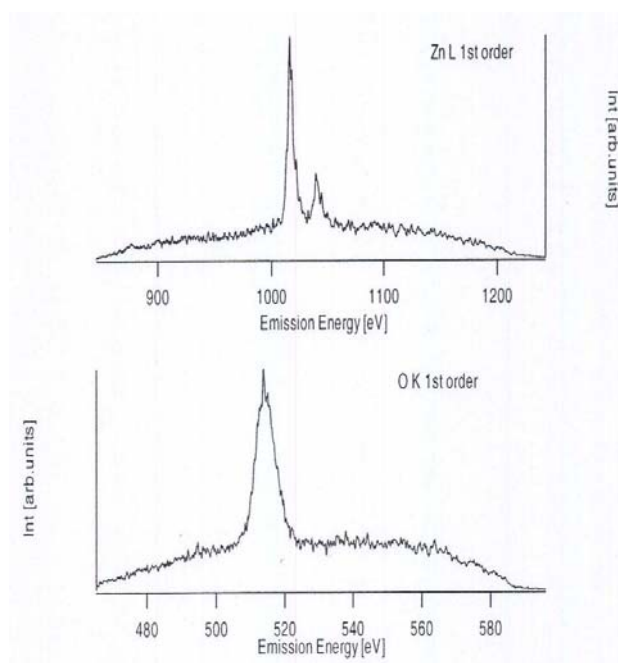
Summary

After briefly summarising our previous results, we have discussed the efficacy of BIS measurements as a means of determining the UDOS of Pu and resolving the Pu electronic structure controversy. Technical details and preliminary test results of the new BIS capability have also been presented.

References

[1]   Tobin, J.G., B.W. Chung, R.K. Schulze, J. Terry, J.D. Farr, D.K. Shuh, K. Heinzelman, E. Rotenberg, G.D. Waddill, G. Van der Laan, "Resonant Photoemission in f-electron Systems: Pu and Gd", *Phys. Rev. B*, 68, 155109 (2003).

[2]   Tobin, J.G., P. Soderlind, A. Landa, K.T. Moore, A.J. Schwartz, B.W. Chung, M.A. Wall, J.M. Wills, R.G. Haire, A.L. Kutepov, *Journal of Physics-Condensed Matter* 20, 125204 (2008); K.T. Moore, M.A. Wall, A.J. Schwartz, B.W. Chung, D.K. Shuh, R.K. Schulze, J.G. Tobin, "The Failure of Russell-Saunders Coupling in the 5f States of Plutonium", *Phys. Rev. Lett.*, 90, 196404 (2003).

[3]   van der Laan, G., K.T. Moore, J.G. Tobin, B.W. Chung, M.A. Wall, A.J. Schwartz, "Applicability of the Spin-orbit Sum Rule for the Actinide 5f States", *Phys. Rev. Lett.*, 93, 097401 (2004).

[4]   Tobin, J.G., K.T. Moore, B.W. Chung, M.A. Wall, A.J. Schwartz, G. van der Laan, A.L. Kutepov, "Competition Between Delocalization and Spin-orbit Splitting in the Actinide 5*f* States", *Phys. Rev. B*, 72, 085109 (2005).

[5]   Tobin, J.G., M.T. Butterfield, N.E. Teslich Jr., R.A. Bliss, M.A. Wall, A.K. McMahan, B.W. Chung, A.J. Schwartz, "Using Nano-focussed Bremstrahlung Isochromat Spectroscopy (nBIS) to Determine the Unoccupied Electronic Structure of Pu", in *Recent Advances in Actinide Science*, Royal Society of Chemistry, R. Alvarez, N.D. Bryan, I. May (Eds.), 773 (2006).

[6]   Baer, Y., J.K. Lang, *Phys. Rev B,* 21, 2060 (1980).

[7]   Tobin, J.G., S.W. Yu, T. Komesu, B.W. Chung, S.A. Morton, G.D. Waddill, "Facilities for the Performance of Fano Measurements as a Probe of Electron Correlation", *Matl. Res. Soc. Symp. Proc.*, 986, 63 (2007), Document # 0986-OO01-08.

[8]   Butterfield, M.T., J.G. Tobin, N.E. Teslich, Jr., R.A. Bliss, M.A. Wall, A.K. McMahan, B.W. Chung, A.J. Schwartz, A.L. Kutepov, "Utilizing Nano-focussed Bremstrahlung Isochromat Spectroscopy (nBIS) to Determine the Unoccupied Electronic Structure of Pu", *Matl. Res. Soc. Symp. Proc.*, 893, 95 (2006).

[9]   Knapp, B.J., J.G. Tobin, "The Unoccupied Electronic Structure of Au and Ag on Ge(111)", *Phys. Rev. B*, 37, 8656 (1988), and references therein; J.G. Tobin, "Photoemission and Inverse Photoemission", in *Determination of Optical Properties*, Vol. VIII in *Physical Methods of Chemistry*, 2nd edition, B.W. Rossiter, R.C. Bretzold (Eds.), John Wiley and Sons, New York (1993), and references therein.

[10]   Tobin, J.G., S.W. Yu, T. Komesu, B.W. Chung, S.A. Morton, G.D. Waddill, *EuroPhysics Letters*, 77, 17004 (2007); S.W. Yu, T. Komesu, B.W. Chung, G.D. Waddill, S.A. Morton, J.G. Tobin, *Phys. Rev. B*, 73, 075116 (2006).

[11]   *X-ray Data Booklet*, LBNL/PUB-490 Rev. 2, Lawrence Berkeley National Laboratory, University of California, Berkeley, CA, January 2001, A. Thompson, *et al*.

Resonant inelastic X-ray scattering spectra of actinides

S.M. Butorin
Department of Physics and Materials Science
Uppsala University, Sweden

Abstract

RIXS measurements at the actinide 5d threshold provide an opportunity to study in detail elementary excitations in actinide compounds due to higher resolution of such experiments in comparison with those at the actinide 3d and 4d thresholds. It has turned out that the technique is very sensitive to the valency and the chemical state of actinides in contrast to X-ray absorption spectroscopy, which has a drawback of substantial smearing of spectral structures due to large core-hole lifetime broadening. In this situation, the virtually unlimited resolution (defined by the response function of the instrument) of the RIXS technique and its ability to enhance transitions to low-lying excited states are especially useful. RIXS spectroscopy provides good signatures in terms of new distinct transitions, representing electronic excitations within the 5f shell and having a characteristic profile. This helps to distinguish between actinide species with different oxidation states, especially in case when one of species has much lower concentration than another. Experimental data for systems of light actinides are presented and discussed along with the results of model calculations.

Introduction

To successfully describe various physical properties of a system in question it is necessary to obtain knowledge about the ground state and low-energy excited states of this system. For actinide compounds with a partly filled f shell, strong correlation effects (when the dispersional part of f bandwidth is smaller than the on-site Coulomb interaction between localised electrons) break down a single-particle picture and an atomic-like approach to characterise the electronic structure of these compounds is more appropriate.

In this case a state of the system without a core hole is described in terms of intra-atomic neutral excitations (a multiplet structure of the ground state electronic configuration due to electrostatic, exchange, crystal field, spin-orbit interactions, etc.) and/or inter-atomic charge-transfer excitations. The latter are the result of electron hopping from delocalised states to a localised state and are treated by short-range models, such as an Anderson impurity model [1], using a set of parameters. The values of model parameters are optimised by fitting both high-energy spectroscopic and low-energy transport data and then employed to describe the character of the ground state, different ground-state properties, the nature and size of the band gap in insulators [2], etc.

Since the interpretation of transport measurements in these regards is often hampered by the presence of defects and by the importance of electron-lattice interactions, high-energy spectroscopies which directly probe the electronic degrees of freedom are often used for preliminary estimations of model parameters. In this situation, X-ray scattering techniques become very attractive because the scattering process is charge-neutral.

By now, it has been proven that at some core-thresholds of electron-correlated systems X-ray emission spectroscopy with monochromatic photon excitation can be considered as an analogue of such techniques so that the excitation-radiative de-excitation channel can be treated as a resonant inelastic X-ray scattering (RIXS) process [3-7]. Final states probed via such a channel represent eigenvalues of the ground state Hamiltonian. The core-hole lifetime is not a limit on the resolution in this spectroscopy.

Experimental

The experiments were performed at undulator beamline 7.0 of the Advanced Light Source (ALS), LBNL, employing a spherical grating monochromator [8]. Resonant ultra-soft X-ray scattering spectra from the samples were recorded using a grazing-incidence grating spectrometer [9] with a two-dimensional detector. The incidence angle of the photon beam was approximately 15° from the sample surface and the spectrometer was placed in the horizontal plane at an angle of 90° with respect to the incidence beam. The bandwidth of the excitation was about 65 meV. The total energy resolution of the RIXS data was estimated from the full width at half maximum of the elastic peak to be 160 meV.

Results and discussion

The case of uranium is quite illustrative for what the RIXS technique can do. RIXS measurements at the U 5d threshold provide an opportunity to study in detail elementary excitations in U compounds due to the higher resolution of such experiments in comparison with those at the U 3d and 4d thresholds. It has turned out that the technique is very sensitive to the valency and the chemical state of uranium in contrast to X-ray absorption spectroscopy (XAS). Figure 1 shows X-ray absorption spectra of a number of U compounds recorded across the U 5d edge in the total electron yield mode. The 5d core-hole lifetime broadening is quite large, thus reducing the utility of XAS. As a result, the U 5d absorption spectra in Figure 1 do not exhibit sharp features. The substantial smearing of spectral structures hampers the analysis of the chemical state and the chemical environment of uranium in various compounds. In particular, it is difficult to distinguish between uranium species with different oxidation states, especially in case when one of the species has a much lower concentration than the other.

In this situation, the virtually unlimited resolution (defined by the response function of the instrument) of the RIXS technique and its ability to enhance transitions to specific excited states are especially useful. The RIXS profile strongly depends on the choice of the excitation energy. The spectral

Figure 1: Total electron yield spectra of UF$_4$, UO$_2$, U$_3$O$_8$ and UO$_3$ near the U 5d absorption edges
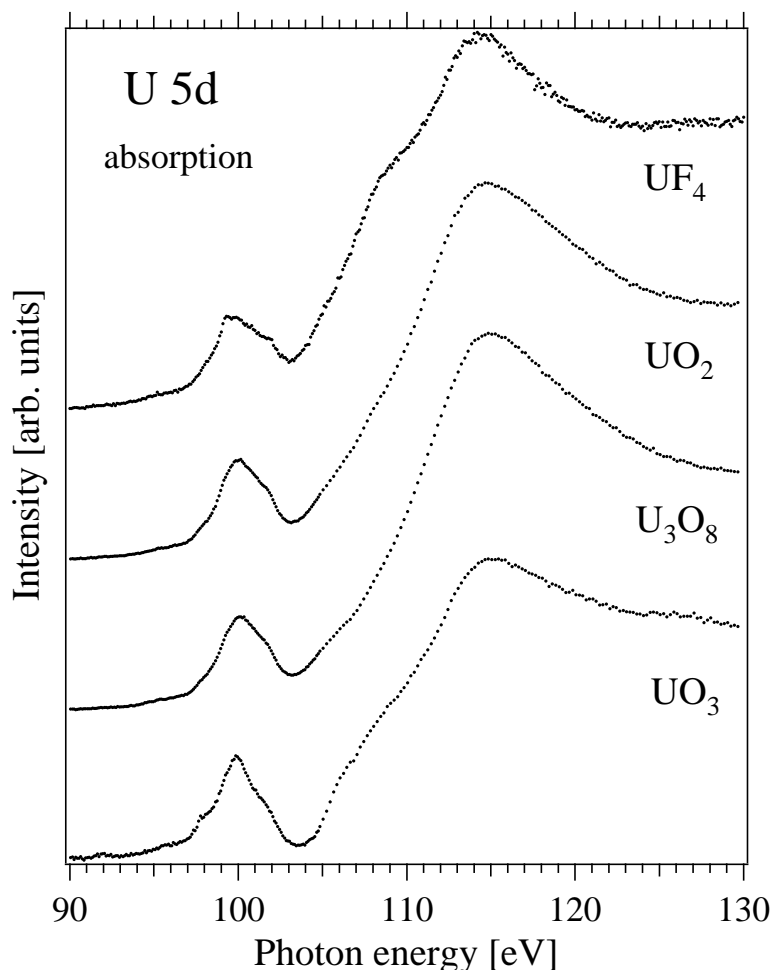
weight corresponding to electronic transitions within the 5f shell is enhanced at excitation energies close to 100 eV while at higher energies of the incident photon beam, set to the main 5d absorption edge, inter-ionic excitations of charge-transfer character, such as ligand 2p→U 5f charge-transfer, dominate the RIXS spectra. This has been established by measurements on a set of model U compounds and by model calculations. The spectral pattern of intra-ionic f-f excitations is mainly determined by the formal valency of U, in turn, the charge-transfer transitions strongly depend on the chemical environment of U ions.

An example of probing the f-f excitations in U systems is illustrated in Figure 2 where the RIXS spectra of single-crystal UO$_2$, recorded for various incident photon energies in the pre-5d-threshold region, are displayed. The assignment of sharp inelastic scattering structures to the f-f transitions is supported by atomic multiplet calculations for the U^{4+} ion. The spectra were calculated using the Kramers-Heisenberg equation, where the varying lifetime of core-excited states due to the autoionisation via the 5d-5f5f super Coster-Kronig decay was taken into account. The autoionisation into the continuum of g symmetry only was considered since it is the most dominant path. Matrix elements were obtained from Cowan's programs [10] so that Slater integrals were scaled down to 75%, 75%, 66% and 80%, respectively, from the Hartree-Fock values. The reduction factors for Slater integrals represent the effect of the intra-atomic configuration interaction; the same factors were used in a number of publications to successfully reproduce 4d XAS and 4d photoemission spectra of various rare-earth systems. The density of states of the continuum was assumed to be constant and the kinetic energy of the continuum electron was set to the value which made the average energies of 5d^9f^3 and 5d^{10}5f $^1\varepsilon_g$ equal.

Figure 2: Resonant X-ray scattering spectra of single-crystal UO$_2$ recorded at different excitation energies close to the U 5d threshold (lines with markers) together with the results of atomic multiplet calculations (sticks with thin lines) for the U(IV) ion. Excitation energies are indicated by arrows on the total electron yield spectrum at the U 5d absorption edge shown in the top panel.
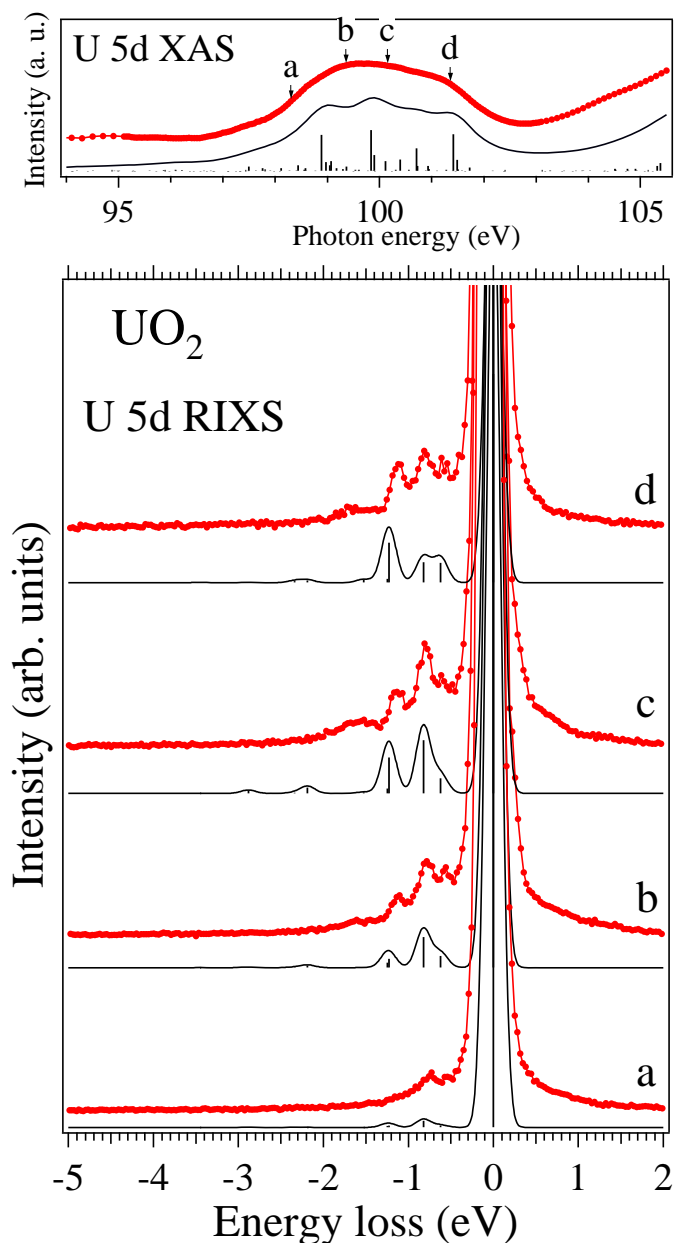
The calculations reproduce all of the spectral structures very well especially an enhancement of the peak at about 1.2 eV with increasing excitation energies. The growth of the peak is due to enhanced transitions into the $^1G_4$ state. Changes in absolute intensities of inelastic scattering structures corresponding to the f-f transitions are reproduced on going from spectrum a to spectrum b. For spectra c and d, such changes in calculated intensities are about three times higher as compared to those in the experiment. The discrepancy may originate from the normalisation procedure for the experimental spectra to account for variations in the incident photon flux. The intensity of the elastic peak was used as a reference in this procedure. However, the elastic peak contains some contribution of diffuse scattering which may vary with varying excitation energies.

RIXS profiles, corresponding to the *f-f* excitations, are found to be very sensitive to the chemical state of U in different systems [5]. For example, it is a matter of the presence or absence of these excitations when going from U^{4+} to U^{6+} compounds. Therefore, RIXS measurements near the U 5*d* threshold provide good fingerprints for the chemical state of U in different systems in contrast to X-ray absorption spectra which show only small differences at the U 5*d* edge.

An example to show is our findings about the chemical state of U in U_3O_8 and reduced UO_3. In particular, for U_3O_8, it was discussed in the literature that the chemical state of U is described as either $U^{VI}U^V_2O_8$ or $U^{VI}_2U^{IV}O_8$. To our knowledge, there is no clear and convincing answer to this question and it is still under debate. Thus, core-level photoemission [11-13] and electron spin resonance [14,15] data have been interpreted in favor of either situation by different groups and therefore these techniques cannot really provide an unambiguous answer. It turns out that the RIXS technique can. RIXS spectra of *f-f* excitations are a good indicator of whether uranium is in the U(IV), U(V) or U(VI) state. The data are easy to interpret and not very difficult to calculate. Establishing the real chemical state of U in oxides is important for both applied, environmental and fundamental science (*e.g.* a development of theory of non-stoichiometry is a fundamental problem).

Figure 3 displays RIXS spectra of *f-f* transitions for a number of U oxides. Close similarity of the *f-f* transitions profile in U_3O_8 to those in UO_2 as well as to that calculated for the U(IV) ion (see Figure 2) unambiguously indicates the presence of the U(IV) fraction in U_3O_8, thus favouring the $U^{VI}_2U^{IV}O_8$ description of the uranium chemical state in this oxide. Furthermore, a similar pattern is observed for reduced UO_3, thus indicating that oxygen deficiency leads to the creation of U(IV) species in the compound.

Figure 3: Resonant inelastic X-ray scattering spectra of
U oxides recorded at the incident photon energy of 99.9 eV
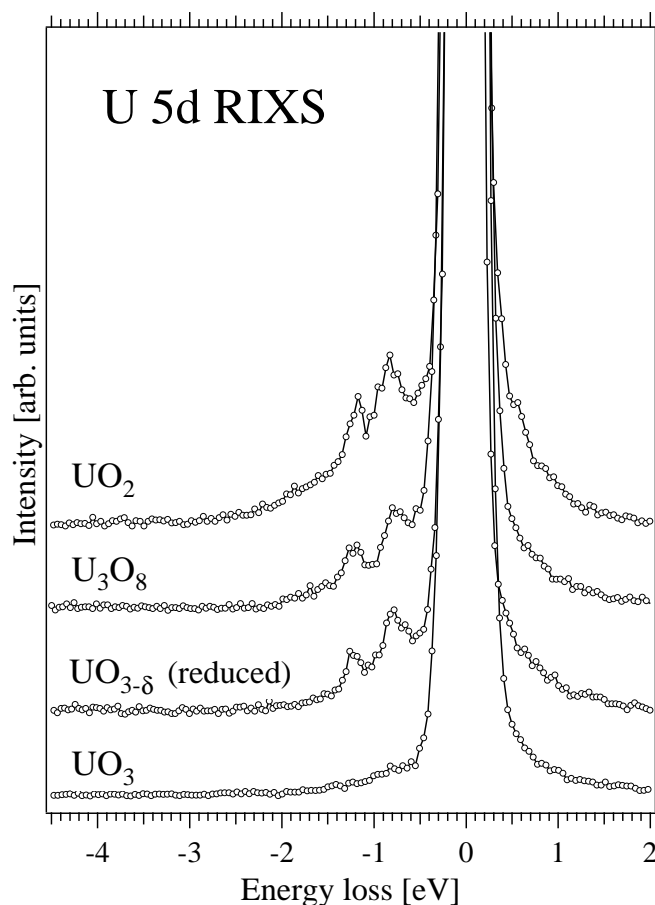
Charge-transfer effects are expected to be significant in actinide compounds as a result of metal 5f-ligand 2p hybridisation. The analysis of data obtained at U 3$d_{5/2}$ threshold shows that the ligand 2p→U 5f charge-transfer plays an important role in uranium compounds, such as UO_2, $UO_3(NO_3)_2 \cdot 6H_2O$, and even in UF_4.

This is also supported by theoretical studies. Molecular-orbital calculations by several research groups [16-19] gave values for the 5f occupancy, which range from 2.3 to 2.9 electrons, while this occupancy was estimated at about 2.3 electrons from the analysis of X-ray absorption and photoemission data within an Anderson impurity model [20,21]. These results indicate a significant degree of covalency for U–O chemical bonds in UO_2. For UF_4, a 5f contribution of ~0.3 electrons to the bonding orbitals was also predicted from relativistic Dirac-Slater local-density calculations [22]. For compounds containing U^{6+}, the degree of covalency for metal-ligand bonds is expected to be even higher than that for U^{4+} systems. For example, molecular-orbital calculations yielded the 5f occupancy of ~2.6 electrons for the uranyl ion UO_2^{2+} (Refs. [23,24]). Although, the values for the 5f occupancy obtained from molecular-orbital calculations seem to be overestimated [25] one cannot rule out the importance of the U 5f-ligand 2p hybridisation even in a compound with "ionic" bonds such as UF_4.

The consequence of high covalency and hybridisation in the ground state is an appearance of charge-transfer satellites in high-energy spectroscopic data. Figure 4 illustrates the dependence of the RIXS spectra on the chemical environment of U atoms in various compounds. The spectra were measured under condition when the inelastic RIXS cross-section is enhanced for the ligand 2p→U 5f charge-transfer transitions, in particular, when the energy of the incident photon beam is tuned to the main edge of the U 5d X-ray absorption spectrum (see Figure 1). At these energies, the charge-transfer excitations dominate RIXS spectra, thus defining the RIXS profile. The profiles can be clearly divided into three groups: *i)* UF_4; *ii)* UO_3 and $UO_{3-\delta}$; *iii)* U_3O_8 and UO_2. The differences between profiles are determined by the character of the bonding and the local geometrical arrangement of ligands, *i.e.* local crystal structure.

**Figure 4: Resonant inelastic X-ray scattering spectra of a number of
U compounds recorded at the incident photon energy of 115.0 eV**
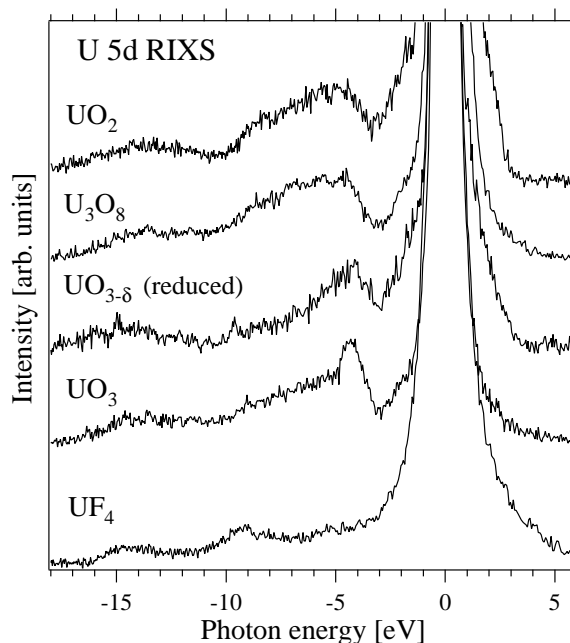
Such RIXS probing of eigenvalues of model Hamiltonian for the ground state helps to more accurately estimate the physical quantities used in short-range interaction theories, such as the Anderson impurity model and to built-up more accurate description of various ground state properties of systems in question.

References

[1] Anderson, P.W., *Phys. Rev. B*, 124, 41 (1961).

[2] Zaanen, J., G. A. Sawatzky, J. W. Allen, *Phys. Rev. Lett.*, 55, 418 (1985).

[3] Butorin, S.M., D.C. Mancini, J-H. Guo, N. Wassdahl, J. Nordgren, M. Nakazawa, S. Tanaka, T. Uozumi, A. Kotani, Y.Ma, K.E. Myano, B.A. Karlin, D.K. Shuh, *Phys. Rev. Lett.*, 77, 574 (1996).

[4] Zatsepin, D.A., S.M. Butorin, D-C. Mancini, Y.Ma, K.E. Miyano, D.K. Shuh, J. Nordgren, *J. Phys.: Condens. Matter.,* 14, 2541 (2002).

[5] Butorin, S.M., D.K. Shuh, K. Kvashnina, I.L. Soroka, K. Ollila, K.E. Roberts, J-H. Guo, L. Werme, J. Nordgren, *Mat. Res. Soc. Symp. Proc.*, Vol. 807, 113 (2004).

[6] Shuh, D.K., S.M. Butorin, J-H. Guo, J. Nordgren, *Mat. Res. Soc. Symp. Proc.*, Vol. 802, 131 (2004).

[7] Kvashnina, K.O., S.M. Butorin, D.K. Shuh, K. Ollila, I.L. Soroka, J-H. Guo, L. Werme, J. Nordgren, NEA, No. 6288, p. 115 (2007).

[8] Warwick, T., P. Heimann, D. Mossessian, W. McKinney, H. Padmore, *Rev. Sci. Instrum.*, 66, 2037 (1995).

[9] Nordgren, J., G. Bray, S. Cramm, R. Nyholm, J-E. Rubensson, N. Wassdahl, *Rev. Sci. Instrum.*, 60, 1690 (1989).

[10] Cowan, R.D., *The Theory of Atomic Structure and Spectra*, University of California Press, Berkeley (1981).

[11] Pireaux, J.J., J. Riga, E. Thibaut, C. Tenret-Noël, R. Caudino, J.J. Verbist, *Chem. Phys.*, 22, 113 (1977).

[12] Teterin, Yu.A., V.M. Kulakov, A.S. Baev, N.B. Nevzorov, I.V. Melnikov, V.A. Streltsov, L.G. Mashirov, D.N. Suglobov, A.G. Zelenkov, *Phys. Chem. Minerals*, 7, 151 (1981).

[13] Madhavaram, H., P. Buchanan, H. Idriss, *J. Vac. Sci. Technol.*, A 15, 1685 (1997).

[14] Verbist, J.J., J. Riga, C. Tenret-Noël, J.J. Pireaux, G. Dúrsel, R. Caudino, E.G. Derouane, in *Plutonium and Other Actinides*, H. Blank, R. Lindner (Eds.), North-Holland, Amsterdam (1976), p. 409.

[15] Allen, G.C., A.J. Griffiths, C.W. Suckling, *Chem. Phys. Lett.*, 53, 309 (1978).

[16] Gubanov, V.A., A. Rosén, D.E. Ellis, *Solid State Commun.*, 22, 219 (1977).

[17] Heera, V., G. Seifert, P. Ziesche, *Phys. Stat. Sol. (b)*, 118, K107 (1983).

[18] Ellis, D.E., G.L. Goodman, *Int. J. Quant. Chem.*, 25, 185 (1984).

[19] Goodman, G.L., *J. Alloys & Compounds*, 181, 33 (1992).

[20] Gunnarsson, O., D.D. Sarma, F.U. Hillebrecht, K. Schönhammer, *J. Appl. Phys.*, 63, 3676 (1988); Gunnarsson, O., T.C. Li, *Phys. Rev. B*, 36, 9488 (1987).

[21] Kotani, A., H. Ogasawara, *Physica C*, 186-188, 16 (1993).

[22] Pierloot, K., A. Reinders, G.L. Goodman, D. Devoghel, C. Görller-Walrand, L.G. Vanquickenborne, *J. Chem. Phys.*, 94, 2928 (1991).

[23] Walsh, P.F., D.E. Ellis, *J. Chem. Phys.*, 65, 2387 (1976).

[24] Wood, J.H., M. Boring, S.B. Woodruff, *J. Chem. Phys.*, 74, 5225 (1981), and references therein.

[25] Cox, L.E., *J. Electr. Spectrosc.*, 26, 167 (1982).

Fermiology of f-electron systems based on soft X-ray photoemission spectra and band calculations

Hiroshi Yamagami,[1,2] **Yuji Saitoh,**[2] **Tetsuo Okane,**[2]
Shin-Ichi Fujimori,[2] **Takuo Ohkochi,**[2] **Akira Yasui**[3], **Atsushi Fujimori**[3]
[1]Department of Physics, Faculty of Science, Kyoto Sangyo University, Kyoto, Japan
[2]Synchrotron Radiation Research Centre, Japan Atomic Energy Agency, Hyogo, Japan
[3]Department of Physics, University of Tokyo, Tokyo, Japan

Abstract

The f-electron systems, consisted of actinides and/or lanthanides atoms, show the various phenomena of condensed matters, such as heavy-fermion behaviour, quantum criticality and unconventional superconductivity, since the f electrons are in the intermediate states between the itinerant and localised nature through the hybridisation with the valence electrons of their adjacent atoms. In non-magnetic metals, the f electrons form energy bands by this hybridisation to contribute on the Fermi surface, thus characterising directly to such interesting physical quantities. The key for solving transport phenomena like super-conductivity from the electronic structure is to clarify formation of the Fermi surface in the normal state and superconducting state, and therefore investigation of the detailed shape of the Fermi surface in low temperatures has been performed by measurement of the de Haas-van Alphen effect.

Fermiology of f-electron systems using the angle-resolved photoemission spectroscopy (ARPES) with photons in the soft X-ray (SX) region of synchrotron radiation has been carried out recently [1-3]. The advantages of the SX-ARPES are: i) that it is suitable for probing the f bands, since the relative intensity of the photoionisation cross-section of the f orbital over incident photon energy is stronger than that of the other orbitals; ii) that the bulk band structure is more observable in the SX region than in the lower photon energies, since the photoelectron escape depth is several nanometers [4]; iii) that it is able directly to observe not only the low-temperature Fermi surface but the temperature-dependent band structure. In rare-earth compounds, furthermore; iv) the 4f bands are experimentally separable with the others, if the 3d-4f resonant ARPES is tuned in the photon energy. The new features of f-electron band structure in the occupied states are found out using some of these advantages, comparing with the band structure and Fermi surface calculated by a relativistic band theory.

This talk reports some recent results concerning the electronic structure and the Fermi surface for uranium compounds of antiferromagnetic superconductor UPd_2Al_3 [1], paramagnet UB_2 [5] and so on, obtained in our electronic-structure research group of Japan Atomic Energy Agency (JAEA). Besides, we detected the 4f-rich Fermi surfaces of typical heavy-fermion compound $CeRu_2Si_2$ and superconductor without inversion symmetry $CeIrSi_3$ by resonant ARPES, and also the obtained results are illustrated together with the 4f band structure. Our ARPES measurement was performed in RI laboratory by JAEA beam line BL23SU of Spring8, and all the theoretical analysis were done by the relativistic linear augmented-plane-wave (RLAPW) method [6] in a local density approximation.

In this year, the Apple-II undulator of BL23SU was replaced with the in-vacuum twin-helical undulator. Since the photoelectron scattering intensity of the new undulator is estimated as being two times and more of the previous one, we expect that the ARPES measurement will be improved in time and resolution. The outline of the future research in our group will be shown.

References

[1]   Fujimori, S-I., Y. Saito, T. Okane, A. Fujimori, H. Yamagami, Y. Haga, E. Yamamoto, Y. Onuki, *Nature Physics 3*, 618-622 (2007).

[2]   Yano, M., A. Sekiyama, H. Fujiwara, T. Saita, S. Imada, T. Muro, Y. Onuki, S. Suga, *Phys. Rev. Lett.,* 98, 036405 (2007).

[3]   Im, H.J., T. Ito, H-D Kim, S. Kimura, K.E. Lee, J.B. Hong, Y.S. Kwon, A. Yasui, H. Yamagami, *Phys. Rev. Lett.,* 100, 176402 (2008).

[4]   Sekiyama, A., T. Iwasaki, K. Matsuda, Y. Saitoh, Y. Onuki, S. Suga, *Nature*, 403, 396 (2000).

[5]   Ohkochi, T., S-I. Fujimori, H. Yamagami, T. Okane, Y. Saitoh, A. Fujimori, Y. Haga, E. Yamamoto, Y. Onuki, to be submitted to *Phys. Rev.* B (2008).

[6]   Yamagami, H., *J. Phys. Soc. Jpn.,* 67, 3176 (1998).

Probing radiation damage in plutonium alloys, especially the PuCoGa$_5$ superconductor

Corwin H. Booth
Chemical Sciences Division, Lawrence Berkeley National Laboratory
Berkeley, California, USA

Abstract

Radiation damage of materials affects many aspects of science and industry, for example, in semiconductors, nuclear power generation and its associated waste disposal, as well as the ageing nuclear stockpile. Consequently, radiation damage has been studied for over a century, and intensely since World War II. Although experimental measures have provided ample verification of long-range (>10 nm) structural effects due to radiation damage, atomic-resolution descriptions of such damage have relied almost exclusively on theoretical calculations. Experimental studies have not generally kept pace with theoretical treatments of fully relaxed damage cascade structures at the atomic level. Therefore, damage cascade calculations have not been quantitatively compared to any atomic-resolution experiments until very recently [1,2], and never to our knowledge in intermetallics [3] or technologically important materials such as δ-Pu. Measurements of such structural changes are vital to verify and improve these theories, and for comparison to more complex theories of dislocation loops, He bubble formation, and volume expansion. For example, recent [1] nuclear magnetic resonance experiments revealed that radiation damage accumulates about five times faster in zircons and other ceramics than calculations indicate, calling into question both the theoretical calculations and the viability of nuclear waste containment schemes.

The 18.5 K superconductor PuCoGa$_5$ offers new avenues for understanding radiation damage, as it has many unusual properties due to damage induced by self-irradiation. For instance, the superconducting transition temperature decreases sharply with time, suggesting a radiation-induced Frenkel defect concentration much larger than predicted by current radiation damage theories. Extended X-ray absorption fine-structure measurements [2] demonstrate that while the local crystal structure in fresh material is well ordered, aged material is disordered much more strongly than expected from simple defects, consistent with strong disorder throughout the damage cascade region. These data highlight the potential impact of local lattice distortions relative to defects on the properties of irradiated materials and underscore the need for more atomic-resolution structural comparisons between radiation damage experiments and theory.

In this talk, I will review the relevant aspects of radiation damage theory as it applies to PuCoGa$_5$, extend the results to preliminary data on PuGa$_3$ and PuAl$_2$, as well as discuss the implications, especially with regard to other types of materials.

References

[1]   Farnan, I., H. Cho, W.J. Weber, *Nature*, 445, 190 (2007); Farnan, I., E.K.H. Salje, *J. Appl. Phys.,* 89, 2084 (2001).

[2]   Booth, C.H., M. Daniel, R.E. Wilson, E.D. Bauer, J.N. Mitchell, N.O. Moreno, L.A. Morales, J.L. Sarrao, P.G. Allen, *Phys. Rev. B*, 76, 064530 (2007); Booth, C.H., M. Daniel, R.E. Wilson, E.D. Bauer, J.N. Mitchell, N.O. Moreno, L.A. Morales, J.L. Sarrao, P.G. Allen, in *Proceedings of Pu Futures: The Science,* Monterey, California, 9-13 July 2006, M.J. Fluss, D.E. Hobart, P.G. Allen, G.D. Jarvinen (Eds.), *J. Alloys and Compd*., 444, 119 (2007).

[3]   Averback, R.S., R. Benedek, K.L. Merkle, *Phys. Rev. B*, 18, 4156 (1978); these authors model electrical resistivity with a defect model.

Nuclear fuels studies using synchrotron radiation

P.M. Martin,[1] **S. Grandjean,**[2] **P. Garcia,**[1] **R.C. Belin,**[3] **G. Carlot,**[1] **C. Sabathier,**[1]
H. Palancher,[1] **C. Valot,**[1] **P.J. Valenza,**[3] **M. Ripert,**[1] **B. Arab-Chapelet,**[2]
A.C. Robisson,[2] **A.C. Scheinost,**[4] **C. Hennig,**[4] **O. Proux,**[5] **J-L. Hazemann**[6]
[1]CEA, DEN, DEC, SESC, LLCC, Cadarache, St. Paul-lez-Durance, France
[2]CEA, DEN, DRCP, SCPS, LCA, Bagnols-sur-Cèze, France
[3]CEA, DEN, DEC, SPUA, LMPC, Cadarache St. Paul-lez-Durance, France
[4]Forschungszentrum Dresden-Rossendorf (FZD), Institute of Radiochemistry, Dresden, Germany
[5]Laboratoire de Géophysique Interne et Tectonophysique, UMR CNRS/Université Joseph Fourier,
Saint-Martin-D'Hères, France
[6]Institut Néel, CNRS, Grenoble, France

Abstract

The goal of this talk is to illustrate through three examples of studies, that XAS is a powerful tool for enhancing understanding of processes encountered in nuclear fuels.

The first application is connected to the manufacturing of nuclear fuels dedicated to Gen-IV reactor systems. Current concepts for future nuclear systems aim at improving the fuel cycle along the following criteria: economy of resources, minimisation of the volume of waste, decrease in the long-term radiotoxicity of ultimate wastes and proliferation risk reduction. Co-management of two (or more) actinides has been then put forward recently with a new procedure for $(U,Pu)O_2$ manufacturing based on the oxalic co-precipitation of U(IV) and Pu(III) followed by the thermal conversion of the co-precipitate into oxide. Control of the $(U,Pu)O_2$ homogeneity at a microstructural scale and of its physicochemical properties could be of prime importance [1]. In order to fully investigate the ideality of a solid solution containing Pu between 50 and 7 at.%, XRD and XAS characterisations at uranium and plutonium edges have been undertaken. XRD measurements showed a face centred cubic structure for each composition and the cell parameters appeared to follow Vegard's law. But XAFS results revealed that for Pu contents below 30 at.%, a disordered hyperstoichiometric structure $(U_{1-y}Pu_y)O_{2+x}$ is observed with a non-random distribution of plutonium atoms within the uranium sites of the $(U_{1-y}Pu_y)O_{2+x}$ structure [2]. After several optimisation stages in the calcination process, new XAS characterisation clearly demonstrated the formation of an ideal $(U,Pu)O_2$ solid solution using this oxalic co-conversion method via the co-precipitation of a U(IV)-Pu(III) mixed oxalate [3].

The second application deals with modelling of fission gas behaviour in UO_2 during in-pile operations. An essential ingredient in fission gas behaviour models lies in their capacity to predict the proportion of rare gas atoms which are isolated in the matrix and that of atoms which form bubbles. XAS experiments performed at the xenon K-edge on a set of uranium dioxide samples implanted with 10^{17} xenon.cm^{-2} at 800 keV clearly demonstrated that the gas forms highly pressurised nanometre size bubbles (2.8±0.3 GPa) [5] and those aggregates are stable up to 1 073 K. Above this temperature, bubbles will trap migrating vacancies and their inner pressure is seen to decrease substantially. Absorption measurements on ion-implanted samples therefore confirm the scarce experimental data available pertaining to irradiated fuels [4].

The last application deals with the management of long-lived nuclear wastes through the study of the structural transition due to self-alpha irradiation observed in zirconate pyrochlore $^{241}Am_2Zr_2O_7$. In an effort to understand the underlying phenomena of the pyrochlore to fluorite transition, powder X-ray diffraction (PXRD) and X-ray absorption fine-structure (XAFS) spectroscopy experiments were conducted

on two samples aged for 40 days and one year, respectively. The XAFS data confirm the phase transition observed using XRD, but reveal different local environments for americium and zirconium atoms. The XAFS results reveal that the ZrO polyhedron is stable during the self-irradiation process; this stability is probably one of the main factors in explaining the excellent resistance to amorphisation of americium zirconia fluorite structures. Based on the experimental data, the possible mechanisms underpinning the observed phase transitions are discussed.

References

[1]   Grandjean, S., B. Chapelet-Arab, S. Lemonnier, A-C. Robisson, N. Vigier, *MRS. Symp. Proc.*, Vol. 893, Materials Research Society (2006).

[2]   Martin, P., S. Grandjean, C. Valot, G. Carlot, M. Ripert, P. Blanc, C. Hennig, *J. Alloys Comp.*, 444-445, 410-414 (2007).

[3]   Grandjean, S., B. Arab-Chapelet, A.C. Robisson, F. Abraham, Ph. Martin, J-Ph. Dancausse, N. Herlet, C. Léorier, *Plutonium Futures 2008 Conference*, Dijon, France, 7-11 July 2008 (submitted to *Journal of Nuclear Materials*).

[4]   Nogita, K., K. Une, *Nucl. Instrum. and Meth. B*, 141, 481-486 (1998).

[5]   Martin, P., P. Garcia, G. Carlot, C. Sabathier, C. Valot, V. Nassif, O. Proux, J-L. Hazemann, *Nucl. Instrum. and Meth. B*, 266, 2887-2891 (2008).

Lattice vibrations in α-uranium:
Non-linearity, localisation and impurity stiffening

Michael E. Manley

Abstract

Lattice vibrations in crystals are generally described as plane waves with vibrational frequencies determined by fixed interatomic potentials. Recent experiments on α-uranium, however, are showing that these notions do not always apply. First, a large softening of phonon density of states (DOS) has been attributed to thermal changes in the electronic structure, defying the notion of a fixed interatomic potential [1]. Second, evidence shows that significant quantities of intrinsically localised modes (ILM) form at high temperatures, defying the plane-wave notion [2]. Another common belief is that trace amounts of impurities do not affect the phonon DOS. By contrast, as little as 0.4 at.% carbon dissolved in uranium causes a significant stiffening of the phonon DOS [3]. In this talk I will summarise these surprising results as well as some of their implications for thermodynamic, transport and mechanical properties. I will also discuss a possible role for the ILM in a solid-state phase transformation in uranium metal [4].

References

[1]   Manley, M.E., B. Fultz, R.J. McQueeney, C.M. Brown, W.L. Hults, J.L. Smith, D. Thoma, R. Olsborn, J.L. Robertson, *Phys. Rev. Lett.,* 86, 4076 (2001).

[2]   Manley, M.E., M. Yethiraj, H. Sinn, H. Volz, A. Alatas, J.C. Lashley, W.L. Hults, G.H. Lander, J.L. Smith, *Phys. Rev. Lett.,* 96, 125501 (2006).

[3]   Manley, M.E., W.L. Hults, J.C. Cooley, R.E. Hackenberg, D.J. Thoma, M.W. Koby, J.L. Smith, K. Littrell, *Phys. Rev. B,* 72, 184302 (2005).

[4]   Manley, M.E., J. Lynn, Y. Chen, G.H. Lander, *Phys. Rev. B,* 77, 052301 (2008).

Session IV

Modelling and simulation tools

Chair: Christophe Den Auwer

Nature of the electronic and magnetic ground state of actinide metals

Gerrit van der Laan
Diamond Light Source
Didcot, Oxfordshire, UK

Kevin Moore
Lawrence Livermore National Laboratory
Livermore, California, USA

Abstract

Using electron energy-loss spectroscopy (EELS) in a transmission electron microscope (TEM) we studied the electronic structure of the actinide metals, Th, U, Np, Pu, Am, and Cm, and compared the results to many-electron spectral calculations. Sum rule analysis of the branching ratio at the $N_{4,5}$ edge yields the angular part of the spin-orbit interaction per hole. The results show that the light metals (Th and U) follow LS coupling, but heavier metals (Pu, Am, and Cm) follow intermediate coupling of the 5f states. The intermediate coupling is near the jj limit for Pu and Am, but strongly shifted towards the LS coupling limit for Cm.

Introduction

At the Actinide-XAS 2008 workshop, where the technique of X-ray absorption spectroscopy is featuring so highly, it is worthwhile to address the question of why a transmission electron microscope (TEM) is used for acquisition of electron energy-loss spectroscopy (EELS) spectra of actinides. This has several answers. First, the TEM utilises small samples, allowing one to avoid the handling of appreciable amounts of toxic and radioactive materials. The alternative XAS performed at a multi-user synchrotron radiation facility is usually less well-adapted for the delicate and secure handling of radioactive materials. Second, the technique is bulk sensitive due to the fact that the electrons traverse ~40 nm of metal, this being the appropriate thickness for quality EELS spectra of actinide materials. A few nanometres of oxide do form on the surfaces of the TEM samples, but this is insignificant in comparison to the amount of metal sampled through transmission of the electron beam. Third, actinide metals at or near the localised-itinerant transition exhibit numerous crystal structures that can coexist in metastable equilibrium due to close energy level between phases. Therefore, acquiring single-phase samples of metals at or near this transition, such as Mn (four phases), Ce (four phases) and Pu (six phases), is uncertain, making spectroscopic techniques with low spatial resolution questionable. Finally, actinide metals readily react with hydrogen and oxygen, producing many unwanted phases in the material during storage or preparation for experiments. The TEM has the spatial resolution to image and identify secondary phases [1,2,3], ensuring examination of only the phase(s) of interest. A field-emission-gun TEM, such as the one used in these experiments, can produce an electron probe of ~5 Å, meaning recording spectra from a single phase when performing experiments is easily achieved. Quantitatively measuring the reflections in the electron diffraction pattern, as well as other crystallographic orientations, proves that the correct phase is examined [4,5].

Actinide physics and chemistry are of great interest due to the unique behaviour of the $5f$ states that dominate the electronic and magnetic structure [6,7]. For accurate modelling of the behaviour of these materials, a better understanding of the basic aspects of actinide metals, alloys, and materials is required through experiment and theory. We discuss here the fundamental issue of the filling of the $j = 5/2$ and $7/2$ levels in the $5f$ state, $i.e.$ the type of angular-momentum coupling, across the series [8,9]. To this end, the electronic and magnetic structure of actinide metals, Th, U, Np, Pu, Am, and Cm, is investigated using EELS in a TEM [10] and compared with many-electron spectral calculations.

At the $N_{4,5}(4d \rightarrow 5f)$ edge the core level spin-orbit interaction is much larger than the core-valence interaction. The branching ratio of the $N_{4,5}$ edge in EELS or XAS can be related via a sum rule to the expectation value of the angular part of the $5f$ spin-orbit interaction per hole [11]. Analysis of the branching ratio in the actinide metals gives an interesting trend for the spin-orbit interaction as a function of the number of $5f$ electrons per atom: while light metals (Th, U) follow LS coupling, heavier metals (Pu, Am, Cm) obey intermediate coupling of the $5f$ states [12].This intermediate coupling is near the jj limit for Pu and Am, but is strongly shifted towards the LS coupling limit for Cm [13].

Calculations

The core-level spectra for EELS and XAS at the $N_{4,5}(4d \rightarrow 5f)$ and $O_{4,5}(5d \rightarrow 5f)$ edges are calculated using multiplet theory. The calculations for the transitions $f^n \rightarrow d^9f^{n+1}$ are performed in the same way as for the $M_{4,5}$ and $N_{4,5}$ absorption edges in the lanthanides [14,15], only with different radial parameters of the spin-orbit and Slater integrals. We discuss here only the $N_{4,5}$ edges, the results for the $O_{4,5}$ edges can be found elsewhere [16,17].

First, the initial and final state wave functions are calculated in intermediate coupling using the atomic Hartree-Fock method with relativistic correction [18,19]. The intermediate coupling treats spin-orbit, Coulomb, and exchange interactions on equal footing. After empirical scaling of the Slater integrals to typically 80% of the atomic value [14], the electric-dipole transition matrix elements are calculated from the initial state to the final state levels. The electric-dipole selection rules from the ground state strongly limit the number of accessible final states, so that compared to the total manifold of final states, the allowed transitions are located within a narrow energy region [14].

Spin-orbit interaction and sum rule analysis

The number of electrons, n_f, and the expectation value of the angular part of the spin-orbit interaction, $\langle w^{110} \rangle$, are related to the electron occupation numbers $n_{7/2}$ and $n_{5/2}$ of the angular-momentum levels $j = 7/2$ and $j = 5/2$ in the f shell as [20]:

$$n_f = n_{7/2} + n_{5/2} \tag{1}$$

$$\left\langle w^{110} \right\rangle \equiv \frac{2}{3} \left\langle \sum_{i=1}^{n} \mathbf{l}_i \cdot \mathbf{s}_i \right\rangle = n_{7/2} - \frac{4}{3} n_{5/2} \tag{2}$$

where $\mathbf{l}_i$ and $\mathbf{s}_i$ are the orbital and spin angular momentum operators of the i-th electron in the f shell.

The branching ratio for the $N_{4,5}$ edge of the core d to valence f transitions in EELS, or X-ray absorption spectroscopy (XAS) [11,20] is defined as:

$$B = \frac{I(N_5)}{I(N_5) + I(N_4)} \tag{3}$$

with $I(N_5)$ and $I(N_4)$ the integrated intensities of the $N_5(4d_{5/2} \rightarrow 5f_{5/2,7/2})$ and $N_4(4d_{3/2} \rightarrow 5f_{5/2})$ peaks.

The spin-orbit sum rule relates $\langle w^{110} \rangle$ and B as [8]:

$$\frac{\left\langle w^{110} \right\rangle}{14 - n_f} - \Delta = -\frac{5}{2}\left(B - \frac{3}{5}\right) \tag{4}$$

where the correction term Δ can be calculated using Cowan's relativistic Hartree-Fock code [8]. In the same way as the spin magnetic moment sum rule in X-ray magnetic circular dichroism (XMCD) [21], the sum rule in Eq. (4) is strictly only valid in the absence of core-valence electrostatic interactions, or so called jj mixing, in which case the correction term Δ becomes zero [8]. In the Periodic Table, the different transition-metal series show a different behaviour due to diverse valence-electron interaction. For $3d$ transition metals, the application of the spin-orbit sum rule for the $L_{2,3}$ branching ratio is severely hampered by the large $(2p,3d)$ exchange interaction that is of similar size as the $2p$ spin-orbit interaction [11,22,23]. The same is true for the $M_{4,5}$ edges of the lanthanides, where the $(3d,4f)$ exchange interaction is quite strong compared to the $3d$ core spin-orbit interaction [14]. On the other hand, for the $L_{2,3}$ edges of $4d$ and $5d$ transition metals, associated with the deep $2p$ core level, the sum rule is expected to hold quite well [6]. However, even in the worst case of the rare earth elements, the trend in the branching ratio can be used to obtain the relative population of spin-orbit split states, as was demonstrated for Ce systems [24]. The situation is favourable for the $M_{4,5}$ and $N_{4,5}$ edges of the actinides, given the small exchange interactions between the $3d$ and $4d$ core levels and the $5f$ valence states. This means that the EELS and XAS branching ratios depend almost solely on the $5f$ spin-orbit expectation value per hole, thus affording an unambiguous probe for the $5f$ spin-orbit interaction in actinide materials.

Since the expectation value of the spin-orbit interaction is for the angular part, it does not include the radial part, which is approximately constant for given atomic shell. Therefore, the spin-orbit sum-rule analysis is complementary to optical spectroscopy, where energy level separations are measured. Thus the sum rule analysis reveals the proper angular-momentum coupling scheme in the material.

The calculated electric-dipole transitions $4d^{10}5f^{n} \rightarrow 4d^{9}5f^{n+1}$ for $N_{4,5}$ EELS or XAS spectra using many-electron atomic theory in intermediate coupling for [92]U $5f^1$ to f^5 and [100]Fm $5f^7$ to f^{13} are shown in Figure 1 [20]. The line spectra are convoluted by 2 eV, which corresponds to the intrinsic lifetime broadening. The spectrum for f^6 (not shown) contains only a $4d_{5/2}$ peak but no $4d_{3/2}$ peak. In order to visualise the spin-orbit analysis of the EELS spectra in relation to our atomic calculations, both are shown on a plot of $\langle w^{110} \rangle /(14-n_f) - \Delta$ as a function of the number of f electrons in Figure 3(a). The curves for the three theoretical angular-momentum coupling schemes, LS, jj, and intermediate, as calculated using a many-electron atomic model, are plotted as a short-dashed, long-dashed, and solid line, respectively.

Figure 1: Calculated electric-dipole transitions for the $N_{4,5}(4d \rightarrow 5f)$ EELS or XAS spectra using many-electron atomic theory in intermediate coupling for ^{92}U $5f^1$ to f^5 and ^{100}Fm $5f^7$ to f^{13}

The convolution by 2 eV corresponds to the intrinsic lifetime broadening.
The spectrum for f^6 (not shown) has only a $4d_{5/2}$ peak but no $4d_{3/2}$ peak [20].
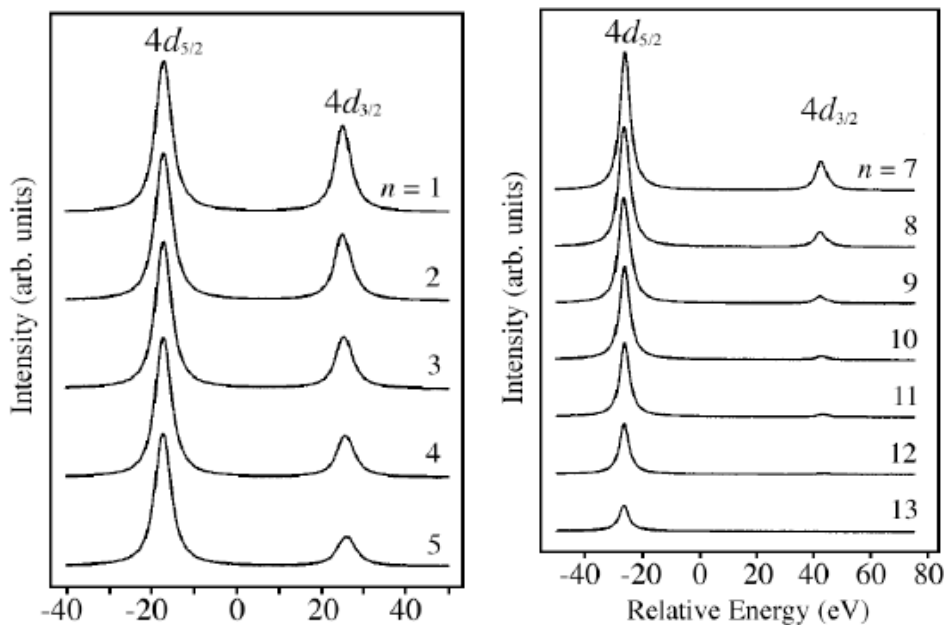
Figure 2: Experimental $N_{4,5}(4d \rightarrow 5f)$ EELS spectra for the α-phase of Th, U, Np, Pu, Am and Cm metal, normalised to the N_5 peak height

Notably the intensity of the N_4 ($4d_{3/2}$) peak gradually decreases in intensity relative to the N_5 ($4d_{5/2}$) peak going from Th to Am, then increases again for Cm.
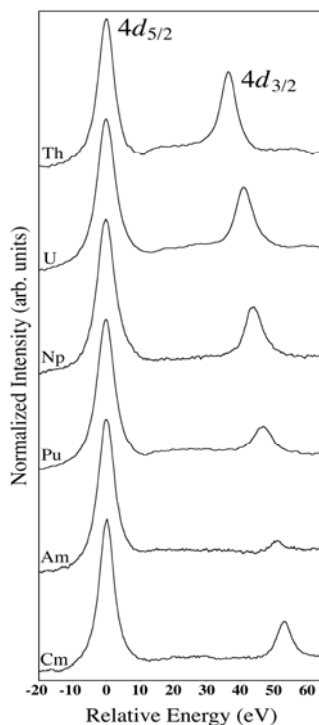
Experimental

EELS spectra were collected at Lawrence Livermore National Laboratory using a Phillips CM300 field-emission-gun TEM, equipped with a Gatan imaging filter [10]. The accelerating voltage of the TEM is 297 keV, which is much higher than the energy of the $N_{4,5}$ and $O_{4,5}$ transitions in the actinides. This allows us to consider these electron excitations as electric-dipole transitions. The $N_{4,5}$ EELS spectra of actinides are displayed in Figure 3. The EELS spectrum at the Pu $N_{4,5}$ edges agrees well with the XAS collected at the Advanced Light Source in total-electron-yield mode, using a 30 mg sample of purified α-Pu [8].

Figure 3(a): Ground-state spin-orbit interaction per hole as a function of the number of 5f electrons (n_f)

The three theoretical angular-momentum coupling schemes are shown: *LS*, *jj*, and intermediate by dotted, dashed and solid lines, respectively. The blue dots give the results of the spin-orbit sum-rule analysis using the experimental $N_{4,5}$ branching ratio of each metal in the figure.
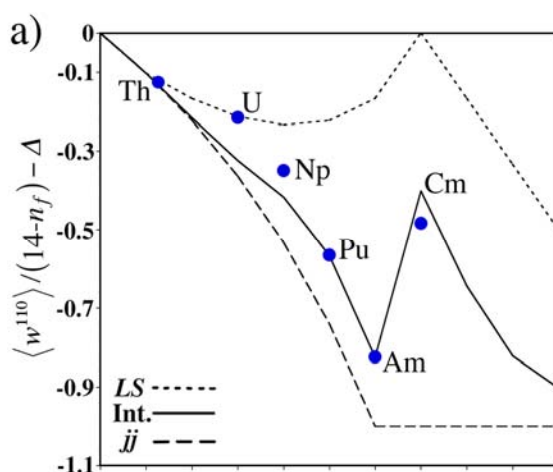
Figure 3(b): The spin-orbit interaction values are converted to the electron occupation numbers $n_{5/2}$ and $n_{7/2}$ of the $j = 5/2$ and 7/2 levels in the 5f state

Shown are the three theoretical coupling schemes (curves for *LS*, *jj*, and intermediate together with the dots representing the experimental EELS results for each metal).
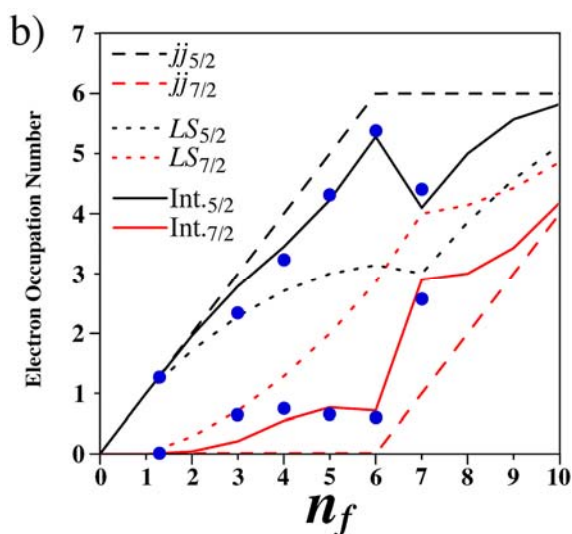
$N_{4,5}$ edges

Figure 2 shows the experimental $N_{4,5}(4d \rightarrow 5f)$ EELS results for α-phase Th, U, Np, Pu, Am, and Cm metal, which are normalised to the N_5 peak height. The experimental results in Figure 2 are in very good agreement with the theoretical spectra shown in Figure 1. Noticeable is the gradually growing separation between the N_4 and N_5 peaks from Th to Cm, in pace with the increase in $4d$ spin-orbit splitting with atomic number. Second and more importantly, the intensity of the $N_4(4d_{3/2})$ peak gradually decreases in intensity relative to the $N_5(4d_{5/2})$ peak going from Th to Am, then abruptly increases for Cm [13]. Applying the sum-rule analysis to the experimental branching ratio gives the values of the $5f$ spin-orbit interaction per hole. The values of $\langle w^{110} \rangle / (14 - n_f) - \Delta$ are shown in Figure 3(a) by the blue dots.

In Figure 3(a), Th metal falls on all three curves, due to the fact that it takes two electrons to tangle and with less than one $5f$ electron in Th there is no difference between the coupling mechanisms. U falls directly on the LS coupling curve, Np between the LS and intermediate curve, and Pu, Am and Cm all fall on or near the intermediate coupling curve. The intermediate curve is strongly shifted towards the jj limit for Pu and Am, evidencing the strong preference of the $5f$ electrons for the $5f_{5/2}$ level in both metals. However, for Cm there is a sudden and pronounced shift in the intermediate coupling curve toward the LS limit.

The values of n_f and $\langle w^{110} \rangle$ can be converted into the electron occupation numbers $n_{7/2}$ and $n_{5/2}$ using Eqs. (1) and (2), which is just a different way of representing the same data. The experimental and theoretical results are displayed in Figure 3(b), where the number of electrons in the $5f_{5/2}$ and $5f_{7/2}$ levels as calculated in intermediate coupling using the atomic model are drawn with black and red lines, respectively, and the experimental EELS results are indicated with blue points. Apart from the slight deviation in the lighter actinides, U and Np, which is caused by delocalisation of the $5f$ states and thus indicates a departure from the atomic model, the EELS results are in excellent agreement with the theoretical curves. Figure 3(b) clearly shows that for the actinide metals up to and including Am, the $5f$ electrons strongly prefer the $5f_{5/2}$ level. However, this is changing in a striking manner at Cm where not only does the electron occupation sharply increases for the $5f_{7/2}$ level, but even *decreases* for the $5f_{5/2}$ level.

The physical origin of the abrupt and striking change in the values between Am to Cm can be understood from the angular momentum coupling. In jj coupling the electrons prefer to be in the $f_{5/2}$ level, which however can hold no more than six, so that the maximal energy gain in jj coupling is obtained for Am f^6, where the $f_{5/2}$ level gets full. However, for Cm f^7 at least one electron will be relegated to the $f_{7/2}$ level. The f^7 configuration has the maximal energy stabilisation due to the exchange interaction, with parallel spin in the half-filled shell, which can only be achieved in LS coupling. Thus, the large changes observed in the electronic and magnetic properties of the actinides at Cm are due to the transition from optimal spin-orbit stabilisation for f^6 to optimal exchange stabilisation for f^7. In all cases, spin-orbit and exchange interaction compete with each other, resulting in intermediate coupling; however, increasing the f count from 6 to 7 shows a clear and pronounced shift in the power balance in favour of the exchange interaction. The effect is in fact so strong that, compared to Am, not one but two electrons are transferred to the $f_{7/2}$ level in Cm [Figure 3(b)]. Therefore, in Cm metal, the angular-momentum coupling in the $5f$ states plays a decisive role in the formation of the magnetic moment, with Hund's rule coupling being the key to producing the large spin polarisation that dictates the newly found crystal structure of Cm under pressure [13,25].

The branching-ratio analysis can also be used to constrain the f-count for given angular-momentum coupling condition [8]. In the case of Pu metal, EELS, XAS and the spin-orbit sum rule suggest an f-count near 5, with 5.4 being a reasonable upper limit [12,13]. Further evidence for this f-count comes from Anderson impurity calculations for Pu [26] that explain photoemission results on 1 to 9 monolayers thin films of Pu metal [27,28]. The $4f$ core-level photoemission spectra display a screened and unscreened peak, thereby acting as a ruler for the degree of localisation. The results for the f-count are in agreement with recent DMFT calculations by Shim, *et al.* [29] and LDA+U calculations by Shick, *et al.* [30], which explain the three-peak structure in $5f$ photoemission and the relatively high electronic specific heat. The absence of experimentally observed magnetic moments in any of the six allotropic phases of Pu metal [31] is thought to be due to Kondo screening and a non-single Slater-determinant ground state in these respective models. Recent magnetic susceptibility measurements have shown that local magnetic moments in the order of 0.05 μ_B/atom form in Pu as damage accumulates due to self-irradiation [32].

Conclusions

We discussed the systematic trends of the actinide metals using the $N_{4,5}$ edge, where the core-level spin-orbit interaction is much larger than the core-valence electrostatic interactions. For such deeper core levels in EELS or XAS the spin-orbit sum rule provides a measure of the angular part of the $5f$ spin-orbit interaction per hole. While the sum rule works qualitatively for $3d$ transition metal $L_{2,3}$ edges and lanthanide $M_{4,5}$ edges, it works quantitatively for $4d$ and $5d$ transition metal $L_{2,3}$ edges and actinide $M_{4,5}$ and $N_{4,5}$ edges. Many-electron spectral calculations confirm that the sum rule can be applied to the actinide $5f$ states. Since the sum rule yields the angular dependent part of the spin-orbit interaction, it gives access to the angular momentum coupling. Applying the sum rule to the EELS results, we find an interesting trend in the momentum coupling across the actinide series. While LS coupling works for light metals (Th and U), heavier metals (Pu, Am, and Cm) adhere intermediate coupling. This change coincides with the $5f$ delocalisation-localisation transition in the actinide series, so that the momentum coupling is sensitive to the degree of delocalisation. The results show that jj coupling is important for Pu and must be taken into account in the Hamiltonian, allowing a significant refinement of the theoretical framework of computational models of the actinides. The spin-orbit sum rule analysis shows that Np is already becoming localised. A pure LS coupling mechanisms is observed for α-U, whereas for Np the spin-orbit expectation value for Np is closer to intermediate coupling. In other words, the very beginning of the transition from LS to intermediate coupling occurs in Np, one element prior to the crystallographic volume jump observed near Pu. The fact that Np metal is the first actinide element to have a small yet measurable degree of localisation in the $5f$ states is further illustrated by photoelectron spectroscopy, temperature-dependent resistivity and electronic specific heat of the metal [6].

Pu, Am, and Cm all follow the theoretical intermediate coupling curve (see Figure 3), which means that Pu and Am are near jj, while Cm is strongly shifted towards LS. While Th to Am show almost full filling of the $5f_{5/2}$ level, not one, but *two* electrons go into the $5f_{7/2}$ level of Cm. In jj coupling, electrons first fill the $f_{5/2}$ level, which can hold no more than six, before the $f_{7/2}$ level is filled. Maximal energy gain in jj coupling is thus obtained for Am f^6, since the $f_{5/2}$ level is filled. However, in Cm f^7 one electron must be relegated to the $f_{7/2}$ level. The f^7 configuration has maximal energy stabilisation due to exchange interaction, with all spins parallel in the half-filled shell, which can only be achieved in LS coupling. Therefore, the large change observed at Cm is due to the transition from optimal spin-orbit stabilisation for f^6 to optimal exchange interaction stabilisation for f^7. The choice of coupling mechanism plays a large influence on the spin and orbital magnetic moments. This is most remarkable for Cm: spin moment is small for jj, but large for LS and intermediate coupling. Thus, the large shift towards LS coupling produces the strong spin polarisation that stabilised curium.

The results are also an indication of the number of f electrons. Pu, Am, and Cm metal are near $5f^5$, $5f^6$, and $5f^7$, respectively. The Pu metal data clearly shows that n_f is near 5, with enough variation to allow up to 5.4; however, f-counts at or near 6 are in disagreement with spectroscopy. Further, the Pu data show the $5f$ states of the metal fall precisely on the intermediate coupling curve. Also the Cm metal result is close to the intermediate coupling curve, but in this case it is bending back to the LS curve. The angular-momentum coupling mechanism dictates large spin polarisation, explaining the observed magnetic stabilisation of Cm [13,25].

References

[1]   Hirsch, P., A. Howie, R. Nicholson, D.W. Pashley, M.J. Whelan, *Electron Microscopy of Thin Crystals*, 2nd Ed., Robert E. Kreiger, Malabar, Florida (1977).

[2]   Reimer, L., *Transmission Electron Microscopy*, 4th Ed., Springer, New York (1997).

[3]   Fultz, B., J.M. Howe, *Transmission Electron Microscopy and Diffractometry of Materials*, 2nd Ed., Springer, New York (2001).

[4]   Zuo, J.M., J.C.H. Spence, *Electron Microdiffraction*, Springer, New York (1992).

[5]   Moore, K.T., M.A. Wall, A.J. Schwartz, *J. Nucl. Mat.,* 306, 213 (2002).

[6]   Moore, K.T., G. van der Laan, "Nature of the 5f States in Actinide Metals", *Rev. Mod. Phys.*, in press (2009), cond-mat. arXiv:0807.0416.

[7]   Laan, G. van der, K.T. Moore, "Magnetic Structure of Actinide Metals", *Lect. Notes Phys.*, in press (2008), cond-mat. arXiv:0812.3868.

[8]   Laan, G. van der, K.T. Moore, J.G. Tobin, B.W. Chung, M.A. Wall, A.J. Schwartz, *Phys. Rev. Lett.*, 93, 097401 (2004).

[9]   Moore, K.T., G. van der Laan, J.G. Tobin, B.W. Chung, M.A. Wall, A.J. Schwartz, *Ultramicroscopy*, 106, 261 (2006).

[10]   Moore, K.T., M.A. Wall, A.J. Schwartz, B.W. Chung, S.A. Morton, J.G. Tobin, S. Lazar, F.D. Tichelaar, H.W. Zandbergen, P. Söderlind, G. van der Laan, *Philos. Mag.,* 84, 1039 (2004).

[11]   Thole, B.T., G. van der Laan, *Phys. Rev. B*, 38, 3158 (1988); *Phys. Rev. A, 38*, 1943 (1988); Laan, G. van der, B.T. Thole, *Phys. Rev. Lett.,* 60, 1977 (1988).

[12]   Moore, K.T., G. van der Laan, M.A. Wall, A.J. Schwartz, R.G. Haire, *Phys. Rev. B*, 76, 073105 (2007).

[13]   Moore, K.T., G. van der Laan, R.G. Haire, M.A. Wall, A.J. Schwartz, P. Söderlind, *Phys. Rev. Lett.,* 98, 236402 (2007).

[14]   Thole, B.T., G. van der Laan, J.C. Fuggle, G.A. Sawatzky, R.C. Karnatak, J.M. Esteva, *Phys. Rev. B*, 32, 5107 (1985).

[15]   Starke, K., E. Navas, E. Arenholz, Z. Hu, L. Baumgarten, G. van der Laan, C.T. Chen, G. Kaindl, *Phys. Rev. B*, 55, 2672 (1997).

[16]   Moore, K.T., G. van der Laan, *Ultramicroscopy,* 107, 1201 (2007).

[17]   Butterfield, M.T., K.T. Moore, G. van der Laan, M.A. Wall, R.G. Haire, *Phys. Rev. B*, 77, 113109 (2008).

[18]   Cowan, R.D., *J. Opt. Soc. Am.,* 58, 808 (1968).

[19]   Cowan, R.D., *The Theory of Atomic Structure and Spectra,* University of California Press, Berkeley, CA (1981).

[20]   Laan, G. van der, B.T. Thole, *Phys. Rev. B*, 53, 14458 (1996).

[21]   Laan, G. van der, *Phys. Rev. B*, 57, 112 (1998).

[22]   Laan, G. van der, B.T. Thole, *Phys. Rev. B*, 43, 13401 (1991).

[23]   Laan, G. van der, I.W. Kirkman, *J. Phys.: Condens. Matter*, 4, 4189 (1992).

[24]   Laan, G. van der, B.T. Thole, G.A. Sawatzky, J.C. Fuggle, R.C. Karnatak, J.M. Esteva, B. Lengeler, *J. Phys. C: Solid State Phys.,* 19, 817 (1986).

[25]   Heathman, S., R.G. Haire, T. Le Bihan, A. Lindbaum, M. Idiri, P. Normile, S. Li, R. Ahuja, B. Johansson, G.H. Lander, *Science* 309, 110 (2005).

[26]   Laan, G. van der, unpublished.

[27]   Gouder, T., L. Havela, F. Wastin, J. Rebizant, *Europhys. Lett.* 55, 705 (2001).

[28]   Havela, L., T. Gouder, F. Wastin, nd J. Rebizant, *Phys. Rev. B*, 65, 235118 (2002).

[29]   Shim, J.H., K. Haule, G. Kotliar, *Nature (London)*, 446, 513 (2007).

[30]   Shick, A.B., J. Kolorenc, L. Havela, V. Drchal, T. Gouder, *Europhys. Lett.*, 77, 17003 (2007).

[31]   Lashley, J.C., A. Lawson, R.J. McQueeney, G.H. Lander, *Phys. Rev. B*, 72, 054416 (2005).

[32]   McCall, S.K., M.J. Fluss, B.W. Chung, M.W. McElfresh, D.D. Jackson, G.F. Chapline, *Proc. Natl. Acad. Sci. U.S.A.,* 103, 17179 (2006).

A dynamical model to understand hydration across the lanthanide series: Bridging the gap between XAS experiments and microscopic structure

Magali Duvail,[1] **Pierre Vitorge,**[1,2] **Paola D'Angelo,**[3] **Riccardo Spezia**[1]

[1]Université d'Evry, CNRS, CEA
Laboratoire Analyse et Modelisation pour la Biologie et l'Environnement, LAMBE
Evry, France
[2]CEA, DEN, Saclay, Laboratoire de Speciation des Radionucleides et Molecules, DPC, SECR, LSRM
Gif-sur-Yvette, France
[3]Dipartimento di Chimica, Università di Roma "La Sapienza"
Roma, Italy

Abstract

The co-ordination numbers (CN) of lanthanide trications (Ln^{3+}) decrease from 9 to 8 across the Ln series. These CN values were recently estimated by comparing the EXAFS data of aqueous solutions with known solids across the Ln^{3+} series. Classical molecular dynamic (CLMD) simulations are here used to propose a complementary atomistic picture of the Ln^{3+} hydrated species in liquid water. The CLMD simulations use explicit polarisation and pair interaction potentials (PIP) built and parameterised from MP2 ab initio calculations of symmetric $La(H_2O)_8^{3+}$ model clusters. To better validate the PIP and CLMD for La^{3+} in liquid water, the EXAFS signal is interpreted and recalculated, with GNXAS software, by directly using the radial distribution functions issued from CLMD simulations. The La^{3+} PIP is thus extended to the whole Ln^{3+} series according to modifications of atomic properties along the series, obtaining results in good agreement with experimental data. Across the series we observed a progressive destabilisation of the CN = 9 stoichiometry, in the form of progressive mean departure of a water molecule from the middle triangle of the tricapped trigonal prism (TTP) geometry, and further rearrangement into the square antiprism (SAP) CN = 8 geometry. This is associated with higher exchange frequencies of water for the Ln^{3+} in the middle of the series ($Ln^{3+} = Eu^{3+}$ to Tm^{3+}), and almost linear decrease – with atomic number – of the Gibb's free energies of the water exchange reactions, or equivalently sigmoid variations of the CN values. This sigmoid curve has not the shape of any "break" as had first been proposed years ago, when appeared the "gadolinium break" expression. Finally, our CLMD simulations based on physical parameters (ionic radius and atomic polarisability) provide a microscopic picture of the geometries and the dynamics of lanthanide series hydration in liquid water.

Introduction

Understanding the hydration structures of heavy atoms – like transition metals, lanthanides (Ln^{3+}) or actinides (An) – is a first step needed to address their chemical behaviours in aqueous solutions. Molecular dynamics (MD) simulations can provide a real help in understanding the molecular structures of hydrated ions and thus better interpret X-ray absorption experiments. When structural experimental data are mainly due to a unique conformation, and the ligand exchange events are negligible in determining the XAS signals, *ab initio* based calculations, both statically and dynamically, can help in the interpretation of those signals [1-3]. Conversely, it is difficult to correctly sample the phase space with such methods, especially when ligand exchanges, occurring at picosecond to nanosecond (or even longer) time scale, are reflected in the mean experimental signal. In that case classical molecular dynamics (CLMD) can be used, since the simulations can now be long enough to observe the exchanges for the water molecules of the first hydration sphere. However, CLMD simulations need the use of reliable metal-water and water-water pair interaction potentials (PIP).

In the present work we focused our attention on hydration of a whole chemical series, the Ln^{3+} series. Light lanthanides are fission products. There aqueous (geo)chemistry is investigated in the framework of waste management studies – specially assessments of the environmental impacts of future geological waste disposals. Lanthanides are also used as chemical analogues to predict the chemical behaviours of Am and Cm – and Pu(III) in reducing conditions as typically in deep groundwaters.

An examination of the literature on CLMD simulations of Ln^{3+} in liquid water (see Ref. [4] and references therein) indicates that it is needed to explicitly calculate the polarisation for such highly charged cation in liquid water, besides the PIP. The model is validated by comparing CLMD simulations results with the available experimental information, being in good agreement with those values. The La-O distance (d_{La-O}) has been originally measured by X-Ray Diffraction (XRD) obtaining different values as a function of the experimental conditions, namely: 2.48 Å in 1.54 to 2.67 mol.kg^{-1} $LaCl_3$ [5], 2.58 Å in 3.808 mol.kg^{-1} $LaCl_3$ [6] and 2.57 in 9.16 mol.L^{-1} ClO_4^- [7]. These two latter values are close to those deduced from more recent EXAFS measurements: 2.56 Å in 0.05 to 0.20 mol.L^{-1} $LaCl_3$ [8], 2.545 Å in 0.8094 mol.L^{-1} $La(ClO_4)_3$ [9], 2.54 Å in 0.25 mo.L^{-1} Cl$^-$ [10] and 2.56 Å (2.515/2.64) in 3.856 mol.L^{-1} ClO_4^- [11]. The influence of the salt concentration is within the scattering of the experimental data, indeed the Ln^{3+} and An^{3+} cations are believed to form only weak outer-sphere complexes with Cl$^-$, and no complex with ClO_4^-. At the same time our CLMD simulations were performed, a thorough new EXAFS study gave 2.55 Å (L3-edge) or 2.58 Å (K-edge) in 0.7 mol.L^{-1} $CF_3SO_3^-$ acidic solutions [12] for mean d_{La-O} assuming two slightly different distances (here averaged) each giving slightly asymmetric peak, the maximum of the averaged peak being at smaller distance (by 0.03 or 0.01 Å).

Observations of macroscopic properties across the Ln^{3+} series have suggested that CN should decrease across the series []13-15], and CN should vary from CN = 9 (for La^{3+}, the first Ln^{3+}) to CN = 8 (for Lu^{3+}, the last Ln^{3+}) by analogy with structures of solid compounds [12,16,17] or analogy with molar volumes of aqueous ions [15,18]. This was confirmed by a recent thorough comparison of new EXAFS data between series of Ln^{3+}(aq) in acidic aqueous solutions and Ln solids [12], where the similarity of the EXAFS signals was used to demonstrate the similarity of the co-ordinations, and the fitting of the EXAFS distances confirms this similarity.

All these data suggest that the decreasing in CN along the series is not a sudden change but a smooth decrease, breaking down the old picture of the "gadolinium break" model used up to the 90s to describe the variations of Ln^{3+} properties across the series. Our simulations agree with this new picture emerging, confirming the previous indirect experimental evidences [15] and the new EXAFS data [12]. Furthermore, our simulations can be used as a complementary tool to interpret EXAFS data, and go further in the microscopic description of the static and dynamic properties of hydrated La^{3+} and other Ln^{3+} ions, as we will report in the present paper. Finally, the analogy with actinide trications water complexes was found also in a similar metal-oxygen distance decreasing along the series for the available aqua ions. Notably, d_{An-O} EXAFS distances are reported for An^{3+} = Pu^{3+} (2.51 Å) [10], Am^{3+} (2.48 Å) [19], Cm^{3+} (2.45 Å) [20] and Cf^{3+} (2.42 Å) [21]. They are slightly bigger by about 0.03 to 0.07 Å than the d_{Ln-O} EXAFS distances for corresponding lanthanides, *i.e.* Sm^{3+}, Eu^{3+}, Gd^{3+} and Dy^{3+}.

Methods

In this section, we describe the force field used in our CLMD simulations. More details on theory and simulation protocol were already presented elsewhere [4,22]. To understand at atomic level the structural and dynamic hydration properties of lanthanides, we have first developed, parameterised and tested a classical polarisable PIP for La^{3+}, the first atom in the series. The PIP was then used in CLMD simulations in explicit bulk water, with standard periodic boundary conditions in the NVE ensemble, where initial velocities were generated at the target temperature, and thus it was observed to slightly oscillate around the target value. This is a standard procedure that allows one to simulate liquid systems. This potential was able to correctly reproduce the d_{La-O} and CN experimental results [4]. Among the functional forms that we have tested for the so called non-electrostatic part of the La-O interaction (*i.e.* high order terms in electrostatic expansion) we found that the Buckingham potential provides the best agreement with experiments [4]. This potential has the following form:

$$V_{ij}^{Buck6} = A_{ij}^{Buck6} \exp\left(- B_{ij}^{Buck6} r_{ij}\right) - \frac{C_{ij}^{Buck6}}{r_{ij}^6}$$

where A_{ij}^{Buck6} = 1.004 10^6 kJ mol^{-1}, B_{ij}^{Buck6} = 3.48 Å^{-1} and C_{ij}^{Buck6} = 3.766 10^4 kJ mol^{-1} Å^6 were fitted to reproduce MP2 *ab initio* calculated energies of La(H$_2$O)$_8^{3+}$ symmetric model clusters [4]. With those values we obtained d_{La-O} = 2.52 Å and CN = 9.02 that are in good agreement with the published EXAFS data [8-12]. Note that the La(H$_2$O)$_8^{3+}$ cluster used for obtaining Buckingham parameters from MP2 calculations includes many-body interactions, but do not correspond to the actual dominating first hydration shell geometry in liquid water, being La(H$_2$O)$_9^{3+}$. Finally, in the electrostatic part we included atomic charges and dipoles, the latter by using the Thole's induced dipole model [23] and the resulting self-consistent equations were solved only at the beginning and thus propagated following a Car-Parrinello like procedure [24].

The classical potential developed for La^{3+} was thus extended to the whole Ln^{3+} series, taking into account modifications in ionic radii and atomic polarisabilities of the cations in the series [22,25]. Namely, we kept the same numerical value of A_{ij}^{Buck6} for all the Ln^{3+}, we changed the B_{ij}^{Buck6} values to reproduce the decrease of the published ionic radii for the Ln^{3+} ions across the series, and we adjusted C_{ij}^{Buck6} to keep the same shape for all the PIP. The resulting parameters are reported in Ref. [22].

Results and discussion

For checking the level of agreement of our CLMD simulations with EXAFS data, we compared experimental EXAFS signal of La^{3+} in water with the corresponding theoretical signal obtained from metal-water radial distribution functions (RDF) extracted from CLMD simulations of La^{3+}(aq). To this aim, the EXAFS theoretical signals associated with the La^{3+}-O and La^{3+}-H two-body distributions have been calculated by means of the GNXAS program starting from the La^{3+}-O and La^{3+}-H RDFs (see Refs. [26,27], for a description of the theoretical framework for the multiple scattering analysis). Therefore, this approach uses the full statistical averaged structural information provided by the RDF as naturally obtained from simulations. Note that it is not necessary to fit the corresponding parameters when using the CLMD simulation RDF to interpret the EXAFS signal, as usually done for typically distances and thermal agitation. The theoretical EXAFS signal generated with the CLMD simulation RDF is in good agreement with experimental EXAFS signal (Figure 1). The theoretical first peak of the signal Fourier transform (FT) shown in Figure 1 is slightly shifted (about 0.02 Å) toward smaller distances. This might reflect a little too attractive PIP. The small shoulder at the end of the first FT peak is more pronounced in the theoretical simulation. Such small differences are usual for similar published studies, so that we can consider our simulations catching the crucial hydration properties of La^{3+} hydration in liquid water.

Figure 1: Fourier transforms of the experimental (solid lines), calculated (dashed lines) and residual (dashed-dotted lines) signals. This analysis was performed by using the GNXAS package [26,27].
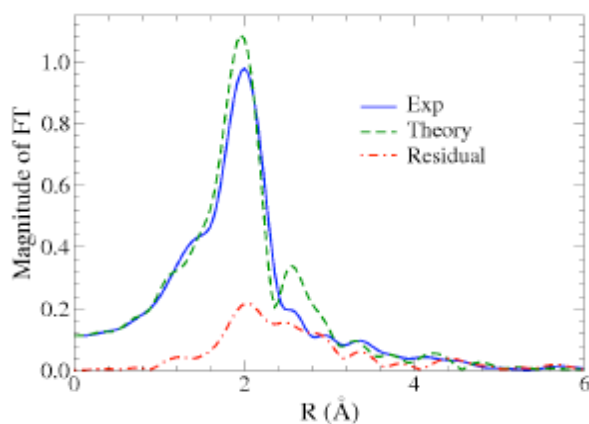
Thus, using the parameters extrapolated for the whole series, we can compare Ln^{3+}-water distances with experimental data available, obtained from different groups by EXAFS experiments. As shown in Figure 2, we are able to reproduce the decrease of d_{Ln-O} across the Ln^{3+} series. Note that we also attempted to parameterise these PIP and others for CLMD simulations without explicitly calculating the polarisation during the simulations. We never succeeded to reproduce both the expected d_{La-O} and CN values [4,28]. This confirms published results indicating that explicit polarisation is needed for such highly charged cations in water.

Figure 2: Ln^{3+}-O distances in liquid water obtained from CLMD simulations (■) with corresponding experimental data taken from literature: (○) [29], (◇) [19], (△) [9] and (▽) [12]. Also available Ac^{3+}-O distances available in literature [19-21] are reported.
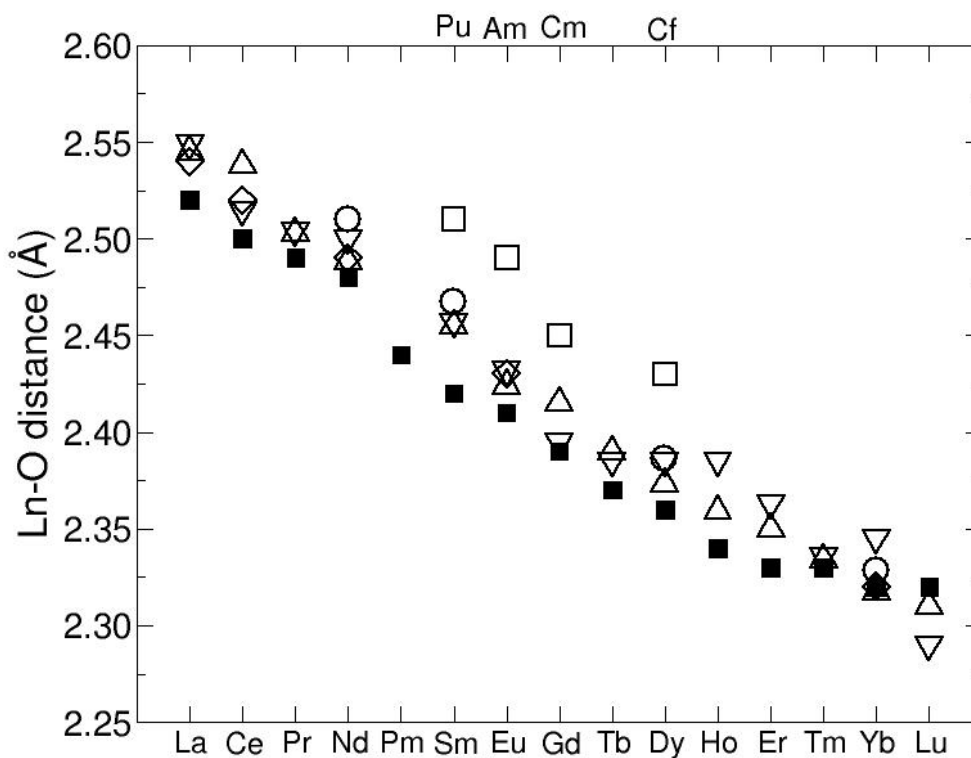
According to the literature and our calculations $La(H_2O)_9^{3+}$ has a tricapped trigonal prism (TTP) geometry as all the other $Ln(H_2O)_9^{3+}$ hydrates while $Lu(H_2O)_8^{3+}$ presents a square antiprism (SAP) geometry as all the other $Ln(H_2O)_8^{3+}$ structures. A set of structures obtained from our simulations presenting both geometries with different orientations is presented in Figure 3 to better elucidate this point and the following discussion. Whereas it is straightforward to calculate co-ordination numbers from the integration of RDF, the determination of the exact symmetric geometries (as done in static approaches) is not trivial in the framework of molecular dynamics simulations, which results are in form of trajectories where thermal agitation always locally breaks exact symmetries. This is much more problematic when the distinction between different geometries is not clear by definition, as occurs in the case of CN=8 structures. In fact, for that structure a bicapped trigonal prism (BTP) structure is also possible and it corresponds to the TTP structure with a water molecule less.

To illustrate this point we report in Figure 3 different views of TTP and SAP geometries. We used one colour for each set of three O atoms in the three parallel triangles to evidence the TTP (or BTP) geometries, where the atoms of the prism are in blue and orange, and the capped ones in red and pink lines to evidence the two parallel (or nearly parallel) square (or nearly square) in the SAP (or SAP like) geometries. Of course one water molecule is missing in BTP $Ln(H_2O)_8^{3+}$ with respect to TTP such that we have only two red oxygens of the medium triangle water molecules. Similarly, the added water molecule in SAP-like $La(H_2O)_9^{3+}$ is perpendicular in the middle of a SAP plan. Note that d_{La-O} is slightly longer for this water molecule as for water molecules in the medium triangle in the TTP geometry.

Figure 3: TTP $La(H_2O)_9^{3+}$ (top) and SAP $Lu(H_2O)_8^{3+}$ (bottom)

La is green, H white and three colours (orange, red and blue) are
used for O (see the text for the distinction used between O atoms)
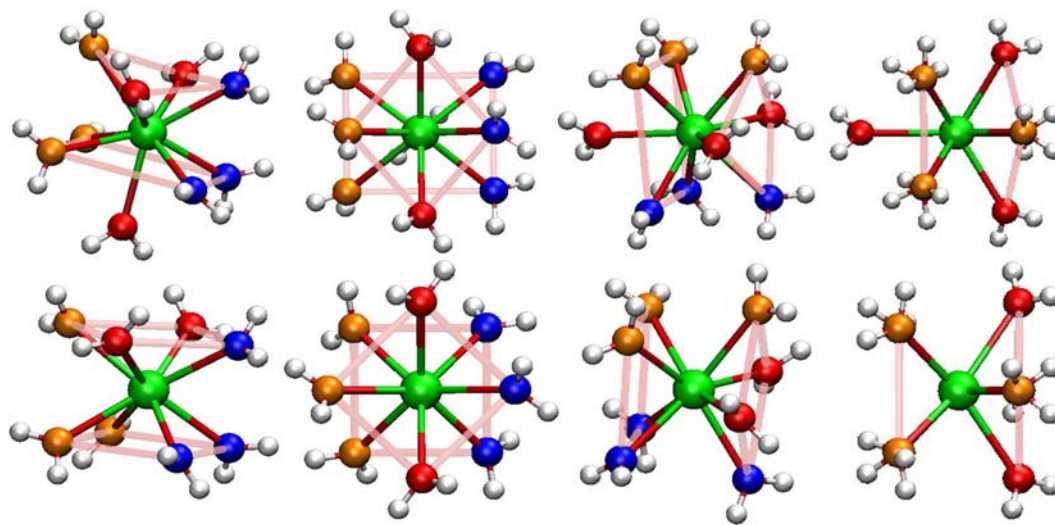
As previously mentioned average CN is obtained by integrating RDF up to a radius where the RDF goes to zero (see RDF presented in our previous work [4,20]). To determine CN for each trajectory snapshot we counted the water molecules within the cut-off distance corresponding to the zero in RDF. This allows us to count the number of configurations having one or another CN and the resulting CN is simply the trajectory average of those values. A no integer CN comes from coexistence of different stoichiometries in a given trajectory. The probability of having one structure can be thus easily calculated from the ratio n_i/n, where n_i is the number of configurations with a given stoichiometry and n the total number of configurations. Smooth variations are obtained for CN across the Ln^{3+} series as shown in Figure 4(a), which cannot be described as "gadolinium break". Furthermore, the shape of the CN curve is approximately sigmoid like: this suggests linear variations for the log of the $K_9 = n_9/n_8$ ratio [lg K_9 points in Figure 4(b)]. Indeed, $CN \approx 9 - 1/(K_9 + 1)$ since only $La(H_2O)_9^{3+}$ and $Lu(H_2O)_8^{3+}$ predominate: it appears that lg K_9 has an almost linear decreasing along the Ln^{3+} series, as shown in Figure 4(a).

Note that these K_9 values extracted from the CLMD simulations correspond to a thermodynamic equilibrium constant, when equilibration is achieved. In our case, exchanges of water molecules in the first hydration shell were observed in the CLMD simulations between $Ln(H_2O)_8^{3+}$ and $Ln(H_2O)_9^{3+}$.

Figure 4: Properties obtained in the Ln^{3+} series (circles) and fitted (full line) following a two-state model (see text for details)

a) Co-ordination number (CN), b) lgK$_9$, c) exchange frequency (EF)
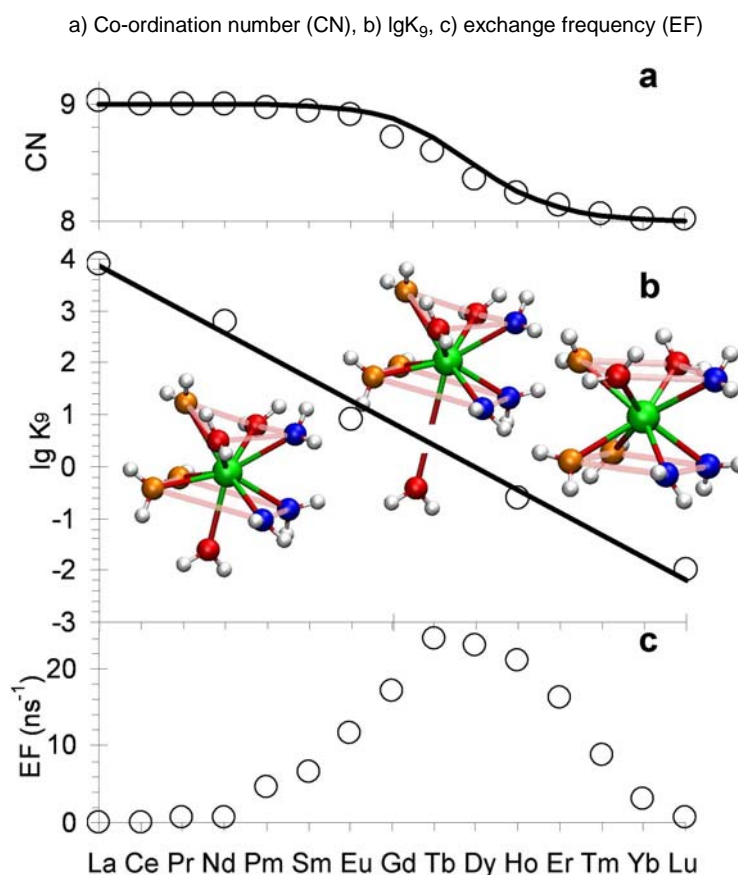
$Ln(H_2O)_9^{3+}$ is observed most of the time during the CLMD simulations for the light lanthanides, and $Ln(H_2O)_8^{3+}$ is only observed during exchanges. Similarly, $Ln(H_2O)_9^{3+}$ is only observed during the exchanges for the heavy lanthanides, where the CN=8 stoichiometry is predominant. In the two extremities of the series we observed a low exchange frequency, while an increasing is observed in the middle of the Ln^{3+} series [Figure 4(c)]. Furthermore, $Ln(H_2O)_9^{3+}$ and $Ln(H_2O)_8^{3+}$ are the most stable stoichiometries in the beginning and the end of the Ln^{3+} series respectively, while they are of closest stabilities in the middle of the Ln^{3+} series as reflected by the co-ordination numbers: more frequent exchanges are thus associated with closest energies for the reactant and product. This high frequent exchange rate suggests low activation energies for the association and dissociation of the ninth water molecule.

Activation energies were obtained for some lanthanides by performing simulations at different temperatures, similarly as we have done for La^{3+} aqua ion equilibria [30]. We obtained 17 kJ.Mol^{-1} for the activation energy of exchange reaction for Lu^{3+}, as calculated from the temperature influence on the mean residence time of a water molecule in the first hydration sphere of $Lu(H_2O)_8^{3+}$. The activation energies are, as expected, smaller in the middle of the series: 10 kJ.Mol^{-1} for Eu^{3+} and Ho^{3+}. More details on kinetcs will be presented and deeply discussed elsewhere [28].

Conclusions

Our simulations have shown that upon moving across the series from lighter to heavier lanthanides, the statistical predominance of one first hydration shell structure containing nine water molecules in the first hydration shell changes in favour of one containing eight water molecules. La$(H_2O)_9^{3+}$ has the TPP geometry, where the water molecules in the middle triangle are less strongly bonded to La (slightly longer d_{La-O}), and this result is strengthened by a fine comparison with EXAFS experiments. Changing the atom along the lanthanide series, one of these middle water molecules more and more easily goes away for heavier – hence smaller – Ln^{3+} ions, providing more frequent exchanges for Ln^{3+} = Eu^{3+} to Tm^{3+}, corresponding to co-ordination numbers between 9 and 8. This can be schematically represented with a progressive departure of a middle triangle water molecule [as schematically showed in Figure 4(b)], finally giving the co-ordination number of 8 for the heaviest lanthanides with the SAP geometry. This statistical picture can explain the hydration behaviour along the series and definitely help in understanding XAS experiments.

Concluding, we have proposed a model that is able to catch crucial properties for a complete chemical series. This approach is based on taking into account physical properties such as ionic radii and polarisabilities and relating parameters of a classical PIP to those physical quantities. This approach has here been used to understand structural and dynamical behaviour of the lanthanide series, without performing high level *ab initio* calculations for all the atoms but just for a minimal set needed to build up and extend the PIP to the series, and it could be used, with careful adaptations, for other chemical series, such as actinides, or other aqueous inorganic limiting complexes [31,32].

References

[1] Spezia, R., M. Duvail, P. Vitorge, T. Cartailler, J. Tortajada, G. Chillemi, P. D'Angelo, M-P.Gaigeot, *J. Phys. Chem.*, A 110, 13081 (2006).

[2] Bresson, C., R. Spezia, S. Esnouf, P.L. Solari, S. Coantic, C. Den Auwer, *New J. Chem.*, 31, 1789 (2007).

[3] Spezia, R., C. Bresson, C. Den Auwer, M-P.Gaigeot, *J. Phys. Chem. B*, 112, 6490 (2008).

[4] Duvail, M., M. Souaille, R. Spezia, T. Cartailler, P. Vitorge, *J. Chem. Phys.*, 127, 034504 (2007).

[5] Smith, L.S., D.L. Wertz, *J. Am. Chem. Soc.*, 97, 2365 (1975).

[6] Habenschuss, A., F.H. Spedding, *J. Chem. Phys.*, 70, 3758 (1979).

[7] Johansson, G., H. Wakita, *Inorg. Chem.*, 24, 3047 (1985).

[8] Solera, J.A., J. Garcia, M.G. Proietti, *Phys. Rev. B*, 51, 2678 (1995).

[9] Ishiguro, S-I., Y. Umebayashi, K. Kato, R. Takahashib, K. Ozutsumi, *J. Chem.Soc. Faraday Trans.*, 94, 3607 (1998).

[10] Allen, P., J.J. Bucher, D.K. Shuh, N.M. Edelstein, I. Craig, *Inorg. Chem.*, 39, 595 (2000).

[11] Näslund, J., P. Lindqvist-Reis, I. Persson, M. Sandström, *Inorg. Chem.*, 39, 4006 (2000).

[12] Persson, I., P. D'Angelo, S. De Panfilis, M. Sandström, L. Eriksson, *Chem. Eur. J.*, 14, 3056 (2008).

[13] Morgan, L.O., *J. Chem. Phys.*, 38, 2788 (1963).

[14] Spedding, F.H., D.A. Csejka, C.W. DeKock, *J. Phys. Chem.*, 70, 2423 (1966).

[15] Helm, L., A.E. Merbach, *Chem. Rev.*, 105, 1923 (2005).

[16]   Spedding, F.H., M.J. Pikal, B.O. Ayers, *J. Phys. Chem.*, 70, 2440 (1966).

[17]   Lindqvist-Reis, P., K. Lamble, S. Pattanaik, I. Persson, M. Sandström, *J. Phys. Chem. B*, 104, 402 (2000).

[18]   Swaddle, T.W., *Advanced Inorg. Bioinorg. Mechanisms*, 2, 95 (1983).

[19]   Allen, P.G., J.J. Bucher, D.K. Shuh, N.M. Edelstein, T. Reich, *Inorg. Chem.*, 36, 4676-4683 (1997).

[20]   Allen, P.G., D.K. Shuh, J.J. Bucher, N.M. Edelstein, T. Reich, *Euroconference and NEA Workshop on Speciation, Techniques, and Facilities for Radioactive Materials at Synchrotron Light Sources*, Grenoble, France, 4-6 October 1998.

[21]   Revel, R., C. Den Auwer, C. Madic, F. David, B. Fourest, S. Hubert, J-F. Le Du, L.R. Morss, *Inorg. Chem.*, 38, 4139-4141 (1999).

[22]   Duvail, M., R. Spezia, P. Vitorge, *Chem. Phys. Chem.*, 9, 693 (2008).

[23]   Thole, B.T., *Chem. Phys.*, 59, 341 (1981).

[24]   Sprik, M., *J. Phys. Chem.*, 95, 2283 (1991).

[25]   Duvail, M., P. D'Angelo, M-P.Gaigeot, P. Vitorge, R. Spezia, *Radiochim. Acta*, accepted.

[26]   Filipponi, A., A. Di Cicco, C.R. Natoli, *Phys. Rev. B*, 52, 15122 (1995).

[27]   *http://gnxas.unicam.it/XASLABwww/pag_gnxas.html*.

[28]   Duvail, M., P. Vitorge, R. Spezia, in preparation.

[29]   Cossy, C., L. Helm, D.H. Powell, A.E. Merbach, *New J. Chem.*, 19, 27 (1995).

[30]   Duvail, M., R. Spezia, T. Cartailler, P. Vitorge, *Chem. Phys. Lett.*, 448, 41 (2007).

[31]   Philippini, V., T. Vercouter, J. Aupiais, S. Topin, Ch. Ambard, A. Chaussé, P. Vitorge, *Electrophoresis*, 29, 2041 (2008).

[32]   Philippini, V., T. Vercouter, A. Chaussé, P. Vitorge, *J. Solid State Chem.*, 181, 2143 (2008).

Structures and stoichiometry of actinide complexes: Challenges of combining EXAFS and quantum chemistry

Satoru Tsushima
Institute of Radiochemistry, Forschungszentrum Dresden-Rossendorf (FZD)
Dresden, Germany

Abstract

EXAFS spectroscopy has been proved to be a very powerful tool for studying the structures of actinide complexes in aqueous and non-aqueous systems. The application of EXAFS spectroscopy has been extended to the systems with mixed species and/or species with very dilute concentration. Using EXAFS alone, however, has inherent limitations such as a lack of spatial information of the molecules and rather poor radial resolutions which make it difficult to differentiate two or more bonds with similar distances. Factor analysis by Rossberg, et al., for example, was proven to be an effective method for separating individual species from the mixed ones [1]. Such a method becomes even more powerful if corresponding 3-D structural information can be provided by quantum chemical calculations.

Here, I show two examples in which density functional theory (DFT) calculations are proved to be very helpful for actinide speciation studies. In the first case, Th(IV) hydroxo and sulphato complexes were studied by DFT calculations. A significant decrease in the co-ordination number (CN) was observed as a stepwise hydrolysis reaction of Th^{4+} ion proceeds. The fourth hydrolysis product, $Th(OH)_4^0$, has a reduced CN of 6 and readily forms a dimeric complex via a Th-OH-Th bridging. The oligomerisation makes $Th(OH)_4^0$ to be an unstable aqueous species. In case of sulphate, the CN and the average Th-O distance of $Th(SO_4)_2^0$ remains essentially the same as the Th^{4+} aquo ion. This result is in agreement with the EXAFS study by Hennig, et al. [2].

In the second example, the reduction potential of Pu(VIII)/Pu(VII) couple was studied as the same way as in a recent study [3]. The geometries and the energies of the complexes were calculated at the B3LYP level. The spin-orbit effect for Pu(VII) species was corrected at the CASSCF level. The redox potential of the $Pu^{VIII}O_4(OH)_2^{2-}/Pu^{VII}O_4(OH)_2^{3-}$ couple was found to be as high as ~1.7 V in alkaline solution which indicates that it is difficult to obtain Pu(VIII) in aqueous solution.

References

[1]   Roßberg, A., T. Reich, G. Bernhard, *Anal. Bioanal. Chem.*, 376, 631-638 (2003).

[2]   Hennig, C., K. Schmeide, V. Brendler, H. Moll, S. Tsushima, A.C. Scheinost, *Inorg. Chem.,* 46, 5882-5892 (2007).

[3]   Tsushima, S., U. Wahlgren, I. Grenthe, *J. Phys. Chem. A*, 110, 9175-9182 (2006).

Theoretical studies of covalent interactions in actinide-ligand bonds

P. Yang, E.R. Batista, R.L. Martin, P.J. Hay, D.L. Clark, S.A. Kosimor
Los Alamos National Laboratory
Los Alamos, New Mexico, USA

Abstract

The actinide series marks the emergence of 5f electrons in the valence shell, but the extent of 5f orbital participation in covalent bonding remains a source of controversy. Theoretical and spectroscopic studies indicate that variations in orbital character and metal d-and f-covalency are connected with differences in chemical reactivity. Quantum chemical simulations are able to provide a first-principle description of the metal-ligand bonding. We have applied this analysis to the series of neutral $Cp^*_2MCl_2$ complexes (where M=Ti, Zr, Hf, Th, U) in order to understand the participation of d-f electrons with increasing period. These studies were also conducted as function of the oxidation state of uranium on the octahedral molecules UCl_6^{n-} (n = 1..3), as function of change in the symmetry of the ligands on $UOCl^{5-}$ and $UO_2Cl_4^{2-}$, and as function of the axial ligand on $U(N R_2)_2Cl_4^{2-}$. We will show that time-dependent hybrid density functional theory (TD-DFT) calculations reproduce the experimental ligand K-edge X-ray Absorption Spectra and provide a microscopic picture of the covalent interactions of the actinide-ligand bond, in a quantitative manner.

The structure of polynuclear uranyl sorption complexes at the gibbsite/water interface

A. Rossberg, S. Tsushima, A.C. Scheinost
Forschungszentrum Dresden-Rossendorf, Institute of Radiochemistry, Dresden, Germany
The Rossendorf Beamline at ESRF, Grenoble, France

Abstract

Up to now only occasionally polynuclear sorption complexes of uranyl have been reported. This is undoubtedly surprising, since polynuclear hydrolysis species dominate aqueous uranyl speciation across a wide pH range and at solution concentrations typically used for sorption studies (10^{-6}-10^{-4} M). Using U-L_{III} EXAFS spectroscopy at 15 K, we demonstrate here that polynuclear sorption complexes occur consistently at the gibbsite surface. They were observed across a pH range of 5.5 to 7.5 in equilibrium with atmospheric CO_2, and at pH 8.5 in absence of CO_2.

At these conditions, thermodynamic calculations predict the trimeric $(UO_2)_3(OH)_5^+$ complex to be the predominant hydrolysis species in the aqueous phase. This complex has been investigated recently by EXAFS spectroscopy and DFT calculations [1]. Both methods showed a stoichiometry of $(UO_2)_3O(OH)_3^+$ for this complex with a central oxo bridging, and provided a relatively short U-U distance of 3.8 Å. In contrast, co-ordination numbers and radial distances found for the sorption complex are $2 \times O_{axial}$ @ 1.8 Å, $6 \times O_{equatorial}$ @ 2.4 Å and $1 \times U$ @ 4.2 Å. Both EXAFS shell fitting and a newly developed approach for the calculation of the radial pair distribution function achieved the same result. The U-U distance of 4.2 Å together with the co-ordination number of six for equatorial oxygen are in line with formation of uranyl dimers, where the two uranyl units are linked in edge-sharing configuration. This unusual structure is currently further investigated by DFT calculations.

Reference

[1]   Tsushima, S., A. Rossberg, A. Ikeda, K. Mueller, A.C. Scheinost, *Inorganic Chemistry*, 46, 10819-10826 (2007).

Session V

Facility tools and upcoming techniques

Chair: Bruno Sitaud

A double barrier cell for high temperature EXAFS experiments in molten actinide fluoride mixtures

**Catherine Bessada, Anne-Laure Rollet, Didier Zanghi, Philippe Melin,
Eric Labrude, Séverine Brassamin, Olivier Pauvert, Christophe Thefany**
CEMHTI-CNRS
Orleans, France

Haruaki Matsuura
Research Laboratory for Nuclear Reactors, Tokyo Institute of Technology
Tokyo, Japan
(Associated scientist STUDIUM at the CEMHTI)

Dominique Thiaudière, Bruno Sitaud, Pier Lorenzo Solari
Synchrotron SOLEIL
Gif-sur-Yvette, France

Abstract

Because of their strong reactivity at high temperature (up to 1 500°C for fluorides) towards a great number of materials, and their sensitivity to moisture and oxygen, the experimental analysis of molten fluorides is extremely difficult and requires specific development of the cells currently used in EXAFS experiments. We have built a sample container compatible with the molten fluorides and X-ray spectroscopy requirements. The aim is to strengthen the air tightness and to avoid any possible leakage but with no influence on the signal quality. The dimensions of the heating chamber have been also minimised to be compatible with the limited space available usually on synchrotron beam lines and its geometry is designed for absorption-diffraction measurements at high temperature.

Introduction

The Molten Salt Reactor (MSR) concept has been proposed as one of the possible nuclear reactors in the frame of the Generation IV International Forum. The main originality of such concept is the use of molten salts as both fuel and coolant and a possible online processing. The choice of the salt is of major importance and will influence the efficiency of chemical extraction of the various components (U, Th, minor actinides) prior to lanthanides that poison the neutronic reaction. The knowledge of the different ionic species existing in the melt, in terms of distribution, co-ordination and oxidation is required for a better understanding of the physical and chemical properties of the molten salts proposed for the MSR. Our objective is to describe the local structure in fluoride melts involved in such processes. We use an experimental approach combining two spectroscopy both sensitive to the microstructure of solid or liquid materials: NMR for the light cations (^{23}Na, ^{7}Li) and anions (^{19}F, ^{17}O) and EXAFS for the heaviest such as rare earths, La, Y, Nd, and actinides, thorium and uranium nuclei [1]. These techniques allow to determine the co-ordination, the nature of neighbours and then to identify the complex formation in molten media. Because of their strong reactivity at high temperature (up to 1 500°C for fluorides) towards a great number of materials, and their sensitivity to moisture and oxygen, the experimental analysis of molten fluorides is extremely difficult and requires specific development of the cells currently used. In the case of NMR, a new device was developed in our laboratory (CEMHTI, Orléans, France) a few years ago and was based on a laser heating system associated with a close boron nitride crucible. Thanks to this crucible we are able to follow *in situ* in molten fluoride mixtures, the effect of the temperature or the composition on the speciation in such systems [1-3].

For EXAFS, we have developed for ten years a suitable environment (sample container, heating device, etc.) for lanthanides and actinides fluorides. Because of the manipulation hindrances most of the X-rays studies on high temperature molten salts have dealt with chlorides and bromides but not fluorides. Okamoto, *et al.* used for chloride salts a specific quartz cell with two compartments [4]. The salt is first in the upper part and on heating it flows in the lower compartment in the X-rays pathway. Unfortunately, such cell cannot be used with molten fluorides because they dissolve quartz. For fluorides, Watanabe, *et al.* used pellets made of salt mixed with boron nitride powder [5]. Due to their sensitivity towards atmosphere this conditioning can be not suitable to preserve the sample from oxides or moisture interactions, moreover, for fluorides mixtures, changes on composition can occur because of vaporisation. It can be critical especially in case of actinides containing fluoride mixtures.

In order to overcome these problems, we have developed a new device for high temperature EXAFS experiments in molten lanthanide fluoride salts.

Sample holder

The requirement of the sample container is to be airtight, inert towards molten fluorides and compatible with high temperature up to 1 500°C and X-ray transmission. We have designed a "two plate" cell with a geometry adapted for absorption-diffraction measurements at high temperature. In order to avoid any leakage out of the cell on melting, or evaporation at high temperature, the sample is first packed inside a boron matrix pellet, and then inserted between two pyrolitic boron nitride plates tightly closed with screws. Boron nitride (BN) is one of the few materials able to resist to high temperature (up to 1 800°C under inert atmosphere) and to molten fluoride salts [1,2]. The quality of boron nitride must be free of oxide binders that may chemically react with the molten fluoride at high temperature. For X-rays experiments in transmission mode, we have to insure a weak thickness to limit the BN absorbance, thus the boron nitride ceramics must be solid enough with negligible porosity and high thermal conductivity, which is why we selected the pyrolitic boron nitride (PBN) quality. In order to avoid any interaction with the surrounding atmosphere or problems of volatility, the cell is hermetically closed. The air tightness is realised by a large surface of contact between the two plates of PBN tightly maintained in contact by stainless steel screws or refractory metals depending on the temperature range [6,7]. Because of the high sensitivity of fluorides towards atmosphere, the samples must be prepared in a gloves box under dried argon. The design of the cell implies a small fixed volume, the amount of absorber atoms cannot be regulated in modifying the thickness of the cell as for EXAFS in solution. The proportions of sample and boron nitride powders pressed in the pellet are fixed by the total X-ray absorption

The boron nitride powder in the pellet plays also a role of a porous network in which the molten salt is confined. In consequence, it constitutes a first barrier to salt leakage. This configuration was successfully used in a first experiment on H10 beamline in LURE in 2002. We have managed to record EXAFS spectra over several hours in solid and molten mixtures of lanthanide or actinide fluorides with alkali fluorides without any change in the composition [6].

Figure 1: Cell for EXAFS measurements in molten fluorides

Heating device and chamber

The cell was initially heated using a tubular furnace under vacuum up to 950°C. The large size of the furnace was difficult to adapt with the quite limited space on synchrotron beamlines. Its high thermal inertia was also not compatible with the short experimental time generally available for experiments. Different optimisations were done on the heating device.

The new system was based on two parallel heating elements (5×4 cm) made of a refractory wire (Kanthal®) woven in a ceramic plate [8]. With these elements, the heating and cooling durations were less than 20 minutes instead of 2 hours with the tubular furnace. A specific chamber was designed to confine the system and to control the atmosphere around the cell.

The chamber walls were cooled down using water circulation. The design of the high temperature chamber was made also in agreement with possible measurements coupling X-ray absorption and diffraction. This chamber figures also a second barrier in the case of salt leakage during the experiment (Figure 2). Using these developments, we have recorded the XAFS spectra of ThF_4-LiF up to 700°C at the L_{III} edge of thorium on BM02 beamline in ESRF (Grenoble, France) [1].

Figure 2(a): Vacuum EXAFS chamber   **Figure 2(b): 3-D sight of the heating elements**
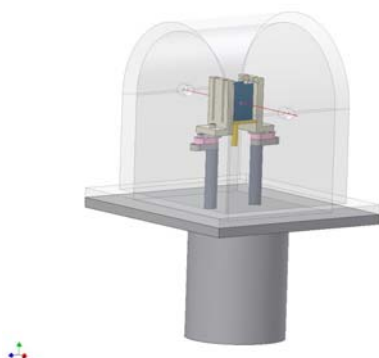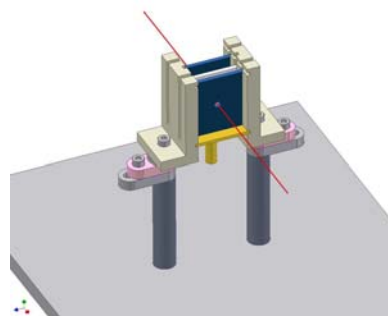
In order to reach higher temperature (up to 1 500°C), the heating system has been further modified and is now based on two heating elements in graphite covered with boron nitride (MCSE, France). A 3 mm diameter hole is drilled in their middle for X-ray pathway. These two heating elements are fixed on two zirconia supports to insure good heat and electric insulation. The sample cell described above fits exactly the space between these two elements. The heating elements are connected in

parallel (to minimise the electric resistance) with kanthal ribbons maintained by molybdenum screws connected with the arrivals of current by platinum wires. This heating system [Figure 2(b)] is inserted in the vacuum chamber and can be placed on the goniometer of a synchrotron's beamline. The atmosphere of the chamber is controlled by a constant helium gas flow (0.2 l/min).

This system has been successfully used for EXAFS measurements in molten mixtures of ZrF_4-LiF at the zirconium K-edge at 17.9 keV on DIFFABS beamline in SOLEIL, France. In parallel, the sample cell has been also used on BL27B beam line, in Photon Factory, KeK in Tsukuba, Japan, using a similar electric furnace. In both cases, BN cells described above were successfully used. They were liquid tight and no leak of the molten fluorides was observed during the experiments.

EXAFS measurements at the zirconium K-edge in fluoride mixtures

To compensate for the glitches resulting from the Si(111) monochromator, two thin Si photodiodes (10 μm) for I_0 and I_1 (transmission mode) were used. The linear coefficient of X-ray absorption was made on an energy range from 17.8 keV to 18.8 keV separated in three areas (17.8-17.9 keV; 17.9-18.5 keV; 18.5-18.8 keV) for minimising the time of acquisition. By using a step of 4 eV/s for the first and the third zones, and a step of 2 eV/s for the second zone, the collection time of one scan in energy is limited to 20 minutes. In order to have a good signal to noise ratio on the absorption data, we performed four scans in energy for the liquid phase and only two for the solid phases.

Several compositions from 0 to 50 molar % of ZrF_4 were studied. For each composition, EXAFS oscillations were recorded at room temperature (before and after heating) and at high temperature (liquid phase). Figure 3 shows the EXAFS oscillations of different ZrF_4-LiF compositions and the module of the Fourier transform corresponding. The EXAFS data were extracted by using Athena software [9]. After normalisation of the absorption coefficient by standard way, the post-edge background was extracted from experimental data by using the Autobk algorithm [10]. This background-removal method consists in subtracting the best spline which eliminates the non-structural information in the low frequency components of the Fourier transform of the data.

Figure 3: EXAFS oscillations of different ZrF_4-LiF compositions in the liquid phase

In insert, module of the Fourier transforms corresponding
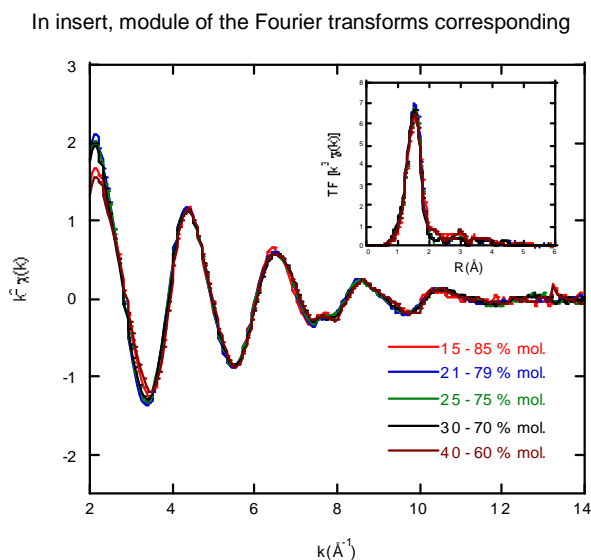
The spline used to approximate the background is a fourth-order polynomial spline with knots that are equally spaced in k space, and at which one degree of freedom in the spline is allowed. For the different ZrF_4-LiF compositions, the EXAFS oscillations in the liquid phase do not change when the ZrF_4 amount increases. Then the local structure around the zirconium cations does not vary with the content in ZrF_4 on this domain of composition. This preliminary result is in agreement with the results obtained by [91]Zr nuclear magnetic resonance (NMR) measurements.

Figure 4 presents the evolution of the EXAFS signal versus the temperature for the composition ZrF_4-LiF (30-70% mol.). The good agreement between the signal obtained at room temperature (before heating) and the theoretical signal calculated by the Feff code indicates that no transformation of ZrF_4 beta phase occurred. Contrary to the signal of the solid, the signal of the liquid phase is less structured. The important damping out of the signal is due to the increase of the disorder induced by the thermal effect. The shift indicates a contraction of the distances between the absorber atom (Zr) and its closer neighbours (F). This effect shows itself on the Fourier transform of the EXAFS signal by a decrease of the amplitude of the first peak and a shift towards the weak values of R (Figure 6). The absence of peaks at higher distance signifies the absence of a long distance order. During the cooling, as the temperature decreases, the amplitude of the first peak increases. Therefore, the EXAFS oscillations at room temperature after cooling are different from the initial EXAFS oscillation of ZrF_4 at room temperature. According to the phase diagram, this difference is interpreted by the formation of a mixture of compounds Li_4ZrF_8 and Li_2ZrF_6.

Figure 4: EXAFS signal and its Fourier transform vs. temperature for ZrF_4-LiF (30-70% mol.)
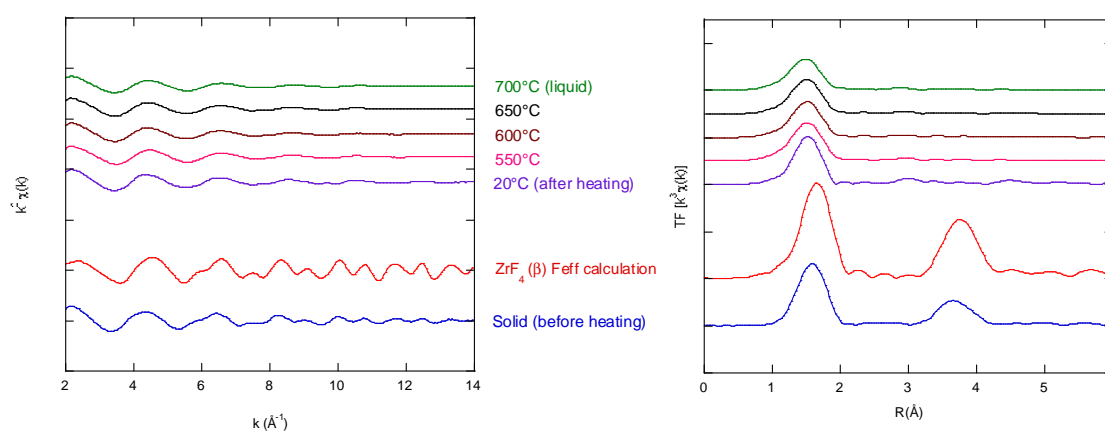
Conclusion

The cell developed in our laboratory is well adapted for EXAFS measurements in molten fluorides salts. Its liquid tightness allows us to work at high temperature on the liquid phase for long acquisition times. For radioactive materials (U, Pu….), because of the additional risk linked to radioactivity, we will adapt the existing cell with an additional barrier in order to fulfil all the safety requirements for such kind of experiments. The aim is to strengthen the air tightness and to escape any possible leakage but with no influence on the signal quality. This development will be tested on BL27B in KEK and MARS on SOLEIL beam lines, both dedicated to radioactive materials.

References

[1]   Bessada, C., A. Rakhmatullin, A-L. Rollet, D. Zanghi, *J. Nucl.Mater.*, 360, 43 (2007).

[2]   Lacassagne, V., C. Bessada, P. Florian, S.B. Bouvet, J-P. Ollivier, C. Coutures, D. Massiot, *J. Phys. Chem. B*, 106, 1862 (2002).

[3]   Bessada, C., A. Rakhmatullin, A-L. Rollet, D. Zanghi, *J. Fluor. Chem.,* forthcoming (2008).

[4]   Okamoto, Y., M. Akabori, H. Motohashi, H. Shiwaku, T. Ogawa, *J. Synchrotron Rad.,* 8, 1191 (2001).

[5]   Watanabe, S., A.K. Adya, Y. Okamoto, N. Umesaki, T. Homma, H. Deguchi, M. Horiuchi, Y. Yamamoto, S. Noguchi, K. Takase, A. Kajinami, T. Sakamoto, M. Hatcho, N. Kitamura, H. Akatsuka, H. Matsuura, *J. Alloys and Compounds*, 408, 71 (2006).

[6]   Rollet, A.L., C. Bessada, Y. Auger, P. Melin, M. Gailhanou, D. Thiaudière, *Nucl. Instr. and Meth. B,* 226, 447 (2004).

[7]   Rollet, A.L., C. Bessada, A. Rakhmatullin, Y. Auger, P. Melin, M. Gailhanou, D. Thiaudiere, *C. R. Chimie*, 7 (12), 1135 (2004).

[8]   Rousseau, B., D. De Barros, J. La Manna, F. Weiss, G. Duneau, P. Odier, D. De Sousa Meneses, Y. Auger, P. Melin, P. Echegut, *Rev. Sci. Instrum.*, 75 (9), 2884 (2004).

[9]   Ravel, B., M. Newville, *J. Synchrotron Rad.,* 12 (4), 537 (2005).

[10]   Newville, M., P. Livins, Y. Yacobi, J.J. Rehr, E.A. Stern, *Phys. Rev. B*, 47, 14126 (1993).

Advances on the MARS beamline at SOLEIL

Pier Lorenzo Solari,[1] **Hervé Hermange,**[1] **Stéphane Lequien,**[2] **Sandrine Schlutig,**[1] **Bruno Sitaud**[1]
[1]Synchrotron SOLEIL, Gif-sur-Yvette, France
[2]Laboratoire Pierre Süe, CEA-CNRS, CEA Saclay, Gif-sur-Yvette, France

Abstract

The Multi-analyses on Radioactive Samples (MARS) beamline is under commissioning at the synchrotron SOLEIL. The first experimental end station of the MARS beamline is planned to be operational during the second semester of 2009 for a selection of radioactive samples with an activity below the exemption limit in a first time and then, for all radionuclides with higher activities according to the French official authorisations which have to be obtained (licensing expected by the end of 2010).

This beamline which has been built thanks to a close partnership with CEA, has been optimised for performing X-ray characterisations (diffraction, scattering, absorption spectroscopy, fluorescence imaging) on a very large variety of radioactive elements (α, β, γ and neutron emitters). The activity per sample should be authorised up to 18.5 GBq. The sample dose rates must be compatible to the levels authorised inside the beamline (the so-called "yellow area" in the controlled zone for radiation protection) and outside the beamline (public area). The future of this new beamline is clearly to get an extension of the possibilities for chemical and physical analyses on radioactive samples towards higher activities without affecting the quality of data. Hence, for example, investigations of spent and non-irradiated fuels as well as fuel reprocessing, transmutation targets and vitrified wastes will be possible on this beamline.

In this contribution we give an overview on the progresses that have been made in the last two years in the design and installation of the beamline, as well as on the future programmes foreseen.

Introduction

MARS (Multi-Analyses on Radioactive Samples) beamline is a hard X-ray beamline dedicated to the study of radionuclides (RN), built at the third generation synchrotron SOLEIL, the French facility located at Saint-Aubin (near Paris). The beamline, which seats on the bending magnet port D03-1 of the storage ring, has been designed to provide X-rays in the energy range of 3.5 keV to 35 keV. This one allows to encompass M and L absorption edges of actinides, as well as K edges of transition metals (that are present in alloys and fuel claddings) up to heavy halogens, rare gases and alkalis (fission products in nuclear fuels).

The MARS project aims to extend the possibilities of synchrotron based X-ray characterisations towards a wider variety of radioactive elements (α, β, γ and n emitters) than what is currently available at other facilities. The infrastructure has been then optimised in order to carry out analyses on materials with activities up to 18.5 GBq per sample. So, today, more than 70 different elements and more than 350 different isotopes have been proposed for studies on the beamline by the involved user community.

Advances on the infrastructure

Due to the particularity of the samples to be studied and the high activities foreseen, the MARS beamline is characterised by a specific innovative infrastructure. Indeed, apart from the standard lead shielded optics hutch and the main control room, special infrastructural requirements are necessary to guarantee safe activities with RN samples for the remainder central part (Figure 1) of the beamline [2].

Figure 1: Top view of the central part of the MARS beamline showing the different hutches, several equipments and the pipe network of the ventilation system
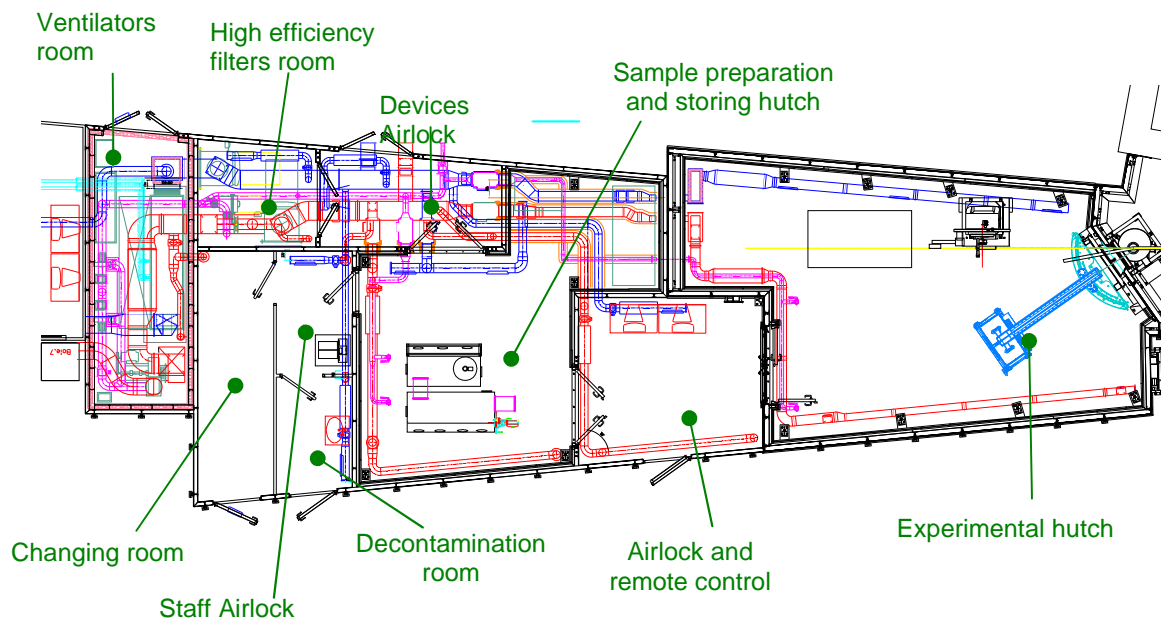
The main beamline external infrastructure was built between August and December 2006. The two lead shielded hutches (optics and experimental), the several metallic rooms of the area under authorisation, as well as the control room were concerned. The internal infrastructure of the beamline was settled up between January and April 2007 except for the experimental hutch which took place between February and October 2008. Like in nuclear industry, the ventilation system is particularly important to dynamically confine the beamline in case of a contamination incident. Recently, this latter was successfully tested inside the central part of the beamline. The gradient of negative pressures from the synchrotron hall to the experimental hutch as well as the associated levels of air renewals were successfully achieved demonstrating thus the suitable air tightness of the infrastructure which

is mandatory for all duties with contaminant samples. Typically, pressures of around -80 Pa with five complete volume changes of air per hour were obtained inside both preparation and experimental hutches.

The last task which is planned for the first semester 2009 is the installation of the fire detection system network which must be interlocked with the ventilation controller. Indeed, in case of a fire detection inside or near around the beamline, the ventilator inlet has to be stopped, the fire shutters inserted inside the air tube will be closed as well as the fire-resistant doors and the fire shutter in front of the Be windows of the experimental hutch.

Advances on optical elements

The arrangement of the different elements in the optics hutch is based on an original scheme which permits to have two alternative optical configurations (monochromatic or dispersive) depending on the nature of experiments to be performed. The X-ray optical system of this beamline is then based on the use of a collimator mirror (M1) upstream of a double crystal monochromator (DCM) with a sagittal focusing bender, a vertical focusing mirror (M2) and a single bent crystal monochromator (SCM). To switch from the monochromatic mode to the dispersive mode, the DCM is moved down into beam and the height of the M2 is reduced to a value depending on the glancing angle of both mirrors. Details on the optical configurations, as well as on the main optical elements were given earlier [1,2].

Before the installation of the optical elements, which started during summer 2007, a successful radioprotection test with white beam in air was realised to qualify the shielding of the hutch (Figure 2). The MARS beamline was thus the thirteenth beamline to receive its first photons from the storage ring of SOLEIL. Subsequently, all the optical elements have been installed and aligned by the end of 2007 except the single crystal monochromator for dispersive studies.

Figure 2: First beam observed in the air just after the front end during the radioprotection test
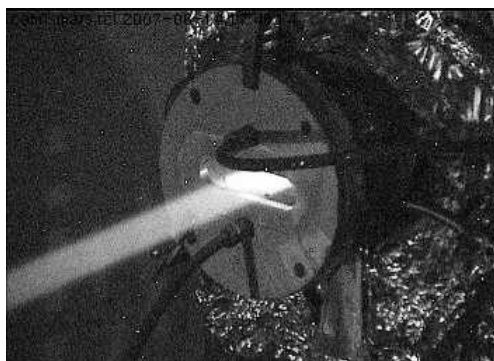
Mirrors M1 and M2

Both mirrors and benders were designed and manufactured by the SESO company, and their integration inside high vacuum vessels equipped with several motorised stages was done by the IRELEC firm. Prior their installation, in-house optical tests showed that the slope errors for M1 and M2 are equal to 1.5 µrad and 1.0 µrad RMS respectively and the roughness of both mirrors is around 0.25 nm (averaged values obtained along the 1 200 mm by 110 mm active surface). Because of the heat load and the dispersive configuration, both mirrors are water-cooled by copper blades inserted into grooves. The contact between the mirror and the blade is achieved with liquid gallium eutectic (Figure 3).

In order to optimise the flux on the sample whatever the energy range, the active surface of each Si mirror is composed of two strips: *i)* a 60 mm width uncoated strip; *ii)* a 50 mm width platinum (Pt) coating strip with a thickness of 60 nm.

Figure 3: Pictures taken during the installation of mirrors

Left: Mirror M1 with its U-bender on the top; Right: Mirror M2 with its active surface upstream on which
both strips and the cooling system are clearly visible (Si strip on the left and Pt strip on the right)
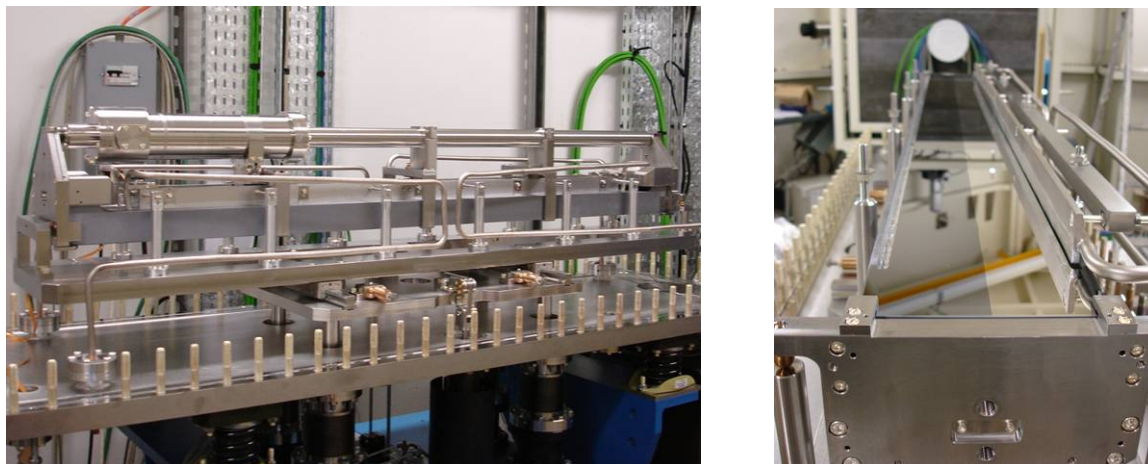
Monochromator DCM

The double crystal monochromator (DCM) has been fully subcontracted to Oxford Danfysik (Figure 4). This DCM is equipped with 14 independent motorised stages in order to optimise its alignment and then to assure a fixed exit beam over the entire energy range. Optical alignment of the crystal Bragg axes was done with a particular attention because of its criticalness. The original feature of this DCM, designed for relatively large beams (H $\times$ V = 30 mm $\times$ 5 mm) delivered by the bending magnet, is its ability to exchange crystal sets under vacuum, *i.e.* from Si(111) crystals to Si(220) crystals and vice versa. By this way, such operation including realignment can be done in less than 30 minutes. This is very useful either when several ranges of energies have to be explored during a same experiment or an increase of energy resolution or on the contrary of X-ray flux is needed.

Figure 4: Pictures taken during the installation of the double crystal monochromator

Left: The complete crystal cage fixed on the Bragg axis
Right: Focus on the crystals along the beam axis
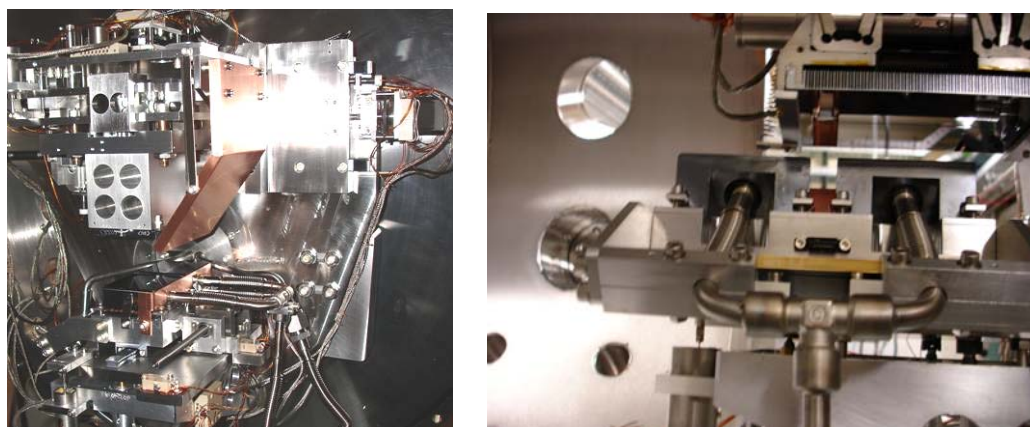
The DCM is also equipped with a bender device on which the two second crystals are mounted to perform the horizontal dynamic focusing of the beam on the sample. We have currently limited our tests at a minimum radius of curvature value of 1.5 m for the Si(220) crystal corresponding to a minimum value of 1.4 m for the Si(111).

Advances on experimental stations

Three end stations will be progressively installed in the experimental hutch. Two of them, respectively the high resolution X-ray diffraction and the standard X-ray spectroscopy end stations are located on the monochromatic branch of the beamline and are preceded by a beam conditioning stage (with attenuators and slits) (see Figure 5). The third station is expected to be installed in 2009-2010 along the dispersive branch.

Figure 5: Side view of both experimental stations using the monochromatic branch of the beamline (the beam comes from the right side)

Left: Optical elevating table for standard X-ray spectroscopy
Right: Two-circle diffractometer for high resolution X-ray diffraction and beam conditioning stage
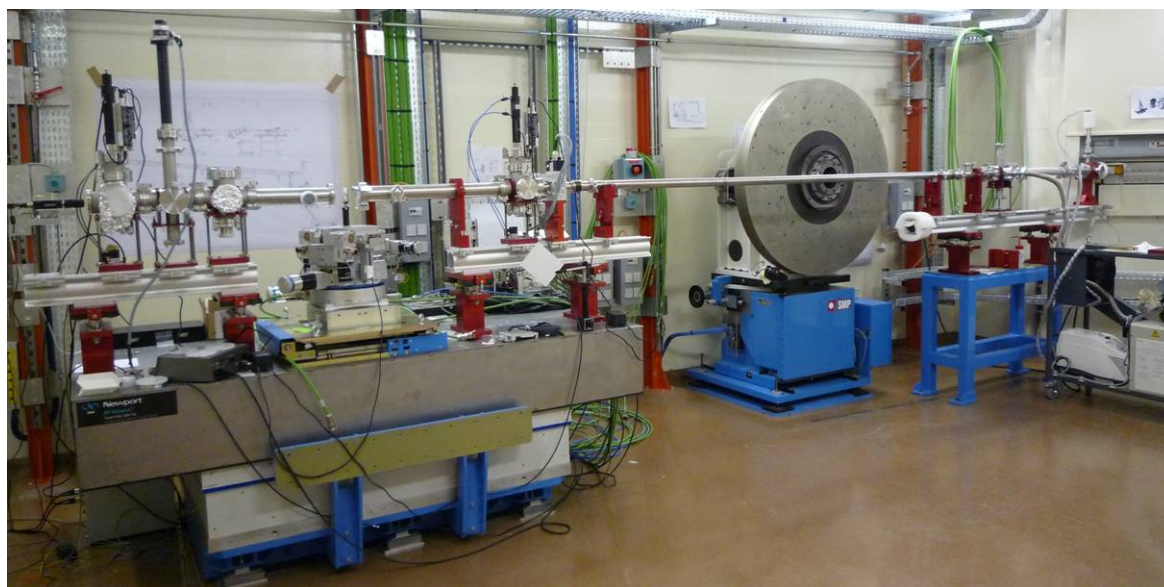
High resolution powder diffraction station

The high-resolution diffraction station mainly consists of a robust two-circle diffractometer [2] which has been installed 23 m downstream the X-ray source. An inner sample-holder goniometer (Khi and Phi circles and x,y,z stages) and a multi-crystal analyser detection system have also been designed and should be added to the diffractometer before the end of 2009. Improvements in the design and characteristics of these latter two equipments have been made thanks to a large implication and participation of CEA.

Absorption station

The standard X-ray absorption spectroscopy station, which will also permit X-ray fluorescence and X-ray diffraction measurements, consists of a highly rigid experimental table with a honeycomb breadboard support (provided by Newport Company) and a motorised base with micrometric vertical elevation (manufactured by AZ-SYSTEMES Company). Samples will be positioned in the central part of the board at 26 m from the X-ray source. At present two different sample holders are foreseen: a special multi-axis motorised stage (manufactured by AZ-SYSTEMES) and a He flow cryostat to allow measurement down to T = 10 K (manufactured by Air Liquide), described previously [2]. The different intensity monitors, experimental slits (provided by JJ X-ray) and reference sample-holder are supported on two aluminium rails which are positioned on either side of the sample (Figure 5). Apart from intensity monitors for transmission XAS detection (in-house device based on photodiodes), several different detection systems are being progressively installed on this station: an imaging plate scanner detector (MAR345 from Marresearch Gmbh) has been purchased for transmission X-ray

diffraction; a multi-element high germanium detector as well as a silicon drift detector are foreseen for X-ray fluorescence measurements; an in-house X-ray camera has been manufactured by SOLEIL's Detectors Group to monitor the X-ray beam.

Moreover, it is planned to install a crystal analyser spectrometer (project in collaboration with the French CRG beamline Fame at ESRF, Grenoble) in order to perform X-ray fluorescence measurements with a high energy resolution. This is particularly important for studies on samples with high natural radioactive emission levels.

Finally, it is also foreseen to mount on this experimental station, a Kirkpatrick-Baez mirrors optics system to achieve focusing into a spot size of micrometric range (in-house upgrade of a system provided by CEA). The present calculations envisage a spot size of $9 \times 9~\mu m^2$ with an estimated flux of 5×10^{10} phot/s at 10 keV and 10^{10} phot/s at 20 keV (the upper limit of the energy range with the KB optics) with a current of 500 mA. This will extend the performances of the beamline towards the micrometric scale characterisations by XRF mapping as well as XAS and possibly XRD.

First results from the commissioning

Since September 2008, the MARS beamline commissioning is progressing, starting from the optics up to the end stations. Currently, only the absorption station is considered. Thanks to the precise pre-alignment of the optics vessels (M1, DCM, M2) done by the Alignment Group of SOLEIL, a monochromatic beam was observed relatively rapidly at the end station. Optimisation of the alignment has been undertaken step by step at increasing energies. A perfect alignment of optical components taking into account corrections due to several mechanics or optics imperfections correspond certainly to one of the most crucial commissioning tasks for a beamline. The aim is of course to obtain results as close as possible as those predicted from ray-tracing calculations (flux, beam sizes). To illustrate the commissioning, first results obtained at 17 keV, energy with a particular interest for actinide elements, are presented. Si(220) crystals and Pt mirror strips were set up while measurements were carried out with an electron beam current around 220 mA. The first images of the focused beam are displayed in Figure 6.

Figure 6: First images of the focus beam at 17 keV showing the effect of the horizontal gap of the primary slits (left with a gap of 20 mm and right with a gap of 3 mm)
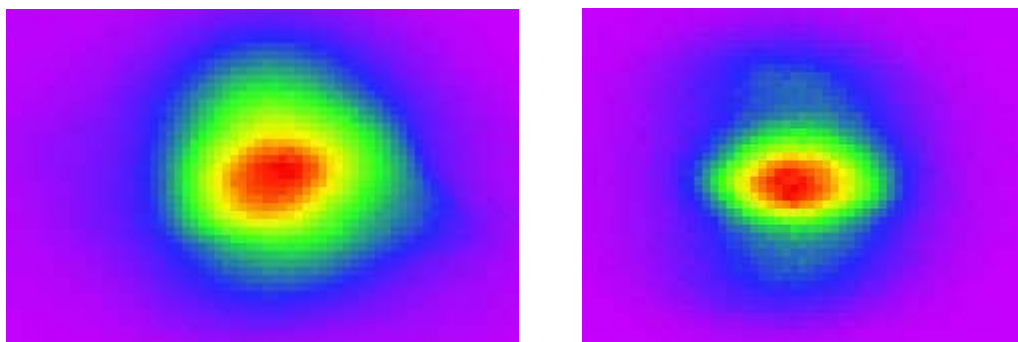
The first XAS test measurements in transmission mode have been conducted using two thin Si photodiodes directly inserted in the X-ray beam. XANES and EXAFS spectra were recorded from a pure yttrium foil (see Figure 7). Only a shift of 14 eV was observed between the reference value for the K-edge and the alignment position of the DCM. The quality of the spectra (noise/signal circa 10^{-3}) will be improved from a further development of the detectors which is already foreseen.

Replacing the second photodiode after the sample (I1) by the MAR345 detector, first transmission diffraction spectra were also recorded with different values of the gaps of primary slits. With the lower value of 3 mm $\times$ 1.5 mm (H $\times$ V), well defined patterns were obtained after only 10 s of exposure time (Figure 8). These first tests demonstrated that complementary tungsten carbide slits followed by a cleaning pinhole setting just before the sample are necessary to reach beam sizes down to 100 $\mu m \times$ 100 μm (global full width *i.e.* 4 σ).

Figure 7: First XAS spectrum obtained on a yttrium foil (left) and the corresponding k³-weighted EXAFS data (main oscillation coming from the Y-Y scattering contribution at ~3.6 Å)
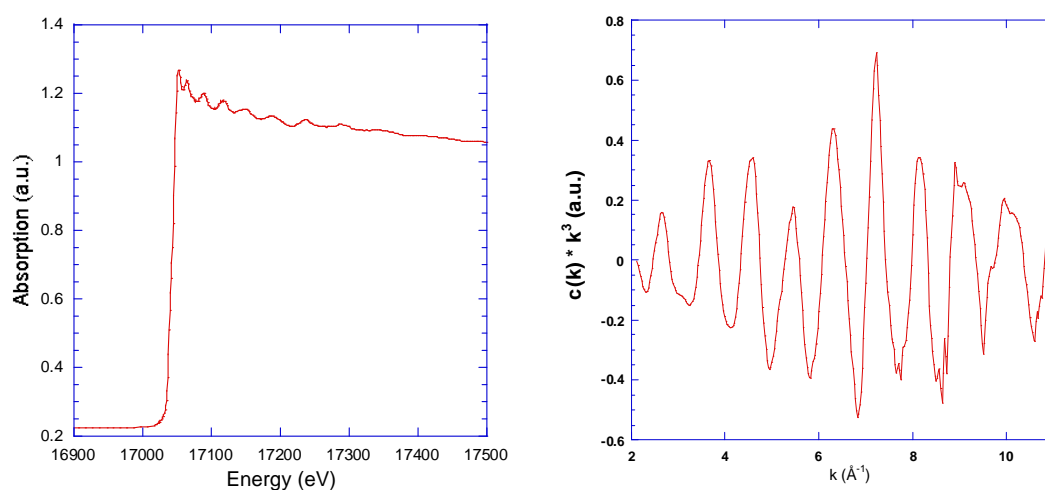
Figure 8: First two-dimensional X-ray diffraction patterns of LaB_6 (left) and pure yttrium (right) collected with a sample to detector distance of 290 mm and an energy of 17 keV
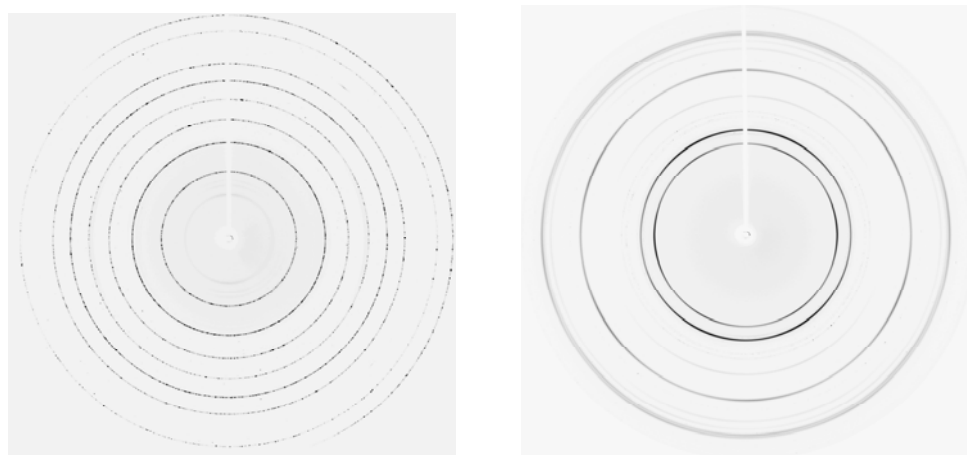
Conclusion and perspectives

The main phase of installation of the infrastructure and equipment of the MARS beamline has now been completed. Commissioning of the elements that have been installed are now in progress allowing then first test experiments.

During the next year, the whole energy range of the beamline will be explored using particularly the DCM to optimise the settings for standard XAS measurements. In addition, it is planned to complete the installation of the high resolution diffraction station with the sample-holder goniometer and detection system. Concurrently, first experiments with expert users will start on non-radioactive samples at room temperature (also samples with an activity below the exemption limit will be allowed). To go further, different sample environment like cryostat, furnace or high pressure cell will be tested in connexion with the available techniques, that is, transmission X-ray diffraction, XAS in transmission and fluorescence.

Experiments with radioactive samples (above the exemption limit) will take place as soon as the French government authorisation to receive radioactive samples is be given (currently, licensing is expected by the end of 2010).

References

[1]   Sitaud, B., S. Lequien, *Speciation Techniques and Facilities for Radioactive Materials at Synchrotron Light Sources, Workshop Proceedings*, Berkeley, CA, USA, NEA No. 6046, pp. 71-79 (2006).

[2]   Sitaud, B., S. Lequien, H. Hermange, P.L. Solari, *Speciation Techniques and Facilities for Radioactive Materials at Synchrotron Light Sources, Workshop Proceedings*, Karlsruhe, Germany, NEA No. 6288, pp. 151-157 (2007).

The INE-Beamline for actinide research at ANKA

Boris Brendebach, Kathy Dardenne, Melissa A. Denecke, X. Liu, Jörg Rothe, Tonya Vitova
Forschungszentrum Karlsruhe, Institut für Nukleare Entsorgung
Karlsruhe, Germany

Abstract

The INE-Beamline for actinide research at the synchrotron source ANKA commenced regular user operation in October 2005. The beamline was designed, built and is operated by the Institut für Nukleare Entsorgung (INE) at the Forschungszentrum Karlsruhe (FZK), Germany. Experiments on radioactive samples with activities up to 10^6 times the limit of exemption at X-ray energies from around 2.1 keV (P K-edge) to 25 keV (Pd K-edge) are possible. The close proximity of the beamline to INE's radiochemical laboratories with their spectroscopic, analytical and microscopic equipment is unique in Europe. The beamline design follows a modular concept, which allows implementation of a variety of methods. Recent instrumental developments at the INE-Beamline are presented: first measurements using a microfocus option, implementation of a fully digital read-out of the fluorescence detectors and additional sample environments, like a liquid N_2 cryostat and an inert gas cell for air sensitive samples. Future upgrades, like realising confocal irradiation-detection geometry, adapting and testing a high resolution energy dispersive fluorescence detector (HRXES), are planned.

Introduction

The Institut für Nukleare Entsorgung (INE) at the Forschungszentrum Karlsruhe (FZK) has constructed and commissioned a beamline dedicated to actinide research at the synchrotron source Ångströmquelle Karlsruhe (ANKA). Official operation of the INE-Beamline began on 1 October 2005. The symbiosis of the INE-Beamline at the ANKA accelerator and INE radiochemical laboratories, which are both located within the same FZK site, is unique in Europe. Samples can be prepared and then characterised and analysed before and following synchrotron based investigations at the INE-Beamline using the state-of-the-art spectroscopic, analytical, microscopic and structural methods available at INE laboratories.

The major research and development activities at INE concern high level nuclear waste disposal safety. Speciation investigations of the actinide elements are a major topic as they mainly contribute to the long-term radiotoxicity of high level nuclear waste. Actinide speciation in nuclear waste disposal is manifold and the systems of interest heterogeneous, so that the major goal in INE-Beamline design and development is to provide a multi-purpose station, where a number of methods are possible, including standard, surface sensitive and spatially resolved techniques. The INE-Beamline is optimised for spectroscopic X-ray methods, X-ray absorption fine structure (XAFS), X-ray fluorescence (XRF) and combined XAFS and X-ray diffraction (XRD). Scientific investigations related to nuclear waste disposal safety often involve reactions of actinides in the hydro- and geosphere at interfaces and junctions. For this reason emphasis at the INE-Beamline is placed on surface sensitive techniques based on grazing incidence (GI) geometry such as GI-XAFS. In addition, spatial resolution in the micrometer range is desirable to investigate heterogeneous natural systems. Recently, such an option has been implemented at the INE-Beamline.

Beamline design and recent developments

A schematic drawing of the INE-Beamline is presented in Figure 1. Details of the optics design are published elsewhere [1,2]. Recent beamline improvements and technical upgrades installed include both hardware and software, which are primarily driven by in-house and external users' needs. For example, ACTINET, the European Network of Excellence for Actinide Science, projects with expressed scientific intentions partially financed XIA digital electronics for INE's Canberra LE-Ge fluorescence detector and a new Vortex silicon drift detector.

Figure 1: Schematic drawing of the INE-Beamline for actinide research at ANKA
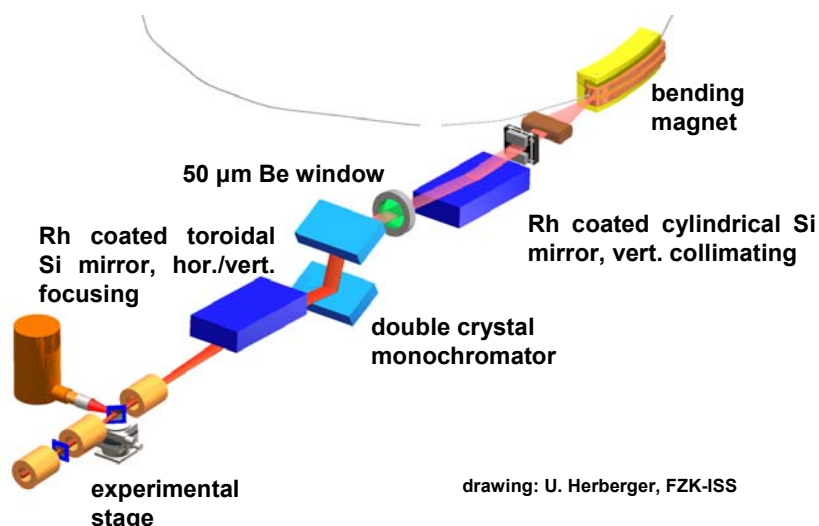
The following discussion of hardware and software upgrades at the INE-Beamline in 2007/08 are arranged according to the beamline's beam path, starting with components in the optical hutch, followed by those in the experimental hutch and finishing with the sample environment.

Beamline optics

To increase flux at low energies (S and P K edges), the 100 μm Be window separating the storage ring vacuum from the double-crystal monochromator was replaced by a 50 μm window. The beamline design is such that one can theoretically reach energies down to the Si K-edge (1.8 keV) using a pair of InSb(111) monochromator crystals. First tests at this energy have already been performed.

An additional crystal alignment stage for the second monochromator crystal, allowing the fine tuning of the roll adjustment, was installed and setup in co-operation with the Physical Institute, Bonn University, Germany. This upgrade allows precise beam adjustment, which facilitates optimisation of the primary beam focus from the second mirror. Optimisation of the primary focus is necessary for successful installation of a secondary focusing optic for achieving beam spots in the micrometer range (μ-focus). The first step towards a μ-focus at the INE-Beamline was performed with focusing in one dimension (vertical) using planar compound refractive lens (CRL) arrays fabricated by the Institute for Microstructure Technology (FZK-IMT) (Figure 2). The CRL serves as a virtual slit and was first applied in surface specific grazing incidence (GI-) XAFS investigations of the corrosion layer on a UO_2 pellet [3]. The advantage of using a virtual slit over a conventional slit system is to increase the photon flux. In our case a gain factor of approximately two was achieved.

Figure 2: (a) One-dimensional CRL (FZK-IMT) are used as a virtual slit
(b) The CRL array is positioned on a hexapod (PI, Germany)
(c) The primary beam is focused to around 45 μm in the vertical direction
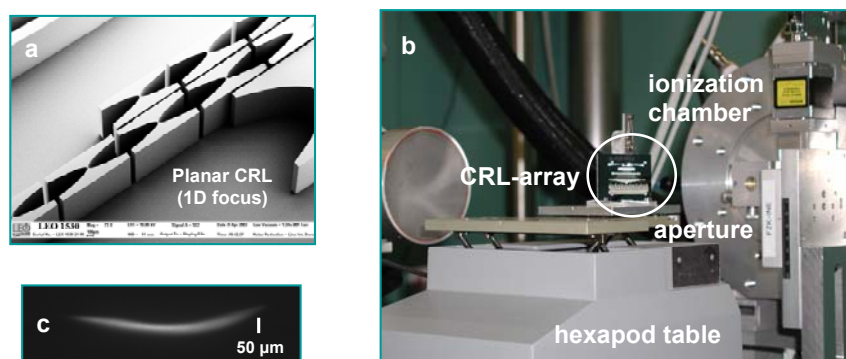
Using a polycapillary lens, loaned from HASYLAB, we successfully focused the primary beam with a spot size of approximately 500 μm in diameter down to a focal spot of around 30 μm (Figure 3). In a first test experiment at the INE-Beamline, the U distribution over a 2×1 mm² area in a uranium-rich clay sample originating from autunian shales in the Permian Lodève Basin (France) was recorded. μ-XANES measured on U-high concentrated areas revealed the uranium to be in the tetravalent state [4].

Figure 3: (a) μ-focus set-up using a polycapillary (HASYLAB loan). (b) The primary beam is
focused down to a beam spot of around 30 μm, as can be seen from the resolution of the
SESO X-ray beam position monitor used. The pixels with a width of 7 μm are clearly visible.
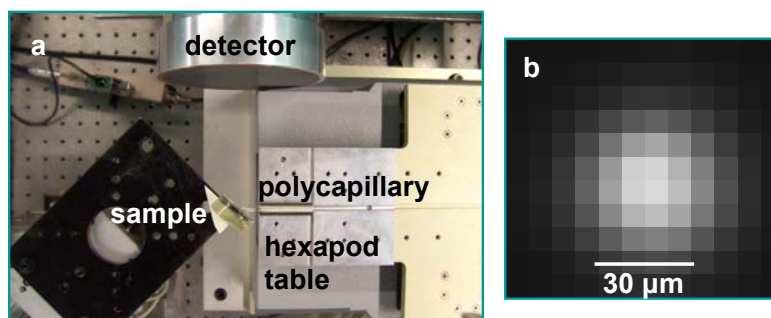
Detector upgrades

The most important upgrade in the X-ray detection system was the replacement of the Canberra LE-Ge five pixel fluorescence detector analogue read-out by a fully digital XIA system. This upgrade was performed in co-operation with the Institute for Synchrotron Radiation (FZK-ISS) and 50% funded by ACTINET. The digital electronics permits storing the complete fluorescence spectrum in digitised form for single scans (as opposed to storing windowed counts in selected regions of interest = single channel analyser). This will enable scanning μ-XRF to, *e.g.* determine elemental distributions through multi-line peak fitting of the digital MCA data recorded while scanning a sample area. IGOR PRO visualisation software already in use at other ANKA beamlines for the digital electronics has also been implemented at the INE-Beamline (Figure 4).

Figure 4: Visualisation of the measured data using the IGOR PRO software
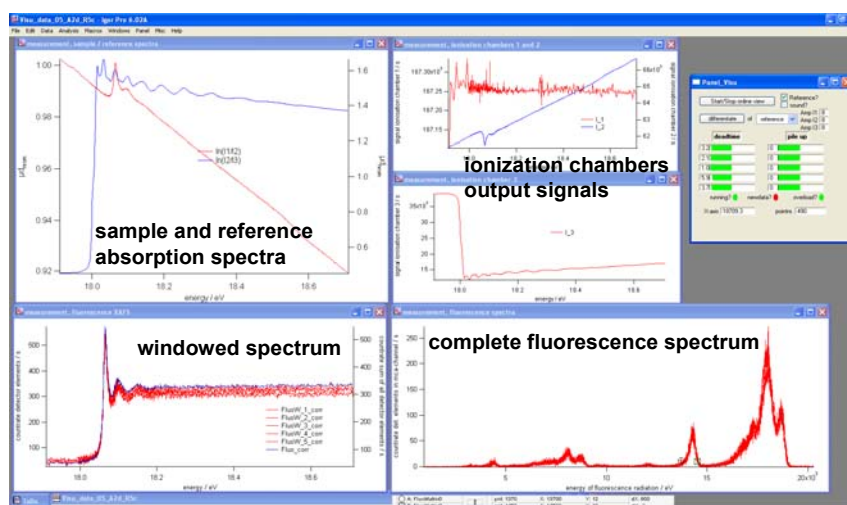
Recording XAFS data at lower concentrations was crucial for in-house investigations, where Th oxy-hydroxide polynuclear species identified by nano-electrospray mass-spectrometry as a function of the pH value and Th total concentration [5] was corroborated by XAFS results. The XIA electronics also exhibits a lower noise level than the previous analogue read-out, which allowed for the first time measurement of a 0.7 mM Th solution with good statistics (Figure 5).

Figure 5: Th L3-edge XAFS spectrum of a 0.7 mM Th solution

(a) Fourier Transform with fit result as symbols and (b) corresponding Fourier filtered EXAFS $\chi(k)$
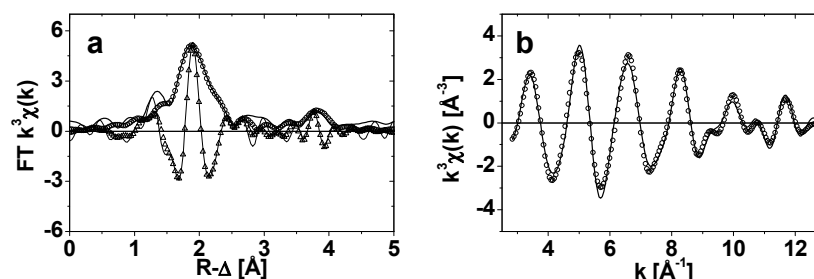
Iron, calcium and lanthanum distribution maps on a sediment thin-section from the nuclear waste repository Schacht Konrad, Germany, were recorded with a spatial resolution of approximately 30×30 μm^2 using our new Vortex silicon drift detector (Figure 6). Light areas in the distribution maps represent regions with a high concentration of the respective element. A positive correlation of Fe and La is visible, whereas the Ca signal is originating from the host material around the iron nodules.

Figure 6: (a) μ-XRF setup using a polycapillary as secondary focusing optic and a Vortex silicon drift detector. (b) The optical microscope image shows the area of the sample scanned. (c) – (e) show iron, lanthanum and calcium distribution maps (step size 30 μm) recorded at 18 keV excitation energy.

(b) microscope image

(c) Fe Kα

(d) La Lα

(e) Ca Kα
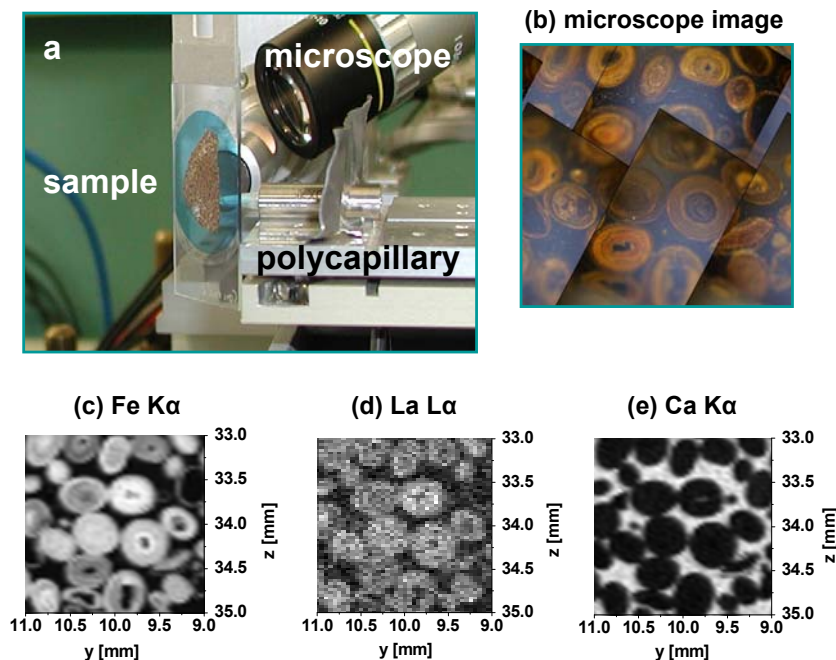
Sample environments

An Oxford Instruments (OptistatDN) liquid N_2 cryostat, financed through an ACTINET project with ITU, was commissioned and first active measurements were performed. The low temperature enhances the EXAFS signal by dampening atomic thermal vibrations. For example, in the U L3 EXAFS of a pentavalent uranyl co-ordination polymer (ACTINET project between INE, CEA-Grenoble and the University of Manchester), pronounced oscillations are still visible in the EXAFS up to k = 20 Å^{-1} (Figure 7).

Figure 7: (a) Cryostat (Oxford Instruments) mounted onto the sample stage. (b) EXAFS χ(k) measured of a (c) pentavalent uranyl co-ordination polymer is still visible up to k = 20 Å^{-1}.
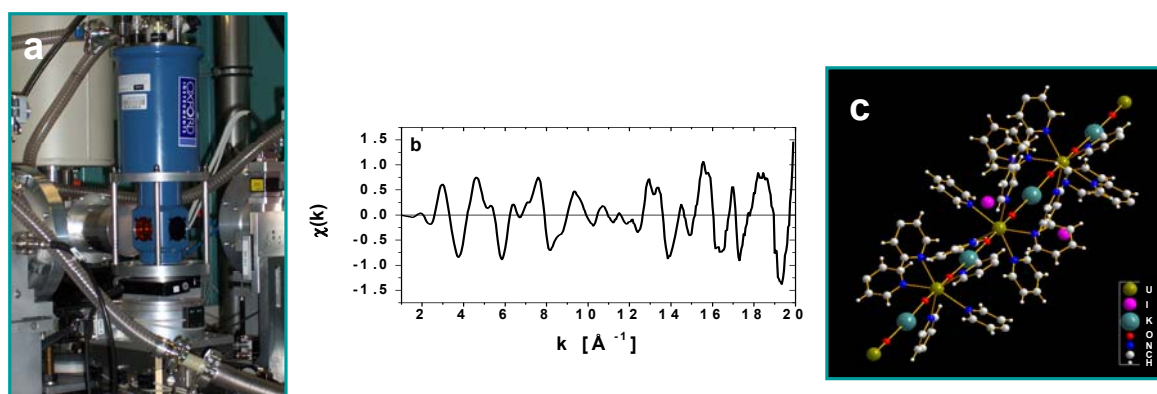
Following first measurements on U(III) samples in 2006 [6] using a prototype inert gas sample environment, an inert gas sample cell with standard INE sample holder design was constructed and successfully tested on U(III), Np(III) and Pu(III) containing systems linked to both ACTINET and in-house projects (Figure 8). The inert gas holder is loaded with samples inside inert gas glove boxes in INE's active laboratories, transported under Ar to the beamline and connected to an appropriate gas supply (Ar, He, N) at the beamline to guarantee constant inert gas flow. For example, using this inert gas holder U(III), Np(III) and Pu(III) samples were observed to remain stable over a period of several hours.

**Figure 8: (a) Inert gas sample holder. (b) XANES spectra of
Np(III) solution samples show no oxidation for several hours.**
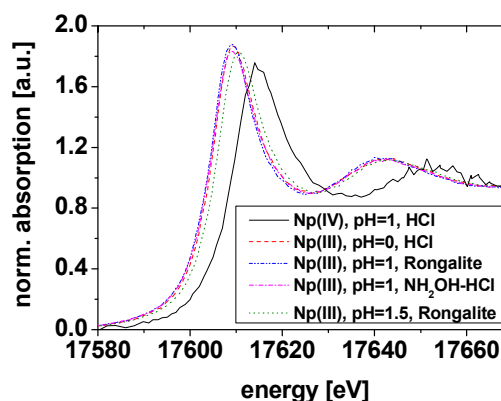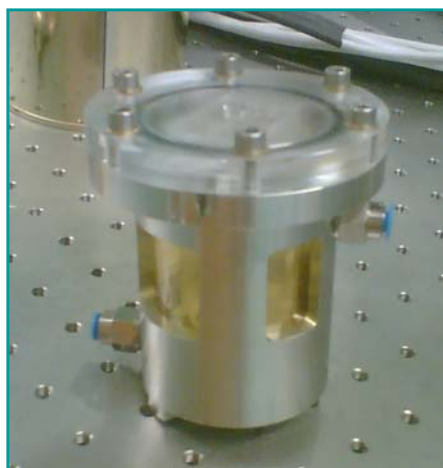
Planned upgrades

Instrumentation development and upgrades planned at the INE-Beamline are related to lowering the attainable energy, optimising the μ-focus option at the beamline, initiation of a project to develop, construct and test a high resolution energy dispersive fluorescence detector (HRXES) and designing new sample holders for special requirements. The planned activities involve specifically:

- Increase the monochromator stabilisation unit (MOSTAB) time stability. The incident beam intensity as MOSTAB feedback input parameter will be normalised to the ring current.

- Installation of new low energy ionisation chambers (OKEN chambers). This setup has an improved sensitivity and will allow, *e.g.* better P and S K edge measurements and 5f element M4,5 edge studies.

- Continued activities to implement a μ-focus option. This includes tests of confocal irradiation detection geometry, characterisation of beam size and beam profile at different energies for a set of polycapillary lenses (IfG, Germany) and two-dimensional CRL arrays (possibly including a new mosaic CRL design).

- Purchase and installation of a CCD camera for XRD characterisation of small crystallites and spatially resolved measurements, as well as for tomography experiments.

- Development of a Johann spectrometer for HRXES and for resonant inelastic X-ray scattering (RIXS). Initial RIXS investigations of Eu incorporation into hematite and goethite crystalline phases were performed at the W1 Beamline at HASYLAB in 2007. After testing a prototype spectrometer at the SCU-beamline at ANKA [8] a redesigned set-up will be made available at the INE-Beamline.

- Development, fabrication and first inactive tests of an electrochemical cell for *in situ* XAFS investigations were just completed [9]. First active tests will be performed later in 2008.

Beamtime requests

The INE-Beamline and INE active laboratories are one of the pooled facilities of the European Network of Excellence for Actinide Science (ACTINET) and access to the beamline is possible via this avenue. A portion of annual beamtime at the INE-Beamline (30%) is available via the standard ANKA facility proposal procedure (for detailed information see [10]). ACTINET users are prompted to also submit a proposal to the ANKA facility for their beamtime. Experiments are also possible through co-operation with INE. INE-Beamline scientists are to be contacted prior to proposal submittal to ensure feasibility of any experiment involving radioactivity (contact persons can be found in [11]). INE provides a radiation protection officer during active measurements, who is responsible for all radioactive substances.

References

[1]   Denecke, M.A., J. Rothe, K. Dardenne, H. Blank, J. Hormes, *Physica Scripta*, T115, 1001-1003 (2005).

[2]   Rothe, J., M.A. Denecke, K. Dardenne, Th. Fanghänel, *Radiochimica Acta*, 94, 691-696 (2006).

[3]   Metz, V., E. Bohnert, K. Dardenne, B. Brendebach, J. Rothe, M.A. Denecke, V. Nazmov, *ANKA Annual Report 2007*, 169-171.

[4]   Michel, P., K. Dardenne, M.A. Denecke, T. Schäfer, B. Brendebach, J. Rothe, T. Vitova, F. Huber, K. Rickers, M. Elie, G. Buckau, these proceedings.

[5]   Walther, C., M. Fuss, S. Büchner, *Radiochimica Acta*, 96, 411-425.

[6]   Denecke, M.A., P.J. Panak, F. Burdet, M. Weigl, A. Geist, R. Klenze, M. Mazzanti, K. Gompper, *Comptes Rendus Chimie Academie des Sciences*, 10, 872-882 (2007).

[7]   Banik, N.L., C.M. Marquardt, B. Brendebach, A. Geist, M.A. Denecke, submitted to *Inorganic Chemistry*.

[8]   Vitova, T., B. Brendebach, K. Dardenne, M.A. Denecke, A. Lebid, J. Rothe, these proceedings.

[9]   Liu, X., B. Fiehn, M.A. Denecke, C. Marquardt, B. Brendebach, K. Dardenne, J. Rothe, these proceedings.

[10]   *http://ankaweb.fzk.de.*

[11]   *http://ankaweb.fzk.de/instrumentation_at_anka/beamlines.php?id=9&field=7.*

Recent developments of the JAEA beamlines in SPring-8 and other topics

Tsuyoshi Yaita, Hideaki Shiwaku, Yoshihiro Okamoto, Shinichi Suzuki
Actinide Co-ordination Chemistry Group, Synchrotron Radiation Research Centre (SRRC)
Quantum Beam Science Directorate, Japan Atomic Energy Agency (JAEA)
Hyogo, Japan

Abstract

SPring-8 is a third-generation synchrotron radiation facility, and was constructed as RIKEN-JAERI (present JAEA) joint project. In SPring-8, JAEA's four beamlines are included. Especially, the BL22 and BL23 are introduced into the radioisotope (RI) laboratory. In the RI laboratory, the sealed Th, U, Np, Am, Cm and Tc samples can be measured and also in the other beamlines, the sealed Th and U can be used. Recently, the QXAFS system was installed into the BL11XU and confirmed to be excellent system for XAFS measurement at the undulator beamline. Also, the useful results for characterisation of Pd adsorption on chromatography have been obtained. In this report, a brief introduction of SPring-8 and JAEA's beamlines, and other recent topics, are discussed.

Introduction

The Super Photon Ring 8 GeV (SPring-8) is the largest third-generation synchrotron light source and is located at the Harima Science Garden City of the Hyogo Prefecture (Nishiharima area) in Japan, surrounded by a wonderful natural environment. Japan Atomic Energy Research Institute (JAERI), currently Japan Atomic Energy Agency (JAEA) and the RIKEN (Institute of Physical and Chemical Research) were jointly responsible for the planning and construction of SPring-8. Japan Synchrotron Radiation Research Institute (JASRI) is responsible for the operation, management, maintenance and upgrading of SPring-8 since 1997. The synchrotron radiation of SPring-8 ranging from the soft X-ray (photon energy 200 eV) to hard X-ray region (300 keV) is available with the highest brilliance in the world. High-energy gamma rays (1.5-2.9 GeV) and infrared radiation are also available. Advanced experimental facilities (Biomedical Imaging Centre, Radioisotope (RI) Laboratory, and 1 km-long Beamline Facility) are available. The SPring-8 has 63 beamlines including 53 operational ones used for more than 1 300 users a year.

After 2005, the JAEA, Quantum Beam Science (QuBS) directorate proposed the concept of a "Quantum Beam Platform", which means that several kinds of beam technologies, *e.g.* SPring-8 (X-ray), J-PARC, JRR-3 (pulse and continuous neutron sources), TIARA (ion beam) and so on, are effectively and mutually used for an issue regarding the science and engineering and are aiming at the application of beam technologies to science. On the basis of this concept, four beamlines are operated by the Synchrotron Radiation Research Centre (SRRC) of the JAEA at SPring-8. In the research fields, general materials science, especially focusing on actinide science, are ranked as an important application field in the JAEA, and thus, these beamlines have been designed and upgraded for these studies to date.

In this paper JAEA's beamlines and recent upgraded system and topics are first discussed. Also, this paper describes a few other topics, and provides information about becoming a user of the public beamline and the JAEA's beamlines.

Outlook of the JAEA beamline SPring-8

The four JAEA beamlines (BL11XU, BL14B, BL22XU and BL23SU) shown in the beamline map (Figure 1 [1]) are located at SPring-8.

The BL11XU [Figure 2(a)] is the undulator beamline and is designed for the quantum dynamics studies using Mossbauer spectroscopy, X-ray nuclear resonance scattering, high energy QXAFS and ID-XAFS [2], X-ray diffraction, and inelastic X-ray scattering (RIXS) spectroscopy in the energy range from 6~150 keV. The beamline is equipped with the monochromator switchable between Si(111) and Si(311) crystals within five minutes [3], and can use X-rays of a wide energy range.

The BL14B1 [Figure 2(b)] is the bending magnet beamline and is designed for the various kinds of material sciences using X-ray diffraction and XAFS spectroscopy in the energy range of 5~90 keV for monochromatised beams and 5~150 keV from white beams for DXAFS shown in Figure 3. The main optics refers to the standard SPring-8 bending magnet system with two mirrors and a fixed-exit double crystal monochromator. These optical elements can be removed completely for the experiment with white beams.

The BL22XU [Figure 2(c)] is the undulator beamline and is designed for quantum structural science using X-ray diffraction measurement on substances including liquid state under high pressure and resonant X-ray diffraction measurement mainly on correlated electron systems. Recently, residual stress distribution measurement became available. The last half of the beamline is introduced into the RI laboratory. High energy X-ray is useful for high-pressure diffraction measurements with a multi-anvil press or a diamond anvil cell [9], while low energy X-ray is indispensable for resonant diffraction measurements for materials including some specific elements. The lower limit of available X-ray energy is determined in the light of the M-edge of uranium (~3.5 keV) at which the magnetic scattering is significantly enhanced. In order to cover a wide energy range two sets of double crystal monochromators are installed in an optics hutch: the first monochromator covers the energy region of 3~37 keV and the second one the energy region 35~140 keV. In addition, movable beryllium windows are adopted to avoid the absorption of X-rays for a low energy region around 3~4 keV.

Figure 1: The beamline map of SPring-8 [1]
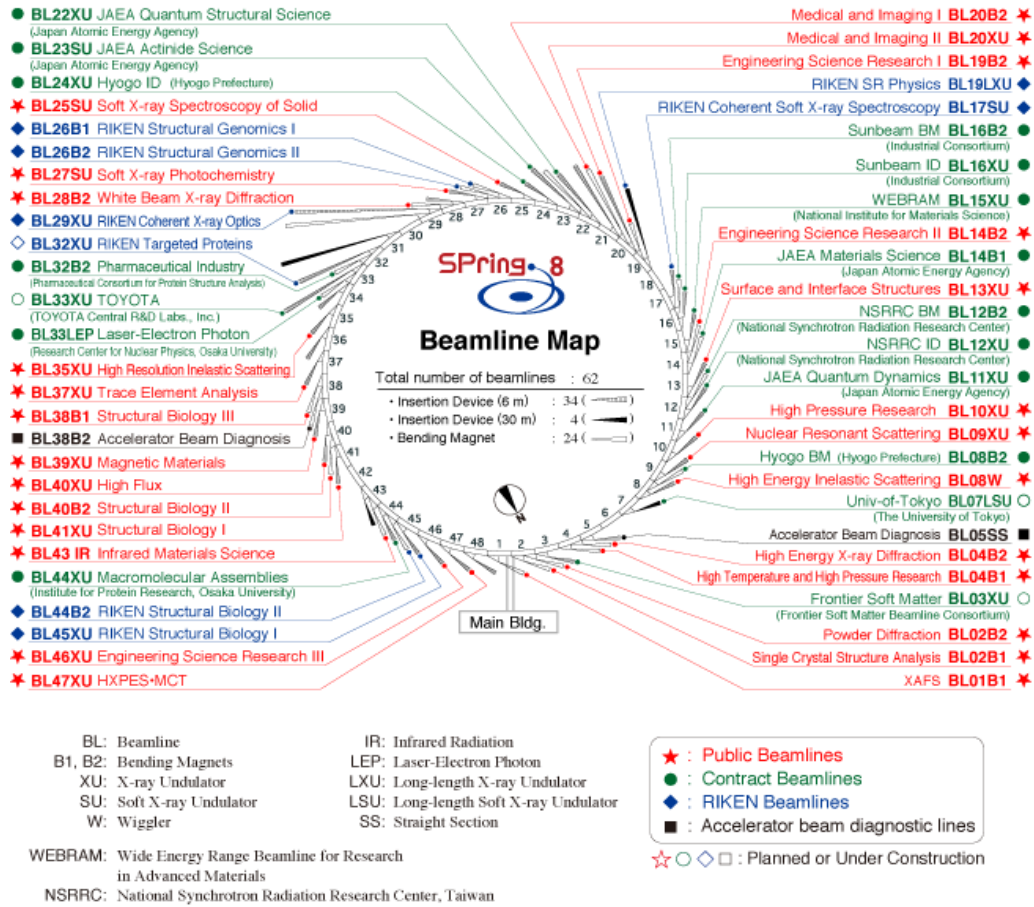
Figure 2: The outlook of JAEA's beamlines in the SPring-8

a) BL11XU: Undulator beamline; b) BL14B1: Bending beamline;
c) BL22XU: Undulator beamline; d) BL23SU: Soft X-ray undulator beamline
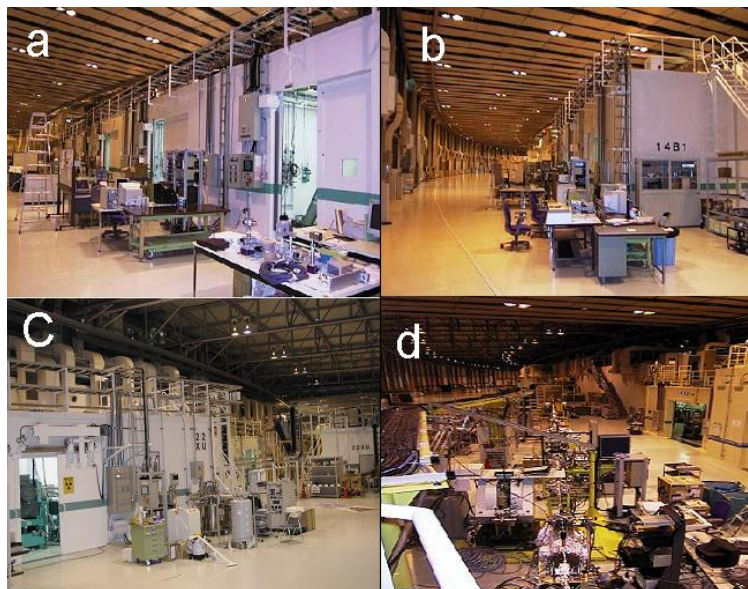
The BL23SU [Figure 2(d)] is the soft X-ray undulator beamline and designed for actinide and surface sciences using angle resolved photoemission spectroscopy (ARPES) and X-ray magnetic circular dichroism (XMCD) in the energy range from 0.2 to 2.0 keV. This beamline is also constructed for a wide variety of scientific research areas, surface chemistry, biophysical spectroscopy and solid-state physics. The light source "Twin Helical Undulators (THU)" is designed for switching of helicity of circularly polarised radiation. The THU consists of two helical undulators and five kicker magnets which generate a bump electron orbit at each undulator. The experimental stations are also located at the experimental hall and inside the RI laboratory.

The RI laboratory shown in Figure 4 is the full-controlled area designed for handling radioactive materials. This laboratory is isolated from the general experimental hall [Figure 2(c) and 2(d)] and equipped with the controlled drain system and the controlled air-conditioning system keeping negative pressure. The air ducts of chemical hood and glove box are introduced into each room. However, these systems in the area are not still fully operated so far. Therefore, the radioactive samples are prepared in the other hot laboratory and shipped to the SPring-8. The sealed radioactive materials are only conducted into the laboratory. In this laboratory, the samples including significant amount of ^{99}Tc (~160 MBq), Th, U, ^{237}Np (~18.5 MBq), ^{243}Am (~204 MBq) and ^{248}Cm (~3.6 MBq) can be conducted to the experiments using SR beam as listed in the Table 1. However, the use of the special container which passes the endurance test defined by JIS (Japan Industrial Standard) [8] is requested for sealing the radioactive samples.

Figure 3: The layout of Dispersive XAFS (DXAFS) of BL14B

The total reflection mirror is set up to remove the higher order harmonics and focus the synchrotron radiation; the corresponding energy range is 5 to 80 keV; the time resolution is 10 ms.
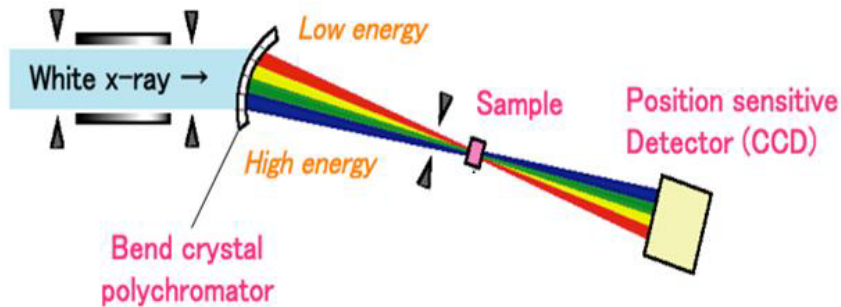
Figure 4: The location of the RI laboratory in the Spring-8

This area is isolated from the general experimental hall
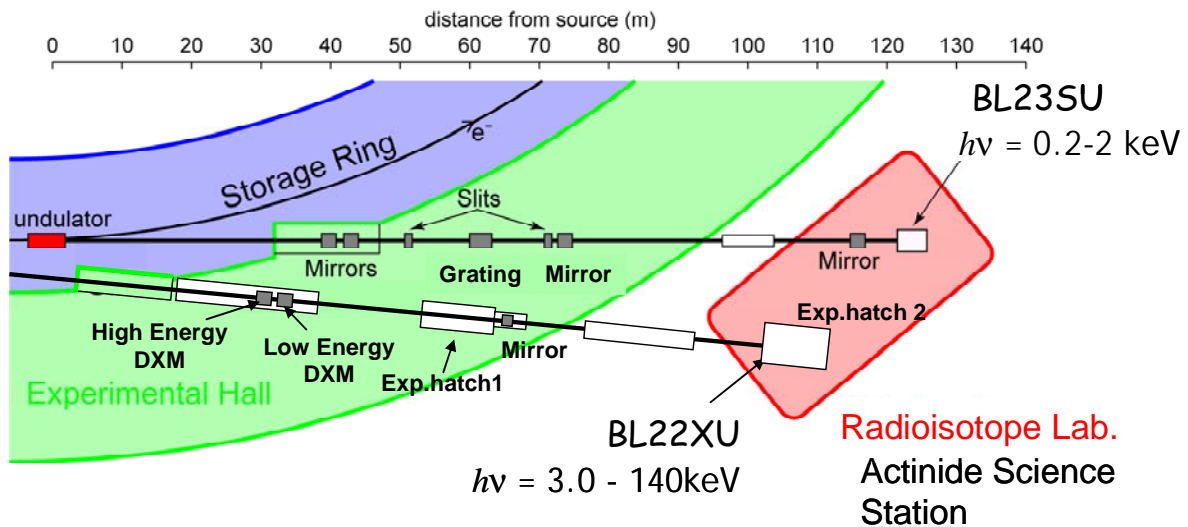
Table 1: The authorised radioactive elements in the JAEA beamline in the SPring-8

The solid and solution radioactive samples can be used in BL22XU, while the
solid radioactive sample except for Tc sample can be used in other beamlines

	Beamline	Light Source	Energy (keV)	Rad. Treatment	Radioactive Nuclides
SPring-8 (8GeV, Top up 100mA)	BL11XU	Insertion Device	5 ~ 130	sealed	Tc, Th, U
	BL14B1	Bending Magnet	5 ~ 150	sealed	Tc, Th, U
	BL22XU	Insertion Device	3 ~ 70	sealed	Tc, Th, U, Np, Am, Cm
	BL23SU	Insertion Device	0.2 ~ 2	sealed	Tc, Th, U, Np,

Recent topics of JAEA beamline

The recent topic in the JAEA beamlines that should be introduced is the QXAFS system [10] installed into BL11XU. To date, the application of high brilliance X-ray to XAFS measurement has been tried in the BL11XU of the SPring-8. The development of ID-XAFS system that synchronised monochromator scanning with the ID gap value on XAFS measurement was one of our attempts [2]. This method can apply transmission mode to a target-diluted materials with high sensitivity comparable to fluorescence mode, and ease a limitation of sample form for XAFS measurement in the transmission mode. However, the XAFS measurement using this system requires making rocking curve with piezoelectric device in addition to gap moving, so that it needs more time between the monochromator steps compared to the general XAFS system. Therefore, this system tends to pick up the vibration of this system by nitrogen cooling system and others, which becomes noise on XAFS spectrum. On the other hands, the time-resolved XAFS [4,5] have been developed for following a chemical reaction, while QXAFS is also effective for decreasing the noise on XAFS spectrum. The merit of QXAFS is that the continuity of absorbance between energies is improved due to the shortening of the step interval between energies and so the noise on XAFS spectrum reduces. However, this QXAFS system of BL11XU cannot make the monochromator scanning synchronise with gap moving. Thus the gap value of ID must be fixed for XAFS measurement so far. Therefore, the X-ray slightly brightness becomes a victim to fixed gap value but the brightness in the BL11XU is still higher than that in the bending beamline as shown in Figure 5.

Figure 5: Intensity profiles of BL11XU (ID beamline): red and BL1B (bending magnet beamline): blue
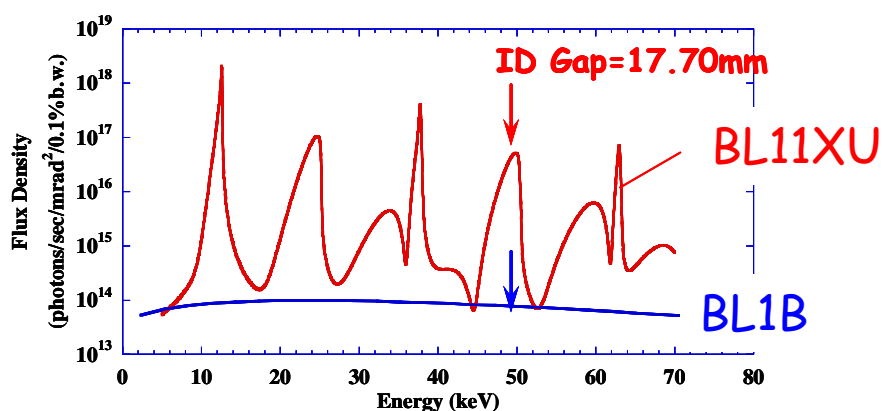
As an example of application, the characterisation of Pd on the adsorbent shown in Figure 6 was performed. Recently, the extraction chromatography has been attracted and tested for the treatment of HLW solution as an alternative method of solvent extraction [6]. The silica-based BTP (bis-triazinyl-pyridine) extraction resin is promising from the standpoint of separation of trivalent actinides from lanthanides, while the problem of which the Pd is not almost eluted in the separation system still remains [7]. Therefore, the adsorption species of Pd in various kinds of eluents were characterised by the QXAFS system. Figure 7 shows the XANES spectra of Pd in the column and Pd foil. The spectrum of the Pd in this system shifted to 6 eV higher than that of Pd foil, suggesting that Pd in this system was divalent. The radial structural functions (RSF) of Pd are shown in Figure 8(a). The elution procedures were: 1) charging of Pd on the resin by 3M HNO_3 (+HCl arising from the stock solution); 2) and 3) rinsing and elution of the charged Pd by H_2O; 4) and 5) elution of charged Pd by tiourea. All the data were corrected within 5 minutes. The three significant peaks at 1.7 Å, 1.9 Å and 2.5 Å, and one shoulder at 1.6 Å were observed in Figure 8(a). Those position values agreed with the bond distances: Pd-O, N, Cl, S and --C previously measured using PdO (r_{Pd-O}), Pd-BTP complex (r_{Pd-N} and $_{--C}$, where --C denotes non-co-ordinative carbon beside the N of BTP), $PdCl_2$ (r_{Pd-Cl}), and Pd-tiourea complex (r_{Pd-S}), and the brief characterisation, therefore, can be performed. Firstly, the peaks corresponding to Pd-N and Cl were observed on the process of charging on the resin: 1) to 3), suggesting that Pd immediately co-ordinates to the silica based BTP and Cl occupies the remaining co-ordination site of Pd. The evidence for a slight formation of oxide was also found as the shoulder at 1.6 Å. Accordingly, the poor elutability of Pd in this system would be derived from the formation of a tight complex with the BTP. On the other hand, the significant peak at 2.5 Å immediately appeared after adding tiourea solution into the column corresponding to 4) and 5). It suggested that the tiourea co-ordinates to Pd, and also this complex formation with tiourea agrees to the elution peak of Pd in the chromatography in Figure 8(b). Accordingly, these results indicated that the tiourea mostly works well as an elutant in this system. However, the peaks arising from the oxides still remained, and therefore, there would be problem that small amount of passivity palladium oxides possibly accumulate in the resin. As mentioned above, the QXAFS system is quite effective tool for the speciation of Pd in the chromatography.

Becoming a JAEA beamline user

SPring-8 is open to international user and many users come from various countries. The guidelines for becoming public beamline users are found on the SPring-8 web site *www.spring8.or.jp/en/users/new_user/*. We have two proposal calls and review sessions per year. Up to 10% of total beamtime is allocated to proprietary general proposals. On the other hand, the JAEA beamlines are also available. However, an applicant is requested to contact to JAEA's staff, and then, get the JAEA's proposal form. The channel for a proposal toward the JAEA's beamline is different from that of the public beamline, because the JAEA's beamlines are procedurally regarded as one of the JAEA's facilities. If a user wishes to use the radioactive samples except for solid state U and Th, JAEA's staff co-operation will be requested. Regarding the proposal for the solid state U and Th experiments, a user can use these materials in the general experimental hall and so user can access to Spring-8 directly.

Figure 6: The set-up of *in situ* measurements for the extraction chromatography.
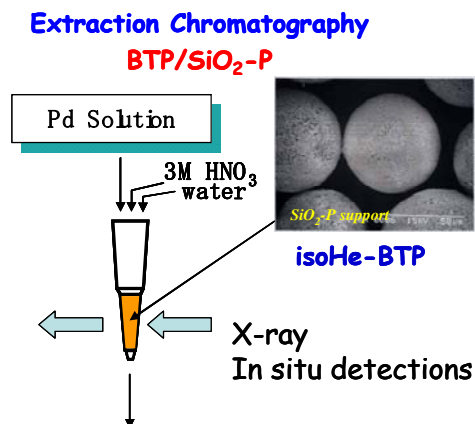
Figure 7: The XANES spectra of Pd-K edges for Pd-BTP complex (dotted) and Pd foil (solid)
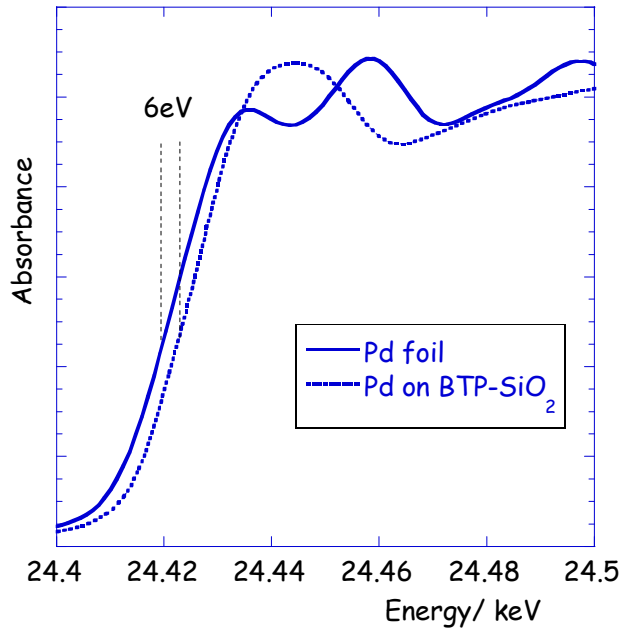
Figure 8: (a) The radial structural functions of Pd-K EXAFS in the column (phase shifts were not corrected). (b) The elution curve of Pd in this chromatography system.
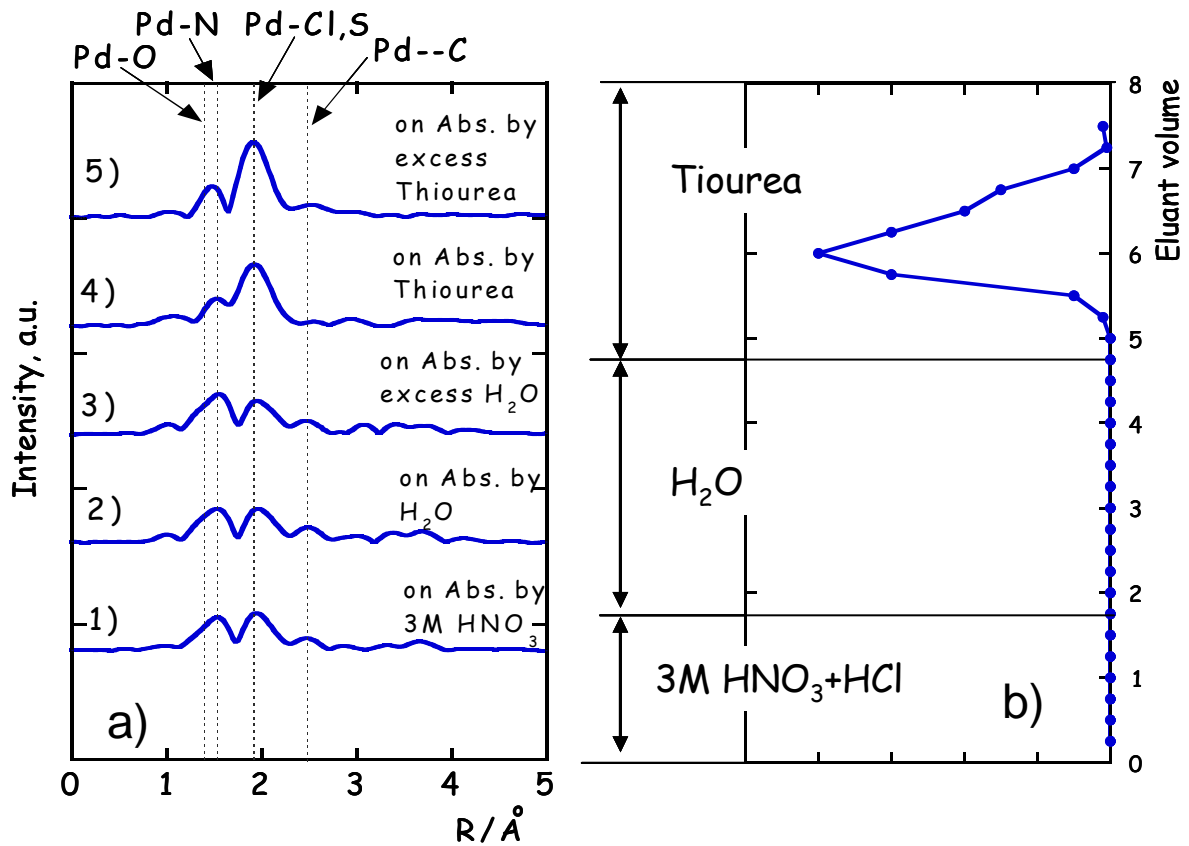
References

[1]   SPring-8 web site, "The Beamline Map of Spring-8",
        *www.spring8.or.jp/en/users/current_user/bl/beamline/BLmap/publicdocument_view?set_language=
        en&cl=en.*

[2]   Yaita, T., H. Shiwaku, H. Tanida, Y. Okamoto, H. Narita, S. Suzuki, S. Tachimori, H. Motohashi,
        "Development of ID Drive XAFS System for Undulator Beamline of SPring-8 and K, LIII EXAFS of
        Lanthanum in the Nitrate Solution", *Speciation, Technique and Facilities for Radioactive Materials at
        Synchrotron Light Sources, Workshop Proceedings of AnXAS2000*, pp. 353-358 (2000).

[3]   Shiwaku, H., T. Mitsui, K. Tozawa, K. Kiriyama, T. Harami, T. Mochizuki, "Cryogenically Cooled
        Monochromator with Multi-crystal Switching System on BL11XU at SPring-8", *AIP CP705,
        Proceedings of Synchrotron Radiation Instrumentation Conference*, pp. 659-662 (2004).

[4]   Frahm, R., "Quick Scanning EXAFS: First Experiments", *Nucl. Instrum. Methods Phys. Res.*, A270,
        578-581 (1988); Frahm, R., "New Method for Time Dependent X-ray Absorption Studies", *Rev. Sci.
        Instrum.*, 60, 2515-2518 (1989).

[5]   Marsushita, T., R.P. Phizackerley, "A First X-ray Absorption Spectrometer for Use with Synchrotron
        Radiation", *Jpn. J. Appl. Phys.*, 20, 2223-1118 (1981).

[6]   Hoshi, H., Y-Z. Wei, M. Kumagai, T. Asakura, Y. Morita, "Separation of Trivalent Actinides from
        Lanthanides by Using R-BTP Resins and Stability of R-BTP Resin", *JALCOM*, 408-412, 1274-1277
        (2006).

[7]   Wei, Y-Z., H. Hoshi, M. Kumagai, T. Asakura, Y. Morita, "Separation of Am(III) and Cm(III) from
        Trivalent Lanthanides by 2,6-bistriazinylpyridine Extraction Chromatography for Radioactive
        Waste Management", *J. Alloys. Compd.*, 374, 447-450 (2004).

[8]   JISZ4821-2, "Sealed Radioactive Sources – Leakage test methods", includes punk test, leaking
        test, high- and low-pressure tests and so on.

[9]   SPring-8 web site, "Outline of BL22XU: High Pressure Experiments can be Carried Out at the
        General Experimental Hall",
        *www.spring8.or.jp/en/users/current_user/bl/beamline/BLmap/publicdocument_view?set_language=
        en&cl=en.*

[10]   SPring-8 web site, "Quick XAFS", Quick XAFS (QXAFS) mode is a recently developed technique to
        measure XAFS spectra in a short time. At present, most of the transmission XAFS measurements
        in BL11XU are performed in the QXAFS mode, and high quality data can be taken in 3-15 min
        (20-50% compared with a conventional step-scanning mode). A time-resolved QXAFS mode is
        possible with a time resolution of seconds to tenth seconds. Unlike energy dispersive XAFS
        (DXAFS), QXAFS can be used for the fluorescence and conversion electron yield mode.
        www.spring8.or.jp/wkg/BL01B1/solution/lang-en/SOL-0000001211?set_language=en&cl=en.

High resolution spectroscopy using a crystal analyser system

I. Alliot,[1] **A. Braillard,**[2] **C. Da Silva,**[2] **W. Del Net,**[3] **M.A. Diot,**[2] **J.L. Hazemann,**[2]
E. Lahera,[3] **V. Nassif,**[1] **H. Palancher,**[4] **O. Proux,**[3] **D. Testemale**[2]
[1]CEA/Grenoble, INAC/SP2M/NRS, Grenoble, France
[2]Institut Néel, MCMF, CNRS, Grenoble, France
[3]Lab. de Géophysique Interne et Tectonophysique, UMR CNRS, Université Joseph Fourier
St. Martin-d'Hères, France
[4]CEA Cadarache, Department for Nuclear Fuel Study, St. Paul-lez-Durance, France

Abstract

The CRG-FAME (French Absorption Spectroscopy beamline in Material and Environment sciences) beamline at the European Synchrotron Radiation Facility (Grenoble, France) installed on a classic 0.8 T bending magnet is dedicated to X-ray Absorption Spectroscopy (XAS) on highly diluted samples [1,2]. XAS fluorescence measurements are currently achieved using a Ge-solid state detector. A way to improve the detection is to use a crystal analyser spectrometer (CAS) with a higher energy resolution (about 1 to 2 eV, to be compared to typical 150 eV of a Ge solid state resolution) coupled to a detector with a very large dynamic.

The CAS is composed of a bent crystal and a detector in the Johann geometry [Si(111) spherical crystal with a solid angle of 11° and a 0.5 m radius of curvature] [3,4].

The use of such a simple device improve the quality of the spectra: EXAFS acquisitions on dilute elements can be performed in all type of the matrix (i.e. even if its main constituents are excited by the X-ray beam or are radioactive), and XANES spectra are obtained with an improved resolution. Moreover, new spectroscopic techniques can now be performed, to probe the various electronic transitions of the absorption process (Resonant Inelastic X-ray Spectoscopy) or to perform an XAS-like experiment of a light element using hard X-ray (X-ray Raman Spectoscopy). One of the limitations is the small solid angle of detection and thus the statistics of measurement: a spectrometer including five bent crystals has been designed and is now under construction. The feasibility of different types of experiments will be demonstrated, including High Resolution XAS, RIXS and XRS experiments.

References

[1]   Proux, O., X. Biquard, E. Lahera, J.J. Menthonnex, A. Prat, O. Ulrich, Y. Soldo, P. Trévisson, G. Kapoujvan, G. Perroux, P. Taunier, D. Grand, P. Jeantet, P. Deleglise, J.P. Roux, J.L. Hazemann, *Phys. Scr.*, 115, 970-973 (2005).

[2]   Proux, O., V. Nassif, A. Prat, O. Ulrich, E. Lahera, X. Biquard, J.J. Mentonnex, J.L. Hazemann, *J. Synchrotron Rad.*, 13, 59-68 (2006).

[3]   Johann, H.H., *Z. Phys.*, 69, 185-206 (1931).

[4]   Collart, E., A. Shukla, F. Gélébart, M. Morand, C. Malgrange, N. Bardou, A. Madouri, J-L. Pelouard, *J. Synchrotron Rad.*, 12, 473-47 (2005).

The Rossendorf Beamline at ESRF: The next ten years of actinide XAFS

Andreas C. Scheinost, Harald Funke, Christoph Hennig,
Andre Rossberg, Dipanjan Banerjee, Marco Hesse
Molecular Structure Group, Institute of Radiochemistry, FZD, Dresden, Germany
Rossendorf Beamline at ESRF, Grenoble, France

Abstract

The Rossendorf Beamline as a dedicated X-ray absorption spectroscopy station for actinide research has been in operation since 1998. It has served for hundreds of experiments over the past 10 years, ranging from materials science to aquatic and environmental chemistry of actinides and other radionuclides. A short overview on research highlights will be given, including the current extensive work on redox processes.

The beamline's strength is built on the high reliability and flux of the ESRF, which allows to run samples even at very low concentrations of a few ppm, and on the long experience with actinide EXAFS. After 10 years of operation, the beamline is ready to take the next step in order to further lower the concentration limits of XAFS and to extend the array of methods to μ-XRF, μ-XAFS and XRD. Essential optical components will be replaced parallel to the upgrade of the ESRF to increase the photon flux by about one order of magnitude to 10^{12} photons/sec on the sample, and to prepare the microfocus. Additional modifications like easily exchangeable monochromator crystals, additional mirror coatings and a routine quick-XAFS mode will widen the experimental possibilities without sacrificing the user-friendly operation of the beamline.

These changes are planned for 2010, and will be installed and commissioned with little loss of beamtime. This is especially important, since the Rossendorf Beamline will continue to provide its facilities to the actinide community within the ACTINET network, in addition to the routine beamtime application paths via ESRF and FZD collaborations.

An overview on the current status of operation modes, technical details, access conditions and user support with advanced data analysis methods is presented, by updating earlier information and summarising the features most important for prospective users.

Beaming in on radioactive materials:
The microXAS beamline project at the Swiss Light Source

D. Grolimund,[1,2] **C.N. Borca,**[1,2] **D. Gavillet,**[1] **E. Wieland,**[1] **A. Froideval,**[1] **B .Meyer,**[2] **M. Willimann**[2]
[1]Nuclear Energy and Safety Department, Paul Scherrer Institut (PSI), Villigen, Switzerland
[2]Swiss Light Source (SLS), Paul Scherrer Institut (PSI), Villigen, Switzerland

Abstract

With the increasing recognition that macroscopic material properties and chemical reactivity are triggered by nano- and microscopic processes, the need for "X-ray microscopes" grew rapidly. However, micro-focusing of X-rays represents a considerable optical and technical challenge. The realisation of efficient X-ray microprobes had to wait until the availability of most modern light sources. Such third-generation synchrotrons are characterised by small source sizes, high photon fluxes as well as low beam divergences. Simultaneous to the realisation of these high performance light sources, remarkable breakthroughs have been achieved in the area of X-ray optics. The advancements in these two areas resulted in a significant increase in the available photon flux and flux density within X-ray microprobes.

Based on the initiative and under the direction of the Laboratory for Waste Management (Department of Nuclear Energy and Safety, Paul Scherrer Institute), a high resolution hard X-ray microprobe station was built at the Swiss Light Source: the microXAS beamline. This analytical facility allows for the investigation of materials and matter by means of high intensity X-ray beams with a spatial resolution of approximately 1 μm^2. The microXAS microprobe facility is optimised for X-ray absorption spectroscopy (XAS), X-ray fluorescence (XRF) and X-ray diffraction (XRD) experiments requiring high spatial resolution. The microprobe facility is designed to deliver both monochromatic and pink X-ray beams with high flux and energy resolution combined with dynamic (sub-)micron focusing capabilities. The focal spot size can be adjusted to the problem investigated ranging from a few mm^2 down to even below 1 μm^2. The accessible energy range of ~4 to ~23 keV covers most K- respectively L-edges of transition metals, lanthanides and actinides.

Without doubt, the capability to determine element-specific chemical properties such as local co-ordination environments or oxidation states by means of X-ray absorption spectroscopy is of fundamental importance in several research fields including nuclear science. Using micro-focused X-ray beams, chemical speciation can be determined within single micro-domains simultaneously with local structural analysis.

The federal license authorising the investigation of radioactive materials makes the microXAS beamline into an exclusive X-ray microprobe facility. At present, only a limited number of X-ray microprobe facilities around the globe allow "beaming in" on radioactive samples.

In addition to a brief technical overview of the beamline concept, we will present several illustrative examples demonstrating the potential of the microXAS beamline to enlighten complex problems related to nuclear (including actinide) science. The presentation will be complemented by addressing future prospects and outlining arising new research opportunities.

References

Grolimund, D., A.M. Scheidegger, J.F. van der Veen, R. Abela, "Layout of the microXAS Beamline at SLS", *PSI Scientific Report*, 4, 139-148 (2002).

Jefimovs, K., O. Bunk, F. Pfeiffer, D. Grolimund, J.F. van der Veen, C. David, "Fabrication of Fresnel Zone Plates for Hard X-rays", *Microelectronic Engineering*, 84, 1467-1470 (2007).

Maaß, R., S. Van Petegem, D. Grolimund, H. Van Swygenhoven, M.D. Uchic, "A Strong Micropillar Containing a Low Angle Grain Boundary", *Applied Physical Letters*, 91, 131909 (1-3) (2007).

Maaß, R., S. Van Petegem, H. Van Swygenhoven, P.M. Derlet, C.A. Volkert, D. Grolimund, "Time Resolved Laue Diffraction of Deforming Micropillars", *Physical Review Letters,* 99 (14), Art. No. 145505 (2007).

Ingold, G., P. Beaud, S.L. Johnson, D. Grolimund, V. Schlott, T. Schmidt, A. Streun, "FEMTO: A Sub-ps Tunable Hard X-ray Undulator Source for Laser/X-ray Pump-probe Experiments at the SLS", *Synchroton Radiation News*, 20, 5, 35-39 (2007).

Froideval, A., R. Iglesias, M. Samaras, S. Schuppler, P. Nagel, D. Grolimund, M. Victoria, W. Hoffelner, "Magnetic and Structural Properties of Fe-Cr Alloys", *Physical Review Letters,* 99 (23), Art. No. 237201 (2007).

Scientific capabilities of the Advanced Light Source for radioactive materials investigations

David K. Shuh
Chemical Sciences Division, Lawrence Berkeley National Laboratory
Berkeley, CA, USA

Abstract

The Advanced Light Source (ALS) of Lawrence Berkeley National Laboratory (LBNL) is a US Department of Energy (DOE) third-generation synchrotron radiation national user facility. The ALS has more than forty operational beamlines providing synchrotron radiation for a diverse range of experiments for more than 2 000 users per year. Access to ALS experimental beamtime and resources is through the standard DOE general user programme model established by the merit-based peer-review of user proposals. Several ALS beamlines are being used on a regular basis for radioactive materials investigations. The radiation safety aspects of experiments at the ALS are reviewed and implemented on a graded hazard approach basis by the ALS in conjunction with the LBNL Radiation Protection Program administered by the LBNL Environmental, Health and Safety Division. The ALS provides radiological support/assistance for accepted user experiments and nearby LBNL radioactive materials laboratories can be used to stage experiments.

The capabilities of the ALS beamlines for radioactive materials investigations and several examples of current research, along with descriptions of new emerging capabilities and opportunities, will be presented. The ALS is supported by the Director, Office of Science, Office of Basic Energy Sciences, US Department of Energy at Lawrence Berkeley National Laboratory under contract no. DE-AC02-05CH11231.

Closing session

Discussion and conclusions

Why we're passionate about the actinides: The most recent strange behaviour in U/PuO$_{2+x}$

Steven Conradson
Materials Science and Technology Division
Los Alamos National Laboratory
Los Alamos, NM, USA

Synthesis

The question I would like to pose for the closing discussion is the same one I used at the last meeting: Given the difficulties involved, what special or even unique properties of actinides and their compounds compel us to continue working with them? This is not asking what future directions should be, but is intended to focus on current challenges and even mysteries. I will begin the closing session with a brief description of some of our current findings on local structure and speciation in UO$_{2+x}$ for $0 \leq x \leq 0.25$. The primary issue here has been the nature of the adventitious O in the superstoichiometric compound and whether it forms oxo groups or not. Using thermogravimetric methods that constitute an easier route to obtaining intermediate compositions has allowed us to measure the U L$_3$ XAFS oF series of compounds that show as their most prominent change the monotonic growth of a feature fit with an O atom around 1.74 Å. We have also performed neutron and X-ray pdf, inelastic X-ray scattering, O K edge XAS, Raman measurements, and some preliminary variable temperature XAFS below 200 K, as well as DFT calculations to explore the relative energies of various types of O cluster configurations. The results indicate not only that collective behaviour in the form of strong interactions between the O defects resulting in local composition fluctuations and nanoscale heterogeneity is important but also point to a strong role for dynamical processes, even at low temperature.

Poster session contributions

Po(IV) solvation in aqueous solution: An interplay between computational chemistry and X-ray absorption spectroscopy

Regla Ayala,[1] **Elizabeth C. Beret,**[2] **José Manuel Martínez,**[2] **Rafael R. Pappalardo,**[2]
Adela Muñoz-Páez,[1] **Enrique Sánchez Marcos**[2]
[1]ICMSE-CSIC, Department of Inorganic Chemistry, University of Seville, Spain
[2]Department of Physical Chemistry, University of Seville, Spain

Abstract

The aim of this work is studying Po(IV) in aqueous solution using an interplay between computational chemistry and XANES spectroscopy. Two independent Car-Parrinello Molecular Dynamics (CP-MD) trajectories are produced, the structure around the metal centre being characterised as an equilibrium between the $[Po(H_2O)_4(OH)_2]^{2+}$ and $[Po(H_2O)_3(OH)_3]^+$ species in one case, and between the $[Po(H_2O)_5(OH)_2]^{2+}$ and $[Po(H_2O)_4(OH)_3]^+$ species in the other, although for both trajectories the predominant structure is that containing 3 OH– ligands. Average XANES spectra of the L_{III}-edge of Po are theoretically computed using a large number of structures selected from the CP-MD simulation trajectories. XANES spectra are also calculated for the structures of Po(IV)-ligand (ligand Ξ H_2O and OH–) clusters derived from quantum-mechanical optimisations which incorporated solvent effects by means of a semi-continuum solvation model. The spectra obtained from CP-MD trajectories are compared with those derived for the clusters. A good agreement is observed between the average spectra calculated for Po(IV) in solution and the spectra obtained for the clusters representing the predominant co-ordination numbers around Po(IV) in solution. These theoretically simulated spectra allow the establishment of a criterion for the determination of Po(IV) hydrated species in aqueous solution in future experimental XANES measurements.

Introduction

It is well-known that multivalent cations in aqueous solutions can participate in a series of consecutive hydrolysis reactions [1]. In the case of tetravalent cations, the dominant species are hydrolysed forms of the aqua ions along with polynuclear products, depending on the pH of the solution. This is the case of the hydration of Po(IV). However, its chemistry in solution is scarcely known, likely due to its rareness and high toxicity. To our knowledge, the only experimental information reported so far about Po(IV) hydration is that the hydration number is between 6 and 8 [1]. Hopefully, computational chemistry can help overcoming the limitations presented by the experimental determination of this element, and can provide an atomistic insight into the structure and dynamics of polonium ion in solution. In previous studies of Po(IV) in aqueous solutions using semi-continuum models [2,3], we have verified its strong tendency towards hydrolysis. The phenomenon has a significant impact on the hydration number, ranging from 8-9 in the aqua ion case ($[Po(H_2O)_n]^{4+}$, n = 8-9) to 4 for the hydroxyde ($[Po(OH)_4]$). The hydrolysis of polonium can be considered as a chain of proton release reactions transforming aqua ions $[Po(H_2O)_n]^{4+}$ into hydrolysed species $[Po(H_2O)_{n'}(OH)_m]^{4-m}$. The nature of these hydrated/hydrolysed structures and the dynamic equilibria established between them are of fundamental interest because the diffusive and migrative behaviour of the ion as well as its reactivity can show an intricate dependence on them. We also found that more than one species can coexist simultaneously for the same medium conditions. These results were obtained considering the ion and its first solvation shell explicitly, whereas further solvent molecules were represented by a dielectric continuum. Although it has been proven that continuum methods can provide reliable results [4,5], the absence of some specific interactions further from the first hydration shell, along with the flatness of the potential energy surfaces of our system, compel us to carry out *ab initio* molecular dynamics simulations. Statistical averages are accounted for in this type of numerical simulation, and the variety of Po(IV)-solvent species and their associated hydrolysis processes as well as quantum effects associated to the proton dynamics can be observed as time proceeds.

X-ray absorption spectroscopy (XAS) is element-specific, needs only a short-range order and can be applied to samples containing the system of interest over a wide range of concentrations (from milimolar to molar) [6]. These features make XAS one of the most suitable techniques to supply structural information on highly dilute electrolyte solutions. The XANES region has shown to be dependent on many parameters of the system under study: the oxidation state of the absorber atom, bond angles, co-ordination geometry, distance of the absorbing atom to the first and higher co-ordination shells, etc. [6,7]. XANES information has been used on a qualitative level that envisages the spectrum as a *fingerprint* of the system under study. To our knowledge there are no experimental XANES data of Po(IV) in water solution whatsoever. In this scenario theoretical computation of XANES spectra can serve both as a source of further physico-chemical information on the system under study and as a reference for future experimental measurements. In particular, it has been thoroughly shown that the use of information derived from quantum-mechanical calculations and computer simulations for the computation of theoretical XANES spectra can be quite useful in the structural elucidation of electrolyte solutions [8-13].

The aim of the present paper is to study the hydration of Po(IV) using an interplay between computational chemistry (Car-Parrinello molecular dynamics (CP-MD) simulations and semi-continuum solvation model) and XANES spectroscopy. A description of how explicitly accounting for all the species in the solution can modify the results obtained by means of semi-continuum models are performed. The representative or predominant species in solution under the medium conditions imposed by our simulations are investigated. Theoretical XANES spectra are computed from the structures obtained by a semi-continuum solvation model and from the CP-MD trajectories. Differences in the spectra arising from the consideration of different co-ordination numbers around Po and from different degrees of hydrolysis of the aquated species are investigated. This interplay between theoretical computations and X-ray absorption spectroscopy allows us to establish a criterion to distinguish between different Po(IV) species in aqueous solutions, to be applied onto future experimental information.

Methodology

CP-MD simulations

Ab initio molecular dynamics simulations using the Car-Parrinello scheme were performed on a system containing 1 Po(IV) and 60 water molecules in a periodic box of size 12.898 Å. The LDA functional was used to solve the Kohn-Sham equations. The valence electrons (6 for Po, 6 for O and 1 for H) were expanded in plane waves with an energy cut-off of 90 Ry. The time step was equal to 5 au (0.121 fs). The fictitious mass of the electrons was equal to 600 au. All simulations were run in the NVT ensemble. The temperature of the nuclei was kept around 300 K using a Nose-Hoover thermostat with a time constant of 1 500 fs. For the core electrons of polonium, oxygen and hydrogen atoms, Goedecker-Tetter-Hutter pseudopotentials [14] were used. The Po pseudopotential was built using Po(0) as the reference oxidation state. It would have been worthy to have a Po pseudopotential constructed taken into account a higher oxidation state. However, the absence of it compelled us to use the one available in the literature. The development of a new Po pseudopotential considering higher quality functionals and higher oxidations states is nowadays in progress. A homogeneous background charge was applied to compensate for the net charge of the system. Ewald summation was applied to compute long-range interactions. All the CP-MD simulations were performed with the CPMD program [15]. Two different trajectories were run. The first one (A) begun from a hexahydrate of Po(IV) ($[Po(H_2O)_6]^{4+}$) plus 54 water molecules. The second trajectory (B) started from a system containing an octahydrate of Po(IV) ($[Po(H_2O)_8]^{4+}$) plus 52 water molecules. The systems were equilibrated for around 5-8 ps followed by at least 20 ps of data collection. Configurations were saved every 10 steps for further analysis.

Theoretical XAS spectra

XANES spectra of the L_{III} edge of Po were simulated for microsolvated clusters of Po(IV) showing different degrees of hydrolysis. The structures of these clusters had been optimised in two previous works [2,3], using a semi-continuum representation of the solvent. The optimisations were performed at the MPW1PW91 level using aug-cc-pVDZ basis sets for Po, O and H. In the case of the polonium ion a relativistic small core pseudopotential was also considered for the core (60) electrons. Solvent effects further from the first solvation shell were taken into account using the polarisable continuum model (PCM) [16] in the integral equation formalism (IEFPCM) [17] implementation.

L_{III} XANES spectra were also computed for structures selected from the two CP-MD simulation trajectories of Po(IV) in water. In particular, 150 statistically independent snapshots were extracted from each trajectory, evenly separated by a time interval of 0.12 ps. These individual spectra were later averaged to yield a global spectrum for Po(IV) in solution. All the calculations were performed with the FEFF code [18]. The atomic backscattering potentials were calculated self-consistently, starting from a muffin-tin potential constructed using Mattheiss prescription [19] and applying the Hedin-Lundqvist self-energy approximation [20]. A SCF radius of 6 Å around each type of atom was used. Hydrogen atoms were considered in the computation of the potentials but not in the full multiple scattering process, since their scattering factor is usually overestimated in this type of calculation [9]. When the aquated Po(IV) species are in solution, the water molecules in the close environment of the metal are strongly polarised, in contrast to the much less perturbed bulk H_2O. This chemical difference is taken into account by computing distinct backscattering potentials for first-shell and bulk oxygen atoms. No variations in the spectra were observed when a third oxygen potential was introduced in order to distinguish between water and hydroxyl ligands. Full multiple scattering computations were performed within a sphere of 6.0 Å around the Po centre.

Results

CP-MD simulations

An analysis of the trajectories derived from simulations A and B indicates that during the first two picoseconds of the equilibration period several processes take place. In the case of simulation A, the initial configuration around the metal centre was a hexahydrate. Although the number of ligands around the ion is maintained during all the simulation time, an exchange of a ligand between the first and the second hydration shell was observed. Simultaneous to the exchange process, different hydrolysis events were identified ending up with hydrolysed Po(IV) clusters containing between 2 and 3 OH$^-$ groups.

In the case of simulation B, the initial configuration around the Po ion was an octahydrate. During the equilibration time, the number of ligands was reduced down to 7. Not only there was a decrease in the co-ordination number but also an exchange of ligands from different solvation shells. The decrease in the hydration number is in agreement with our previous results obtained by a semi-continuum model [3]. As in the case of simulation A, ligand exchange only takes place during the equilibration time, and after this period the hydrolysis processes are responsible for the changes in the close environment of the Po ion.

Comparison of simulations A and B allows us to conclude that the CP-MD simulation where the starting Po(IV) aqua ion is a hexahydrate (trajectory A) is easily stabilised by a set of deprotonation processes, while the CP-MD simulation starting with the octahydrate (trajectory B) needs of both deprotonation and dehydration processes to reach thermalisation. In both simulations, A and B, the number of OH$^-$ groups in the first solvation shell of Po(IV) (after the equilibration period) oscillates between 2 and 3. The conversion between clusters two- and threefold hydrolysed is mainly due to a forward and backward proton transfer process between a water molecule and a hydroxyl group. In the case of simulation A there is a significant proportion of species with 3 OH$^-$ groups (80%) whereas for simulation B the proportion of species with 3 OH$^-$ groups is slightly larger (87%). This information along with the integration of the Po-O RDFS (not shown in this paper) indicates that in simulation A an equilibrium between $[Po(H_2O)_4(OH)_2]^{2+}$ and $[Po(H_2O)_3(OH)_3]^+$ species is observed, while for simulation B this equilibrium involves $[Po(H_2O)_5(OH)_2]^{2+}$ and $[Po(H_2O)_4(OH)_3]^+$ clusters. Both equilibria are displaced towards the species containing three OH$^-$ ligands. Figure 1 collects representative structures of the previously mentioned clusters. These findings are in agreement with our previous results obtained using a semi-continuum model of solvation [3]. No exchange among ligands in the first and outer solvation shells was observed, at least during our production times (~20 ps), the protonation and deprotonation processes being responsible for the changes observed in the close environment of aqueous Po(IV). The dehydration processes that would interconnect the sixfold and sevenfold co-ordinated species obtained respectively in simulations A and B must be costly from the energetic point of view and would likely require long simulation times. Rare event techniques would be needed to observe them. In the absence of other experimental or theoretical results concerning the determination of the co-ordination number of Po(IV) in water solution, it is difficult to estimate the possible bias introduced by the initial configurations in our simulations.

Theoretical XAS spectra

Figure 2 shows the L$_{III}$-edge XANES spectra computed for the microsolvated clusters of Po(IV). The spectra have been distributed so that each panel of Figure 2 corresponds to species with the same degree of hydrolysis and different co-ordination numbers. Interestingly, clusters containing the same number of hydroxyl ligands generate spectra of similar shape. The first and second resonances are more intense in the case of the aqua ions (m = 0). For species containing only one OH$^-$ ligand (m = 1) the second resonance is much less defined. When two OH$^-$ groups are present (m = 2) a change of slope appears at around 13 860 eV, this feature appearing nearer to the signal of the first resonance when the species contains three OH$^-$ ligands (m = 3). The clusters with four OH$^-$ groups (m = 4) generate XANES spectra with a wider first resonance peak.

Minor changes are observed when the total co-ordination number around the Po centre increases (from bottom to top in each panel). For the aqua ions (m = 0) the first and second resonances become sharper and more intense with the increasing co-ordination number. Also, the maxima of these two resonances appear at lower energies for larger co-ordination numbers. A similar although less defined behaviour is observed for clusters containing one hydroxyl group (m = 1): the first and second resonances are slightly displaced towards lower energies when the total co-ordination number increases. On the contrary, the spectra computed for clusters with two hydroxyl ligands (m = 2) show a different behaviour: the first resonance becomes less intense when going from the $[Po(H_2O)_3(OH)_2]^{2+}$ species to $[Po(H_2O)_4(OH)_2]^{2+}$, and its height and position remain thereafter unmodified. It is the second resonance which becomes more intense and which displaces towards lower energies with the increasing co-ordination number. A change of slope at around 13 860 eV also grows more defined, even generating a small hump at around 13 850 eV in the case of $[Po(H_2O)_7(OH)_2]^{2+}$. This change of slope close to the first resonance is also observed for the structures containing three hydroxyl ligands (m = 3).

Although their overall shape is different from the case with two hydroxyl ligands, their behaviour towards increasing co-ordination number is analogous. Finally, the case of structures containing four OH⁻ groups (m = 4) also shows small variations of the spectral shape with the co-ordination number.

Figure 3 shows the theoretical XANES spectra simulated using the two CP-MD trajectories. The global spectrum is obtained as an average over all the individual spectra computed for the selected snapshots. Thus, the standard deviation associated with each [$\mu x(E)$] point used in the construction of the averaged XANES can be evaluated. This is plotted as dashed-and-point lines in Figure 3. For the sake of comparison, weighted linear combinations of the spectra computed for the microsolvated clusters that represent the predominant species in solution as deduced from our simulations are also shown. These linear combinations account for their relative abundance in the simulated solution (80% [$Po(H_2O)_3(OH)_3$]$^+$ and 20% [$Po(H_2O)_4(OH)_2$]$^{2+}$ in trajectory A, and 87% [$Po(H_2O)_4(OH)_3$]$^+$ and 13% [$Po(H_2O)_5(OH)_2$]$^{2+}$ in trajectory B). For each trajectory the average spectrum closely resembles the corresponding spectrum obtained as a linear combination of the cluster spectra. However, in the average solution spectra the features are dumped due to the dispersion exerted by the second hydration shell, which is not considered in the cluster spectra, as well as to the inclusion of thermal fluctuations (*i.e.* considering a large number of independent snapshots). When the standard deviation of the average spectra is taken into account, the agreement between the average spectrum and the corresponding cluster spectrum is improved for both trajectories.

Concluding remarks

CP-MD simulations have been performed for Po(IV) in aqueous solution. The structural picture of the simulated solution is in agreement with previous results obtained using a semi-continuum solvation model: the co-ordination number around Po(IV) cannot be uniquely assigned, and water molecules in the first co-ordination shell of the metal show a strong tendency towards hydrolysis. Although a single representative species cannot be designated for this system, equilibrium is observed between structures containing two and three hydroxyl groups, the predominant form being that with three OH⁻ ligands.

Theoretical XANES spectra of Po L_{III}-edge have been obtained for the trajectories of the CP-MD simulations. Their analysis in terms of the XANES calculated for the predominant structures in the solution is consistent with the structural information obtained from the CP-MD simulations. XANES spectra have also been calculated for structures with different total co-ordination numbers and different degrees of hydrolysis. This systematic study has allowed the identification of a pattern in the spectral shape for structures containing the same number of OH⁻ groups, while only minor changes are observed when the total co-ordination number of Po is modified. Thus, the resulting spectra can serve as a criterion for determining the degree of hydrolysis of the predominant aqueous form of Po(IV) in solution when a future experimental XANES spectrum is available. However, elucidation of the co-ordination number of Po(IV) in water solution will probably need of analysis of the EXAFS function. This will be undertaken in a second piece of work which is currently under development.

References

[1]   Richens, D.T., *The Chemistry of Aqua Ions*, John Wiley and Sons, Ltd (1997).

[2]   Ayala, R., J.M. Martínez, R.R. Pappalardo, A. Muñoz-Páez, E. Sánchez Marcos, *J. Phys. Chem. B*, 112, 5416-5422 (2008).

[3]   Ayala, R., J.M. Martínez, R.R. Pappalardo, A. Muñoz-Páez, E. Sánchez Marcos, *J. Phys. Chem. B,* 113, 487-496 (2009).

[4]   Martínez, J.M., R.R. Pappalardo, E. Sánchez Marcos, *J. Phys. Chem. A*, 101, 4444-4448 (1997).

[5]   Martínez, J.M., R.R. Pappalardo, E. Sánchez Marcos, B. Mennucci, J. Tomasi, *J. Phys.Chem. B*, 106, 1118-1123 (2002).

[6]   *X-ray Absorption: Principles, Applications, Techniques of EXAFS, SEXAFS and XANES*, D.C. Koningsberger, R. Prins (Eds.), John Wiley and Sons, Ltd, New York (1988).

[7]   Díaz-Moreno, S., A. Muñoz-Páez, J. Chaboy, *J. Phys. Chem. A*, 104, 1278-1286 (2000).

[8]   Ayala, R., E. Sánchez Marcos, S. Díaz-Moreno, V. Armando Solé, A. Muñoz-Páez, *J. Phys. Chem. B*, 105, 7588-7593 (2001).

[9]   Merkling, P.J., A. Muñoz-Páez, E. Sánchez Marcos, *J. Am. Chem. Soc.*,124, 10911-10920 (2002).

[10]   Carrera, F., F. Torrico, D.T. Richens, A. Muñoz-Páez, J.M. Martínez, R.R. Pappalardo, E. Sánchez Marcos, *J. Phys. Chem. B*, 111, 8223-8233 (2007).

[11]   D'Angelo, P., A.D. Nola, A. Filipponi, N.V. Pavel, D. Roccatano, *J. Chem. Phys.*, 100, 985-994 (1994).

[12]   Palmer, B.J., D.M. Pfund, J.L. Fulton, *J. Phys. Chem.*, 100, 13393-13398 (1996).

[13]   Campbell, L., J.J. Rehr, G.K. Schenter, M.I. McCarthy, D. Dixon, *J. Synchrotron Radiat.*, 6, 310-312 (1999).

[14]   Goedecker, S., M. Teter, J. Hutter, *Phys.Rev. B*, 54, 1703-1710 (1996).

[15]   *CPMD V3.11*, Copyright IBM Corp. 1990-2008, Copyright MPI für Festkörperforschung Stuttgart 1997-2001. CPMD, *www.cpmd.org/*.

[16]   Tomasi, J., M. Persico, *Chem. Rev.*, 94, 2027-2094 (1994).

[17]   Mennucci, B., J. Tomasi, *J. Chem. Phys.*, 106, 5151-5158 (1997).

[18]   Zabinski, S.I., J.J. Rehr, A. Ankoudinov, R.C. Albers, M. Eller, *J. Phys. Rev. B*, 52, 2995-3009 (1995).

[19]   Mattheis, L., *Phys. Rev. A*, 133, 1399-1403 (1964); Mattheis, L., *Phys. Rev. A*, 134, 970-973 (1964).

[20]   Hedin, L., Lundqvist, S., in *Solid State Physics*, H. Ehrenreich, F. Seitz, D. Turnbull (Eds.), Academic Press, Vol. 23, pp. 1-181 (1969).

Figure 1: Snapshots of the CP-MD simulations where the most probable structures are shown

From simulation A) (top) $[Po(H_2O)_4(OH)_2]^{2+}$ and $[Po(H_2O)_3(OH)_3]^+$ aggregates are displayed.
From simulation B) (bottom) $[Po(H_2O)_5(OH)_2]^{2+}$ and $[Po(H_2O)_4(OH)_3]^+$ clusters are shown.
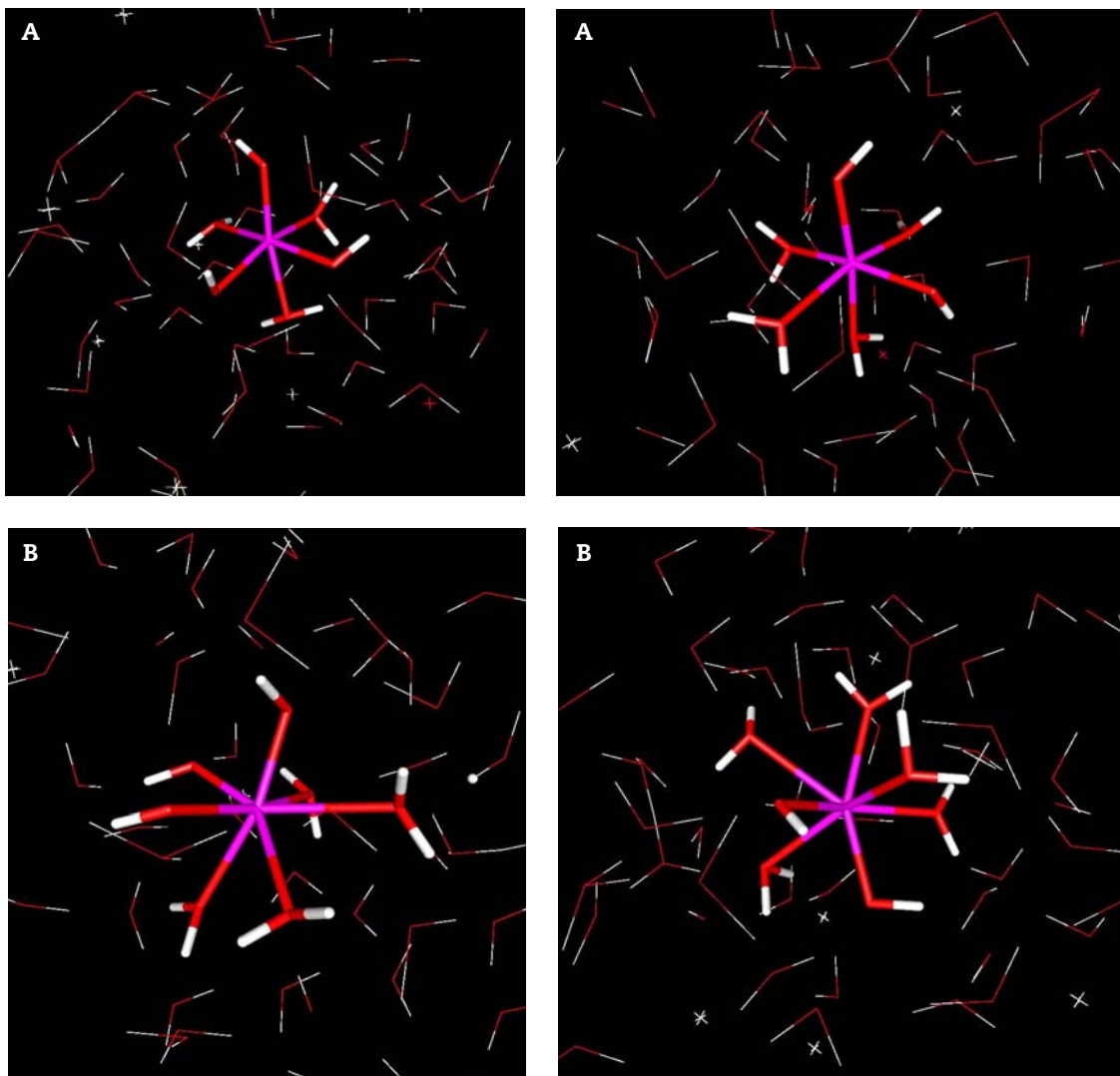
Figure 2: Theoretical XANES spectra computed for clusters of Po(IV) co-ordinated by different numbers of water molecules and hydroxyl ligands

The structures of the clusters were optimised with a continuum method in a previous work [3]. m labels the number of OH^- groups contained in each cluster.
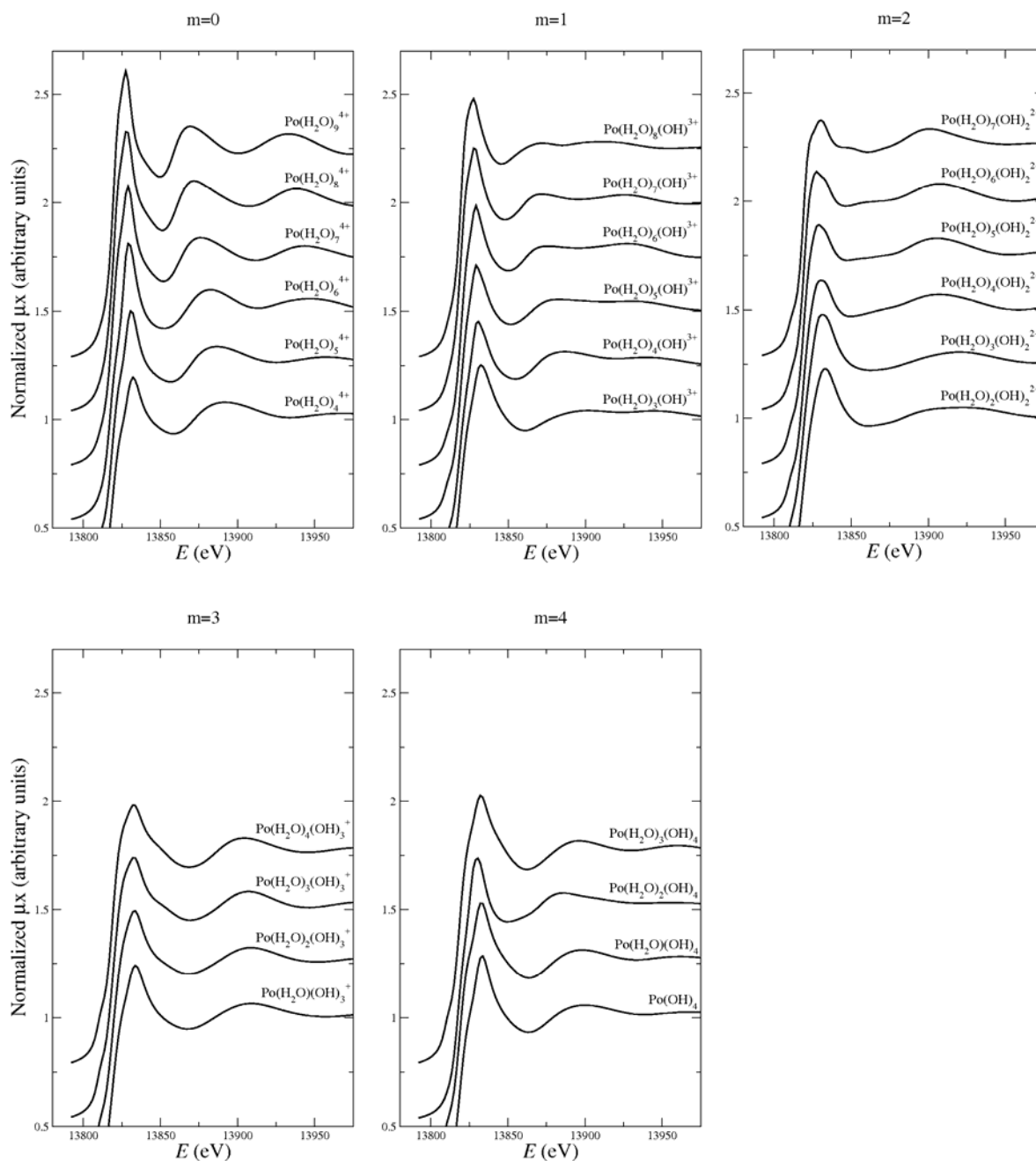
**Figure 3: Theoretical XANES spectra computed using snapshots extracted
from the CP-MD simulations (labelled "Trajectory A" and "Trajectory B")**

The dashed-and-point lines represent the standard deviation associated to the average spectrum. Weighted linear combinations of the theoretical spectra of the optimised clusters of $[Po(H_2O)_3(OH)_3]^+$, $[Po(H_2O)_4(OH)_2]^{2+}$, $[Po(H_2O)_4(OH)_3]^+$ and $[Po(H_2O)_5(OH)_2]^{2+}$ are plot in dashed lines for comparison with the average spectra obtained from the simulations.
Linear combination A: $0.8*\mu x([Po(H_2O)_3(OH)_3]^+) + 0.2*\mu x([Po(H_2O)_4(OH)_2]^{2+})$
Linear combination B: $0.87*\mu x([Po(H_2O)_4(OH)_3]^+) + 0.13*\mu x([Po(H_2O)_5(OH)_2]^{2+})$
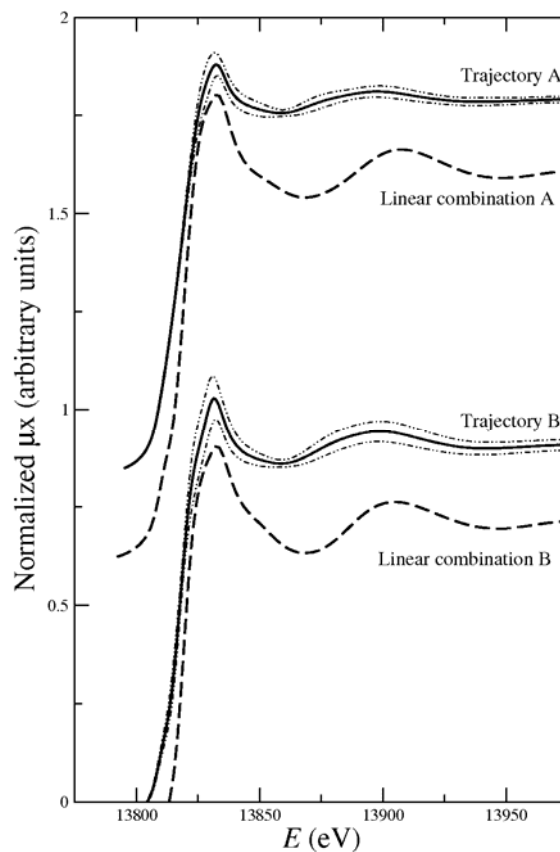
Design of a spectro-electrochemical cell for *in situ* XAFS studies of actinides

Xiaolan Liu, Burkhardt Fiehn, Boris Brendebach, Kathy Dardenne,
Christian M. Marquardt, Jörg Rothe, Melissa A. Denecke
Forschungszentrum Karlsruhe, Institut für Nuklear Entsorgung (INE)
Karlsruhe, Germany

Abstract

A spectro-electrochemical cell has been developed, in order to study the speciation of radio-elements in thermodynamic unstable redox states using in situ XAFS spectroscopy. The co-ordination structure and chemical valences of radionuclide species can be investigated in the cell by applying dynamic or constant potentials, in order to simulate conditions relevant to proposed nuclear disposal sites. In our spectro-electrochemical design, sample volume is small (up to 7 ml), thereby reducing the amount of activity needed in experiments. Both working and auxiliary electrodes are separated by a fritted glass tube in order to minimise ion migration between electrodes. The electrode's geometry ensures minimised ohmic drop between the reference (Ag/AgCl) and working electrode and provides a uniform distribution of current density and potential over the working electrode. The cell window is made of chemical resistant Kapton™ film. Both transmission and fluorescence mode XAFS can be performed with our cell. The cell can be placed within a second containment with standard sample holder design at the INE-Beamline for actinide research at the synchrotron source ANKA (Germany). This assures radiological safety for active samples and ease of placement onto the sample positioner. The reliability of our experimental set-up was validated by experiments at the INE-Beamline with reduction of non-radioactive Se(IV) to Se(-II), one of the most challenging electrochemical mechanisms. Future work will be focused on in situ protactinium (IV/V) speciation investigations combined with theoretical quantum chemical studies. The close proximity of the INE-Beamline to the INE radioactive laboratories is an advantage for the progress of these experiments.

Introduction

Predicting or ultimately controlling or prohibiting the transport of released radionuclides through the environment is essential to design safe repositories for disposal of high level nuclear waste. This requires a detailed understanding of the physical and chemical factors and processes determinant in their transport. Of central importance is the radionuclide speciation. *In situ* X-ray fine absorption spectroscopy (XAFS) is a useful speciation method that provides element-specific valence and short range information. In this contribution, a spectro-electrochemical cell has been developed, in order to study the speciation of radio-elements in thermodynamic unstable redox states using *in situ* XAFS spectroscopy. The co-ordination structure and chemical valences of radionuclide species can be investigated in the cell by applying dynamic or constant potentials, in order to simulate conditions relevant to proposed nuclear disposal sites. This is one of the reasons that coupling XAFS with electrochemistry receives growing attention in recent years [1-3]. In our work, long-lived nuclides relevant to the long-term safety of nuclear waste disposal are of special interest. This includes the actinide elements, as well as radionuclides which are relatively poorly sorbed onto geological media such as ^{99}Tc and ^{79}Se. The reliability of the experimental set-up was validated by experiments with non-radioactive Se. The electrochemical reduction of Se(IV) to Se(-II), one of the most challenging electrochemical mechanisms, was investigated at the INE-Beamline for actinide research at the synchrotron source ANKA (Germany) [4]. Recently, this device was successfully used to study the redox behaviour of Np(III)-Np(VI) ions in aqueous perchlorate solution by *in situ* XANES/EXAFS [5].

Cell design

The cell design proposed and tested by Antonio and Soderholm [1] served as a basis for our spectro-electrochemical cell, with the modifications and improvements necessary in order to meet the special specifications of the INE-Beamline set-up. In the new design (see Figure 1), the total cell volume is limited to 10 ml and sample volume reaches up to 7 ml. This small volume reduces the amount of activity needed in experiments. The cell is constructed of Plexiglas (7), which has the advantage of being able to see into it. Our cell has a three-electrode design, with the working and auxiliary electrodes (1 and 3) both made of vitreous (or glassy) carbon. Other electrodes such as Pt and Hg can also be used. These two electrodes, as well as the gas inlet (12), are screwed onto the top of the cell using standard nuts and sealed with matched tight-sealing ferrules on the inside of the cell. The Ag/AgCl reference electrode used (2) is mounted and sealed tight onto the cell top with an O-ring. Different connectors are used to ensure electric connection of the electrodes. The removable working and auxiliary electrodes are separated by a large fritted glass tube (1 cm diameter), in order to minimise ion migration between the two electrodes. This separation made the XANES data free of compositional interferences due to redox products from auxiliary electrode reactions. The reference electrode is placed equidistant to the cathode and anode. The electrode geometry ensures not only a minimised ohmic drop between the reference and working electrodes, but also provides a uniform distribution of current density and potential over the working electrode. Consequently, both potentiostat and galvanostat modes can be performed with the cell for bulk electrolysis. The distance and the angle between the working and counter electrodes are arranged so that X-ray beam pass by the working electrode without hitting the counter electrode in both transmission and fluorescence measuring modes.

The cell can be stirred during measurements with a magnetically driven stirrer outside of the cell and a Teflon coated stir bar. The cell window (4) is made of Kapton™ film, which is known for its resistance to aggressive electrolyte under prolonged experimentation and for its transparency to X-rays. Other types of window materials can also be used according to different experimental aims. The windows are sealed with Viton O-rings (6) and the windows affixed with screws. Both transmission and fluorescence mode XAFS can be performed with our cell. For assuring radiological safety for active samples, the cell can be placed within a windowed second containment (16), which fits onto the standard sample holder/positioner at the INE-Beamline for ease of position adjustment. Meanwhile, all the electrode connectors were enclosed through the use of a Plexiglas box fixed onto the standard sample holder and sealed with a big Viton O-ring (8), whereas all the cables and tubing passed through a docking system (14) mounted on the top of the box and were tightened.

Figure 1: Blue print of the spectro-electrochemical cell design

Left: Drawing of the spectro-electrochemical cell outer casing
Right: Cell inside second windowed containment with protective sleeve covering all electrode connectors and gas inlet/outlet

(1) working electrode position; (2) reference electrode position; (3) auxiliary electrode position; (4) Kapton® film; (5) Al frame; (6) Viton O-ring; (7) Plexiglas cell body; (8) groove for Viton O-ring used to seal the attached Plexiglas sleeve; (9, 10) screw holes for the cell lid and sleeve; (11) gas outlet; (12) gas inlet; (13) cell lid; (14) docking system; (15) protective Plexiglas sleeve; (16) containment corpus
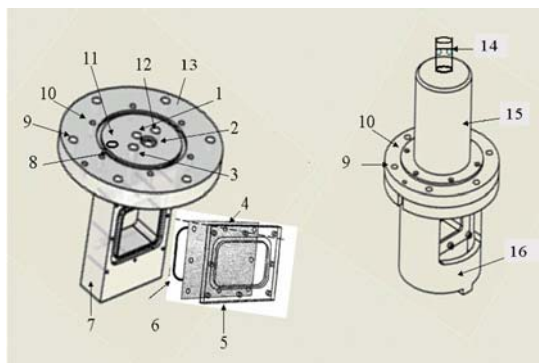
Set-up at the INE-Beamline

A photograph of the actual set-up at the INE-Beamline during initial experiments is depicted in Figure 2. The first measurements were performed without the secondary containment around the electrochemical cell [Figure 2(a)] and the second round of experiments with the containments [Figure 2(b)], although this was an inactive experiment. A remote controlled potentiostat was used (Radiometer Analytical®) for these experiments. Sample concentrations varied from 0.5 mM to 5 mM and applied potentials ranged from -0.8 V to -1.5 V (Ag/AgCl).

Figure 2: Experimental set-up at the INE-Beamline (a) without the outer, second containment, (b) with the containment
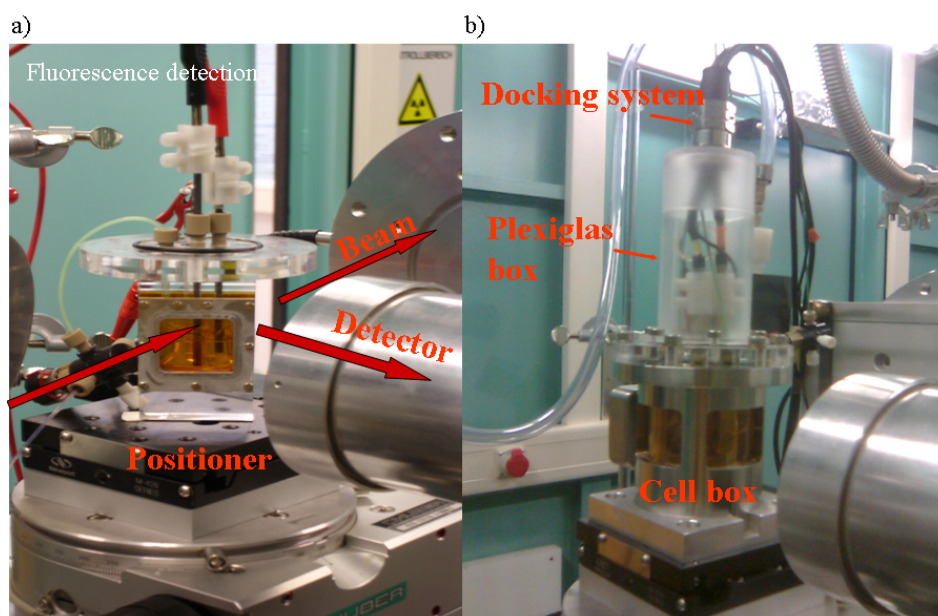
XANES at the Se-K edge were recorded with tuneable monochromatic beam delivered by the Ge(422) crystal pair in the double crystal monochromator (DCM). Higher harmonics were rejected from the two mirrors in the optics of the INE-Beamline and by detuning the second crystal [4]. XANES spectra were recorded in fluorescence mode using a high purity solid state Ge detector (Canberra) and Ar-filled ionisation chamber to record the incident beam intensity. The energy of the radiation coming from the DCM was calibrated against the first inflection point in the Au L3 XANES of an Au foil defined as 11 918 eV. The WINXAS software [6] was used to isolate the background, normalised spectra from the raw data.

Initial experimental results

Selenide solution can be prepared electrochemically by reducing selenite in NH_4Cl electrolyte with mercury-pool electrode, according to the method developed by J.J. Lingane, *et al.* [7], and modified by Liu, *et al.* [8,9]. With this method, a selenide solution of 5×10^{-3} mol/L can be obtained within 2-3 h in a standard electrochemical cell. In this study, two different electrodes were successively used to reduce Na_2SeO_3: a vitreous carbon electrode and a mercury electrode. The initial concentrations of Se(IV) were 0.5 mM and the pH value of 1 M NH_4Cl electrolyte was kept around 8. An *ex situ* experiment was also performed using vitreous carbon electrode under identical conditions. The results are showed in Figures 3 and 4, respectively.

Following the first experiment as well as the *ex situ* test, the final solutions contained numerous red colloids, representing amorphous elemental selenium [7-9]. At the end of the second run, the solution remained colourless, turning orange or red according to the initial concentrations after exposure to air. This strongly suggests the presence of Se(-II) because colourless selenide ions can easily be re-oxidised to red elemental selenium in the presence of oxygen. A simple polarographic test can prove it in this case, as previously reported in the literature [7, 9]. The red colloids obtained at the end of the *ex situ* experiment were collected and re-dispersed in 5×10^{-3} mol/L of Na_2SeO_3. The XANES spectra of this suspension were recorded and used as reference for edge position comparison, as shown in Figures 3 and 4 and Table 1.

As can be seen from both figures, the electrochemical reduction of SeO_3^{2-} is marked by the appearance of a spectral figure at lower ionisation energy position over successive scans. Their respective differences in edge position are found to be 4 eV and 4.5 eV (see Table 1). The reaction kinetics, however, appear to be different. In the first experiment the intensity of the new peak

Figure 3: *In situ* Se K-edge XANES of Se(IV) reduction with vitreous carbon rod as working electrode under -1 000 mV (Ag/AgCl)
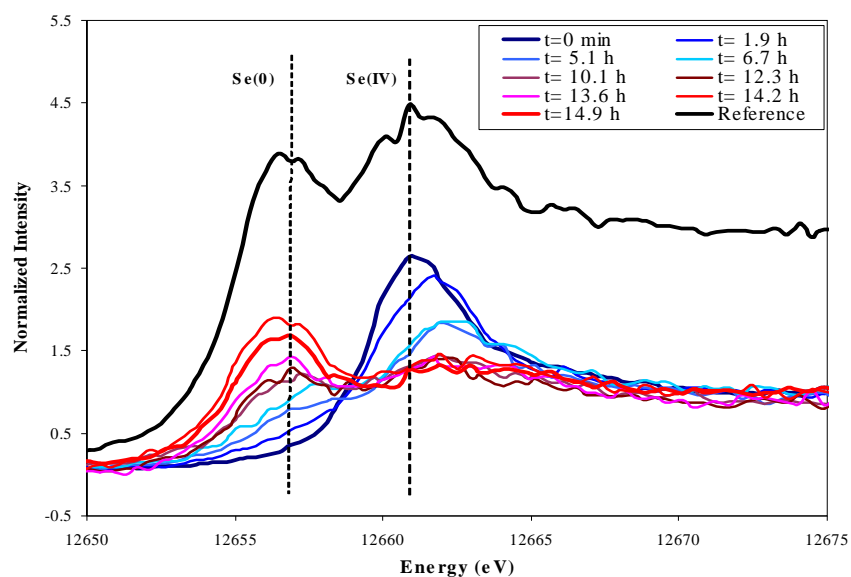
Figure 4: *In situ* Se K-edge XANES of Se(IV) reduction with mercury as working electrode under -1 500 mV (Ag/AgCl)
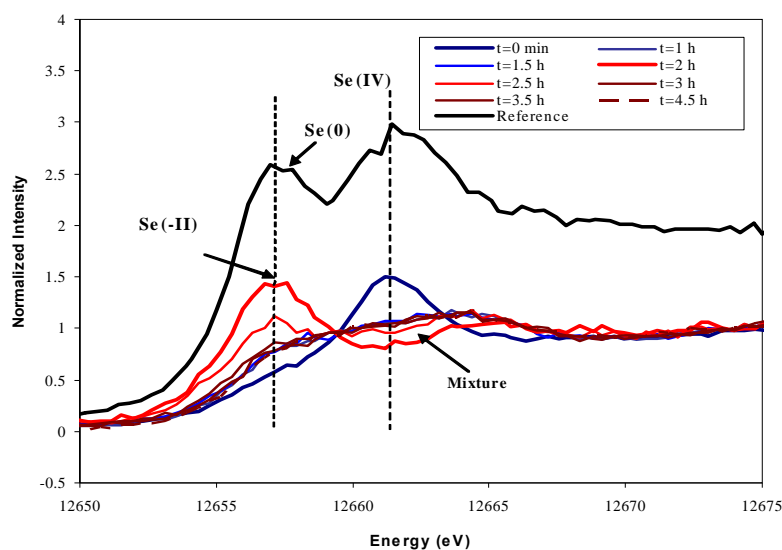
Table 1: Selenium K-edge energies

	Se(-II)	Se(0)	SeO$_3^{2-}$	ΔE (eV)
1. Glassy C electrode	–	12 658 eV *amorphous*		4
2. Hg electrode	12 657-12 658 eV	Not separated	12 662* eV	4-5 (≈4.5)
Reference	–	12 658 eV *amorphous*		4
Literature [8,9]	–	12 660 eV *amorphous*	12 664 eV	4
Literature [10,11]	12 656-12 658 eV FeSe, FeSe$_2$	12 658-12 659 eV *crystalline*	12 662 eV	–

* Defined values.

increased as that of Se(IV) decreased. For the second run, this trend is not evident. The peak of Se(IV) rapidly disappeared as the reaction proceeded, suggesting a rapid reaction kinetics. The intensity of the new figure, however, did not appear as function of time. The quasi-permanent presence of non-resolved valence mixture represents another main spectroscopic feature of the second experiment. By comparing the Se K-edge energies to our reference data and literature values, and to the defined edge position of the Na$_2$SeO$_3$ reference (12 662 eV), we found that the final product of the first experiment with the carbon electrode is amorphous elemental selenium, and that of the second run could be Se(-II), in the presence of counter-cations Na$^+$ and NH$_4^+$. These results are comparable to previously reported values on natural minerals [10,11].

Little ambiguity seems exist in elemental selenium (amorphous or crystalline) edge position interpretation; that of Se(-II) is still a matter of discussion. Generally, the K edge positions of Se(0), Se(-I) and Se(-II) are found to be very close, even overlaid, which hinders an exact interpretation [12]. Moreover, no edge position of aquo selenide ions is available in the literature, which might differ from those of crystalline forms because of different local co-ordination environments. Compared to the first experiment with vitreous carbon electrode, the reduction of Na$_2$SeO$_3$ using mercury-pool electrode exhibited not only different experimental aspect which consists with literature description of Se(-II) behaviour, but also distinguished spectral features, as described above. This can be explained by selenite reduction kinetics (see equations below). Reduction of Se(IV) can form selenide directly, which then reacts with remaining Se(IV) to form Se(0). Se(0) is then reduced to Se(-II) [7]. This three-step reaction mechanism is in good agreement with the results obtained by using mercury working electrode, as shown in Figure 4.

$$HSeO_3^- + 6e^- + 4H^+ \Leftrightarrow HSe^- + 3OH^- \tag{i}$$

$$HSeO_3^- + 2HSe^- \Leftrightarrow 3Se^0 + 3OH^- \tag{ii}$$

$$Se^0 + H^+ + 2e^- \Leftrightarrow HSe^- \tag{iii}$$

However, the conversion of red amorphous selenium to selenide must be therefore conducted very quickly; otherwise colloidal selenium tends to aggregate, as in our test experiment with the carbon electrode. Formation of red colloidal elemental selenium leads not only to loss of reactivity, but also to adsorption of newly-formed selenide onto the colloidal selenium [8-10,13]. As a consequence, no clear selenide solution will be obtained. With a mercury-pool electrode capable of minimising water electrolysis and providing a uniform and reproducible surface, the entire reduction of Se(IV) to Se(-II) can be easily completed under very negative potential. Moreover, mercury can also provide a reducing environment ideal for selenide preservation. This is not the case for the vitreous carbon electrode, although it can also displace water electrolysis. From these points of view, we might conclude that the final product in the second experiment was Se(-II), and the origin of the slight edge position difference (0.5 eV) between two final products of this study must be structural, not experimental.

In these initial measurements with the electrochemical cell we were successful in reducing Se(IV) to Se(-II) using mercury as working electrode and coupling the electrochemical reduction to XANES detection. The slight difference between the (IV)/(-II) and (IV)/(0) redox pairs may be linked to a high degree of covalency of Se(-II) compounds. Covalent bonding draws electron density from the absorber, thereby de-screening core states and leads to a positive shift in ionisation energy. Furthermore, the Se K-edge is sensitive to variations in local co-ordination environment, including crystalline and aqueous forms of the same ions, and different element allotropes [10-12]. The presence of surface sorbed Se(-II) onto the elemental selenium colloids (cf. below) can also be responsible for the small absorption energy difference observed between Se(-II) and Se(0) by shifting the measured average edge energy of the colloids.

Conclusion and outlook

We have constructed a spectro-electrochemical cell and successfully tested its reliability on non-radioactive Se at the INE-Beamline. The reduction mechanism of Se(IV) to Se(-II), one of the most challenging electrochemical mechanisms, was investigated. Differences between results obtained with a vitreous carbon working electrode and a mercury-pool electrode yield tentative insight into reduction mechanism.

Future work will be focused on *in situ* actinide redox experiments, *e.g.* protactinium (IV/V) speciation investigations combined with theoretical quantum chemical studies. The close proximity of the INE-Beamline to the INE radioactive laboratories is an advantage for the progress of this experiment. The spectro-electrochemical cell design is presently being optimised to allow simultaneous UV-Vis spectrometric measurements in order to perform coupled UV-Visible/XAFS electrochemistry experiments.

References

[1]   Antonio, M.R., L. Soderholm, *Journal of Applied Electrochemistry*, 27, 784-792 (1997).

[2]   Poineau, F., M. Fattahi, C. Den Auwer, C. Hennig, B. Grambow, *Radiochimica Acta*, 94, 283-289 (2006).

[3]   Schlegel, M., B. Grambow, M. Fattahi, X. Liu, *Experimental Report*, ESRF (2006).

[4]   Denecke, M.A., J. Rothe, K. Dardenne, H. Blank, J. Hormes, *Physica Scripta*, T115, 1001-1003 (2005).

[5]   Liu, X., N.L. Banik, B. Brendebach, K. Dardenne, J. Rothe, C.M. Marquardt, M.A. Denecke, *Talanta* (2008), submitted.

[6]   Ressler, T., *Journal of Synchrotron Radiation*, 5, 118-122 (1998).

[7]   Lingane, J.J., L. W. Niedrach, *Journal of Chemical Society*, 70, 4115-4120 (1948).

[8]   Liu, X., M. Fattahi, G. Montavon, B. Grambow, *Radiochimica Acta*, 96, 473-479 (2008).

[9]   Liu, X., «La Rétention du Séléniure sur la Pyrite sous Conditions Redox », thèse de l'université de Nantes, France (2008).

[10]   Pickering, I.J., G.E. Brown, Jr., T.K. Tokunaga, *Environmental Science & Technology,* 29, 2456-2459 (1995).

[11]   Sheidegger, A.M., D.S. Grolimund, M. Janousch, D. Cui, document from Paul Scherrer Institut (2003): *Sls.web.psi.ch/view.php/science/docs/annual/Scheidegger03.pdf*.

[12]   Ryser, A.L., D.G. Strawn, M.A. Marcus, J.L. Johnson-Maynard, M.E. Gunter, G. Möller, *Geochemical Transactions*, 6, 1-11 (2005).

[13]   Nuttall, K.L., F.S. Allen, *Inorganica Chimica Acta*, 89, 199-201 (1984).

A combined μ-XRF, μ-XAS, STXM and μ-FTIR investigation on the uranium speciation of samples from Autunian shales of the Permian Lodève Basin (France)

P. Michel,[1] **M.A. Denecke,**[1] **T. Schäfer,**[1] **B. Brendebach,**[1] **K. Dardenne,**[1]
J. Rothe,[1] **T. Vitova,**[1] **F. Huber,**[1] **K. Rickers,**[2] **M. Elie,**[3] **G. Buckau**[1]
[1]Institute für Nukleare Entsorgung (INE), Forschungszentrum Karlsruhe, Karlsruhe, Germany
[2]Hamburger Synchrotronstrahlungslabor (HASYLAB) at DESY, Hamburg, Germany
[3]Gestion des Ressources Minières Minérales et Energétiques-UMR, Vandoeuvre-lès-Nancy, France

Abstract

Spatially resolved spectroscopic investigations with a nanometre to micrometer-scale resolution (μ-XRF, μ-XAFS, STXM and μ-FTIR) focused on the U speciation in two clay-rich samples originating from the Autunian shales (Permian Lodève Basin; France) a natural uranium deposit associated with organic matter (bitumen). The goal of this study was to determine the U oxidation state in the samples and to ascertain if any correlation between the U distribution and that of other selected elements present in the clay (K, Ca, Ti, Fe, Zr and C) exists. Identification of uranium associated with organic matter and/or mineral phases (e.g. iron oxides, clay minerals) can potentially give insight into the mechanism of uranium immobilisation in this sedimentary formation. μ-XRF and μ-XAFS measured in confocal geometry show that the U is present as U(IV) and its distribution is not correlated to areas with a high Fe content, but rather correlates with the distribution of lighter elements. U L3 μ-EXAFS recorded at areas with high U concentration reveals that U in these hot spots is likely present as a nanocrystalline uraninite (UO_2)-like phase. Clay fractions of the samples characterised by XRD are mainly composed of chlorite and illite. STXM carbon K-edge, potassium L-edge and iron L-edge investigations conducted on sulphur-embedded microtomes show two types of organic matter present, one positively correlated with the elements K and Fe and another of pure organic composition building fracture infill. The μ-FTIR measurements clearly reveal a direct association of organic matter with clay minerals. From combined results a tentative hypothesis of U immobilisation is put forward. Such investigations support development of reliable assessment of the long-term radiological safety for proposed nuclear waste disposal sites.

Introduction

Micro-focused synchrotron radiation techniques are becoming an increasingly used tool in nuclear waste disposal research to investigate actinide mobility controlling processes in geological media. Reasons for this are driven by the need to characterise actinide speciation in heterogeneous natural systems [1]. The goal of these investigations is to identify and characterise long term determinant processes of actinide transport in geological media, requisite to establishing reliable prognoses for radionuclide mobility in nuclear waste disposal sites. Investigations of actinide geological transport in the context of nuclear waste disposal are especially challenging, as an accurate prognosis demands process understanding over a geological time domain. One strategy for meeting this challenge is through investigations of natural analogues. Natural analogues help to put these time frames into a comprehensible context by basing prognoses for future assessment time periods on past history. In this way, knowledge gained from natural analogues is used to span the long time scales in a top down approach for predicting repository radiological safety. Claystone formations or argillites are currently favoured as deep geological host rocks in France and Switzerland. The similar sedimentary sequence found in the uranium ore-deposit (Lodève Basin, Massif Central, southern France) investigated in this study with that for proposed spent fuel repository in claystone formations render potentially suitable as an analogue. Samples originating from this formation are subject of this investigation.

Geological setting

The Lodève Basin extends about 150 km^2 north-south and consists of post-sedimentary tectonically overprinted Permian and Carboniferous superior (Stephanian) sequences covering dolomites and schist's of the Hercynian basement (Figure 1). Despite the complex geological history the actual architecture of the basin has kept its original Permian structure [2]. Activation of a listric fault during the lower Thuringian on the southern border of the basin led to a 15-20° southward tilting half-graben structure and extensive erosion between the Upper Permian and Middle Trias removed about 1 500 m of the uppermost sediments [3].

Figure 1: North-South (N-S) cross-section of the Lodève Permian Basin [4].
The geological layering is explained in the legend at the lower left. The origin
of the samples is marked by ★. Faults are indicated with solid and dotted lines.
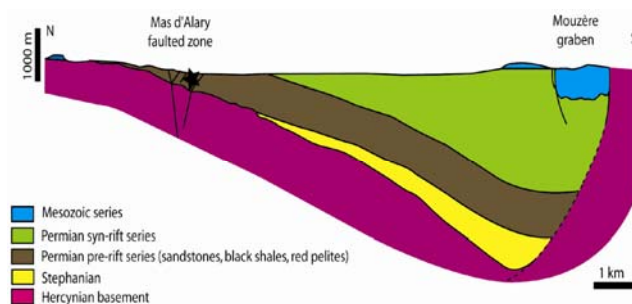
Therefore, on the northern border of the Lodève Basin sediments of the Autunian pre-rift series (Lower Permian) are exposed. This pre-rift series consists of sandstones (fluvio-deltaic deposits), black shales (anoxic deep lacustrine deposits containing organic matter) and pelites (upward to sub-immersive floodplain deposits) [4].

High uranium concentrations are observed in the fluvio to deltaic Autunian deposits and more particularly in the Mas d'Alary faulted zone (Figure 1). The formations of the uranium mineralisation were formed around 173±6 and 108±5 Ma ago corresponding to two major tectonic events (Pyrenean and Alpine formation) [5]. Two types of fluids can be differentiated: *i)* fluids generated during the burial reaching the oil-window stage; *ii)* hydrothermal fluids, which both may have transported metallic ions, notably U(VI). The uranium remobilisation is thus the result of fault zone fluid flow and not a syngenetic or diagenetic deposit [5]. Hercynian granodiorites are assumed to be the initial source of uranium in the Lodève basin. The uranium mineralisations are closely associated with organic matter (mostly marine type III), mainly present in the form of bitumen occurring in the reservoir

facies [6-9]. A genetic link between the natural deposited bitumen and the migrated organic material found in the Permian petroleum source rocks has been shown by biomarker analysis [6]. In the particular case of the Lodève basin the conceptual model is that oxidised U(VI)-bearing fluids reacted within fault zones with the strongly reducing environment of the oil reservoir rocks to form/ precipitate bitumen-type material and uranium ore [6]. The observed inverse relationship between the amount of extractable organics and uranium concentration has been attributed to the radiolytic bitumen degradation [7,8]. Oils acting as reductants to precipitate U(IV) phases from U-bearing hydrothermal fluids circulating in oil reservoirs has also proposed, based on the organic chemistry as well as mineralogy, *e.g.* for the Oklo natural reactors [9].

The goal of this study is to characterise the oxidation state and speciation of uranium found in U-enriched regions of a sediment sample from the Lodève Basin and to elucidate if organic matter was directly responsible for uranium reduction or if Fe^{2+}, Mn^{2+}, S^{-2} containing mineral phases formed by anaerobic degradation of the organic matter may have been responsible for uranium immobilisation and accumulation. For this purpose, investigations with micro- to nanoscale resolution are applied, these are micro-X-ray fluorescence (μ-XRF), micro-X-ray absorption fine structure (μ-XAFS), scanning transmission X-ray microscopy (STXM), as well as synchrotron-based Fourier transform infrared microspectroscopy (μ-FTIR).

Materials and methods

The two uranium ore samples investigated in this study are provided by CREGU (Nancy, France) and originate from the fault zone of the Autunian shales, collected in the breccia facies at the Mas d'Alary uranium mine located near Lodève (Figure 1), taken from the horizon 21. Sample 15 originates from the contact zone adjacent to the fault zone, whereas sample 31 stems directly from the breccia facies within the fault zone. For STXM and μ-FTIR measurements, transmission mode ~100 nm thick sulphur embedded ultra-microtomes on TEM grids are prepared (MVA, Inc., Norcross, GA, USA) to prevent cross-contamination with organic embedding materials (*e.g.* epoxy-resin). The bitumen H/C and O/C atomic ratio are 1.23 and 0.02, respectively [7]. The clay fraction (<2 μm) of these two samples is shown by X-ray diffraction to be composed mainly of illite and chlorite minerals. Autoradiographic images of each sample are recorded with a Cyclone Phosphor Scanner (Packard BioScience, Dreieich, Germany) calibrated for quantitative α-activity analysis with a 500 ppm natural uranium spiked glass disk. Regions showing high α-activity are selected for further μ-XRF and μ-XAFS characterisation.

μ-XRF and micro-X-ray absorption near edge spectroscopy (μ-XANES) measurements are recorded at Beamline L at the Hamburger Synchrotronstrahlungslabor (HASYLAB). A confocal irradiation detection geometry is used, providing added depth information and allowing probing sample volumes below the surface, thereby avoiding any surface oxidation artefacts caused by cutting and polishing of the clay sample. Elemental distribution maps are obtained by means of scanning μ-XRF and plotting recorded relative fluorescence intensities for each pixel. The pixels are scaled linearly according to their fluorescence intensity, with dark pixels corresponding to high fluorescence counts. By scanning arbitrary sample areas (x,y scans) at different depths (z) using the confocal set-up, stacks of tomographic cross-sections can easily be recorded [10,11]. Poly-capillary half lenses are used for both focusing and collimating optics. The focal spot diameter is approximately 16 μm. μ-XRF measurements are recorded using a band pass of wavelengths with an average weighted energy of 17.6 keV delivered by a Mo/Si multi-layer pair (AXO Dresden GmbH, Germany) and a Si drift detector (Vortex, SII NanoTechnology USA Inc., Northridge, CA). U L3 μ-XANES are recorded using monochromatic X-rays at selected sample volumes of high U concentration identified in the μ-XRF maps at Beamline L. XAFS spectra are registered with a high purity Ge detector (Canberra) at the INE-Beamline at the Ångströmquelle Karlsruhe, ANKA [12]. U L3-edge EXAFS are measured at positions of high U concentration identified by line scans of windowed U Lα counts using the primary beam coming from the focusing mirror. The measured primary beamspot diameter is 300 μm. A focused secondary beam of around 30 μm is obtained using a poly-capillary lens, loaned from HASYLAB. The U distribution over a 2×1 mm² area of sample 15 and μ-XANES from high-U concentrated areas, recorded with this focused beam is the first spatially resolved experiment conducted at the INE-Beamline. dSi(111) and Ge(422) crystals are used in the double crystal monochromator (DCM) HASYLAB and ANKA, respectively. The DCM energy is calibrated relative to the first inflection point in the K XANES of a Y foil (defined as 17.038 keV).

Scanning transmission X-ray microscopy investigations are conducted at the National Light Source Synchrotron (NSLS), Brookhaven National Laboratories (BNL) in New-York, undulator beamlines X1A1 (C, K and Ca) and X1A2 (O and Fe) operated by the State University of New York at Stony Brook [13]. The principle of this technique is described in detail elsewhere [13]. Carbon K-edge, potassium L-edge and oxygen K-edge spectra are recorded at an undulator gap of 36.8 mm, whereas for iron L-edge and calcium L-edge measurements the undulator gap is 41.7 mm. The Fresnel zone plate used at the end station X1A1 has a diameter (a) of 160 µm and a outermost zone width (δ) of 45 nm; at end station X1A2 a zone plate with a = 80 µm and δ = 30 nm is used. The spherical grating monochromators energy is calibrated using the photon energy of the O_2 gas adsorption band at 530.82 eV for X1A2 and the CO_2 gas adsorption band at 290.74 eV for X1A1 [14].

µ-FTIR measurements are performed at beamline U10B (NSLS, BNL) using a Nicolet Magna 860 Step-Scan FTIR instrument coupled to a Spectra-Tech Continuum IR microscope, which is equipped with a 32x Schwarzschild objective and a dual remote masking aperture [15]. Data acquisition is controlled with the Atlµs software (Thermo Nicolet Instruments), using a 8 µm × 8 µm aperture and 1 024 scans per point in the mid-IR range (600 to 4 000 cm^{-1}), under transmission mode with 4 cm^{-1} spectral resolution. The background signal is measured in sample-free regions of the TEM grid.

Results and discussion

µ-XRF and µ-XAFS results

Autoradiographic images and photographs of the two clay samples studied are shown in Figure 2. Uranium-rich hot spots are visible as dark grey areas in the autoradiographic images. Quantification of the hot spots shows they contain ~2 mg ^{238}U/g material (sample marked 31) and ~25 mg ^{238}U/g material (sample 15). The measured distributions of K, Ca, Ti, Fe, Zr, and U in the area with the highest radioactivity at the top of sample 15 are shown in Figure 3.

Figure 2: Photographs of the samples studied embedded in epoxy-resin and their corresponding autoradiographic images

Sample 15   Sample 31

25 mm
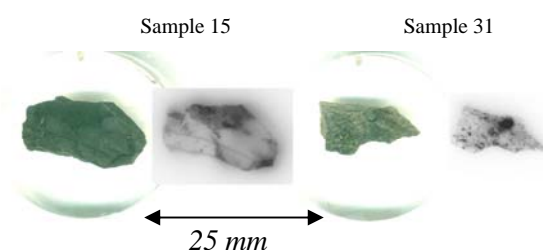
Figure 3: Distribution maps for the elements in a 800 µm × 760 µm section (20 × 20 µm step size), recorded near the surface of sample 15

K K$_\alpha$ Ca K$_\alpha$ Ti K$_\alpha$ Fe K$_\alpha$ Zr K$_\alpha$ U L$_\alpha$
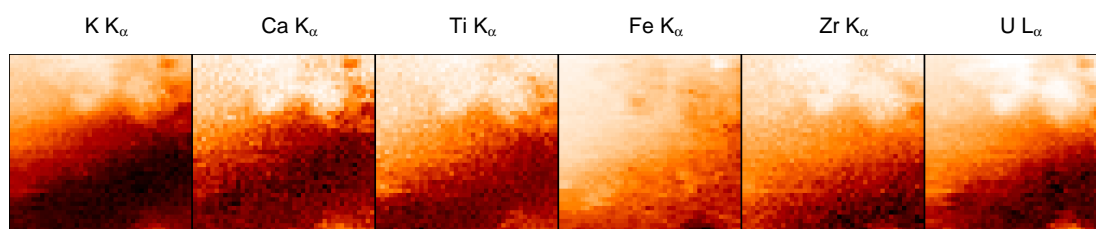
These graphs reflect three general observations: *i)* distinct patterns of element distributions are observed, despite the sample's general heterogeneous optical appearance; *ii)* the U distribution is often correlated with the distributions of lighter weight elements Ca, K and Ti (especially notable in the round features in the upper right corner of the maps) and *iii)* the U distribution seems to be inversely correlated to Fe hot spot areas.

A comparison of K, Ca, Ti, Fe, Zr and U elemental distributions for an area with high radioactivity at the top of sample 31 is depicted in Figure 4. A red-green-blue (RGB) overlay image of regions exhibiting the highest Ti, Fe and U fluorescence intensities, respectively, is also shown. A direct correlation between Ti and U is visible as purple areas in the RGB image, but none between Fe and U; the Fe-rich areas remain green in the RGB overlay. In contrast to the positive correlation between Ca and U observed for sample 15 (Figure 3), no correlation between Ca and U is observed for sample 31. Instead we observe a localised area with strong Ca fluorescence, covering a number of tens of μm. This is likely a calcite particle.

Figure 4: Distribution maps for K, Ca, Ti, Fe, and U in a 400 μm × 400 μm section (10 × 10 μm step size, 1 s counting time), recorded under the surface of the sample 31 area marked in the microscope image at far right. RGB overlay image for regions of highest Ti, Fe, and U concentrations is shown.
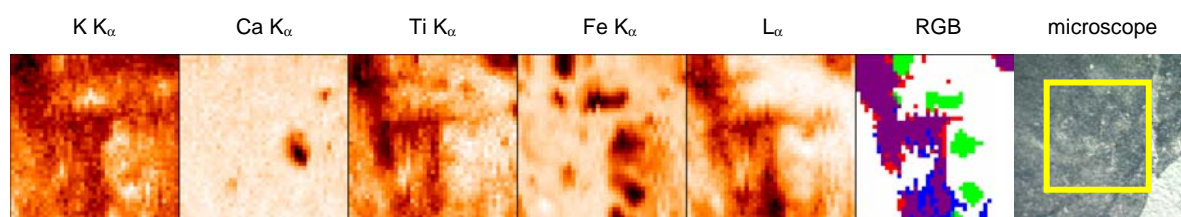
The distribution maps reveal: *i)* this sample exhibits are more pronounced pattern of element distributions compared to sample 15; *ii)* the U distribution tends to be correlated with the K and Ti distributions; *iii)* the U distribution is generally inversely correlated to the Fe content; *iv)* we find indirect evidence for calcite.

In order to determine the valence state of the U in the pelites, U L3 μ-XANES (Figures 5 and 6) and μ-EXAFS (Figure 7) are recorded at volumes and areas with high U Lα intensity. The energy position of the most prominent absorption peak in the XANES (the white line, WL) measured for different sample regions at two different beamlines (INE-Beamline Figure 5 and Beamline L Figure 6) all lie within less than 1 eV of that for the U(IV) reference. The XANES features themselves also provide further evidence that the U hot spots contain U(IV). No evidence for the presence of any U(VI), which would be indicated by a decreased WL intensity and multiple scattering feature around 10 eV above the WL [16], was found. We conclude that U is likely present in the sample in the tetravalent state.

Figure 5: Left: U distribution for a 2 000 × 1 000 μm² section (30 × 30 μm² step size) recorded at the INE-Beamline at the surface of sample 15. The normalised U Lα intensity scale bar is indicated.
Right: U L3 μ-XANES recorded at four independent areas with high U Lα intensity.
Approximate areas from where the XANES were collected are circled in the U distribution map.
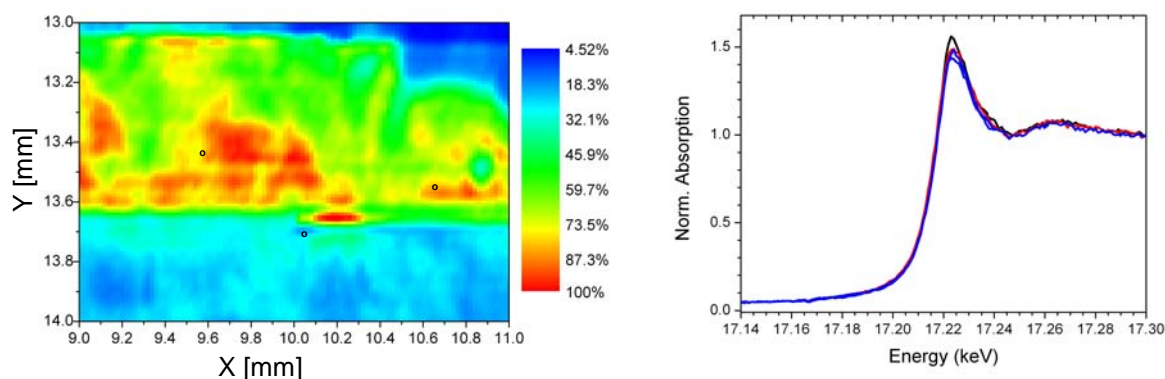
Figure 6: U L3 μ-XANES recorded at U hot spots of sample 15 at Beamline L (symbols) and compared to two U(IV) and U(VI) reference spectra (bottom)
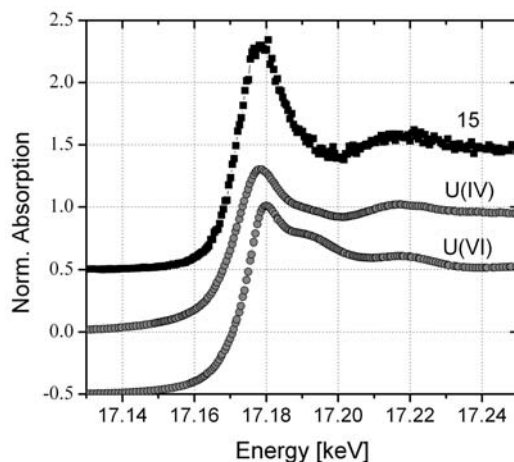
Figure 7: U L3 k^2-weighted EXAFS [χ(k); left bottom], Fourier-filtered data and best fit results (left top) and corresponding k^2-weighted Fourier transform (FT) data (right) plotted with best fit results.

Experimental data = lines. Fit curves = symbols.
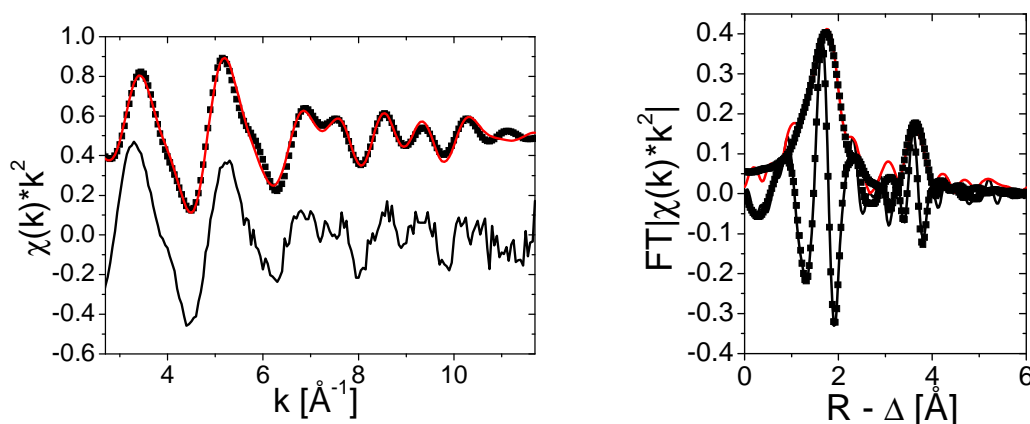
This interpretation is corroborated by the U L3 EXAFS spectrum (Figure 7). No short U-O distance expected for the U(VI) uranyl moiety is found in the EXAFS spectrum [16]. The data is fits well, beginning with a structural model similar to uraninite, UO_2 [17]. Best fit results are obtained with 4-5 O atoms at 2.29 Å with $\sigma^2 = 0.013$ Å^2 and 2-3 U atoms at 3.78 Å with $\sigma^2 = 0.008$ Å^2. The distances are 2-3% smaller than expected for UO_2 and the intensities lead to a much smaller co-ordination number than expected [N(O) = 8; N(U) = 12]. This may indicate that the UO_2-like phase is present as a nano-particulate material with large surface area having relaxed (shortened) distances at the surface.

STXM results

The results of principle component analysis (PCA) and cluster analysis of STXM data for sample 15 are depicted in Figure 8. We observe a homogeneous distribution of organic carbon, with the exception of one strip (grey area, upper right in Figure 8), where no absorption at the carbon K-edge is detected. The yellow and red areas found in cluster analysis differ in their optical density (OD, a measure of absorption = ln(I0/I1)) and K content. The red areas exhibit a significantly higher OD below the carbon K-edge (OD ~0.8; see Figure 9) and significant absorption bands at potassium $L_{2,3}$-edge energies. This indicates that this organic material is associated with clay minerals possibly of illite-type. The relatively

Figure 8: STXM PCA and cluster analysis of sample 15

Left: Distribution of organic functionality with two distinguishable clusters found using
PCA and cluster analysis. Right: Distribution of iron absorption. The scale bar is 10 μm. As the
Fe L-edge region is slightly rotated counter-clockwise numbers are inserted for orientation.
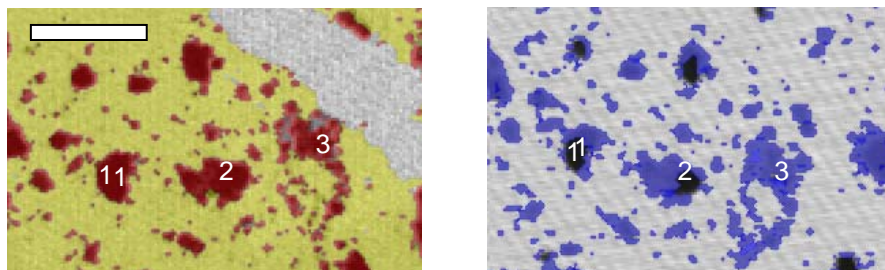
large edge jump (ΔOD ~0.4) of these regions shows that a rather large amount of organic material is associated with these clay minerals. The yellow areas indicated in the Figure 8 are additional organic material, which is not directly associated to these mineral phases. The low OD (<0.1) below the carbon edge found for this material might indicate that it is of almost pure organic nature. The average cluster C(1s)-edge spectra extracted from both regions (Figure 9) are not very different, except for the yellow areas appearing to have a higher aromatic content (absorption at 285 eV) and the illite-clay associated organics show higher absorption in the 287 eV region that suggest a higher aliphatic character or metal complexation [18].

Three distinct regions in the iron L-edge image of sample 15 are identified. The grey cluster shows no OD; the cluster marked with black colour does not show any iron $L_{2,3}$-edge features but a generally high OD (see Figure 9); the blue region is characterised by absorption features at the Fe L-edge. The areas are nearly coincident with areas exhibiting potassium absorption peaks and highest organic absorption. Spectral feature changes within particles in the blue cluster region (not shown separately) appear to indicate that the core part of these particles either exhibit no iron content or a higher absorption in the Fe(II) energy region, whereas in the rim region of these particles have a higher Fe(III) content.

Figure 9: Average C(1s) XANES of sample 15 of the yellow and red areas indicated in Figure 8 (left) and average Fe L-edge spectra marked in blue and black (right)
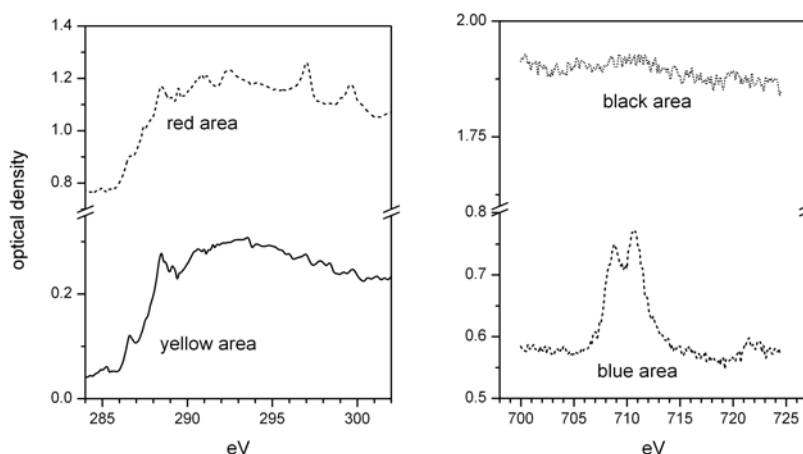
In the fault breccia sample 31 STXM results, PCA and cluster analysis reveal two distinct regions of organic matter. The fracture network infill region (Figure 10) is characterised by organic material with a high content of oxygen containing functional groups (*i.e.* carboxyl-type groups absorbing around 288.6 eV) and a clear π^* peak near 290.2 eV, indicative of carbonate. The second region of generally higher OD is associated with clear absorption bands at 297 and 300 eV, indicative of the potassium L-edges. This organic material is apparently associated with K-containing minerals.

**Figure 10: Average C(1s) XANES of sample 31 fracture infill and the mineral
associated organics (left). The mineral associated organics are clearly linked
to potassium containing phases as indicated by the L-edges at 297 and 300 eV.
Average Fe L-edge spectra from areas marked in red in Figure 11 (right).**
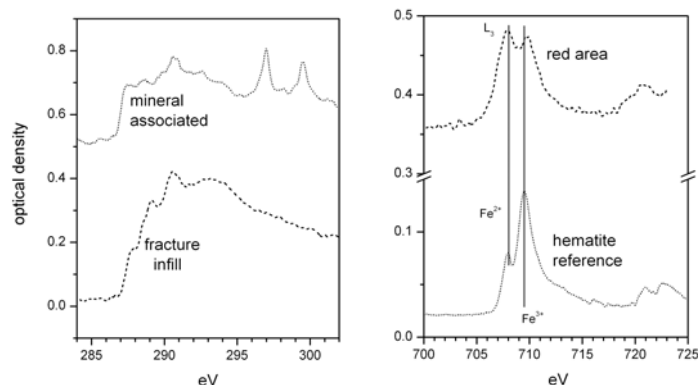
Interestingly, both carbon spectra show no C_{arom} absorption (~285 eV), but the mineral associated organics have a significant higher aliphatic content (~287.4 eV absorption). Some but not all K-rich regions coincide with Fe regions, as shown in Figure 11. The iron L_3-edge in Figure 10 shows there is a high content of Fe(II) phases, which is visualised in the comparison with a hematite reference spectrum at the bottom of Figure 10.

**Figure 11: (Top row from left to right) STXM absorption image at 290 eV
and carbon distribution map; (bottom row from left to right) potassium and iron
distribution maps taken from XANES ratio images (sample 31). High colour intensity
indicates high content of selected element. The scale bar represents 10 μm.**
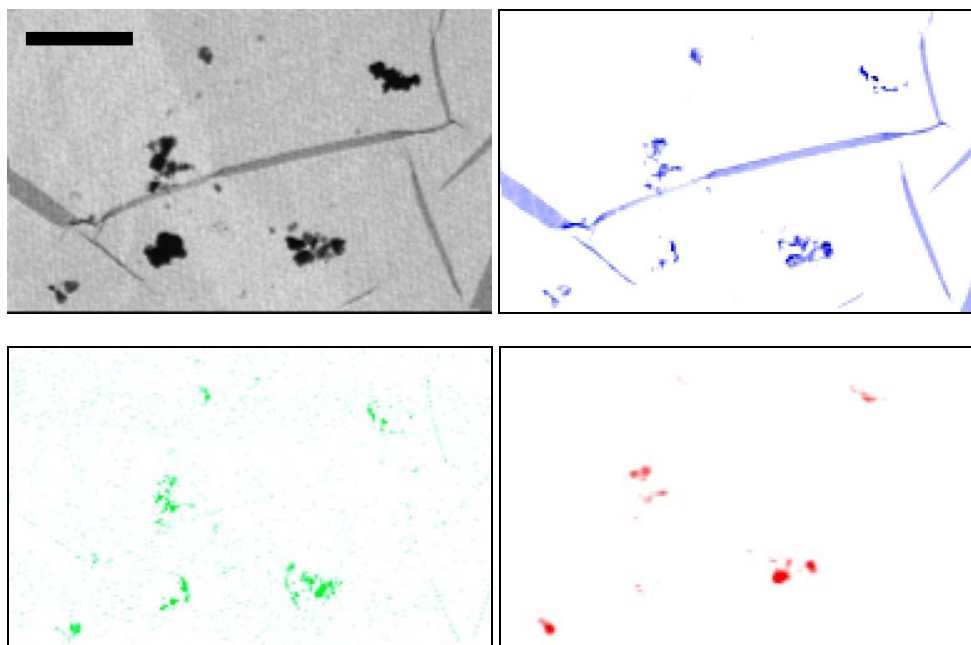
µ-FTIR results

Spectral maps imaging the spatial distribution of functional groups in the sample including aliphatics (ν_{CHali}; 3000-2800 cm^{-1}), aromatics ($\nu_{C=C}$; 1 750-1 500 cm^{-1}), alcohols (ν_{OH}; 3 600-3 100 cm^{-1}) or OH vibrations of clay minerals ("OH" 3 720-3 680 cm^{-1}) are extracted from scanning µ-FTIR data. An example of the maps is illustrated in Figure 12. Inspection of the functional group distributions reveals a correlation between the clay mineral vibration bands ("OH") and the organic matter functionalities (ν_{CHali}, $\nu_{C=C}$, ν_{OH}). This observation confirms the potassium (*i.e.* illite-type clay mineral) – organic matter correlation observed in the STXM investigations.

Figure 12: (Top left) Visible light microscope (VLM) image of the microtome sample 15 studied and (lower left) µ-FTIR spectrum of the spot marked by the cross line in the VLM image. (Right) Maps of organic functional group distributions extracted from µ-FTIR data: alcohols (ν_{OH}; 3 600-3 100 cm^{-1}), aliphatics (ν_{CHali}; 3 000-2 800 cm^{-1}) and aromatics ($\nu_{C=C}$; 1 750-1 500 cm^{-1}), as well as OH vibrations of clay minerals ("OH": 3 720-3 680 cm^{-1}).
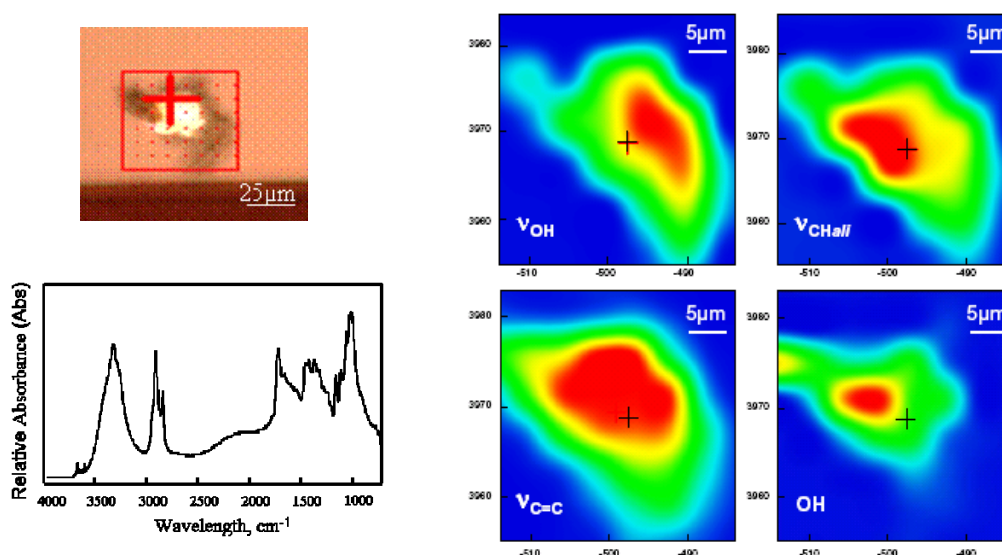
Conclusions

In summary, application of various spatially resolved spectroscopic methods have been successful in characterising the uranium speciation in sediment samples from the Lodève Basin and in evaluating if organic matter or Fe^{2+}, Mn^{2+}, S^{2-} mineral phases were responsible for uranium immobilisation/enrichment in the sediment. µ-XANES and µ-EXAFS results show that uranium in both sediment samples studies is found in the tetravalent state, most probably in the form of nano-crystalline UO_2-like phase. The correlations between elements obtained by means of different techniques (µ-XRF, STXM and µ-FTIR) allow us to conclude the following. The uranium distribution in sample 15, originating from the contact zone adjacent to the fault zone, is positively correlated to the distribution of lighter weight elements (Ca, K, Ti). We deduce a correlation between clay minerals of illite type and organic matter in the sample based on the observation that potassium (as indicator element) is found associated with both organic carbon and Fe and the observed spatial coincidence between µ-FTIR clay OH vibrations and various vibrations of organic functional groups.

Sample 31, originating from the breccia facies within the Lodève Basin fault zone, also exhibits a positive correlation between uranium and the elements K, Ti and a negative or anti-correlation between the distribution of uranium and those of Ca and iron. In sample volumes of highest potassium content, no Fe Kα signal is observed. Two distinguishable clusters of organic material in sample 31 are identified. The first type is associated with fracture infill and lacks K and Fe signatures,

but displays a detectable carbonate peak in its C(1s) XANES. The second cluster type of organic material is associated with discrete mineral aggregates, exhibiting a spatial coincidence between carbon absorption and Fe and K absorption. Because an anti-correlation between uranium and Ca/Fe exists and because carbonates (likely Ca-containing) are associated with organics in the fracture infill we conclude that the fracture infill in this sample is not associated with uranium.

From these observations we attempt to put forward a tentative hypothesis for the mechanism of uranium immobilisation. Due to the lack of the correlation between uranium and Fe, we exclude Fe-minerals as dominant reductant during immobilisation of U(VI) to U(IV). Combining the knowledge that uranium is found associated with potassium and that clay minerals of illite type are associated with organic matter we conclude that organic material associated with clay minerals might have played a role as reductant thereby reducing incoming groundwater dissolved U(VI) to less soluble U(IV). This hypothesis remains speculative; numerous unanswered questions remain. For example, what role did the clay play? Did it act as a catalyst [19] or was it merely an anchor for the organic material? In addition, how do we explain the apparent discrepancy between the spatial relationship between potassium and iron distributions observed in the μ-XRF maps with that from STXM results? To help refine our understanding of the redox partner involved in the reduction of U(VI) in this sediments combined μ-XRD/μ-XRF studies are planned.

We note a critical aspect of the comparison of μ-XRF and STXM results made in this study: the sample region actually analysed. Disregarding the depth resolution used in the confocal setup (providing volume information), the estimated area probed with μ-XRF is 608 000 μm^2 for sample 15 and 160 000 μm^2 for sample 31. The STXM measurements are limited to an area of 1 600 μm^2 for both samples. The STXM area investigated in this study represents only 1% (sample 31) and 2.6%of the μ-XRF region probed. Expressed in another way, STXM results stem from an area equivalent to only 16 data points of all the data points plotted in the Figures 4 and 6 combined. This points to the imminent difficulty of nano-focused techniques, namely to which extent selected sample regions studied are representative of the macro-scale system of interest. With this in mind, the correlations made in this study are surprisingly consistent with one another.

Acknowledgements

References

[1] Liu, C., *et al*., "Microscopic Reactive Diffusion of Uranium in the Contaminated Sediments at Hanford, United States", *Water Resources Research*, 42, p. W12420 (2006).

[2] Wibberley, C.A.J., J.P. Petit, T. Rives, "The Effect of Tilting on Fault Propagation and Network Development in Sandstone-shale Sequences: A Case Study from the Lodève Basin, Southern France", *Journal of the Geological Society*, 164, pp. 599-608 (2007).

[3]   Joussineau, G. de, *et al.*, "Morphology, Intersections, and Syn/Late-diagenetic Origin of Vein Networks in Pelites of the Lodève Permian Basin, Southern France", *Journal of Structural Geology*, 27 (1), pp. 67-87 (2005).

[4]   Lopez, M., *et al.*, "The Playa Environments of the Lodève Permian Basin (Languedoc-France)", *Journal of Iberian Geology*, 34 (1), pp. 29-56 (2008).

[5]   Lancelot, J., B. de Saint André, H. de la Boisse, "Systématique U-Pb et évolution du gisement d´uranium de Lodève (France) ", *Mineral. Deposita*, 19, pp. 44-53 (1984).

[6]   Landais, P., "Organic Geochemistry of Sedimentary Uranium Ore Deposits", *Ore Geology Reviews*, 11 (1-3), pp. 33-51 (1996).

[7]   Schlepp, L., *et al.*, "Influence of Paleoenvironment and Radiolytic Alteration on the Geochemistry of Organic Matter from Autunian Shales of the Lodève Uranium Deposit, France", *Bulletin de la Société Géologique de France*, 172 (1), pp. 99-109 (2001).

[8]   Landais, P., J. Connan, "Relations uranium-matière organique dans deux bassins permiens français: Lodève (Hérault) et Cerilly-Bourbon l'Archambault (Allier) " *Bull. C. R. EP Elf Aquitaine*, 4, pp. 709-757 (1980).

[9]   Nagy, B., *et al.*, "Organic Matter and Containment of Uranium and Fissiogenic Isotopes at the Oklo Natural Reactors", *Nature*, 354 (6353), pp. 472-475 (1991).

[10]   Denecke, M.A., *et al.*, "Confocal Micrometer-scale X-ray Fluorescence and X-ray Absorption Fine Structure Studies of Uranium Speciation in a Tertiary Sediment from a Waste Disposal Natural Analogue Site", *Environmental Science & Technology*, 39 (7), pp. 2049-2058 (2005).

[11]   Janssens, K., K. Proost, G. Falkenberg, "Confocal Microscopic X-ray Fluorescence at the HASYLAB Microfocus Beamline: Characteristics and Possibilities" *Spectrochimica Acta Part B-Atomic Spectroscopy*, 59 (10-11), pp. 1637-1645 (2004).

[12]   Denecke, M.A., *et al.*, "The INE-Beamline for Actinide Research at ANKA", *Physica Scripta*, T115, pp. 1001-1003 (2005).

[13]   Jacobsen, C., *et al.*, "Diffraction-limited Imaging in a Scanning Transmission x-ray Microscope", *Optics Communications*, 86, pp. 351-364 (1991).

[14]   Hitchcock, A.P., D.C. Mancini, "Bibliography of Atomic and Molecular Inner-shell Excitation Studies", *Journal of Electron Spectroscopy and Related Phenomena*, 67, pp. 1-132 (1994).

[15]   Dumas, P., L. Miller, "The Use of Synchrotron Infrared Microspectroscopy in Biological and Biomedical Investigations", *Vibrational Spectroscopy*, 32 (1), pp. 3-21 (2003).

[16]   Denecke, M.A., "Actinide Speciation Using X-ray Absorption Fine Structure Spectroscopy", *Coordination Chemistry Reviews*, 250 (7-8), pp. 730-754 (2006).

[17]   Rundle, R.E., *et al.*, "The Structures of Carbides, Nitrides, and Oxides of Uranium", *Journal of the American Chemical Society*, 70, pp. 99-105 (1948).

[18]   Plaschke, M., *et al.*, "Near Edge X-ray Absorption Fine Structure (NEXAFS) of Model Compounds for the Humic Acid/Actinide Ion Interaction", *Journal of Electron Spectroscopy and Related Phenomena*, 148 (3), pp. 151-157 (2005).

[19]   Giaquinta, D.M., *et al.*, "The Speciation of Uranium in a Smectite Clay: Evidence for Catalysed Uranyl Reduction", *Radiochimica Acta*, 76, pp. 113-121 (1997).

Efficiency calibration of HPGe detectors with line sources for radioactivity measurements of volume samples

Nader M.A. Mohamed
Atomic Energy Authority, ETRR2
Cairo, Egypt

Abstract

An experimental efficiency calibration method is proposed to measure radioactivity of volume samples with HPGe detectors. The method procedure is: i) positioning a standard-gamma ray line source, with length equals to the length of the sample to be measured, along the sample at different radial distances, r, and measuring at each position the detector absolute efficiency $\varepsilon(r)$; ii) finding an interpolation equation, which describes the variation of the efficiency with the radial distances; iii) integrating the equation over the entire sample radius to obtain the required efficiency.

Introduction

Accurate calibrated g-ray sources are difficult to be prepared for all the geometrical arrangements used in g-ray spectroscopy. Many papers are published to determine the absolute efficiency of Ge spectroscopy during the last decade. Most of these papers are concentrated on how to calculate, directly, the detector efficiency or to transfer, by calculations, point source calibrations to be suitable for volume sources. Calculations of detector efficiency require accurate dimensions of the detector and knowing the concentration of major elements in the sample matrix. The EUROMET project 428 [1] points out that the parameters provided by the detector suppliers are insufficient for accurate efficiency computation.

Also the EUROMET project 428 noted that the efficiency computation codes cannot be used directly for metrological purposes (*i.e.*, for precise measurements) and that experimental calibrations with standard sources remain unavoidable. However, most of the tested programs are operational for routine measurements, such as environmental or survey monitoring when efficiency uncertainties of 5-10% are acceptable.

In this paper we purposed an experimental method to calibrate HPGe detectors for cylindrical samples using standard gamma ray line sources. In this method we use the sample to be measured itself in measuring the detector absolute efficiency. The method procedure is:

i)   positioning a standard gamma ray line source, with length equals to the length of the sample to be measured, along the sample at different radial distances, r and measuring at each position the detector absolute efficiency $\varepsilon(r)$;

ii) finding an interpolation equation, which describes the variation of the efficiency with the radial distances;

iii) integrating the equation over the entire sample radius to obtain the required efficiency.

Assume that a line source is poisoned at different radial distances along a cylindrical sample, with radius R, set on an HPGe detector cap as shown in Figure 1. The absolute efficiency of the detector for the whole sample, ε, is given by:

$$\varepsilon = \frac{1}{\pi R^2} \int_0^R 2\pi r \varepsilon(r) dr$$

or:

$$\varepsilon = \frac{2}{R^2} \int_0^R \varepsilon(r) r dr \quad (1)$$

where $\varepsilon(r)$ is the absolute efficiency of the detector for the line source at radial distance r.

Experiment

The detector used in the experiment is a coaxial P-type HPGe detector of relative efficiency 100% with size of 7.83 $cm^D \times$ 9.78 cm^H. The sample used is a polyethylene container filled with stones. The size of the sample is 8.5 $cm^D \times$ 7.5 cm^H and the filling density is 2.2 g/cm^3. The source is a pipe, with diameter of 3 mm and length equals to the sample length, filled with very small stones. The gaps between the stones (in the pipe) are filled with 0.3 ml water which contains traces of Eu-152 with activity 3 800 Bq. The density of the source mixture was measured and it was found to be 1.95 g/cm^3. With these specifications of the source, the error results from the difference between the self absorption of the source and the sample can be neglected. The energies considered are 122, 245, 444, 779, 1 112 and 1 408 keV.

The source (the pipe) is positioned along the sample, as shown in Figure 1, at radial distances, r: 0, 2, 2.8, 3.5 and 4.1 cm and in each case the absolute efficiency $\varepsilon(r)$ is measured. Because the absolute efficiency $\varepsilon(r)$ is strongly dependent on the radial distance, the measurement is repeated three times and the average values are taken.

Figure 1: Schematic view of a detector irradiated by a line source positioned inside a cylindrical sample
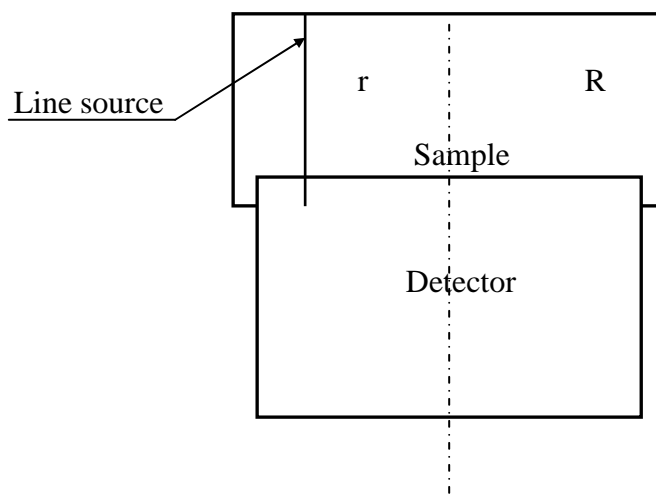
Results and discussion

The absolute efficiency $\varepsilon(r)$ is plotted versus the squared radial distance, r^2 as shown in Figure 2. The interpolation equation, which describes the variation of the efficiency with the radial distances, is obtained by polynomial fitting. As mentioned above $\varepsilon(r)$ is measured at five radial distances (r: 0, 2, 2.8, 3.5 and 4.1 cm), so fourth order polynomial can be deduced. But, as shown in Figure 2, there is a very good agreement between the measured data and a third order polynomial fitting. The deviations between the measured data and fitted data are less than 1% for all results. Therefore third-order polynomial is sufficient to describe the variation of the efficiency $\varepsilon(r)$ with the squared radial distance, r^2. That is $\varepsilon(r)$ can be represented by the following function:

$$\varepsilon(r) = a_o + a_1 r^2 + a_2 r^4 + a_3 r^6 \tag{2}$$

where, a_0, a_1, a_2 and a_3 are the coefficients of the polynomial. These coefficients are given in Table 1.

Figure 2. $\varepsilon(r)$ versus r^2 for the case studied
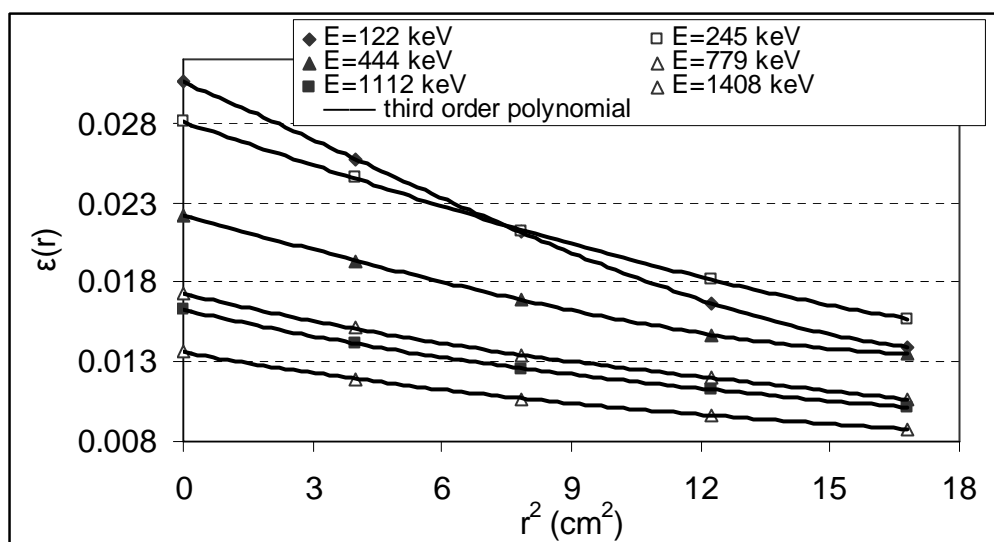
Table 1: The coefficients of Eq. (3) and the detector efficiencies at the energies considered for the case studied

E (keV)	122	245	444	779	1112	1408
a_0	3.057E-02	2.807E-02	2.221E-02	1.730E-02	1.627E-02	1.361E-02
a_1	-1.160E-03	-9.165E-04	-7.290E-04	-6.420E-04	-6.099E-04	-4.800E-04
a_2	-1.882E-05	3.560E-06	1.419E-06	2.327E-05	2.144E-05	1.644E-05
a_3	1.721E-06	4.282E-07	6.618E-07	-5.133E-07	-4.103E-07	-2.984E-07
E	**0.02058**	**0.02081**	**0.01676**	**0.01328**	**0.01249**	**0.01062**

Substituting Eq. (2) in Eq. (1) yields:

$$\varepsilon = a_0 + \frac{a_1}{2}R^2 + \frac{a_2}{3}R^4 + \frac{a_3}{4}R^6 \tag{3}$$

By putting R = 4.25 (the radius of the sample used), the absolute efficiency of the detector for the whole sample, ε is obtained. Table 1 gives ε at the energies considered. Figure 3 gives the detector efficiencies at these energies as fitted using the Gamma Vision software [2] for the sample considered.

Figure 3: The detector efficiencies at the energies considered for the sample considered
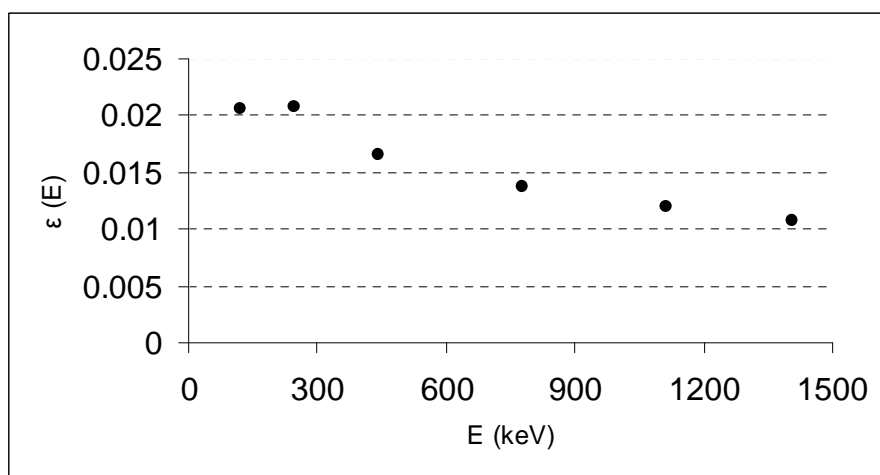
Conclusion

HPGe detectors can be calibrated using line sources to measure radioactivity of volume samples. The method of calibration is to position a standard-gamma ray line source along the sample to be measured at different radial distances, and finding an interpolation equation, which describes the variation of the efficiency with the radial distances, then integrating the equation over the entire sample radius to obtain the required efficiency. The case studied in this paper shows that the interpolation equation could be represented by a third order polynomial of the square radial distance with high precision.

References

[1]   Lepy, M.C. and all participants "Intercomparison of Efficiency Transfer Software for Gamma-ray Spectrometry", *Applied Radiation and Isotopes*, 55, 493 (2001).

[2]   *A66-B1, Software User's Manual*, Gamma Vision software, EG&G ORTEC (1997).

EXAFS studies of uranium ions in calcium chloride hydrate melts

Akihiro Uehara,[1] **Toshiyuki Fujii,**[1] **Haruaki Matsuura,**[2]
Nobuaki Sato,[3] **Hajimu Yamana,**[1] **Yoshihiro Okamoto**[4]
[1]Division of Nuclear Engineering Science, Research Reactor Institute, Kyoto University, Osaka, Japan
[2]Research Laboratory for Nuclear Reactor, Tokyo Institute of Technology, Tokyo, Japan
[3]Institute of Multidisciplinary Research for Advanced Materials, Tohoku University, Sendai, Japan
[4]Quantum Beam Science Directorate, Japan Atomic Energy Agency, Ibaraki, Japan

Abstract

The co-ordination of UO_2^{2+} and U^{4+} in $CaCl_2$ hydrate melts was studied by U L_{III} edge extended X-ray absorption fine structure (EXAFS) spectroscopy and UV-VIS absorption spectroscopy. For $CaCl_2 \cdot nH_2O$ with n less than about 10, it was confirmed that, with the increase of water content from $CaCl_2 \cdot 6H_2O$ to $CaCl_2 \cdot 10H_2O$, the Cl ion co-ordination number N_{Cl} in the UO_2^{2+} co-ordination sphere decreased from 2.2 to 1.8, while the hydration number N_O in it increased from 1.4 to 2.1. The N_O and N_{Cl} and bond distance of U-Cl in $CaCl_2 \cdot 6H_2O$ were similar to those in 14 M LiCl, however it was found that the distance of $U-O_{eq}$ in $CaCl_2 \cdot 6H_2O$ was longer than that in 14 M LiCl. By adding HCl into the system, we found a change in the UO_2^{2+} co-ordination sphere was observed. The EXAFS spectra of U^{4+} in the $CaCl_2$ hydrate melts showed three peaks which could be assigned as the U-OH, $U-OH_2$ and the U-Cl bonds.

Introduction

The molten hydrated salt, which is generally called hydrate melt, is a very highly concentrated electrolyte. Because of the limited amount of water, the hydrate melt gives a characteristic chemical behavior to solutes within it. Yamana and co-workers have studied extraction equilibrium of lanthanides and actinides between a tri-*n*-butyl solution and a hydrate melt [1]. Calcium nitrate hydrate melt, $Ca(NO_3)_2 \cdot nH_2O$, which contains *f*-element ions has been chosen as a substitute for an aqueous phase. From the observed distribution ratios, variation of activity coefficients of lanthanide nitrates within the hydrate melt has been analysed as a function of water content [1]. The dependence of the activity coefficient on the water content showed a different trend compared to that in the water-abundant solutions. In order to clarify the mechanism of the characteristic variation of the activity coefficient in hydrate melts, some spectroscopic analyses, that is, electronic absorption spectrometry, fluorescence spectrometry, emission lifetime analysis, Raman spectrometry, and EXAFS analysis, have been performed [2]. The analytical results demonstrated that the hydration number decreases with the water content, but could not explain the peculiar change in the activity coefficient.

A difficulty in studying the $Ca(NO_3)_2 \cdot nH_2O$ medium may be that both hydrated water and nitrate ion include oxygen atoms. While the EXAFS analysis is a superior technique for investigating the co-ordination circumstance, it is less useful to distinguish the oxygen atoms due to H_2O and NO_3^- in these ligands. To avoid the problem, in the present study, we focus on a chloride medium. Calcium chloride hexahydrate, $CaCl_2 \cdot 6H_2O$, has a melting point at 303.1 K, and its melt acts as the hydrate melt. Hence, we study the co-ordination circumstance of uranium in $CaCl_2 \cdot nH_2O$.

Allen, *et al.* [3] and Hennig, *et al.* [4] have recently investigated the structure of UO_2^{2+} complexes in concentrated LiCl solutions by EXAFS spectrometry. For concentrations up to 14M Cl^-, Allen, *et al.* [3] observed the species $UO_2(H_2O)_5^{2+}$, $UO_2(H_2O)_xCl^+$, $UO_2(H_2O)_xCl_2$ and $UO_2(H_2O)_xCl_3^-$ with U-Cl distances varying from 2.71 to 2.73 Å. Hennig, *et al.* [4] developed an electrochemical cell for *in situ* EXAFS measurement to prepare UO_2^{2+} and U^{4+} by the controlled potential electrolysis. They observed $UO_2(H_2O)_5^{2+}$, $UO_2(H_2O)_4Cl^+$, $UO_2(H_2O)_3Cl_2$ and $UO_2(H_2O)_xCl_3^-$ for UO_2^{2+} with Cl^- increasing from 0 to 9 M, $U(H_2O)_9^{4+}$, $U(H_2O)_8Cl^{3+}$, $U(H_2O)_{6-7}Cl_2^{2+}$, and $U(H_2O)_5Cl^{3+}$ for U^{4+} with Cl^- increasing from 0 to 9 mol dm^{-3}, M. The distances in the UO_2^{2+} co-ordination sphere are U-O_{ax} (O_{ax}; uranyl oxygen atom) = 1.76 Å, U-O_{eq} (O_{eq}; equatorial oxygen atom) = 2.41 Å, and U-Cl = 2.71 Å, and the distances in the U^{4+} co-ordination sphere are U-O = 2.41 Å and U-Cl =2.71 Å.

The concentration of Cl^- in 14 M LiCl is close to that in $CaCl_2 \cdot 6H_2O$, while the hydration energy of Ca^{2+} is larger than that of Li^+. Hence, the co-ordination circumstances of uranium ions in these media may be different. In the present study, we studied the co-ordination spheres of the U^{4+} and UO_2^{2+} in $CaCl_2 \cdot nH_2O$ and concentrated LiCl solution by EXAFS measurement. From the results obtained and the reported data [3,4], we discuss the difference in the co-ordination circumstance of uranium complexes between these concentrated media.

Experimental

Sample preparation

Anhydrous uranium tetrachloride was prepared by the chlorination of U_3O_8 with CCl_4 at 623 K. The product was identified to be the anhydrous UCl_4 by X-ray diffraction spectrometry. Hydrated uranyl dichloride, $UO_2Cl_2 \cdot nH_2O$, was prepared by drying up a HCl solution containing UO_2^{2+}. Calcium chloride hexahydrate, $CaCl_2 \cdot 6H_2O$, was once melted at 323 K, and then the hydrate melt was used at room temperature. The water content of calcium chloride hydrate melt, $CaCl_2 \cdot nH_2O$ ($n > 6$) was controlled by adding deionised water. Concentrated LiCl solutions (< 14 M) were also prepared. The synthesised uranium compounds were dissolved in the hydrate melts or the concentrated LiCl solutions. Concentrations of UO_2^{2+} and U^{4+} in these samples were 0.05 M and 0.02 M, respectively. As a reference, a 0.05 M UO_2^{2+} solution in 0.1 M $HClO_4$ was prepared. All the chemical reagents were of reagent grade. Two cm^3 of each sample was sealed in a thin polyethylene bag which was fabricated for the X-ray measurement. A 5 mm thick Teflon plate, which has a hole with 8 mm diameter, was set inside the bag in order to keep the light path to be 5 mm. EXAFS measurements were carried out at room temperature.

EXAFS data acquisition and analysis

XAFS measurements were carried out at BL27B beamline [5] of the Photon Factory in High Energy Accelerator Research Organisation (KEK), Japan. Hard X-ray ranging 5-20 keV is available in this beamline with a Si(111) double-crystal monochromator. XAFS measurements based on the U L_{III}-absorption edge (E_0 = 17.153 keV) were performed. All the solutions were measured in fluorescence mode using a Ge solid state detector. The XAFS spectra were analysed by using WinXAS ver. 3.1 code developed by Ressler [6]. Multiple XAFS scans were collected from each sample at ambient temperature (298 K), and the results were averaged.

The EXAFS data were fit using theoretical phase and amplitudes calculated from the program FEFF 8 Rehr, *et al.* [7]. For UO_2^{2+}, single and multiple scattering paths were calculated on the basis of the structure of $UO_2Cl_2 \cdot H_2O$ [8] and a hypothetical cluster for $UO_2(H_2O)_5$ [4]; for U(IV) the structures of UCl_4 [9] and $U(H_2O)_4(SO_4)_2$ [10] were used. Due to increasing noise levels at higher k-range, data analysis was restricted to the k-range 3.0-12.0 Å^{-1} for UO_2^{2+} and 2.6-12.0 Å^{-1} for U^{4+}. The amplitude reduction factor, S_0^2, was defined as 0.9 in the FEFF calculation and fixed to that value in the data fits. In all fits the co-ordination number of the uranyl oxygen atoms (O_{ax}) was held constant at 2. The fitted energy shift parameter, ΔE_0, was linked for all shells. Bessel function was used as a window function for the Fourier transforms (FT).

Results and discussion

UO_2^{2+} chloride complexes

U L_{III}–edge k^3-weighted EXAFS spectra and corresponding FT are shown in Figure 1. Structural results of the standard EXAFS shell fitting including phase correction are summarised in Table 1. The FT of the UO_2^{2+} aquo-ion (sample 0 M Cl$^-$) shows two peaks which arise from 2 axial oxygen atoms of the linear UO_2^{2+} unit, O_{ax}, and 5 co-ordinated oxygen atoms of the hydrated water in the equatorial plane perpendicular to the UO_2^{2+} axis, O_{eq}. The U-O_{ax} distance was determined to be 1.76 ± 0.02 Å, while the U-O_{eq} distance was 2.41 ± 0.02 Å. Our result is in agreement with the structural parameters reported for the same medium [11].

The FT of the chloride solutions show an additional peak at the distance of 2.73 ± 0.02 Å indicative of Cl in the first co-ordination sphere. The intensity of this peak increases with increasing chloride concentration. It should be noted that EXAFS analysis reflects only the average co-ordination and is not able to differentiate between coexisting species if the bond lengths are equal. Therefore, in the fit procedure, the bond lengths of possible solution species comprising $UO_2(H_2O)_5^{2+}$ and $UO_2(H_2O)_xCl_y^{2-y}$ are averaged to a common radial distribution. The Debye-Waller factors, σ^2, were fixed for the EXAFS fit procedure to make the relation between O_{eq} and Cl comparable and avoid the correlation problems between N and σ^2. For the U-O_{eq} shell, σ^2 = 0.0075 Å^2 was estimated from $UO_2(H_2O)_5^{2+}$ in 0.1 M HClO$_4$ solution. The σ^2 for the U-Cl shell was fixed at 0.0050 Å^2 as obtained from $UO_2Cl_4^{2-}$ [3].

With the decrease of n of CaCl$_2 \cdot n$H$_2$O from 10 to 6, which means the increase of the concentration of Cl$^-$, [Cl$^-$], from 9.4 M to 13.8 M, the co-ordination number N_{Cl} increased from 1.8 to 2.2, while the co-ordination number N_O decreased from 2.1 to 1.4. The result indicates that even in a medium with very high [Cl$^-$] such as CaCl$_2 \cdot 6$H$_2$O, the equatorial shell of UO_2^{2+} possesses hydrated waters. In this region, the co-ordination number in the equatorial plane, $N_{Cl} + N_O$, was about 4. This is smaller than that of the 0.1 M HClO$_4$ system. A similar phenomenon has been found for UO_2^{2+} in the concentrated LiCl solution [4].

In general, U-O_{eq} and U-Cl distances become shorter if the co-ordination number in the equatorial plane is reduced 5 to 4 [12]. A counter example can be seen in the concentrated LiCl system between 3 and 9 M [4]; with the decrease of water content, $N_{Cl} + N_O$ decreased from 5.2 to 4.1, but the U-O_{eq} distance becomes longer from 2.41 Å to 2.51 Å. We also found a similar trend between the water abundant system (0.1 M HClO$_4$) and hydrate melt systems. For example (see Table 1), let us compare the 0.1 M HClO$_4$ and CaCl$_2 \cdot 6$H$_2$O systems. The UO_2^{2+} complex in the hydrate melt possesses the smaller co-ordination number in the equatorial plane N_O and the longer U-O_{eq} distance.

In water abundant systems, the structure of the UO_2^{2+} complex changes by changing pH. Hence, the effect of coexisted H^+ in the hydrate melt is of interest. The XAFS spectrum of UO_2^{2+} was measured for 9 M LiCl + 0.1 M HCl (see Figure 1 and Table 1). The U-O$_{eq}$ and U-Cl distances determined in this study reproduced the reported values [4]. On the other hand, the U-O$_{eq}$ distance determined for 14 M LiCl was found to be shorter than the value reported for 14 M LiCl + 0.01 M HCl [3]. The difference may be due to the co-existed H^+ ion. For concentrated LiCl systems with H^+, the U-O$_{eq}$ distances showed similar values, *i.e.* 2.51 Å (this study), 2.52 Å [3] and 2.51 Å [4], while shorter distance (2.47 Å) was observed without H^+ ion. The interaction between H^+ ions and hydrate waters would depress the hydration of UO_2^{2+}, and this would result in the longer U-O$_{eq}$ distance.

In order to know the relation of water activity on the co-ordination sphere of UO_2^{2+} complex, we analysed as a function of water activity, a_{H2O}, the N_O and N_{Cl} and the bond distances U-O$_{eq}$ and U-Cl determined. The results are shown in Figure 2. Here, a_{H2O} was calculated based on Ref. [13] and density of each sample. The N_O decreased with the decrease of a_{H2O}, on the other hand, N_{Cl} increased with the decrease of a_{H2O}. The N_O and N_{Cl} in CaCl$_2$ hydrate melts seem to be in alignment with those in LiCl. The bond distance U-Cl was almost constant for both CaCl$_2$ hydrate melts and 14 M LiCl. The bond distance U-O$_{eq}$ increased with the decrease of a_{H2O} and the linear relation was not observed between CaCl$_2$ hydrate melts and LiCl. These results suggested that U-O$_{eq}$ was not affected by the co-ordination strength of Ca-O more than that of Li-O.

U^{4+} chloride complexes

Figure 2 shows the EXAFS spectra of U^{4+} in CaCl$_2$ hydrate melts and concentrated LiCl solutions. The three peaks were observed at $\Delta + R = 1.3$, 1.9, and 2.2 Å in FT. The second and third far peaks were assigned to be the co-ordinations of U-O and U-Cl. Since no acid exists in our U^{4+} systems, if U^{4+} is partly oxidised to be UO_2^{2+}, the XAFS spectrum should possesses a peak at a shorter distance corresponding to U-O$_{ax}$ of UO_2^{2+}. To verify this, the UV-VIS absorption spectra of all samples were checked. Figure 3(a) shows the absorption spectra of U^{4+} and UO_2^{2+} complexes in CaCl$_2$·6H$_2$O and 14 M LiCl. Figure 3(b) shows the spectra U^{4+} and UO_2^{2+} in CaCl$_2$·10H$_2$O + 0.1 M HCl and 9 M LiCl + 0.1 M HCl, respectively. It was found that, in the absence of HCl, the U^{4+} was not oxidised to form UO_2^{2+}. A similar peak has been observed in the EXAFS spectrum for 9 M LiCl + 0.1 M HCl [4], in which its origin was not clarified. According to a structural study by the density functional theory [14], the U-O distance of a hydrolysis species $U(OH)_2^{2+}$ was calculated to be 1.92 to 2.14 Å. This is shorter than the U-O distance corresponding to the hydration. The first peak possibly originates from the hydrolysis.

The most possible second and third far peaks were tentatively analysed under the assumption that the first peak can be excluded. The Δ^2 value of the U-O shell was fixed in the fit to 0.0070 Å^2, as obtained for the U^{4+} aquo ion, and that of the U-Cl shell was fixed to 0.0050 Å^2 assuming the same value as obtained for UO_2^{2+}. The co-ordination numbers N_O and N_{Cl} in CaCl$_2$·6H$_2$O were close to those in 14 M LiCl even in similar concentration of Cl$^-$. The co-ordination circumstance of U^{4+} would not be affected by the kinds of the cations in the concentrated solution.

References

[1]   Yamana, H., T. Kaibuki, Y. Miyashita, S. Shibata, H. Moriyama, *J. Alloys Compd.,* 271-273, 701 (1998).

[2]   Fujii, T., H. Asano, T. Kimura, T. Yamamoto, A. Uehara, H. Yamana, *J. Alloys Compd.,* 408, 989 (2006).

[3]   Allen, P.G., J.J. Bucher, D.K. Shuh, N.M. Edelstein, T. Reich, *Inorg. Chem.*, 36, 4676 (1997).

[4]   Hennig, C., J. Tutschku, A. Rossberg, G. Bernhard, A.C. Scheinost, *Inorg. Chem.,* 44, 6655 (2005).

[5]   Konishi, H., A. Yokoya, H. Shiwaku, H. Motohashi, T. Makita, Y. Kashihara, S. Hashimoto, T. Haramai, T.A. Sasaki, H. Maeta, H. Ohno, H. Maezawa, S. Asaoka, N. Kanaya, K. Itoh, N. Usami, K. Kobayashi, *Nucl. Instrum. Methods Phys. Res.* A, 372, 322 (1996).

[6]   Ressler, T., *J. Synchrotron Radiat.*, 5, 118 (1998).

[7]   Ankudinov, A.L., J.J. Rehr, *Phys. Rev.* B, 56, R1712 (1997).

[8]   Taylor, J.C., P.W. Wilson, *Acta Crystallogr.*, B30, 169 (1974).

[9]   Schleid, T., G. Meyer, *J. Less-Common. Met.,* 132, 69 (1987).

[10]   Kierkegaard, P., *Acta Chim. Scan.,* 10, 599 (1956).

[11]   Vallet, V., U. Wahlgren, B. Schimmelpfennig, H. Moll, Z. Szabo, I. Grenthe, *Inorg. Chem.,* 40, 3516 (2001).

[12]   Taylor, J.C., P.W. Wilson, *Acta Crystallogr.* B, 29, 1073 (1973).

[13]   Aseyev, G.G., *Electrolytes Equilibria in Solutions and Phase Equilibria*, Begell House Inc., New York (1999).

[14]   K.R.S. Chandrakumar, T.K. Ghanty, S.K. Ghosh, T. Mukherjee, *J. Mol. Str. Theochem.*, 807, 93 (2007).

Table 1: EXAFS structural parameters for UO_2^{2+} chloride solutions

	[Cl⁻]	U–O$_{ax}$	U–O$_{eq}$		U–Cl		ΔE_0 (eV)
		σ^2	R (Å)	N_O	R (Å)	N_{Cl}	
CaCl$_2$·6 H$_2$O	13.8	0.0003	2.50	1.4	2.73	2.2	15.6
CaCl$_2$·8 H$_2$O	11.2	0.0008	2.46	1.5	2.72	2.2	15.2
CaCl$_2$·10H$_2$O	9.4	0.0006	2.46	2.1	2.72	1.8	15.3
14 M LiCl	14	0.0002	2.47	1.3	2.73	2.4	15.1
9 M LiCl + 0.1 M HCl	9	0.0025	2.51	1.7	2.73	1.8	16.4
0.1M HClO$_4$	0	0.0012	2.43	4.8	–	–	15.5
14 M LiCl + 0.01 M HCl[a]	14	0.0018	2.52	1.9	2.73	2.6	-9.6
9 M LiCl + 0.1 M HCl[b]	9	0.0014	2.51	1.4	2.74	2.7	0.1

Errors in distances R are ±0.02 Å, errors in co-ordination numbers N are ±15%. The Debye-Waller factor σ^2, distance R and co-ordination number N were held constant for the shells U-O$_{ax}$, R = 1.76 Å and N = 2, U-O$_{eq}$, σ^2 = 0.0075 Å^2 and U-Cl, σ^2 = 0.0050 Å^2, respectively. A k range of 3-12 was used. [a] Ref. [3]. [b] Ref. [4].

Figure 1: U L$_{III}$-edge k^3-weighted EXAFS data (left) and corresponding Fourier transforms (right) taken over k = 3-12 Å^{-1} for UO$_2^{2+}$ as a function of Cl$^-$ concentration
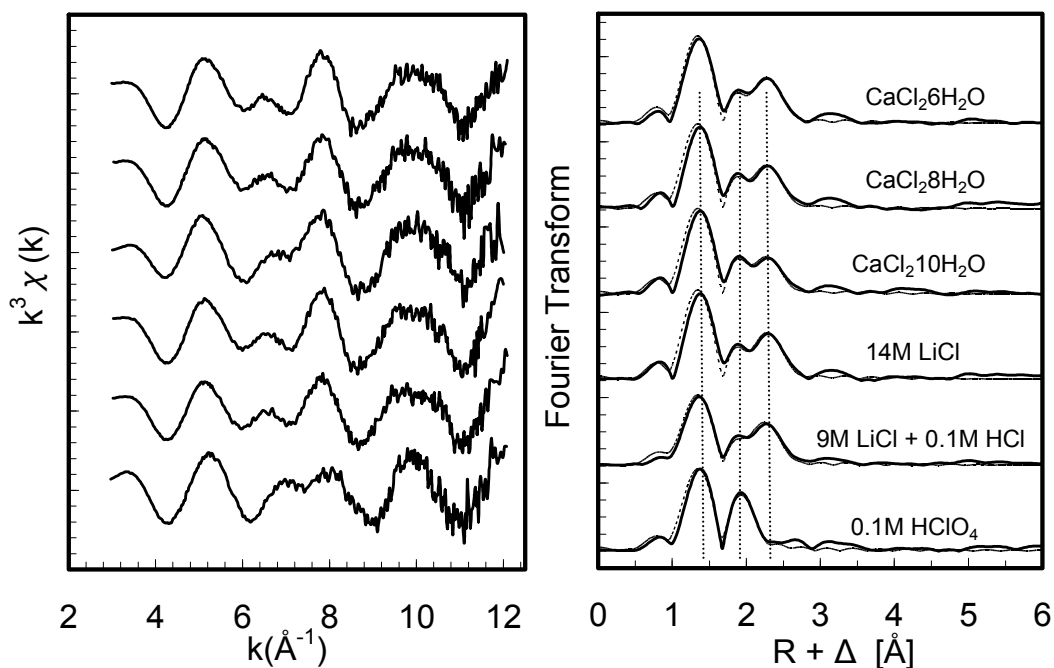
Figure 2. (a) Dependence of co-ordination numbers N_O and N_{Cl} on the water activity in CaCl$_2 \cdot n$H$_2$O and concentrated LiCl. ●: N_O and ■: N_{Cl} in CaCl$_2 \cdot n$H$_2$O, ○: N_O and □: N_{Cl} in LiCl. (b) Dependence of bond distances U-O$_{eq}$ and U-Cl on the water activity in CaCl$_2 \cdot n$H$_2$O and concentrated LiCl. ●: U-O$_{eq}$ and ■: U-Cl in CaCl$_2 \cdot n$H$_2$O, ○: U-O$_{eq}$ and □: U-Cl in LiCl.
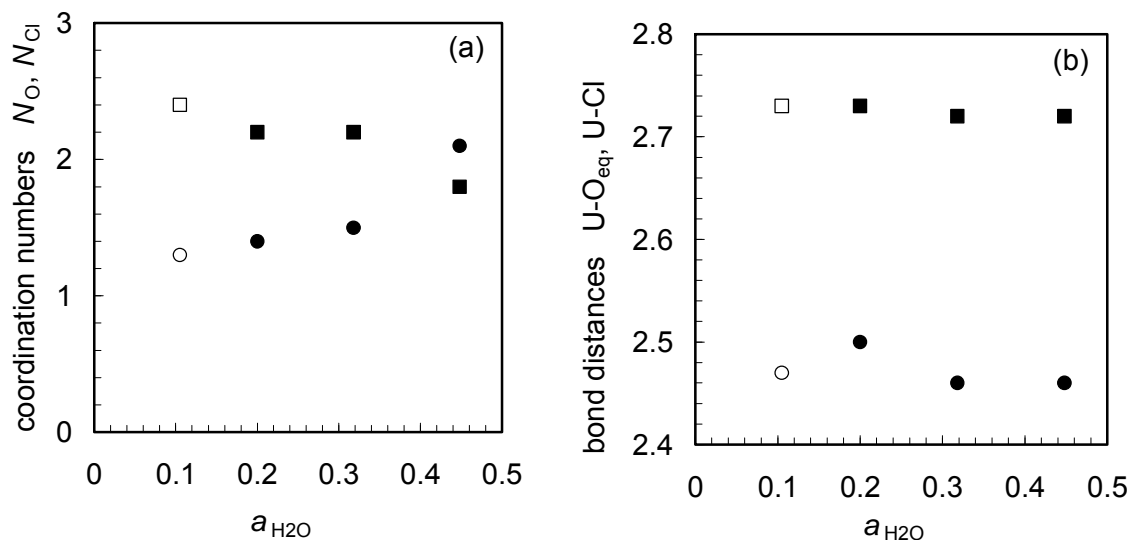
Figure 3: U L$_{III}$-edge k^3-weighted EXAFS data (left) and corresponding Fourier transforms (right) taken over k = 2.6-12 Å^{-1} for U^{4+}
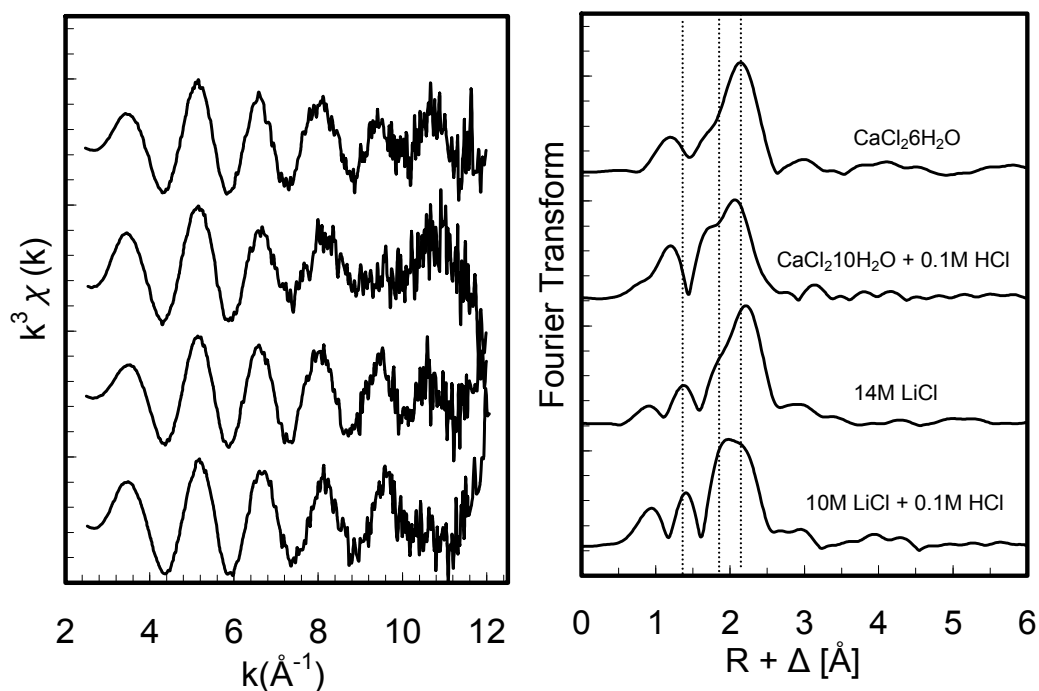
Figure 4: UV-VIS absorption spectra of 0.02 M U^{4+} and 0.05 M UO$_2^{2+}$ in concentrated CaCl$_2$ and LiCl in absence (a) and presence (b) of 0.1 M HCl
(a) Curve 1; U^{4+} in CaCl$_2$·6 H$_2$O, curve 2; U^{4+} in 14 M LiCl, curve 3; UO$_2^{2+}$ in CaCl$_2$·6 H$_2$O and curve 4; UO$_2^{2+}$ in 14 M LiCl
(b) Curve 1; U^{4+} in CaCl$_2$·10 H$_2$O + 0.1 M HCl, curve 2; U^{4+} in 9 M LiCl + 0.1 M HCl, curve 3; UO$_2^{2+}$ in CaCl$_2$·10 H$_2$O + 0.1 M HCl and curve 4; UO$_2^{2+}$ in 9 M LiCl + 0.1 M HCl
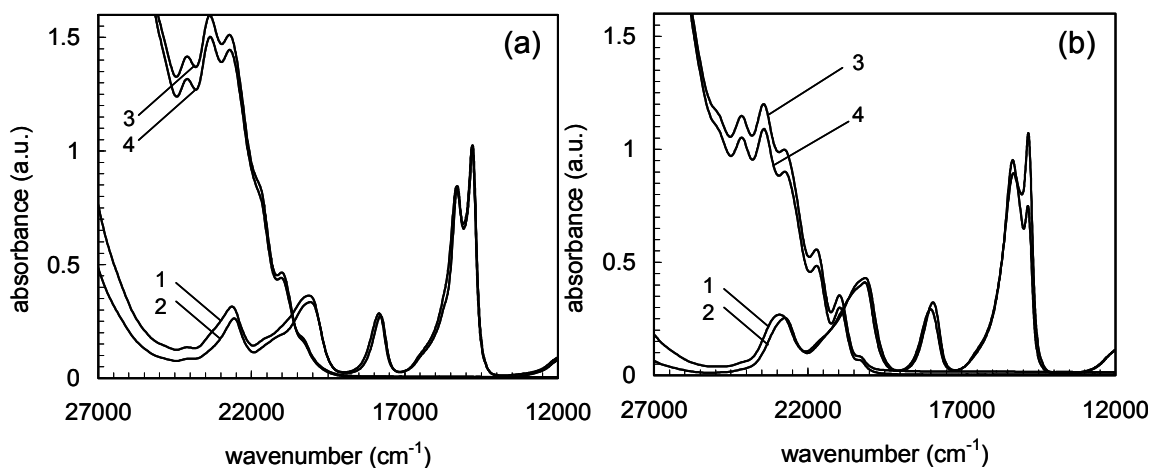
The high resolution X-ray fluorescence spectrometer (HRXF): An advanced tool for actinide research

T. Vitova, A. Lebid, D. Liu,* K. Dardenne, B. Brendebach, J. Rothe, J. Hormes,* M.A. Denecke
Forschungszentrum Karlsruhe, Institut für Nukleare Entsorgung, Karlsruhe, Germany
*Physikalisches Institut, Bonn, Germany

Abstract

High resolution X-ray fluorescence (HRXF) measurements are becoming increasingly important for our understanding of electronic and co-ordination structures. A HRXF spectrometer disperses the emitted photon energies from a sample excited by incident X-rays and focuses them onto a position sensitive detector, e.g. a CCD camera. This set-up can be used to remove lifetime broadening by registering the partial fluorescence yield emitted by the sample (i.e. recording a windowed signal from the energy dispersed fluorescence emission while varying incident photon energy), thereby yielding highly resolved XAFS spectra, which often display resonant features not observed in conventional XAFS. The spectrometer can also be used for a wide range of other experiments, for example, resonant inelastic X-ray scattering (RIXS), which can be used to obtain bulk electron configuration information, valence-selective XAFS studies, where differences in local structure of an element present in multiple valence states can be studied, as well as site-selective XAFS studies, where the co-ordination structure of a metal bound to selected elements can be differentiated from that of all the other metal atoms. Numerous challenges in actinide science can be addressed using these approaches.

A HRXF spectrometer is being built and will be made available for use at the INE-Beamline for actinide research at the synchrotron source ANKA. Presently, a spectrometer prototype is being tested. We present the concept of the HRXF spectrometer, which is of a compact, modular design, optimised for attaining a wide range of energies with a dynamically bent analyser crystal. The crystal itself is changeable and the diameter of the Rowland circle variable. Examples of applications are shown.

Introduction

High-resolution X-ray fluorescence spectroscopy (HRXF) provides site-selective information on electronic structure and local geometric atomic environment of a chemical element of interest. This is a secondary optical process having an intermediate state corresponding to a final state in X-ray absorption fine structure (XAFS) spectroscopy. The core hole created after an electron is excited from a core level is filled by transition from an upper electronic state followed by emission of a fluorescence photon. The energy resolution (FWHM) of such an emission line measured as function of the excitation energy is determined by both the experimental energy resolution and the energy width of the final hole state, which has longer life time (smaller energy width) than the intermediate deep core hole [1]. HRXFS includes resonant and non-resonant fluorescence emission measured near or above an absorption edge, respectively. In the region of resonant emission the electronic structure of the absorbing atom is probed. It is possible to extract site-selective local geometric structural information from the non-resonant region of the spectrum [1]. The core hole lifetime broadening can be suppressed in an absorption spectrum by measuring the partial fluorescence yield. The resulting XAFS is highly resolved and often displays resonant features not observed in the conventional XAFS spectrum [1].

Motivation

We are constructing and commissioning a HRXF spectrometer for use at the INE-Beamline for actinide research at ANKA [2]. This spectrometer will overcome some of the limitations of the traditional XAFS spectroscopy. The following examples are meant to demonstrate the advantages of the HRXF spectrometer.

A conventionally measured XAFS spectrum is additive, *i.e.* average structural information is measured over all oxidation states. The HRXF spectrometer can be used to differentiate between oxidation states in a mixture. For example, the HRXF emission lines of iron oxides measured at the W1 beamline at HASYLAB, Hamburg are shown in Figure 1(a). The $K\beta_{1,3}$ line narrows with increasing number of 3-D spin-up electrons. This leads to the narrowing of the Fe_2O_3 emission line compared to that of FeO. Therefore, X-ray absorption near edge structure (XANES) spectra extracted from a high resolution fluorescence map [measured emission lines as a function of the excitation energy, shown in Figure 1(b)] at constant emission energies A and B are partially site selective. The resulting XANES A and B spectra, displayed in Figure 1(c), reflect mainly Fe^{2+} and Fe^{3+} sites, respectively. Details can be obtained elsewhere [3,4].

Figure 1: (a) HRXF emission spectra of FeO and Fe_2O_3. (b) $K\beta 1,3$ emission line and HRXF map of a lithium niobate crystal doped with 4 wt.% Fe. (c) Site-selective Fe K-edge XANES spectra A and B extracted from the HRXF map in (b) obtained by integrating ±1 eV around emission energies marked with A and B in (b), respectively.
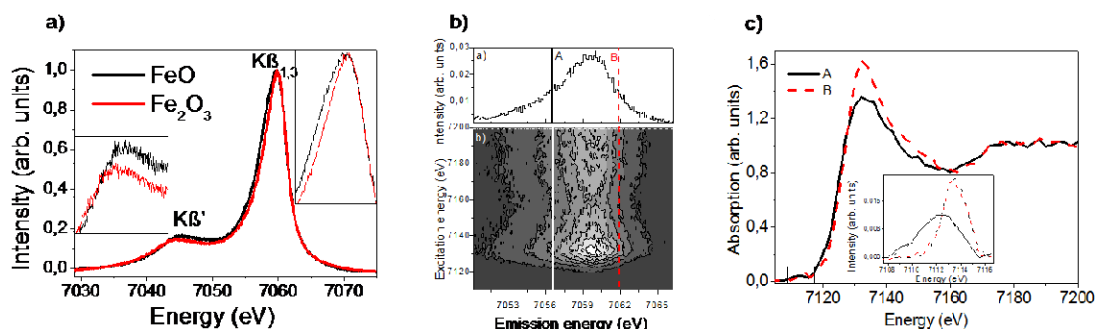
It is difficult or sometimes nearly impossible to measure XAFS from dilute samples in complex matrices. The HRXF spectrometer can be used to successfully separate the emission of an element of interest from that from other interfering elements. For example, the Fe $K\alpha$ and Eu $L\beta_1$ emission lines, shown in Figure 2(a) have a 60 eV energy difference, which is less than the resolution of a conventional solid sate fluorescence detector. This HRXF measurement is of goethite doped with 2% Eu(III), performed

Figure 2: (a) HRXF map in the EXAFS range for a 2 at.% Eu goethite sample. (b) Comparison between EXAFS measured in transmission mode at the Eu LII-edge (TRANS) and extracted from the HRXF map in (a).
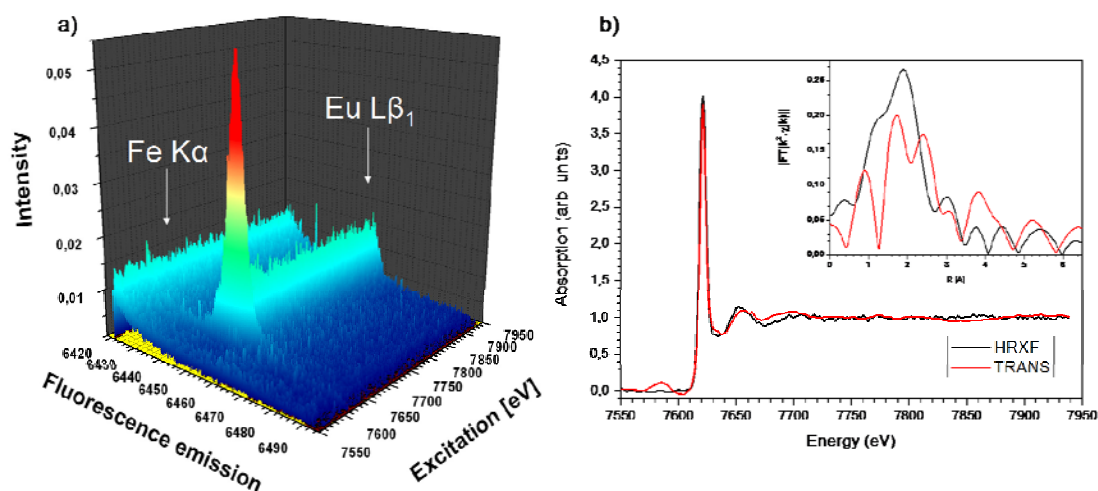
at the W1 beamline at HASYLAB, Hamburg. The high resolution fluorescence map yields higher quality extended X-ray absorption fine structure (EXAFS) data compared to Eu LII transmission data [see Figure 2(b)]. Results reveal number and interatomic distance of second co-ordination shell Fe atoms. Details can be obtained elsewhere [5].

The HRXF spectrometer can be used for two things in the investigation of 4f/5f elements. The LIII and LII absorption edges of 4f elements lie energetically close and limit the energy range available for EXAFS. The analyser crystal of the HRXF spectrometer filters out fluorescence emission due to transitions to LI and LII electronic states, which extends the usable EXAFS k-range. This increases the resolution in EXAFS analysis and leads to interatomic distance determinations, which are more precise [1]. The HRXF spectrometer can also overcome restricted energy resolution, leading to, *e.g.* unresolved transitions to f states in XANES measurements at the LIII absorption edges of actinides and lanthanides. A core hole life-time broadening suppressed spectrum is measured by monochromatising the emitted fluorescence with the HRXF spectrometer analyser crystal. As a result, pre-edge structures due to transitions to f states are resolved and appear in the XANES spectrum, thereby providing electronic structure and site symmetry information.

Status

Test measurements with a HRXF spectrometer constructed by the National Institute of Standards and Technology (NIST) [6], USA have already commenced at the superconducting undulator beamline (SCU-X) at ANKA, Karlsruhe. A similar spectrometer, with the same basic NIST spectrometer design but improved and optimised for actinide M (3-4 keV) and L emission lines (13-23 keV) is in the construction phase [see Figures 3(a) and 3(b)]. First tests will be performed at the INE-Beamline in September. The spectrometer consists of a main block, to which three membrane bellows are attached. Bellow one [see Figure 3 (a)] is mounted to the sample flange, which is 90° with respect to the primary X-ray beam. The analyser crystal, clamped in the bending mechanism, is inside of the second bellow. The crystal itself is changeable. The emitted fluorescence is energetically dispersed by the cylindrically bent triangular crystal and focused onto a position sensitive detector (for example, a CCD camera) mounted onto bellow three. The Bragg angle is changed by a system of movable linkage arms, whose position is determined by a stepping motor and two worm gear pairs. The Bragg angular range covered by the NIST spectrometer is from 30-50°. The bending radius of the analyser crystal can be easily changed by the bending mechanism [7]. A large bending radius (large crystal-detector distance) yields an improved energy resolution, whereas the signal-to-noise ratio (SNR) is improved (short crystal-detector distance) by a small bending radius. The spectrometer design for the INE-Beamline instrument will cover Bragg angles larger than 50°, which will also increase the attainable energies. The compact

Figure 3: (a) Photographs of the NIST HRXF spectrometer being tested at the ANKA SCU-X beamline and (insert) of the bending mechanism with the triangular crystal mount, located inside of bellow #2. The three membrane bellows are numbered (1-3). (b) A 3-D drawing of the Bragg angle adjustment with the bending mechanism for the INE-Beamline spectrometer now under construction.
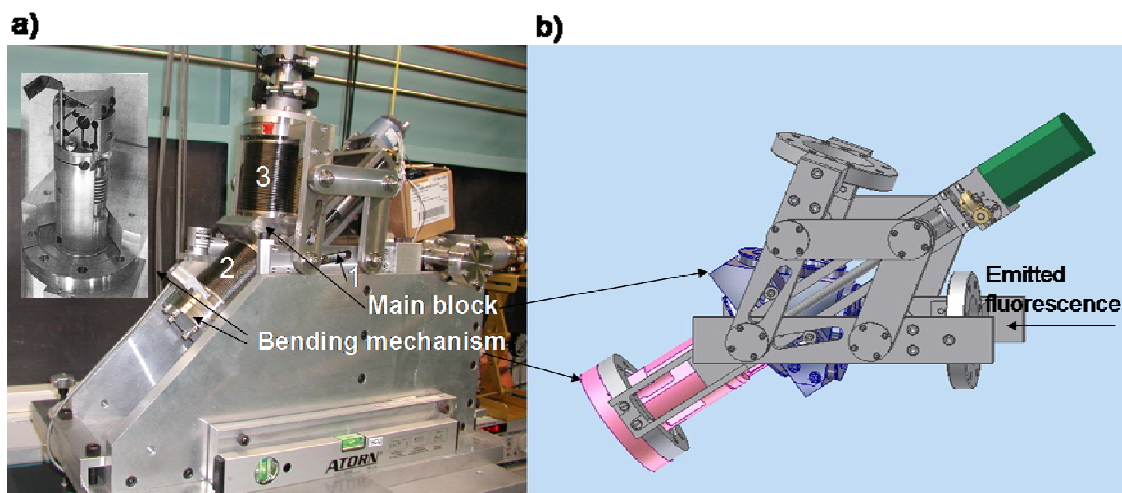
assembly of the spectrometer makes it easily movable and thereby perfectly adapted to the modular design concept of the INE-Beamline. The instrument allows measurements in vacuum, necessary for low energy emission lines. This also leads to an improved SNR, partially overcoming one of the challenges of such experiments, the low fluorescence cross-section.

Summary

INE is constructing together with University of Bonn a HRXF spectrometer optimised for actinide M and L emission line measurements. The spectrometer design is improved over that of a NIST spectrometer by increasing the attainable angular range to Bragg angles higher than 50°.

References

[1]   Groot, F. de, A. Kotani, *Core level Spectrocopy of Solids*, CRC Press, Boca Raton (2008).

[2]   Denecke, M.A., J. Rothe, K. Dardenne, H. Blank, J. Hormes, *Physica Scripta*, T115, 1001-1003 (2005).

[3]   Vitova, T., M. Falk, K. Buse, J. Hormes, *Journal of Applied Physics*, submitted.

[4]   Vitova, T., J. Hormes, *HASYLAB User Reports* (2007).

[5]   Dardenne, K., M.A. Denecke, W. Caliebe, *HASYLAB User Reports* (2007).

[6]   Brennan, S., P.L. Cowan, R.D. Deslattes, A. Henins, D.W. Linde, *Rev. Sci. Insrum.*, 60, 2243 (1989).

[7]   Henins, A., *Rev. Sci. Instrum.*, 58, 1173 (1987).

ANTARES: A soft X-ray scanning photoemission microscope beamline at SOLEIL

Maria C. Asensio
Synchrotron SOLEIL
Gif-sur-Yvette, France

Abstract

A wide range of structural and chemical imaging techniques are now available for research in low dimensional systems. In particular, synchrotrons offer various spectrometers equipped with micrometric or even nanometric beam sizes. It is clear that the highly elevated flux of the third-generation synchrotron sources are essentially profited in the area of the X-ray microscopy. In such a context, microscopy of photoemission SPEM (Scanning Photoemission Microscope) is one of these powerful microscopic techniques, based on the contrast originated by the photoelectric effect. Contrary to the PEEM microscopy, the imagery in SPEM is generated by a simple nanometric sweeping of the samples and a focusing the incident light. ANTARES is one of the first beamlines in Europe that is attempting to extend such demanding technique to the domain of low energy, where the states of the valence band can be detected with high precision as well as their dispersions using angle resolved photoemission (ARPES). The objective is to be able to determine the electronic band structure and the Fermi surface together with the chemical shift of core level of light elements with a nanometre spatial resolution. In essence, this new beamline of SOLEIL will fit the existing emptiness between the atomic information provided by the STM spectroscopy and the low spatially resolved data supplied by traditional ARPES and NEXAFS techniques. Several examples of scanning X-ray microscopic studies will be described. Finally, an overview of the utilisation limits of different X-ray microscopes will be detailed together with future developments based on the detectors of last generation and new focalisation optics. See www.synchrotron-soleil.fr/portal/page/portal/Recherche/LignesLumiere/ANTARES for further details.

Synthesis of thorium dioxide nano-particles incorporated into mesoporous silica and their characterisation by HR-TEM and XAFS

Olga N. Batuk,[1] Melissa A. Denecke,[1] D. Vinga Szabó[2]
[1]Institut für Nukleare Entsorgung, Forschungszentrum Karlsruhe, Karlsruhe, Germany
[2]Institut für Materialforschung, Forschungszentrum Karlsruhe, Karlsruhe, Germany

Abstract

Investigation of nano-sized actinide oxide particles is related to several practical applications including formation of nano-particles under nuclear fuel production procedures and the potential role nano-particles play in radionuclide contaminant migration, which is important, e.g. in performance assessment of nuclear waste repositories for spent nuclear fuel. Understanding actinide oxide nano-particles structure will allow predicting their properties and elucidate mechanisms of formation. The structure of Th(IV) and Pu(IV) oxide nano-sized particles in solution has been studied by XAFS (XANES and EXAFS) and a variation in particle size leads to variation in XANES white line intensity [1,2]. The goal of our study is to synthesise and characterise thorium dioxide nano-particles, considered as models for actinide(IV) oxide eigen-colloids.

Mesoporous silica (MCM-41 and SBA-15 families) with varying pore size (2, 3 and 5 nm) is synthesised, characterised with HR-TEM and BET analysis, and used as a solid template for synthesising thorium dioxide nano-particles with defined size distributions. The mesoporous silica template is subjected to ultrasonic treatment in Th(IV) solutions with selected concentration and pH. The influence of the template surface charge on nano-particle formation is investigated by addition of calcium into the mesoporous framework. Evidence of nano-particle incorporation into the template pore structure is established from HR-TEM and STEM studies. Crystalline nano-particles are observed to form and their lattice parameters calculated from interatomic plane distances measured in HR-TEM images. The concentration of incorporated Th(IV) is controlled by EDX-analysis. Addition of calcium does not affect the nano-particle structure or size, but only the amount of thorium incorporated.

XAFS spectroscopy at the Th L_3 edge in fluorescence mode is applied to characterise the nano-particles. We observe a decrease in XANES white line intensity with decreasing particle size, going from bulk crystalline to 2 nm particles. This variation indicates a decrease in the density of 6d final states involved in the L_3 edge transition with decreasing particle size. We interpret this as resulting from the surface/bulk ratio increase with decreasing particle size, i.e. increasing significance of surface species for smaller sized particles. The increasing significance of surface species is reflected in the overall average structural observed in the corresponding EXAFS. Comparison of Fourier transform magnitude EXAFS spectra shows a decrease of metal-oxygen peak intensity with decreasing cluster size and a disappearance of the metal-metal interaction, indicating a decrease in overall average nano-particle structural order.

References

[1]   Rothe, J., M.A. Denecke, V. Neck, R. Müller, J.I. Kim, *Inorg. Chem.*, 41, pp. 249-258 (2002).

[2]   Rothe, J., C. Walther, M.A. Denecke, Th. Fanghänel, *Inorg. Chem.*, 43, pp. 4708-4718 (2004).

Wide angle X-ray scattering investigation of lanthanide borosilicate glasses

O. Bouty,[1] **J-M. Delaye,**[2] **J. de Bonfils,**[2] **S. Peuget**[2]
[1]CEA Marcoule, DEN/DTEC/SEPE
[2]CEA Marcoule DEN/DTCD/SECM

Abstract

Structural characterisation of nuclear glasses requires the combination of several experimental and simulation techniques. Experimental ones probe the electronic environment at short distances (EXAFS, NMR) or at medium range distances (WAXS, AWAXS) or the nuclear environment (neutron scattering). We have built a new competence in X-ray Wide Angle Scattering (WAXS) by mounting two based-lab diffractometers with Mo X-ray tubes, one of them being located in a shielded glove box, and by writing a new software to easily extract structure factors and radial distribution functions from the experiment.

We present here a preliminary study of a simplified borosilicate glass doped with Eu (europium), which is a fission product, and which is often used as a stimulant of trivalent actinides. The WAXS technique has been successfully applied, the structure factor being in good agreement with the one obtained by Molecular Dynamics (MD) Simulation. Thus, knowledge of the Eu local environment has been deduced and results compared with data from EXAFS analysis.

Optimal sample preparation conditions for the determination of uranium in urine samples by spectrometry alpha analysis

Hakim Brahimi, Omar Amri
Centre de Recherche Nucléaire d'Alger
Division de la sûreté radiologique
Département de Dosimétrie des Rayonnements Ionisants
Laboratoire de radiotoxicologie

Abstract

The measurement of the transmitter's alpha is most delicate to put into practice because it requires that the radioelement be completely separated from the remainder of the matrix. Indeed, the free course of a particle alpha in the matter is extremely short.

In order to be able to measure the particles alpha of uranium under good conditions of resolution and effectiveness of counting by avoiding the phenomenon of reabsorption in the matrix, it is essential to proceed has chemical separation of uranium in the urine and with the electrodepositing on a stainless disc.

The uranium contained in the sample of urine are concentrated by co-precipitation in phosphoric medium, the precipitate collected mineral-bearing then began again in nitric medium, the solution obtained passed on column of TRU-Spec extraction. The elution of uranium is obtained with a diluted solution of acid oxalate of ammonium.

The stainless uranium electrodeposits are measured in spectrometry alpha.

$$\text{Activity of uranium } AU\,(Bq\,/\,l) = \left(\frac{Nu}{Nsd} - \frac{NbfU}{NbfU - sd} \right) * \left(\frac{Asd}{l} \right) \tag{1}$$

References

[1]   Verdingh, V., *The Preparation of Layers by Electrospraying and Electrophoresis*, Central Bureau for Nuclear Measurements, Geel, Belgium, CONF-711002, pp. 160-165.

[2]   Getoff, N., Bildstein, "Molecular Plating IV: A Rapid Method for the Electrodeposition of Pu", *Nuclear Instruments and Methods*, 36, 173-175 (1965).

[3]   Kwinta, J., « Sources Radioactives : Cours destiné aux étudiants en DEA », *Institut des Sciences et Techniques Nucléaires*, Paris (1994-1995).

[4]   Rutherford, P.M., M.J. Dudas, J.M. Arocena, « Radium in Phosphogypsum Leachates", *Journal of Environmental Quality*, Vol. 24, No. 2 (1995).

[5]   Scholten, L.C., C.W.M. Timmermans, "Natural Radioactivity in Phosphate Fertilizers", *Fertilizer Research*, 43, 103-107 (1996).

[6]   Surbeck, Heinz, "Determination of Natural Radionuclides in Drinking Water: A Tentative Protocol", *The Science of the Total Environment*, 173-174, 91-99 (1995).

[7]   Koulouris, G., "Dynamic Studies on Sorption Characteristics of ^{226}Ra on Manganese Dioxide", *Journal of Radioanalytical and Nuclear Chemistry*, Vol. 193, No. 2, 269-279 (1995).

Determination of structural parameters of cobalt-cysteine complexes combining EXAFS experiments and molecular dynamics simulations

C. Bresson, R. Spezia, P.L. Solari, C. Den Auwer

Abstract

Physiological and toxicological effects of metallic ions depend on their speciation and on the structure of their associated bioligands complexes. In the field of chemical and/or nuclear toxicological studies, we are investigating cobalt complexes with biorelevant ligands such as amino acids or peptides. Aqueous reaction of cobalt dichloride with an excess of an amino acid: the cysteine, (Cys, $C_3H_3NSO_2^{2-}$) in basic medium under aerobic or nitrogen atmosphere, afforded the mononuclear complexes Co(III):3Cys and Co(II):3Cys respectively. Further, for a 1:2 metal-to-ligand ratio, the Co(III):2Cys complex has been identified and characterised, where the metal co-ordination sphere is completed by solvent molecules.

A combination of X-ray Absorption Spectroscopy (XAS) measurements and Car-Parrinello Molecular Dynamics (CPMD) simulations allowed us to assess structural features of these complexes. Inclusion of the temperature effects in the CPMD calculations gives an implicit access to disorder effects in the Extended X-ray Absorption Spectroscopy (EXAFS) equation. The very good agreement between the measured and the simulated data showed the accuracy of these models provided by CPMD.

This work contributes to the knowledge of topics such as metal-bioligand interaction which is of major interest in the field of bioinorganic chemistry and toxicological topics.

References

[1]   Spezia, R., C. Bresson, C. Den Auwer, M.P. Gaigeot, *J. Phys. Chem. B* (2008), in press.

[2]   Bresson, C., R. Spezia, S. Esnouf, P.L. Solari, S. Coantic, C. Den Auwer, *New J. Chem.*, 31, 1789 (2007).

[3]   Bresson, C., S. Esnouf, C. Lamouroux, P.L. Solari, C. Den Auwer, *New J. Chem.*, 1, 416 (2006).

μ-XRF and μ-XAFS investigation of uranium-rich clay from a natural analogue site

K. Dardenne,[1] **M.A. Denecke,**[1] **B. Brendebach,**[1] **J. Rothe,**[1]
T. Vitova,[1] **P. Michel,**[1] **T. Schäfer,**[1] **F. Huber,**[1] **K. Rickers,**[2] **M. Elie**[3]
[1]Forschungszentrum Karlsruhe (FZK), Institut für Nukleare Entsorgung (INE), Karlsruhe, Germany
[2]Hamburger Synchrotronstrahlungslabor (HASYLAB) at DESY, Hamburg, Germany
[3]Gestion des Ressources Minières Minérales et Energétiques, Unité Mixte de Recherche
Vandoeuvre-lès-Nancy, France

Abstract

Spatially resolved X-ray fluorescence and absorption investigations with a micrometre-scale resolution (μ-XRF and μ-XAFS) on uranium-rich samples collected from a nuclear waste repository natural analogue site are presented. Natural analogues are considered to simulate conditions near proposed repositories for disposal of high level radioactive waste in deep geological formations over a geological time span [1]; their study provides information crucial for repository safety assessment on a long-term time scale. In this study we determine the uranium speciation in two uranium-rich clay samples originating from Autunian shales from the Permian Lodève Basin (France). The goal of this investigation is to determine the uranium oxidation state in the clay and to ascertain if any correlation between the uranium distribution and that of other elements present in the clay exists, which might give us insight into the mechanism of uranium immobilisation.

μ-XRF and μ-XAFS of the samples were measured at Beamline L at HASYLAB in confocal geometry (focal spot 16 μm). Elemental distributions for K, Ca, Ti, Fe, Zr and U show that the uranium distribution is inversely correlated to areas with high Fe content and positively correlated with the distribution of lighter elements (K, Ca, Ti). U L3 μ-XANES recorded at areas with high uranium concentration reveal that uranium in the hot spots is tetravalent.

More recently the uranium distribution on the sample surface containing about 25 mg ^{238}U/g material has been measured at the INE-Beamline for actinide research at ANKA using a poly-capillary lens (on loan from HASYLAB) to focus the beam to around 25 μm. In these first micro-focus experiments at the INE-Beamline, the uranium distribution over a 2×1 mm^2 area, (30 μm step size) was recorded. Uranium L3 μ-XANES measured at pixels with high uranium concentration in the studied area again reveal uranium to be present in the tetravalent state. U L3 EXAFS recorded with a 300 μm (unfocused) beam at the INE-Beamline revealed uranium to likely be present as a nanocrystalline uraninite (UO_2) like phase [2].

Scanning transmission X-ray spectro-microscopy (STXM) studies show a positive correlation between K (considered an indicator for illite) and organic carbon (see contribution by Michel, et al.). Our results show U(IV) to be correlated to K. Together these results may indicate that the organic material associated with illite-type clay minerals acted as the reducing agent in uranium immobilisation.

References

[1] Denecke, M.A., K. Janssens, K. Proost, J. Rothe, U. Noseck, *Environ. Sci. Technol.*, 39 (7), 2049-2058 (2005).

[2] Denecke, M.A., F. Huber, K. Rickers, P. Michel, T. Schäfer, *HASYLAB Annual Report 2007*, 1293-1294 (2007).

Structural characterisation of actinide metals under pressure and temperature

Ph. Faure, C. Genestier
CEA – Centre de Valduc
Is-sur-Tille, France

Abstract

The way 5f electrons contribute to the bonding within the actinide series remains a question of fundamental interest and one of the last challenges for condensed matter physicists. A systematic understanding of the pressure (P) and temperature (T) behaviour of lanthanides and actinides is critical for developing theories which predict phase stability in f-electron metals under both normal and extreme conditions. To achieve this goal, experimental results are needed to provide a database to allow the proper condensed matter physics and theoretical models to be developed and certified.

Unfortunately experimental data for actinides under both pressure and temperature are lacking because of the difficulties of handling radioactive materials and establishing dedicated devices that can ensure safety concerns. Both laboratory and synchrotron radiation means should be developed and used as they reveal to be complementary. We aim at presenting tools which are or which will soon be used for the structural characterisation of actinide metals under a wide range of pressures and temperatures. Some data on actinides will be presented to illustrate the topics.

Probing the electronic structure of uranium compounds by soft X-ray absorption spectroscopy

C. Fillaux,[1] **J. C. Berthet,**[2] **D. Guillaumont,**[1] **T. Tyliszczak,**[3] **D. K. Shuh,**[3] **C. Den Auwer**[1]

[1]CEA Marcoule, DEN/DRCP/SCPS, Bagnols-sur-Cèze, France
[2]CEA Saclay, DSM/DRECAM/SCM, Gif-sur-Yvette, France
[3]Lawrence Berkeley National Laboratory, Berkeley, CA, USA

Abstract

The actinide L_{III} edges (formally 2p-6d transition) have been the most reported one in the literature for technical experimental reasons (17.2 keV for U). Significant structural information on the co-ordination polyhedron can be obtained from these electronic transitions because of the importance of scattering features in the continuum [1,2]. However, the very short core hole life time broadens the edge signal (7 eV for U) resulting in very little extractable electronic information. In most reported studies, a systematic investigation of the relative L_{III} edge position and width results in a qualitative comparison of the metal environment and its influence on the cation effective charge as well as the influence of the ligands. The N_{III} (4p-6d transition) and $N_{IV,V}$ (4d-5f transition) edges are much less sensitive to scattering resonances. On the other hand, they provide a better means to probe both the 5f and 6d orbitals, because of the larger core hole life time resulting in a much better resolution than at the L_{III} edge. Complementary information can also be obtained from ligand K edge spectroscopy, because of the very small core hole width of the ligand (~0.2 eV for O and N).

In this work, investigation is focused on a series of uranium iodide compounds where the cation exhibits an interesting range of oxidation states: $[U^{(III)}I_3(Py)_4]$, $[U^{(IV)}I_4(Py)_3]$, $[U^{(V)}O_2I(Py)_n]$ and $[U^{(VI)}O_2I_2(Py)_3]$. All these complexes have been prepared and crystallographically characterised at CEA Saclay by J-C. Berthet, et al. [3-7]. For all the samples, NEXAFS spectra at the NIV,V edges of uranium have been collected (778, 736 eV), as well as those at the ligand K edge [oxygen (543 eV) and nitrogen (410 eV)]. Experiments were performed at the 11.0.2 beamline of the Advanced Light Source (Lawrence Berkeley National Laboratory), particularly relevant for soft X-ray experiments on radioactive material [8].

We are interested in the fundamental understanding of submolecular interactions where the actinide cations are involved in ionic to covalent bonding. In particular, we want to determine the electronic configuration of the atoms by combining experiment and theory. A previous work showed that a coupling between simulations of the experimental spectra and quantum chemical calculations is very fruitful, in order to improve the model describing the final states and better understand the bonding properties of the cation with the ligand [9]. In the first step, electronic populations are obtained from a Mulliken population analysis derived from Density Functional Theory (DFT) calculations and used as input parameters in order to simulate NEXAFS spectra. In a second step, simulated spectra are compared to experimental ones in order to better understand the relation between electronic structure and NEXAFS spectrum. Simulation of the NEXAFS spectra also allows to extract quantitative information such as the effective charge of the atoms, the density of state and the hybridisation of the orbitals.

The study of the series will lead to the determination of the influence of the effective charge of uranium on NEXAFS features. The nature of the actinide-ligand bond of the uranium complexes will be compared through the series.

References

[1]   Denning, R., J. Green, T. Hutchings, C. Dallera, A. Tagliaferri, K. Giarda, N. Brookes, L. Braicovich, *J. Chem. Phys.*, 117, 8008 (2002).

[2]   Den Auwer, C., D. Guillaumont, P. Guilbaud, S.D. Conradson, J.J. Rehr, A. Ankudinov, E. Simoni, *New J. Chem.*, 28, 929 (2004).

[3]   Berthet, J-C., P. Thuéry, M. Ephritikhine, *Inorg. Chem.,* 44, 1142 (2005).

[4]   Berthet, J-C., M. Nierlich, M. Ephritikhine, *Chem. Comm., 870* (2004), and *Chem. Comm.*, 1660 (2003).

[5]   Berthet, J-C., M. Nierlich, M. Ephritikhine, *Eur. J. Inorg. Chem.*, 850 (2002).

[6]   Berthet, J-C., M. Lance, M. Nierlich, M. Ephritikhine, *Eur. J. Inorg. Chem.*, 2005 (1999).

[7]   Berthet, J-C., M. Nierlich, M. Ephritikhine, *Angew. Chem. Int. Ed.,* 42, 1952 (2003).

[8]   Nilsson, H.J., T. Tyliszczak, R.E. Wilson, L. Werme, D. K. Shuh, *Anal. Bioanal, Chem.,* 383, 41 (2005).

[9]   Fillaux, C. *et al.*, *C. R. Chimie*, 10, 859-871 (2007).

Structural determination of neptunium species in aqueous solutions by EXAFS and quantum chemical calculations

Atsushi Ikeda,[1,2] **Christoph Hennig,**[1] **Satoru Tsushima,**[1]
André Rossberg,[1] **Andreas C. Scheinost,**[1] **Gert Bernhard,**[1] **Tsuyoshi Yaita**[2]
[1]Institute of Radiochemistry, Forschungszentrum Dresden-Rossendorf, Dresden, Germany
[2]Synchrotron Radiation Research Centre (SPring-8), Japan Atomic Energy Agency, Hyogo, Japan

Abstract

Neptunium (^{93}Np) is one of the most problematic nuclides in the nuclear fuel reprocessing process and the following radioactive waste disposal because of its chemical similarity to the fissile (i.e. reusable) nuclides of uranium (U) and plutonium (Pu). Proper understanding of the behaviour of Np in the reprocessing process or in the migration process on the geological disposal of radioactive wastes requires vast fundamental information about the chemical properties of Np in solutions. As a matter of fact, extensive investigations have been carried out for the last several decades to reveal the chemical properties of Np in solution, such as thermodynamics [1], electrochemical behaviour [2] or co-ordination properties [3]. However, despite a large number of precedent works, the complex structure of Np species is still not understood sufficiently. In the present study, Np solution samples with different oxidation states are electrochemically prepared in aqueous perchlorate, nitrate and carbonate solutions, and the complex structure of Np species in the sample solutions are determined by EXAFS spectroscopy, partly with the help of DFT calculations. The obtained results reveal the structural difference between different Np oxidation states, as well as the different co-ordination behaviour in each solution system. The electrochemical behaviour of Np in each solution system is also discussed.

References

[1]   Lemire, R.J., J. Fuger, H. Nitsche, P. Potter, M.H. Rand, J. Rydberg, K. Spahiu, J.C. Sullivan, W.J. Ullman, P. Vitorge, H. Wanner, *Chemical Thermodynamics of Neptunium and Plutonium*, OECD/NEA (Ed.), Elsevier Science, Amsterdam (2001).

[2]   Kihara, S., Z. Yoshida, H. Aoyagi, K. Maeda, O. Shirai, Y. Kitatsuji, Y. Yoshida, *Pure Appl. Chem.*, 71, 1771-1807 (1999).

[3]   Patil, S.K., V.V. Ramakrishna, M.V. Ramaniah, *Coord. Chem. Rev.*, 25, 133-171 (1978).

Interaction of actinides(IV) with amino-acids: From peptides to proteins

A. Jeanson,[1] **C. Den Auwer,**[1] **C. Berthon,**[1] **L. Bonin,**[1] **P. Callow,**[2]
S. Coantic,[3] **S. Esnouf,**[4] **M. Ferrand,**[5] **D. Guillaumont,**[1] **P. Moisy,**[1] **C. Vidaud**[6]
[1]CEA Marcoule, DEN/DRCP/SCPS, Bagnols-sur-Cèze, France
[2]ILL, Grenoble, France
[3]IBMM/LAPP, UMR 5247, Montpellier, France
[4]CEA Saclay, DSM/DRECAM/LSI, Gif-sur-Yvette, France
[5]CEA Grenoble, iRTSV, Grenoble, France
[6]CEA Marcoule, DSV/DIEP/SBTN, Bagnols-sur-Cèze, France

Abstract

The interaction of actinides with biosystems is of considerable interest to understand the assimilation mechanisms of radioactive elements in living organisms. In case of accidental or long-term release of these elements, internal contamination with actinides under either acute or chronic conditions has the potential to induce both radiological and chemical toxicity. Stable actinide cations at the formal oxidation state IV (Th, Np, Pu) as well as uranyl(VI) are of first concern in case of internal contamination, for they are able to bind to protein domains with great affinity. It is now known from physiological approaches that most actinides can be bound to serum transferrin, an abundant protein in human serum that regulates iron transport in cells. Transferrin is thus likely to be an essential vector for actinides in living organisms.

In order to understand the selective complexation and transport of actinide elements by biological vectors, a parallel strategy to physiological studies is to consider the metallobiomolecule, for instance transferrin, as an elaborate inorganic complex with well-designed metal active sites. Furthermore, in order to mimic these sites, pentapeptides have been synthesised and used to complex actinide(IV) cations. Although these ligands do not take into account all the co-operative effects that might be expected in transferrin, they can cast light on the complexation mechanisms that may occur in the transferrin binding site.

To characterise the co-ordination sphere of actinides(IV) and uranyl(VI) upon complexation with transferrin and pentapeptides, the actinide co-ordination sphere has been characterised with EXAFS spectroscopy. Complementary spectroscopic techniques as spectrophotometry have also been used and combined to the EXAFS data to investigate the actinide binding modes.

This poster will illustrate the influence of biological ligands on the co-ordination sphere of actinides.

Reduction of antimony by nanoparticulate Fe$_3$O$_4$ and FeS

R. Kirsch,[1,2] **A.C. Scheinost,**[1] **A. Rossberg,**[1] **D. Banerjee,**[1] **L. Charlet**[2]
[1]Inst. of Radiochemistry, FZD, Dresden, Germany, and ROBL at ESRF, Grenoble, France
[2]LGIT, Grenoble, France

Abstract

Antimony finds a wide range of industrial applications, e.g. in flame retardants, brake pads and as a lead-alloy in storage batteries and ammunition and is widely distributed in the environment. Sb may occur in several oxidations states (-III, 0, III, V). Under oxic conditions, Sb^0 oxidises prevalently to Sb^V, forming the anionic species Sb(OH)$_6^-$ which is strongly sorbed by Fe oxides [1]. In contrast, Sb^{III} forms an uncharged complex Sb(OH)$_3$(aq), which is more mobile. Under anoxic conditions, Sb^V and Sb^{III} may be reduced by Fe^{II}-bearing minerals. Magnetite (Fe^{II}Fe$^{III}_2$O$_4$) and mackinawite (FeS) have been shown to reduce e.g. Se [2], As [3] and Pu [4]. We therefore investigated the reaction of Sb^{III} and Sb^V with these two minerals at <1 ppm O$_2$ (v/v) using Sb-K XAS.

When Sb^{III} was reacted with magnetite at pH 4.7 to 7.6 during 1 h to 67 d, the oxidation state was stable and only one Sb species was identified by EXAFS. Sb^{III} is co-ordinated with 4 to 5 iron atoms at a distance of 3.6 Å. FEFF Monte Carlo simulations revealed formation of a highly ordered surface complex on the {111} faces of magnetite. The trigonal pyramidal SbO$_3$ units occupy positions of Fe^{III} tetrahedra, which would be ideally co-ordinated to six FeO$_6$ octahedra via corner-sharing. The experimental Fe co-ordination numbers below six suggest that Sb occupies positions near edges of the {111} faces. When Sb^V was reacted with magnetite, reduction to Sb^{III} increased linearly between pH 4.5 and 6.5, with little influence of reaction time. The Sb^{III} produced by the surface reaction formed the same surface complex as after direct addition of Sb^{III}.

In the presence of mackinawite, Sb^V was completely reduced to Sb^{III} within 30 d and in the pH range 4.3-8.4. The local structure shows Sb^{III} surrounded by three sulphur atoms at a distance of 2.5 Å as in Sb$_2$S$_3$. The lack of more distant atomic shells suggests a highly disordered structure. Again the resulting surface complex is the same as after direct addition of Sb^{III}. Cryo-XPS measurements of shock-frozen samples show that the S 2p spectra remain unchanged before and after Sb^V reduction, while a Fe^{III}-shoulder emerged in the Fe 2p spectra after reduction, indicating that Sb^V was reduced by Fe^{II} and not by S. In no case, reduction to an oxidation state below III was observed.

References

[1] Scheinost, *et al.*, *Geochim. Cosmochim. Acta*, 70, 3299-3312 (2006).

[2] Scheinost, Charlet, *Environ. Sci. Technol.* (2008), online.

[3] Gallegos, *et al.*, *Environ. Sci. Technol.*, 41, 7781-7786 (2007).

[4] Powell, *et al.*, *Environ. Sci. Technol.*, 38, 6016-6024 (2004).

EXAFS investigation of U(VI) speciation in cementitious materials

N. Macé, M. Harfouche, R. Dähn, J. Tits, E. Wieland
Paul Scherrer Institute
Villigen, Switzerland

Abstract

Cement-based materials play an important role in multi-barrier concepts developed world wide for the safe disposal of low- and intermediate-level radioactive waste. Cement is used to condition the waste materials and for the construction of the engineered barriers. Understanding the binding mechanisms of radionuclides, such as uranium, in the cement matrix thus enables us to predict their long-term fate in cementitious repositories. This information is essential for detailed assessments of the long-term safety of geologic disposal of radioactive waste.

The XAS technique (X-Ray Absorption Spectroscopy) has proven to be a powerful tool for investigating binding mechanisms in cementitious systems (see e.g. [1-3]). In the case of U(VI), previous studies showed a strong interaction of U(VI) with C-S-H phases (calcium-silicate-hydrate phases); which are a major constituent of the cement paste and the formation of different sorbing species depending on U(VI) loading and bulk-solution composition [4]. EXAFS (Extended X-Ray Absorption Fine Structure) further indicated a co-ordination environment of U(VI) in C-S-H phases similar to that in U(VI) silicate minerals, such as soddyite or uranophane [4]. In particular, a split equatorial oxygen shell with oxygen atoms at short and long distances as well as neighbouring Si atoms at short and long distances was observed [5]. One of the key issues to be addressed in the present study is whether or not the co-ordination environment of U(VI) bound in the cement matrix is similar to that in the U(VI)/C-S-H system.

In a two-year project carried out in the framework of an ACTINET collaborative project (JRP 06-13), the speciation of U(VI) in crushed hardened cement paste is currently being investigated using XAS and time-resolved laser fluorescence spectroscopy (TRLFS). The study aims at identifying the uptake controlling and the solubility limiting phase(s) for U(VI) in cementitious systems. Artificial cement pore-water (ACW, pH =13.3) solutions were used for samples preparation. The low U(VI) loaded samples (c.a. 1 000 ppm) were used to determine the structural environment of U(VI) sorbed surface complexes. The high U(VI) loaded samples (up to 10 000 ppm) were prepared for determining the chemical nature of the U(VI) solubility-limiting phase. The structural parameters obtained for U(VI) in these samples were compared with those of U(VI) reference compounds (e.g. soddyite, K-boltwoodite, schoepite, uranophane...), which were synthesised in the framework of this project. The latter compounds were first characterised using X-ray diffraction (XRD) to determine their purity and crystallinity and then secondly, they have been investigated by EXAFS and TRLFS in order to compare the measured spectroscopic parameters with those published in the open literature.

References

[1]   Scheidegger, A.M., M. Vespa, D. Grolimund, E. Wieland, M. Harfouche, I. Bonhoure, R. Dähn, *Waste Management*, 26, 699-705 (2006).

[2]   Vespa, M., E. Wieland, R. Dähn, D. Grolimund, A.M. Scheidegger, *Cem. Concr. Res.*, 37, 1473-1482 (2007).

[3]   Schlegel, M.L., I. Pointeau, N. Coreau, P. Reiller, *Environ. Sci. Technol.*, 38, 4423-4431 (2004).

[4]   Tits, J., T. Fujita, M. Tsukamoto, E. Wieland, *Mat. Res. Soc. Symp. Proc.* (2007), submitted.

[5]   Harfouche, M., E. Wieland, R. Dähn, T. Fujita, J. Tits, D. Kunz, M. Tsukamoto, *J. Colloid Interface Sci.*, 303, 195-204 (2006).

Utilisation of radiochemical procedures to separate ^{90}Sr in sea water samples

Rachida Maoui, Abdelkader Noureddine
Division de la Surveillance de l'Environnement, de la Sûreté Nucléaire et des Déchets Radioactifs
Nuclear Research Centre of Algiers
Algiers, Algeria

Abstract

Following the discovery of nuclear fission, the development of civil and military application of nuclear energy and the occurrence of the Chernobyl accidents has contributed to the transfer of important quantities of radioactivity to the environment in general and to the seas in particular. Among these artificial radioactivity, the most important radionuclides are ^{137}Cs ($T_{1/2}$ = 30 Y) and ^{90}Sr ($T_{1/2}$ = 28 Y).

The purpose of this work is the determination of the concentration of ^{90}Sr in the Mediterranean Sea. This radionuclide is very soluble in sea water and could be found only as traces. The β-emitter is not easy to detect on site and requires the use of large volumes of water (150 l) in chemical processes in order to extract this radioelement.

In the present paper, two different methods are used to extract this radionuclide and compared.

The first one passes through different steps from the dissolution of the sample in concentrated acids (HF, HCl and HNO$_3$) and the extraction of ^{90}Sr using the Crown ether selective resins, the preparation of the source in wattman type of paper filter of 2 cm diameter. The source is then accounted for using a liquid scintillator type Beckman 6500.

The second method passes through others steps beginning by the elimination of potassium, of calcium and sodium, then the separation of radium and barium and of the actinides. After three weeks storage of the obtained solution, two precipitations of yttrium hydroxide are done in order to maximise the separation of Sr rand Yt. After this step, we prepare a precipitation of yttrium oxalate which is filtered using Gelmann HT-200 filter (porosity of 0.2 μm and 22 mm of diameter). The yield is obtained by weighing; the filter and the precipitate are counted using a beta detector.

According to the results, we noticed the good dissolution obtained with the second method, which leads to a better chemical yield. The second method is also faster than the first one and has provided acceptable results.

Extended X-ray absorption fine structure spectroscopic and time resolved laser fluorescence studies of actinide sorption on montmorillonite: Influence of carbonate complexation

M. Marques Fernandes,[1] **R. Dähn,**[1] **B. Baeyens,**[1] **Th. Rabung,**[2] **M.H. Bradbury**[1]
[1]Laboratory for Waste Management, Paul Scherrer Institut, Villigen, Switzerland
[2]Institut für Nukleare Entsorgung, Forschungszentrum Karlsruhe, Karlsruhe, Germany

Abstract

Clay minerals play an important role in the retention/retardation of radio-contaminants in the near- and far-fields of a radioactive waste repository. Identifying and quantifying the radionuclide sorption processes occurring at clay/solution interface over a representative range of relevant conditions is indispensable for performance assessment [1].

Next to hydroxide ions, carbonate is the predominant inorganic ligand in most natural groundwaters and clay porewaters. Trivalent actinides are known to form very strong carbonate complexes in solution, which could potentially decrease the metal ion sorption and thus increase the migration rates of actinides [2]. Sorption models which neglect the influence of carbonate may incorrectly predict radionuclide sorption in natural clay systems. The aim of this study is to investigate the influence of dissolved inorganic carbon on the sorption behaviour of trivalent actinides onto clay minerals.

Polarised Extended X-ray Absorption Fine Structure Spectroscopy (P-EXAFS) and Time Resolved Laser Fluorescence Spectroscopy (TRLFS) were applied to obtain a molecular level understanding of the uptake processes of Am(III)/Cm(III)-carbonate complexes on clay minerals.

Bulk and P-EXAFS measurements were performed on Am(III) loaded wet montmorillonite pastes and self supporting montmorillonite films respectively. Samples were prepared in the absence (pH = 8) and presence of inorganic carbon (20 mM $NaHCO_3$ at pH 7.4 and 8.3) at a range of Am(III) loadings down to 100 ppm (0.4 $\mu mol \cdot g^{-1}$). One limitation of bulk EXAFS is the difficulty to differentiate between atoms of similar atomic number (Si, Al). The application of P-EXAFS on highly oriented self-supporting montmorillonite films allows the contribution of cations from silicium tetrahedral sheets to be minimised by orienting the film plane parallel to the polarisation direction of the X-ray beam, and, conversely, the contribution of the cations from the aluminium octahedral sheets to be attenuated by orienting the film plane perpendicular to the polarisation direction. The EXAFS spectra obtained by both methods for the samples prepared in the presence and absence of carbonate clearly show different features which might be an indication of the formation of ternary Am-carbonate surface complexes. Furthermore, a polarisation dependency was observed for the Am-carbonate-montmorillonite system.

The EXAFS investigations were complemented with TRLFS measurements on Cm(III) loaded montmorillonite wet pastes. Cm(III) is used instead of Am(III) because it has a much higher fluorescence sensitivity and is considered to be a good chemical analogue for trivalent actinides. The position and intensity of the fluorescence emission peaks allow the identification of different species to be made, and, to differentiate between inner- or outer-sphere complexation. In addition, the fluorescence lifetime provides sensitive information on the co-ordination environment, especially the presence of H_2O/OH^- molecules in the first co-ordination sphere of the Cm(III) ion. The fluorescence emission spectra of the Cm(III)-carbonate-montmorillonite systems investigated are clearly shifted to higher wavelengths compared to the those of the carbonate-free system indicating different co-ordination environments for Cm(III), supporting the results obtained by EXAFS.

References

[1]   Nagra, *Project Opalinus Clay: Safety Report. Demonstration of Disposal Feasibility (Entsorgungsnachweis) for Spent Fuel, Vitrified High-level Waste and Long-lived Intermediate-level Waste*, Nagra Technical Report NTB 02-05, Nagra, Wettingen, Switzerland (2002).

[2]   Fanghänel, T., T. Konnecke, H. Weger, P. Paviet-Hartmann, V. Neck, J.I. Kim, "Thermodynamics of Cm(III) in Concentrated Salt Solutions: Carbonate Complexation in NaCl Solution at 25°C", *Journal of Solution Chemistry*, 28 (4), pp. 447-462 (1999).

XAS study of Am$_2$Zr$_2$O$_7$ pyrochlore: Evolution under alpha self-irradiation

P. Martin,[1] **R. Belin,**[1] **P. Valenza,**[1] **A.C. Scheinost**[2]
[1]CEA Cadarache, DEN/DEC, St. Paul-lez-Durance, France
[2]Forschungszentrum Dresden-Rossendorf (FZD), Institute of Radiochemistry, Dresden, Germany

Abstract

Management of long-lived nuclear wastes is, after safety, the main issue facing the nuclear industry, both in terms of the scientific challenge as well as public acceptance. Among the different options that have been envisioned and explored for minor actinides over the past thirty years, two alternatives currently remain: long-term disposal in a safe repository or "burning" of nuclear wastes in a so-called transmutation process. Materials selected for such applications have to meet the following criteria: high incorporation of actinides, good structural and chemical stability, low thermal dilatation and resistance to radiation.

Among the various ceramics envisaged, zirconia-based pyrochlore oxides of composition An$_2$Zr$_2$O$_7$ (An = actinide) appear to be ideal candidates. Results obtained with lanthanide pyrochlores submitted to ion-beam irradiation show that Zr-based pyrochlores, unlike Ti-based, remain crystalline with a transition from the pyrochlore to a defect fluorite structure [1]. The ordered pyrochlore belongs to the Fd-3m space group and is a superstructure of the ideal defect fluorite structure (Fm-3m) with exactly twice the lattice constant. In the pyrochlore structure, the co-ordination shell of Am cations [8 (2+6) oxygen atoms] is distinct from that of Zr cations (6 oxygen atoms), whereas the second co-ordination shell (cation-cation) is the same for both cations (6xAm + 6xZr at the same distance). The structural phase transition from pyrochlore to defective fluorite involves the randomisation of the oxygen atoms into the anionic and vacant positions of the pyrochlore structure. In the ideal fluorine defect structure, the Am and Zr cations share the same position and thus have the same local environment: a first co-ordination shell consisting of 7 oxygen atoms at the same distance and the same second co-ordination shell as observed in the pyrochlore structure.

The objective of this study was to investigate the radiation tolerance of Zr pyrochlore during a more realistic experiment using alpha-emitting ^{241}Am as structural component. ^{241}Am$_2$Zr$_2$O$_7$ sample was synthesised [2] and its evolution under the effect of alpha self-irradiation as a function of time was followed by XRD. A transition from the pyrochlore phase to a defect-fluorite phase was observed after ~200 days as the superstructure peaks slowly vanished and completely disappeared after about 200 days [3]. The resulting fluorite structure is surprisingly resistant to self-irradiation induced amorphisation as compared to other materials considered for transmutation or long-term storage [4]. In order to better understand the underlying phenomena involved in this phase transition as well as the significant resistance to amorphisation of the defect fluorite phase, we investigated the local environments of Am and Zr by XAS.

XANES and EXAFS spectra of two Am$_2$Zr$_2$O$_7$ samples were collected at Zr-K and Am-L$_{II}$ edges at a temperature of 15 K on the Rossendorf Beamline at ESRF. The first sample (called "fresh") was synthesised a few weeks before the experiment, whereas the second sample (called "old") was a year old. X-ray diffraction measurements performed prior to XAS measurements attested for a pyrochlore structure (Fd-3m a = 10.667 Å) for the "fresh" sample and for a defect-fluorite (Fm-3m a = 5.323 Å) for the "old" one. The Fourier transforms at both edges are compared in Figures 1 and 2.

Figure 1: Fourier transforms at Am-L$_{II}$ edge
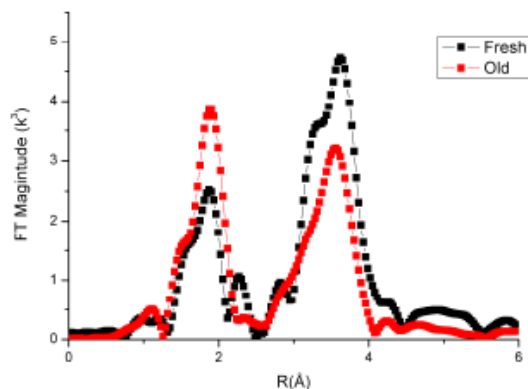
Figure 2: Fourier transforms at Zr-K edge
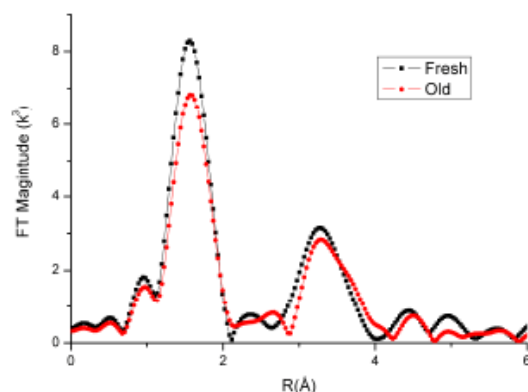
In the case of americium, a clear modification of radial distribution around Am ions can be observed. For the fresh sample, the fit gives the expected pyrochlore local environment with: 2.9 O at 2.33 Å, 4.9 O at 2.53 Å, 6 Am at 3.75 Å and 6 Zr at 3.74 Å. For the old sample, the fit confirms the fluorite structure with a first co-ordination shell consisting of only one shell of 5.3 O at 2.35 Å (peak at ~1.9 Å in Figure 1). The cation-cation shells included in the second (peak at ~3.8 Å in Figure 1) are clearly distorted with 6 Am at 3.76 Å and 6 Zr at 3.67 Å. The Am-Am distance is coherent with the fluorite structure but the Am-Zr distance is shorter than expected. Such observations seem to indicate that the local environment of Zr does not follow the evolution observed around Am ions.

Results obtained at Zr-K edge validate this hypothesis: the Zr-O polyhedra with only one co-ordination shell at ~2.12 Å (peak at ~1.8 Å in Figure 2) remain stable during 1 year of alpha self-irradiation. In contrast, the cation-cation co-ordination sphere (peak at ~3.3 Å in Figure 2) follows the same evolution observed at the Am-L$_{II}$ edge, with a distortion due to different Zr-Zr and Zr-Am distances.

In conclusion, alpha self-irradiation induces substantial changes in the local structure around Am cations, whereas the ZrO$_6$ polyhedra seem to be very robust against irradiation. The same conclusions have been obtained on Gd$_2$(Ti,Zr)$_2$O$_7$ pyrochlore samples submitted to ion irradiation [5]. Thus, the structural phase transition from the pyrochlore structure to the fluorite defect structure appears to be rather a disruption of the long-range order probed by XRD due to cation disorder and interpolyhedral (ZrO$_6$ and AmO$_8$) rotations along edges and corners leading to the change in Am environment and the disorder in second co-ordination shells. To definitively conclude on the mechanisms induced by alpha self-irradiation, XAS measurements on a sample aged for two years are planned.

References

[1]   Sickafus, K.E., *et al.*, *Nature Materials*, 6, 217-223 (2007).

[2]   Belin, R.C., *et al.*, *J. Alloys Compounds*, 448, 321-324 (2008).

[3]   Belin, R.C., *et al.*, *Actinides 2005 Conference – Recent Advances in Actinide Science*, Manchester (UK), 4-8 July 2005, University of Manchester RSC Publishing, p. 352.

[4]   Trachenko, K., *J. Phys.: Cond. Matt.*, 16, 1491-1515 (2004).

[5]   Hess, N.J., *et al.*, *J. Phys. Chem. B*, 106, 4663-4677 (2002).

New crystal-chemical approach to non-Vegardianity and complex defect structure in the fluorite-based MO_2-$LnO_{1.5}$ solid solutions (M = Ce, Th; Ln = lanthanide)

Akio Nakamura
Advanced Science Research Centre, Japan Atomic Energy Agency
Ibaraki, Japan

Abstract

Lattice-parameter (a_0) data of defect-fluorite (DF)-type solid solutions (ss), $M_{1-y}Ln_yO_{2-y/2}$ (M^{4+} = Ce, Th; Ln^{3+} = Y, Gd, Eu, Sm, Nd, La), have been extensively compiled and thoroughly analysed by the crystal-chemical model proposed by us [1,2]. Due to the oxygen vacancy (V_O) formation, their a_0(ss) data exhibit marked positive deviation from the Vegard law (VL) (here-defined non-Vegardianity: Δa_0(ss) = a_0(ss) − a_0(VL) >> 0), which is systematically larger in the M^{4+} = Th than in the Ce systems. Also in the former, this diminishes more evidently with increasing Ln^{3+} ion size. Though not well recognised, including the slightly negatively non-Vegardian M^{4+} = Zr and Hf systems (Δa_0(ss) < 0), to the author's knowledge, these DF oxides are the most markedly and systematically non-Vegardian systems ever known. The proposed model can describe well the remarkably non-Vegardian behaviour of these systems consistently and quantitatively, using newly-devised systematised Shannon's ionic radii of the constituent cations, $r_C(M^{4+})$ and $r_C(Ln^{3+})$, as a function of oxygen co-ordination number (CN). By generalising the random oxygen-CN model in [1,2] to the non-random-CN one, the author shows that their marked non-Vegardianity (in the conventional Vegard law) is in fact primarily the generalised Vegardian behaviour of these oxygen-deficit MO_2-$LnO_{1.5}$ solid solutions at random oxygen CN, $CN(M^{4+})$ = $CN(Ln^{3+})$ = 8-2 y, modified by the non-randomness of the system, i.e. non-random oxygen CN, $CN(M^{4+}) \neq CN(Ln^{3+}) \neq$ 8-2 y. Their detailed numerical a_0(ss) analyses indicate that the Ce systems are basically near random (CN ~ 8-2 y), showing only weak Ln^{3+}-V_O association in the low y range. While, the more non-Vegardian Th systems exhibit an intriguing trend that this shifts from near random for the most non-Vegardian (smallest two) Ln = Y and Gd to extremely non-random tight (Ln^{3+}-V_O) association [$CN(Ln^{3+}) << CN(M^{4+})$] for the least non-Vegardian (largest two) Ln = Nd and La. All these results demonstrate the basic validity and the practical applicability of the present model as a quantitative a_0 model for these DF oxides, providing a new direct link to their local $M^{4+}(Ln^{3+})$-V_O structure. In view of the well-known chemical similarity of Ce and Pu, the present model is expected to be a basis for simulating a_0(ss) behaviour and defect-related local structure in the M^{4+} = Pu (and related Np and Am, etc. = MA) systems.

References

[1]   Otobe, H., A. Nakamura, "SOFC-VI", *The Electrochem. Soc. Proc.*, 99-19 (NJ, USA, 1999), p. 463.

[2]   Nakamura, A., N. Masaki, H. Otobe, Y. Hinatsu, J. Wang, M. Takeda, *Pure and Applied Chem.*, 79 (10), 1691 (2007).

Soft X-ray scanning transmission X-ray microscopy of actinide materials and complexes

David K. Shuh,[1] **Tolek Tyliszczak,**[2] **Rainer Daehn,**[3] **Geza Szigethy,**[1,4] **Kenneth N. Raymond**[1,4]
[1]Chemical Sciences Division, [2]Advanced Light Source Division
Lawrence Berkeley National Laboratory, Berkeley, CA, USA
[3]Laboratory for Waste Management, Paul Scherrer Institute, Villigen, Switzerland
[4]Department of Chemistry, University of California Berkeley, Berkeley, CA, USA

Abstract

The Advanced Light Source (ALS) has several beamlines that are being used for a range of radioactive materials investigations [1]. Of the techniques available at ALS beamlines, soft X-ray scanning transmission X-ray microscopy (STXM) spectromicroscopy at the ALS-Molecular Environmental Science (ALS-MES) Beamline 11.0.2 has been utilised on a regular basis to characterise actinide materials, complexes, and particulates in the soft X-ray regime by near-edge X-ray absorption fine structure (NEXAFS) [2]. The ALS-MES STXM can image and collect NEXAFS spectra of radioactive materials in a non-vacuum environment with a spatial resolution better than 30 nm from approximately 125 eV to 2 150 eV. An important characteristic of the ALS-MES STXM is the capability to directly probe with NEXAFS both actinide 4d core levels (700-900 eV) as well as low Z element K-edges such as carbon, oxygen and nitrogen, which are frequently key constituents of actinide materials. NEXAFS spectromicroscopy experiments of actinide materials have included investigations of actinide reference materials, biological systems, colloids, waste form glasses, clays and cements [3-6].

The spectroscopic results from selected lanthanide complexes, actinide complexes and from recent STXM investigations of transuranium materials will be presented and discussed. The spectroscopic results from recent STXM investigations of transuranium complexes of primarily plutonium, along with those from several corresponding lanthanide complexes (used as a surrogate or for a direct comparison to actinide behaviour) will be presented and discussed in terms of bonding characteristics including contributions from the light element constituents. The actinide complexes include those derived from ligation with simple carboxylic acids and those formed from a modified class of hydroxypyridinone (HOPO) ligands (Raymond ligands) designed for selective complexation of actinides. This will include Pu(IV) maltol and bromomaltol complexes that provide intriguing comparisons to their Ce(IV) analogues and small complexes of plutonium with simple ligands.

During the collection of NEXAFS spectra from several simple light element Pu complexes with normal dwell times, radiation damage can be clearly observed in the light element K-edge NEXAFS spectra and in at least one case, there is an apparent change in actinide oxidation state observed as a charge state shift at the actinide 4d edge. Radiation damage in sensitive actinide complexes can be circumvented by operating the STXM with high scan rates while still retaining outstanding signal to background response. The unique current scientific opportunities, as well as the limitations for the experimental and theoretical investigations of a range of actinide science utilising the ongoing developments of the ALS-MES STXM will be highlighted.

The work at ALS BL 11.0.2 was supported in part by the Director, Office of Science, Office of Basic Energy Sciences, Division of Chemical Sciences, Geosciences, and Biosciences of the US Department of Energy at Lawrence Berkeley National Laboratory under Contract No. DE-AC02-05CH11231.

References

[1]   Shuh, D.K., "Scientific Capabilities of the Advanced Light Source for Radioactive Materials", *Speciation, Techniques and Facilities for Radioactive Materials at Synchrotron Light Sources*, OECD NEA Workshop Proceedings, Karlsruhe, Germany, September 2006, OECD/NEA, Paris, pp. 125-134 (2007).

[2]   Bluhm, H., K. Andersson, T. Araki, K. Benzerara, H. Bluhm, G.E. Brown, Jr., J.J. Dynes, S. Ghosal, H-Ch. Hansen, J.C. Hemminger, A.P. Hitchcock, G. Ketteler, E. Kneedler, J.R. Lawrence, G.G. Leppard, J. Majzlam, B.S. Mun, S.C.B. Myneni, A. Nilsson, H. Ogasawara, D.F. Ogletree, K. Pecher, D.K. Shuh, M. Salmeron, B. Tonner, T. Tyliszczak, T.H. Yoon, *J. Electron Spectros. Rel. Phenom.*, 150, 86-104 (2006).

[3]   Nilsson, H.J., T. Tyliszczak, R.E. Wilson, L. Werme, D.K. Shuh, *J. Anal. Bioanal. Chem.*, 383, 41-47 (2005).

[4]   Nilsson, H.J., T. Tyliszczak, R.E. Wilson, L. Werme, D.K. Shuh, "Soft X-ray Spectromicroscopy of Actinide Particulates", in *Recent Advances in Actinide Science*, R. Alvarez, N.D. Bryan, I. May (Eds.), *Proc. Royal Soc. Chem.*, Cambridge, UK (2006), pp. 56-58.

[5]   Fillaux, C., C. Den Auwer, D. Guillaumont, D.K. Shuh, T. Tyliszczak, *J. Alloy Comp.*, 445-445, 443-446 (2007).

[6]   Fillaux, C., J-C. Berthet, S.D. Conradson, P. Guilbaud D. Guillaumont, C. Hennig, P. Mois, J. Roques, E. Simoni, D.K. Shuh, T. Tyliszczak, I. Castro-Rodriguez, C. Den Auwer, C. R. Chimie, 10, 8459-8471 (2007).

Uranium association and speciation with gram negative bacteria using EXAFS and transmission electron microscopy

G. Untereiner,[1] **O. Proux,**[2] **J.L. Hazemann,**[2] **M. Carrière,**[1] **B. Gouget**[1]
[1]Laboratoire Pierre Süe, CEA-CNRS UMR 9956, CEA/Saclay, Gif-sur-Yvette, France
[2]FAME Beamline (BM30B), ESRF, Grenoble, France

Abstract

Uranium (U) is an element with considerable chemical and radiological toxicity that is of concern in cases of high natural abundance, for incidents of environmental pollution or in connection with storage of nuclear wastes. Uranium can undergo oxidation-reduction reactions in the environment (reduction of U^{VI} to U^{IV}) or reactions to form complexes with anions (e.g. phosphate, carbonate and sulphate ions) and organic matter (humic acids for instance). Conditions that increase the rate of formation of soluble complexes and decrease the rate of sorption of labile uranium in soil enhance its mobility. Besides, its bioavailability and toxicity are strongly dependant on its speciation.

In this work, microbial associations with U were focused on. In vitro studies were conducted with soil bacteria: one with high metal tolerance, Cupriavidus metallidurans CH34 and one with phototrophic ability, Rhodopseudomonas palustris. Bacteria were cultured in the presence of different species of uranium and the effect of different pH was studied.

No major accumulation could be measured at pH 7 but about 20% of the initial amount of uranium was found with bacterial pellet at pH 1. We used a combination of Extended X-ray Absorption Fine Structure (EXAFS) and Transmission Electron Microscopy (TEM) to study the interaction. Our first data indicate that bacteria can precipitate uranyl citrate or uranyl malate complexes to uranyl phosphate. These precipitates have been observed by TEM, they progressively spread over bacterial intracellular compartment. However this precipitation was only observed in lethal conditions, i.e. when uranyl is provided to bacteria at pH 2.

For the first time, these two strains were compared for their capacity to metabolise uranium. Under certain conditions they may be used in bioremediation studies.

Annex 1: List of participants (and final registered persons)

Algeria

Hakim	Brahimi	Nuclear Research Centre of Algiers	hak_brahimi@yahoo.fr
Rachida	Maoui	Nuclear Research Centre of Algiers	r_maoui@hotmail.fr

Belgium

Rik	Van Deun	K.U.Leuven	rik.vandeun@chem.kuleuven.be

Egypt

Nader M.A.	Mohamed	Atomic Energy Authority	mnader73@yahoo.com

France

James	Ablett	Synchrotron SOLEIL	james.ablett@synchrotron-soleil.fr
Isabelle	Alliot	CEA Grenoble	alliot@esrf.fr
Maria-Carmen	Asensio	Synchrotron SOLEIL	asensio@synchrotron-soleil.fr
Jose	Avila	Synchrotron SOLEIL	jose.avila@synchrotron-soleil.fr
François	Baudelet	Synchrotron SOLEIL	françois.baudelet@synchrotron-soleil.fr
Catherine	Bessada	CEMHTI, CNRS Orléans	catherine.bessada@cnrs-orleans.fr
Olivier	Bouty	CEA Marcoule	olivier.bouty@cea.fr
Carole	Bresson	CEA Saclay	carole.bresson@cea.fr
Pascal	Chaix	CEA Saclay	pascal.chaix@cea.fr
Sudipta	Chakraborty	University of Grenoble	Sudipta.Chakraborty@obs.ujf-grenoble.fr
Mireille	Defranceschi	OECD/NEA	Mireille.DEFRANCESCHI@oecd.org
Jean-Marc	Delaye	CEA Marcoule	jean-marc.delaye@cea.fr
Christophe	Den Auwer	CEA Marcoule	christophe.denauwer@cea.fr
Denis	Duflot	University of Lille	denis.duflot@univ-lille1.fr
Philippe	Faure	CEA Valduc	philippe.faure@cea.fr
Clara	Fillaux	CEA Marcoule	clara.fillaux@cea.fr
Hubert	Flocard	CNRS, IN2P3 Orsay	flocard@csnsm.in2p3.fr

Frédérique	Fraissard	Synchrotron SOLEIL	frederique.fraissard@synchrotron-soleil.fr
Lisa	Giachini	CNRS, Univ. of Bourgogne	lisa.giachini@u-bourgogne.fr
Barbara	Gouget	AFSSA	b.gouget@afssa.fr
Denis	Guillaneux	CEA Marcoule	denis.guillaneux@cea.fr
Aurélie	Jeanson	CNRS, IN2P3 Nantes	Aurelie.Jeanson@subatech.in2p3.fr
Sylvie	Koguc	Synchrotron SOLEIL	sylvie.koguc@synchrotron-soleil.fr
Stéphane	Lequien	CEA Grenoble	stephane.lequien@cea.fr
Jean-Marc	Lucacchioni	Synchrotron SOLEIL	jean-marc.lucacchioni@synchrotron-soleil.fr
Philippe	Martin	CEA Cadarache	martinp@drncad.cea.fr
Corinne	Mazouffre	Synchrotron SOLEIL	corinne.mazouffre@synchrotron-soleil.fr
Le Vi	Nguyen	CEA Valduc, Univ. of Bourgogne	le-vi.nguyen@cea.fr
Hervé	Palancher	CEA- Cadarache	herve.palancher@cea.fr
Anthony	Pavan	Synchrotron SOLEIL	sylvie.pavan@synchrotron-soleil.fr
Sylvie	Pavan	Synchrotron SOLEIL	sylvie.pavan@synchrotron-soleil.fr
Sylvain	Peuget	CEA Marcoule	sylvain.peuget@cea.fr
Michel	Schlegel	CEA Saclay	michel.schlegel@cea.fr
Sandrine	Schlutig	Synchrotron SOLEIL	sandrine.schlutig@synchrotron-soleil.fr
Véronique	Schweitzer	Synchrotron SOLEIL	veronique.schweitzer@synchrotron-soleil.fr
Claire	Sergeant	CNRS, Univ. of Bordeaux	claire.sergeant@cnab.cnrs.fr
Eric	Simoni	CNRS, Univ. Paris-Sud 11	simoni@ipno.in2p3.fr
Bruno	Sitaud	Synchrotron SOLEIL	bruno.sitaud@synchrotron-soleil.fr
Pier Lorenzo	Solari	Synchrotron SOLEIL	pier-lorenzo.solari@synchrotron-soleil.fr
Riccardo	Spezia	CNRS, University of Evry	riccardo.spezia@univ-evry.fr
Christophe	Thiebaut	CEA Bruyères-le-Châtel	christophe.thiebaut@cea.fr
Guillaume	Untereiner	CNRS, CEA Saclay	guillaume.untereiner@cea.fr
Michel	van der REST	Synchrotron SOLEIL	michel.vanderrest@synchrotron-soleil.fr
Eléonore	Welcomme	CEA Cadarache	eleonore.welcomme@cea.fr

Germany

Olga	Batuk	Forschungszentrum Karlsruhe	olga.batuk@ine.fzk.de
Boris	Brendebach	Forschungszentrum Karlsruhe	boris.brendebach@ine.fzk.de

Kathy	Dardenne	Forschungszentrum Karlsruhe	kathy.dardenne@ine.fzk.de
Melissa A.	Denecke	Forschungszentrum Karlsruhe	melissa.denecke@ine.fzk.de
Harald	Funke	Forschungszentrum Dresden-Rossendorf	funke@esrf.fr
Christoph	Hennig	Forschungszentrum Dresden-Rossendorf	hennig@esrf.fr
Atsushi	Ikeda	Forschungszentrum Dresden-Rossendorf/ JAEA	a.ikeda-ohno@spring8.or.jp
Regina	Kirsch	Forschungszentrum Dresden-Rossendorf	kirsch@esrf.fr
Oanh Phi	Lam	University of Erlangen-Nuremberg	OanhPLam@gmail.com
Xiaolan	Liu	Forschungszentrum Karlsruhe	xiaolan.liu@ine.fzk.de
Mohamed	Merroun	Forschungszentrum Dresden-Rossendorf	merroun@fzd.de
Pauline	Michel	Forschungszentrum Karlsruhe	Pauline_Michel@ine.fzk.de
Henry	Moll	Forschungszentrum Dresden Rossendorf	h.moll@fzd.de
Tobias	Reich	University of Mainz	tobias.reich@uni-mainz.de
André	Rossberg	Forschungszentrum Dresden-Rossendorf	rossberg@esrf.fr
Sonja	Selenska-Pobell	Forschungszentrum Dresden-Rossendorf	s.selenska-pobell@fzd.de
Satoru	Tsushima	Forschungszentrum Dresden-Rossendorf	S.Tsushima@fzd.de
Tonya	Vitova	Forschungszentrum Karlsruhe	Tonya.Vitova@ine.fzk.de

India

| Jena | Vinod Kumar | University of Raipur | jenavinodkumar@yahoo.com |

Japan

Akira	Kitamura	Japan Atomic Energy Agency	akira.kitamura@psi.ch
Akio	Nakamura	Japan Atomic Energy Agency	nakamura.akio@jaea.go.jp
Haruaki	Matsuura	CNRS Orléans/Tokyo Institute of Technology	hmatsuur@nr.titech.ac.jp
Akihiro	Uehara	Kyoto University	auehara@HL.rri.kyoto-u.ac.jp

Tsuyoshi	Yaita	Japan Atomic Energy Agency	yaita@spring8.or.jp
Hiroshi	Yamagami	Kyoto Sangyo University	yamagami@cc.kyoto-su.ac.jp
Shinichi	Suzuki	Japan Atomic Energy Agency	suzuki.shinichi@jaea.go.jp

Russia

| Stepan | Kalmykov | Lomonosov Moscow State University | stepan@radio.chem.msu.ru |

Spain

| Regla | Ayala Espinar | University of Seville | rae@icmse.csic.es |
| Elizabeth | Corbacho Beret | University of Seville | eli@us.es |

Sweden

| Rajeev | Ahuja | Uppsala University | rajeev@fysik.uu.se |
| Sergei | Butorin | Uppsala University | sergei.butorin@fysik.uu.se |

Switzerland

Rainer	Daehn	Paul Scherrer Institut	rainer.daehn@psi.ch
Daniel	Grolimund	Paul Scherrer Institut	daniel.grolimund@psi.ch
Nathalie	Macé	Paul Scherrer Institut	nathalie.mace@psi.ch
Maria	Marques Fernandes	Paul Scherrer Institut	maria.marques@psi.ch

United Kingdom

Marina	Dawes	Atomic Weapons Establishment	marina.dawes@awe.co.uk
David	Geeson	Atomic Weapons Establishment	davidgeeson@yahoo.co.uk
Simon	MacLeod	Atomic Weapons Establishment	uccamac@ucl.ac.uk
Stephen	Parry	University of Manchester	stephen.parry@manchester.ac.uk
Clint Alan	Sharrad	University of Manchester	clint.a.sharrad@manchester.ac.uk
Helen	Thompson	Atomic Weapons Establishment	helen.thompson@awe.co.uk
Gerrit	van der Laan	Diamond Light Source	g.vanderlaan@dl.ac.uk

United States

Ilham	Al Mahamid	Wadsworth Center – Laboratory of Inorganic and Nuclear Chemistry	almahamid@lbl.gov
Corwin H.	Booth	Lawrence Berkeley National Laboratory	chbooth@lbl.gov
Steven	Conradson	Los Alamos National Laboratory	conradson@lanl.gov
Alison	Costello	Los Alamos National Laboratory	alisonc@lanl.gov
Michael	Manley	Lawrence Livermore National Laboratory	manley3@llnl.gov
Kevin Thomas	Moore	Lawrence Livermore National Laboratory	moore78@llnl.gov
David	Shuh	Lawrence Berkeley National Laboratory	dkshuh@lbl.gov
James G.	Tobin	Lawrence Livermore National Laboratory	Tobin1@llnl.Gov
Marianne	Wilkerson	Los Alamos National Laboratory	mpw@lanl.gov
Ping	Yang	Pacific Northwest National Laboratory	ping.yang@pnl.gov

Annex 2: Committees and invited speakers

Local organising committee

Pascal Chaix (CEA, Saclay)
Christophe Den Auwer (CEA, Marcoule)
Frédérique Fraissard (Synchrotron SOLEIL)
Barbara Gouget (AFSSA)
Sylvie Koguc (Synchrotron SOLEIL)
Stéphane Lequien (CEA, Grenoble)

Jean-Marc Lucacchioni (Synchrotron SOLEIL)
Véronique Schweitzer (Synchrotron SOLEIL)
Eric Simoni (CNRS, Université Paris Sud)
Bruno Sitaud (Synchrotron SOLEIL)
Pier Lorenzo Solari (Synchrotron SOLEIL)

International scientific advisory committee

Corwin Booth (USA)
Steve Conradson (USA)
Rainer Dähn (Switzerland)
Mireille Defranceschi (OECD, NEA)
Christophe Den Auwer (France)
Melissa Denecke (Germany)
Thomas Fanghänel (Germany)
Asun Fernandez (Germany)
Günter Kaindl (Germany)
Stephan Kalmykov (Russia)
Kenneth Kemmer (USA)

Stéphane Lequien (France)
Francis Livens (United Kingdom)
Tobias Reich (Germany)
Andreas Scheinost (Germany)
David Shuh (USA)
Eric Simoni (France)
Bruno Sitaud (France)
Joseph Somers (Germany)
Jim Tobin (USA)
Tsuyoshi Yaita (Japan)

Invited speakers

O. Batuk
Forschungszentrum Karlsruhe, Germany
Moscow State University, Russia

C. Booth
Lawrence Berkeley National Laboratory, USA

B. Brendebach
Forschungszentrum Karlsruhe, Germany

S. Conradson
Los Alamos National Laboratory, USA

R. Dähn
Paul Scherrer Institut, Switzerland

D. Grolimund
Paul Scherrer Institut, Switzerland

O.P. Lam
University of Erlangen-Nuremberg, Germany

P. Martin
Commissariat à l'énergie atomique, France

S. Selenska-Pobell
Forschungszentrum Dresden-Rossendorf, Germany

C. A. Sharrad
The University of Manchester, United Kingdom

D.K. Shuh
Lawrence Berkeley National Laboratory, USA

S. Suzuki
Japan Atomic Energy Agency, Japan

S. Tsushima
Forschungszentrum Dresden-Rossendorf, Germany

G. van der Laan
Diamond Light Source, United Kingdom

T. Yaita,
Japan Atomic Energy Agency, Japan

H. Yamagami
Kyoto Sangyo University, Japan

P. Yang
Los Alamos National Laboratory, USA

Annex 3: Support organisations

Synchrotron SOLEIL

Commissariat à l'Énergie Atomique

ACTINET
European Network of Excellence
for Actinide Sciences

Region Île-de-France

Centre National de la Recherche Scientifique
Programme sur l'Aval du Cycle
et l'Énergie Nucléaire

OECD Nuclear Energy Agency